

Measurement of the $K^\pm \rightarrow \pi^+ \pi^- e^\pm \bar{\nu}_e$ form factors and of the $\pi\pi$ scattering length a_0^0

Dissertation
zur Erlangung des Grades
“Doktor der Naturwissenschaften”
am Fachbereich Physik der
Johannes Gutenberg-Universität Mainz

Lucia Masetti
geboren in Ravenna (Italien)

Mainz 2006

Abstract

The quark condensate is a fundamental free parameter of Chiral Perturbation Theory (χPT), since it determines the relative size of the mass and momentum terms in the power expansion. In order to confirm or contradict the assumption of a large quark condensate, on which χPT is based, experimental tests are needed. In particular, the S -wave $\pi\pi$ scattering lengths a_0^0 and a_0^2 can be predicted precisely within χPT as a function of this parameter and can be measured very cleanly in the decay $K^\pm \rightarrow \pi^+ \pi^- e^\pm \bar{\nu}_e$ (K_{e4}).

About one third of the data collected in 2003 and 2004 by the NA48/2 experiment were analysed and 342,859 $K^\pm \rightarrow \pi^+ \pi^- e^\pm \bar{\nu}_e$ (K_{e4}) candidates were selected. The background contamination in the sample could be reduced down to 0.3% and it could be estimated directly from the data, by selecting events with the same signature as K_{e4} , but requiring for the electron the opposite charge with respect to the kaon, the so-called “wrong sign” events. This is a clean background sample, since the kaon decay with $\Delta S = -\Delta Q$, that would be the only source of signal, can only take place through two weak decays and is therefore strongly suppressed.

The Cabibbo-Maksymowicz variables, used to describe the kinematics of the decay, were computed under the assumption of a fixed kaon momentum of 60 GeV/ c along the z axis, so that the neutrino momentum could be obtained without ambiguity. The measurement of the form factors and of the $\pi\pi$ scattering length a_0^0 was performed in a single step by comparing the five-dimensional distributions of data and MC in the kinematic variables. The MC distributions were corrected in order to properly take into account the trigger and selection efficiencies of the data and the background contamination. The following parameter values were obtained from a binned maximum likelihood fit, where a_0^2 was expressed as a function of a_0^0 according to the prediction of chiral perturbation theory:

$$\begin{aligned} f'_s/f_s &= 0.133 \pm 0.013 \text{ (stat)} \pm 0.026 \text{ (syst)}, \\ f''_s/f_s &= -0.041 \pm 0.013 \text{ (stat)} \pm 0.020 \text{ (syst)}, \\ f_e/f_s &= 0.221 \pm 0.051 \text{ (stat)} \pm 0.105 \text{ (syst)}, \\ f'_e/f_s &= -0.459 \pm 0.170 \text{ (stat)} \pm 0.316 \text{ (syst)}, \\ \tilde{f}_p/f_s &= -0.112 \pm 0.013 \text{ (stat)} \pm 0.023 \text{ (syst)}, \\ g_p/f_s &= 0.892 \pm 0.012 \text{ (stat)} \pm 0.025 \text{ (syst)}, \\ g'_p/f_s &= 0.114 \pm 0.015 \text{ (stat)} \pm 0.022 \text{ (syst)}, \\ h_p/f_s &= -0.380 \pm 0.028 \text{ (stat)} \pm 0.050 \text{ (syst)}, \\ a_0^0 &= 0.246 \pm 0.009 \text{ (stat)} \pm 0.012 \text{ (syst)} \pm 0.002 \text{ (theor)}, \end{aligned}$$

where the statistical uncertainty only includes the effect of the data statistics and the theoretical uncertainty is due to the width of the allowed band for a_0^2 .

Contents

1. Introduction	1
2. Theoretical predictions and previous results	3
2.1. The Standard Model of particle physics	3
2.1.1. Particles, interactions and symmetries	3
2.1.2. The strong interaction	4
2.1.3. The electroweak interaction	6
2.2. Chiral Perturbation Theory (χ PT)	9
2.2.1. The chiral symmetry	10
2.2.2. Spontaneous Chiral Symmetry Breaking (SCSB)	11
2.2.3. The quark condensate	11
2.2.4. The lowest order chiral Lagrangian	12
2.3. The $\pi\pi$ scattering	14
2.3.1. Predictions for the scattering lengths a_0^0 and a_0^2	15
2.4. The K_{e4} decay	17
2.4.1. The Cabibbo-Maksymowicz variables	19
2.4.2. Matrix element and decay rate	19
2.4.3. The Form Factors (FF)	20
2.4.4. The $K^- \rightarrow \pi^+ \pi^- e^- \bar{\nu}_e$ decay	22
2.4.5. The $K_{e4}^{\Delta S = -\Delta Q}$ decay	23
2.5. Previous experimental results	23
2.5.1. $\pi\pi$ scattering lengths	23
2.5.2. K_{e4} form factors	25
2.5.3. Limits on $\Delta S = -\Delta Q$	25
3. Experimental apparatus	27
3.1. The Super Proton Synchrotron (SPS) accelerator at CERN	27
3.2. The NA48/2 beam line	28
3.2.1. The vacuum tank	30
3.3. The NA48/2 detector	31
3.3.1. The KAon BEam Spectrometer (KABES)	31
3.3.2. The magnetic spectrometer	34
3.3.3. The Charged HODoscope (CHOD)	37
3.3.4. The Liquid Krypton electromagnetic calorimeter (LKr)	38
3.3.5. The Neutral HODoscope (NHOD)	43
3.3.6. The HAdron Calorimeter (HAC)	44
3.3.7. The MUon Veto (MUV)	45
3.3.8. The photon anti-counters (AKL)	45

3.3.9. The beam position monitor	46
4. Trigger and data acquisition	49
4.1. The Level 1 trigger (L1)	49
4.2. The Level 2 trigger (L2)	51
4.2.1. The NeUtral Trigger (NUT)	52
4.2.2. The MassBoX (MBX)	54
4.2.3. The Trigger Supervisor (TS)	54
4.3. The Data AcQuisition (DAQ)	57
4.3.1. The PC-Farm	57
4.3.2. The Central Data Recording (CDR)	58
4.4. The Level 3 trigger (L3)	58
5. Reconstruction	61
5.1. The physical objects	61
5.1.1. Decoding, reconstruction and COnPACT output	61
5.1.2. Track reconstruction	61
5.1.3. LKr cluster reconstruction	63
5.1.4. MUV hits	64
5.2. The COnPACT reader program	64
5.2.1. Corrections	64
5.2.2. Vertex reconstruction	66
5.2.3. Muon reconstruction	66
5.2.4. SuperCOnPACT production and filtering	66
6. Monte Carlo simulation	69
6.1. Kaon beam	69
6.2. Kaon decay	69
6.2.1. The K_{e4} generator	71
6.2.2. Other generators	71
6.2.3. Radiative corrections	72
6.2.4. Coulomb correction	73
6.3. Tracking in the detector	73
6.3.1. Electromagnetic showers	74
6.3.2. Pion decay in flight	74
6.4. Reconstruction and corrections	75
6.4.1. The generated four-momenta in SuperCOnPACT	75
7. Event selection and reconstruction	77
7.1. Data and MC samples	77
7.2. Selection criteria	77
7.2.1. Pre-selection	77
7.2.2. Vertex selection	78
7.2.3. Particle identification	80
7.2.4. Differences in the MC selection	82
7.3. Event reconstruction and background rejection	83

7.3.1. K_{e4} events	83
7.3.2. $K_{3\pi}$ events	85
7.3.3. $K_{2\pi D}$ events	86
7.4. Background estimate	87
7.4.1. “Wrong sign” events	88
7.4.2. Accidental background	88
7.4.3. $K_{3\pi}$ with $\pi \rightarrow e\nu$	90
7.4.4. $K_{3\pi}$ with pion mis-identification	90
7.4.5. $K_{2\pi D}$	92
7.4.6. $K_{\pi\pi^0\pi_D^0}$	92
7.4.7. Total background estimate with systematic uncertainty	93
7.5. Summary of selected events, acceptance and background contamination	94
8. Fit method	97
8.1. Computation of the Cabibbo-Maksymowicz variables	97
8.2. Preliminary checks	98
8.2.1. Acceptance	98
8.2.2. Resolution	98
8.3. Corrections applied to the MC	100
8.3.1. Trigger efficiency	101
8.3.2. Electron identification	104
8.3.3. Pion identification	105
8.3.4. Total weight	106
8.4. Fit strategy	107
8.5. Raw result of the first iteration	109
8.6. Raw result of the second iteration	111
9. Corrections and systematic uncertainties	115
9.1. MC tests	115
9.1.1. Corrected result	116
9.2. Systematics of the fit method	116
9.2.1. Convergence	116
9.2.2. Threshold	116
9.2.3. Number of bins	117
9.2.4. MC statistics	118
9.3. Systematics from the uncertainty on efficiencies and corrections	119
9.3.1. Statistical uncertainty	119
9.3.2. Systematic uncertainty	119
9.4. Systematics of the MC simulation and event selection	120
9.4.1. Acceptance	121
9.4.2. Momentum resolution, kaon spectrum and background expectation . .	122
9.4.3. $K_{2\pi D}$ reconstructed as K_{e4}	123
9.4.4. Fit of subsamples	126
9.4.5. Alternative electron identification and computation of the kinematic variables	129
9.4.6. Radiative and Coulomb corrections	130

9.5. Theoretical uncertainty and different constraints on a_0^0	131
9.5.1. Uncertainty on the constraint between a_0^2 and a_0^0	132
9.5.2. Universal band and free a_0^2	132
9.5.3. $\delta_0^0 - \delta_1^1$ as a function of s_π	133
9.6. Summary of the systematic and theoretical uncertainties	134
10. Result and discussion	137
10.1. Fit result	137
10.2. Comparison with previous results	137
10.3. Comparison with the theoretical predictions	140
10.4. Outlook	140
11. Summary	143
A. The K_{e4} matrix element	145
B. Additional Figures and Tables to Chapter 8	149
B.1. Efficiency of tight pion ID in data and MC	149
B.2. K_{e4} MC distributions	150
B.3. Log-likelihood curves	151

List of Tables

2.1. Fermions in the standard model	3
2.2. Interactions and symmetries	4
2.3. Charged kaon decays	10
3.1. Properties of liquid krypton	39
4.1. L1 trigger codes	51
4.2. Trigger-word	56
7.1. Selected data events	95
7.2. Selected MC events	96
8.1. Additional parameters	110
8.2. Raw result of the two iterations	111
8.3. Correlation matrix	113
9.1. Corrected result of the two iterations	117
9.2. Systematics of the fit method	118
9.3. Uncertainty on the MC corrections	120
9.4. Systematic uncertainty on the acceptance	123
9.5. Systematic uncertainty on the reconstruction	124
9.6. Systematic uncertainty on the agreement between data and MC	127
9.7. Systematic uncertainty on the electron ID and kinematic variables	131
9.8. Systematic uncertainty on the radiative and Coulomb corrections	132
9.9. Summary of the sources of systematic uncertainties	135
10.1. Comparison of the form factor parameters with BNL E865	139
10.2. Comparison of the scattering length with BNL E865 and the $K^\pm \rightarrow \pi^\pm \pi^0 \pi^0$ cusp analysis of NA48/2	139

List of Tables

List of Figures

2.1. The lightest pseudo-scalar mesons	7
2.2. The universal band	18
2.3. Tree level Feynman diagram for the K_{e4} decay	18
2.4. The Cabibbo-Maksymowicz variables	19
2.5. Tree level Feynman diagram for the $K_{e4}^{\Delta S=-\Delta Q}$ decay	23
3.1. CERN accelerator complex	28
3.2. NA48/2 beam line	29
3.3. Vacuum tank	30
3.4. NA48 detector	32
3.5. KAon BEam Spectrometer	33
3.6. Magnetic spectrometer	35
3.7. Drift CHamber	36
3.8. Charged HODoscope	38
3.9. Section of the Liquid Krypton calorimeter	40
3.10. Ribbon electrodes of the Liquid Krypton calorimeter	41
3.11. Neutral HODoscope	43
3.12. HAdron Calorimeter	44
3.13. Photon anti-counters	46
4.1. Level 1 and Level 2 trigger	50
4.2. NeUtral Trigger	52
4.3. MassBoX algorithm	55
4.4. Trigger Supervisor	56
4.5. Data AcQuisition system	60
6.1. The kaon spectrum	70
6.2. Coulomb correction	73
7.1. Missing mass	79
7.2. E/p for pions and electrons	81
7.3. LDA output and efficiency for pions and electrons	83
7.4. Missing mass	85
7.5. $m_{3\pi}$ vs. p_T	85
7.6. K_{e4} invariant mass	86
7.7. $K_{3\pi}$ momentum and invariant mass	86
7.8. Time difference between track and vertex	89
7.9. $K_{3\pi}$ with $\pi \rightarrow e\nu$ background	90
7.10. $K_{3\pi}$ background with π mis-identification	91

7.11. $K_{2\pi D}$ background	92
7.12. $K_{\pi\pi^0\pi_D^0}$ background	93
7.13. Expected background	94
8.1. Acceptance	99
8.2. Resolution	100
8.3. Data and MC distributions in the kinematic variables	101
8.4. L1 trigger efficiency	102
8.5. L2 trigger efficiency from $K_{3\pi}$ events	103
8.6. L2 trigger efficiency from $K_{2\pi D}$ events	104
8.7. Efficiency correction for the tight electron ID	105
8.8. Efficiency correction for the LDA	106
8.9. Efficiency correction for the tight pion ID	106
8.10. Effect of the MC corrections on the kinematic variables	108
8.11. Data/MC comparison before and after the fit	112
8.12. Log-likelihood for a_0^0	114
9.1. MC test for a_0^0	116
9.2. L1 trigger efficiency from $K_{2\pi D}$ events	120
9.3. L2 trigger efficiency ($\min(\Delta z_2)$ dependence) from $K_{2\pi D}$ events	121
9.4. L2 trigger efficiency (s_π dependence) from K_{e4} events	121
9.5. Kinematic variables from $K_{2\pi D}$ decays	125
9.6. Data/MC for the kinematic variables from $K_{2\pi D}$ decays	126
9.7. Stability of the F form factor parameters	128
9.8. Stability of the G and H form factors parameters and of a_0^0	129
9.9. Neural network efficiency and correction	130
9.10. Results for different constraints between a_0^2 and a_0^0	133
9.11. δ distribution as a function of s_π	134
10.1. Graphical comparison of the results for a_0^0	140
B.1. Efficiency of tight pion-ID	149
B.2. MC distributions	150
B.3. Log-likelihood curves for the F form factor	151
B.4. Log-likelihood curves for the G and H form factors and a_0^0	152
B.5. 2D Log-likelihood distributions for strongly correlated parameters	153

1. Introduction

The interactions between elementary particles are described by the standard model of particle physics in terms of three forces: strong, electromagnetic and weak. Its theoretical predictions have been confirmed by many experimental measurements. The knowledge on the behaviour of the smallest constituents of matter can be further improved, by searching for new particles at higher and higher energies or by collecting more and more statistics of known processes, in order to measure all their properties.

The kaon, the lightest meson containing a strange quark, was first observed in 1947. In 1964 indirect CP violation was discovered in the mixing between K^0 and \bar{K}^0 . Since then, also direct CP violation has been precisely measured, as well as the branching ratios and form factors of many decay modes for both neutral and charged kaons. The experiment NA48/2 at the CERN SPS took data in 2003 and 2004 with the aim of collecting the highest existing statistics of charged kaon decays, in order to search for direct CP violation in this system, where it was not yet observed and to perform the most precise measurements of other parameters of the theory.

At high energies, strong interactions are described, within the standard model, by quantum chromo-dynamics, which is expanded perturbatively in powers of the strong coupling. At low energies (below 1 GeV), however, the quarks are confined inside mesons and baryons and the strong coupling is too big to allow for a converging expansion. Kaon decays are therefore described by an effective theory, called chiral perturbation theory, that considers the light pseudo-scalar mesons, instead of the quarks, as elementary particles. Chiral perturbation theory contains, as every effective theory, free parameters, whose values have to be determined experimentally.

A fundamental parameter of the theory is the quark condensate, the vacuum expectation value of $\bar{q}q$, that determines the relative size of the mass and momentum terms in the power expansion. If the assumption of a large quark condensate, on which χPT is based, would be experimentally contradicted, the mass terms would have to appear earlier in the expansion and the terms with an odd power of the momentum would not vanish. Experimentally, the size of the quark condensate can be measured in the $\pi\pi$ scattering. The relation between the scattering lengths and the quark condensate is known in chiral perturbation theory with high precision, so that a discrepancy between the predicted and the measured values of the scattering lengths would clearly show a wrong assumption for the size of the quark condensate.

In the decay $K^\pm \rightarrow \pi^+ \pi^- e^\pm \bar{\nu}_e$ (K_{e4}), the leptonic part of the matrix element is known exactly, while the hadronic part can be described in terms of form factors, whose phases are related to the S -wave $\pi\pi$ scattering lengths. Aim of the analysis presented in this thesis is the measurement of the K_{e4} form factors and the extraction of the S -wave $\pi\pi$ scattering lengths. Since the hadronic part of the decay only contains two pions, it can be easily described by the theory, which reduces the theoretical uncertainty of the measurement. On the other hand, the branching ratio of the decay is of the order 10^{-5} , so that a precise experimental measurement requires high statistics and good background rejection.

1. Introduction

Chiral perturbation theory in general and in particular its predictions for the $\pi\pi$ scattering and the K_{e4} form factors are presented in Chapter 2, together with the results of previous experiments.

In Chapter 3, the experimental apparatus is described, starting from the beam line, where the kaons are generated, up to the read-out electronics of each sub-detector, where the signals necessary to identify the decay products are collected. The first decision, whether an event is interesting for the analysis or not, is taken by the trigger system, presented in Chapter 4. In case of a positive trigger decision, the events are written to tape and the physical quantities can be reconstructed offline (Chapter 5).

In order to verify the validity of the theoretical prediction, the expected distribution, obtained from the Monte Carlo simulation, outlined in Chapter 6, is compared with the data. The selection criteria used to identify the different decay channels and to reduce the background contamination are explained in Chapter 7. The form factor parameters of the K_{e4} decay can be measured by fitting the simulated distribution to the one obtained in the experiment, as described in detail in Chapter 8. The effects taken into account in the systematic uncertainty and the method used to estimate them are listed in Chapter 9. Finally, the results obtained in this analysis are discussed in Chapter 10.

2. Theoretical predictions and previous results

2.1. The Standard Model of particle physics

The Standard Model (SM) of particle physics is a gauge theory that combines three of the four known fundamental interactions acting on six fundamental particles and their antiparticles (see Section 2.1.1).

In the 1960s the electromagnetic and the weak interactions were combined into a gauge theory by Glashow, Weinberg and Salam [1, 2, 3], setting the basis for the development of the standard model. In 1964 the quark model was proposed by Gell-Mann and Zweig [4, 5], while the corresponding gauge theory, based on the colour symmetry, was developed by Fritzsch and Gell-Mann [6] and completed by Gross, Wilczek and Politzer with the introduction of the asymptotic freedom [7, 8, 9] in 1974.

The strong and electroweak interactions, that are responsible for the kaon production and decay respectively, will be briefly presented in Sections 2.1.2 and 2.1.3. A detailed description can be found in any textbook of particle physics, for example [10, 11, 12].

2.1.1. Particles, interactions and symmetries

According to the standard model the fundamental constituents of matter are twelve fermions (spin- $\frac{1}{2}$ particles): six leptons and six quarks. The fermions are listed in Table 2.1 together with the interactions they are subject to. The three generations differ only in the mass of the particles, otherwise they are identical copies of the same structure.

Fermions			strong	el.-mag.	weak
Leptons					
ν_e e-neutrino	ν_μ μ -neutrino	ν_τ τ -neutrino	—	—	×
e^- electron	μ^- muon	τ^- tau	—	×	×
Quarks					
u up	c charm	t top	×	×	×
d down	s strange	b beauty	×	×	×

Table 2.1.: The first three columns on the left represent the three generations of fermions. Particles in the same row are identical to each other in all attributes apart from the mass. The columns on the right show which interactions are allowed (“ \times ”) for the different fermions.

In nature four fundamental interactions are known: strong, electromagnetic, weak and gravitational. The first three are described by the SM in terms of the exchange of a spin-1 gauge boson, while gravitation can not be easily inserted into this scheme and is anyway negligible in high energy physics. Quarks are subject to all the interactions, while leptons interact weakly and, if they are electrically charged, also electromagnetically. The gauge bosons are listed in Table 2.2.

Interaction	Gauge bosons (mass/(GeV/ c^2))	Gauge group	C	P	T
strong	8 gluons g (0)	$SU(3)_c$	×	×	×
electromagnetic	photon γ (0)	$SU(2)_L \times U(1)_Y$	×	×	×
weak	W^\pm (80), Z^0 (91)		—	—	—

Table 2.2.: Characteristics of the interactions in the SM and their behaviour with respect to the symmetries C,P and T (\times = conserved, $—$ = violated). The mass values are only indicative, they are known to a much better precision [13].

The SM is invariant under local gauge transformations of the group $SU(3)_c \times SU(2)_L \times U(1)_Y$, where $SU(3)_c$ is the colour group of the strong interaction (see Section 2.1.2) and $SU(2)_L \times U(1)_Y$ are the groups of the electroweak interactions of left and right-handed particles, respectively (see Section 2.1.3).

Symmetries play an important role in physics, since they are related to conservation laws by the Noether theorem (1917). For example the charge conservation follows from the $SU(2)_L \times U(1)_Y$ symmetry and the energy conservation from the invariance under time shift. These are examples of continuous transformations, but there are also important discrete ones, like the Charge conjugation (C), that exchanges each particle with its antiparticle, the Parity transformation (P), that mirrors the space coordinates, and the Time reversal (T). While C, P and T are conserved in the strong and electromagnetic interactions, they are violated in the weak interaction, both separately and in the combination CP. The conservation of the CPT symmetry is predicted by the theory to be valid for all the interactions in the SM: the CPT-theorem [14] attests that, under the assumption of Lorentz invariance, locality and that the interactions are propagated by fields, CPT is an exact symmetry of every interaction. A direct implication of the CPT-theorem is that particles and antiparticles have the same mass and lifetime and opposite charge and magnetic moment. The CPT conservation was tested experimentally to the level of 10^{-18} .

2.1.2. The strong interaction

In order to explain the observation of the Δ^{++} baryon, consisting of three u quarks with a total spin of $\frac{3}{2}$ and therefore apparently violating the Pauli principle that two or more fermions may not exist in the same quantum state, a further degree of freedom was introduced for the quarks: the colour. There are three possible colour charges: red, green and blue. Each quark has a colour charge and each antiquark an anticolour charge. The existence of this degree of freedom was proven experimentally by the measurement of the ratio between the cross

sections for the electron-positron annihilation into two quarks and into two leptons:

$$R = \frac{\sigma(e^+e^- \rightarrow q\bar{q})}{\sigma(e^+e^- \rightarrow \mu^-\mu^+)} = N_c \cdot \sum_q e_q^2, \quad (2.1)$$

where N_c is the number of colours, the sum is over the accessible quark flavours at the considered centre of mass energy and e_q is the electrical charge of quark q .

A quark can be represented as a three-dimensional vector in the colour space and the local unitary gauge transformations in this space form the $SU(3)_c$ group. The description of strong interactions based on the invariance under gauge transformations in $SU(3)_c$ is called Quantum Chromo-Dynamics (QCD) and, since the group is non-Abelian (its elements do not commute with each other), it is a so-called Yang-Mills theory [15].

The Lagrangian of a free quark is

$$\mathcal{L} = \bar{\psi}(i\gamma^\mu \partial_\mu - m)\psi, \quad (2.2)$$

where m represents the mass of the quark and is a free parameter of the theory.

In general a unitary local gauge transformation can be written as

$$U(\alpha(x)) = e^{-i\alpha_a(x)T_a}, \quad (2.3)$$

where the index a goes from 1 to 8 and T_a are the generators of $SU(3)_c$, that have the following commutation relation:

$$[T_a, T_b] = if_{abc}T_c, \quad (2.4)$$

where f_{abc} are the structure functions of the group. A representation of T_a with unitary 3×3 -matrices can be chosen and leads to the t_a matrices (the Gell-Mann matrices divided by two), that are hermitian and traceless.

To make the Lagrangian in Eq. 2.2 be invariant under the local transformation in Eq. 2.3, the derivative has to be replaced by the covariant derivative:

$$D_\mu = \partial_\mu - ig_s t^a G_\mu^a(x), \quad (2.5)$$

where g_s is the coupling of the strong interaction and G_μ^a are the eight gluon fields. To add to the Lagrangian a kinetic term for the gluons, the tensor $G_{\mu\nu}^a$ can be built as

$$G_{\mu\nu}^a = \partial_\mu G_\nu^a - \partial_\nu G_\mu^a + g_s f^{abc} G_\mu^b G_\nu^c. \quad (2.6)$$

The Lagrangian has now the form

$$\mathcal{L} = \bar{\psi}(i\gamma^\mu D_\mu - m)\psi - \frac{1}{4} G_{\mu\nu}^a G_a^{\mu\nu}. \quad (2.7)$$

The last term in Eq. 2.6, that would not be present in an Abelian theory, generates the three and four-gluon vertices. The feature of gluons to have a colour charge and therefore interact with each other leads to the particular form of the scale dependence for the strong coupling “constant” α_s :

$$\alpha_s(\mu^2) = \frac{4\pi}{\beta_0 \ln\left(\frac{\mu^2}{\Lambda^2}\right)}, \quad \beta_0 = 11 - \frac{2}{3}N_F, \quad (2.8)$$

μ is the energy at which α_s is measured, Λ a typical QCD scale of the order of 1 GeV and N_F the number of quark flavours. Since for $N_F \leq 6$ β_0 is positive, α_s is decreasing with energy. Therefore at high energies (corresponding to small distances) the quarks behave like free particles. This characteristic is called *asymptotic freedom*. On the other hand at very low energies α_s increases significantly and forces quarks to only appear in nature as colour singlets, bound in baryons and mesons. Too high values of α_s are also the reason why the perturbative QCD can not be applied to kaon physics. Instead, the theoretical calculations are performed in the framework of Chiral Perturbation Theory (χ PT), as described in Section 2.2.

The lightest pseudo-scalar mesons

The easiest ways to obtain colour singlets out of quarks and antiquarks are to combine three quarks, three antiquarks or a quark and an antiquark. These combinations are called baryons, antibaryons and mesons, respectively.

Mesons have always parity $P = -1$ because particles and antiparticles have opposite parity. Considering only the states with zero orbital angular momentum, mesons can have a total angular momentum $J = 0$ or $J = 1$ according to their spin. States with $J^P = 0^-$ are called pseudo-scalar mesons, while the ones with $J^P = 1^-$ are called vector mesons.

Restricting to the two lightest flavours, four pseudo-scalar mesons can be created. A new quantum number is defined in the $SU(2)_f$ (flavour) space: the isospin. The (u, d) doublet has isospin $I = \frac{1}{2}$, with third component $I_3 = +\frac{1}{2}$ for the u quark and $I_3 = -\frac{1}{2}$ for the d quark. The antiquarks have the opposite values of I_3 . In analogy to the spin, the combination of two doublets creates a triplet with isospin 1 (π^+, π^0, π^-) and a singlet with isospin 0 (η).

In the case of three flavours, u , d and s , $SU(3)_f$ generates

$$3 \otimes \bar{3} = 8 \oplus 1 \quad (2.9)$$

pseudo-scalar mesons, i.e. an octet and a singlet, that are classified using two quantum numbers: the isospin for u , \bar{u} , d and \bar{d} and the strangeness defined as $S = -1$ for s and $S = +1$ for \bar{s} . In Figure 2.1 the octet and the singlet are represented in the S vs. I_3 plane.

2.1.3. The electroweak interaction

The Lagrangian in Eq. 2.2 is valid for any fermion and was originally formulated to reproduce the Dirac equation when applying the Euler-Lagrange equation to it. To make it invariant under local gauge transformations in the Abelian $U(1)$ group

$$U(\alpha(x)) = e^{i\alpha(x)}, \quad (2.10)$$

the covariant derivative

$$D_\mu = \partial_\mu + ieA_\mu \quad (2.11)$$

has to be introduced, where e is the coupling of the electromagnetic interaction and corresponds to the elementary electric charge. A^μ is the field of the gauge boson, the photon. The tensor for the kinetic term of the photon has in this case the simple form

$$F_{\mu\nu} = \partial_\mu A_\nu - \partial_\nu A_\mu, \quad (2.12)$$

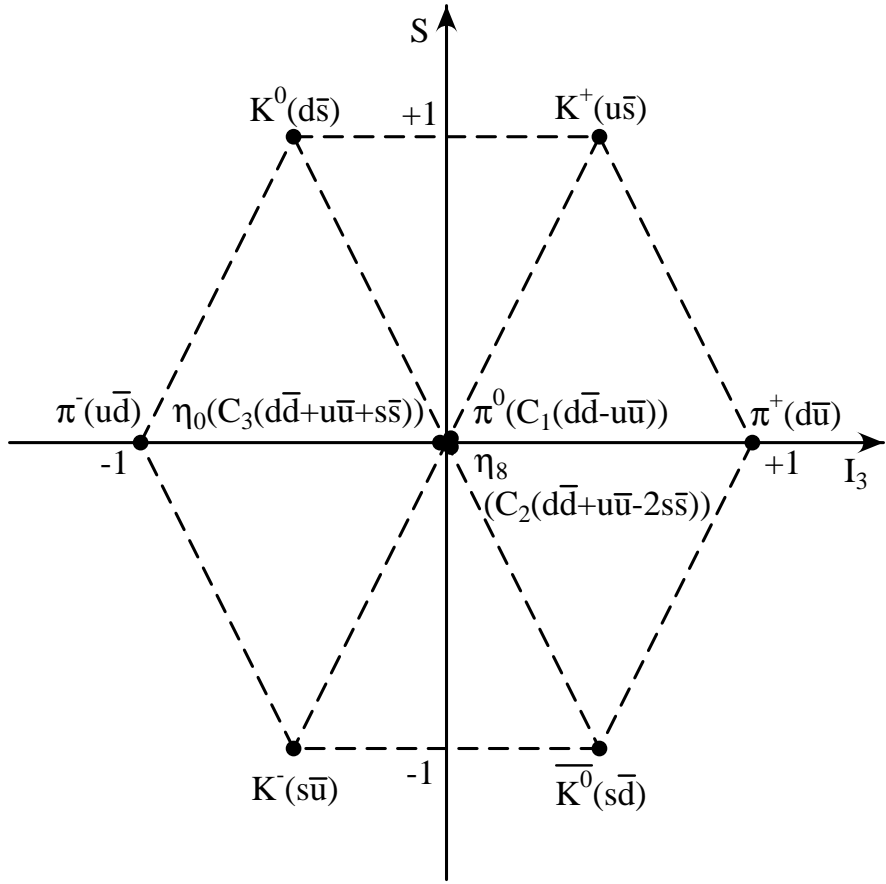


Figure 2.1.: The octet and the singlet (η_0) of the pseudo-scalar mesons with three quark flavours in the plane strangeness (S) versus third component of the isospin (I_3). C_1 , C_2 and C_3 are the Clebsch-Gordan coefficients for the three states with $I_3 = 0$ and $S = 0$ and have the values $C_1 = \frac{1}{\sqrt{2}}$, $C_2 = \frac{1}{\sqrt{6}}$ and $C_3 = \frac{1}{\sqrt{3}}$.

without any second order term. The electromagnetic interaction is then described by the Lagrangian of the Quantum Electro-Dynamic (QED)

$$\mathcal{L} = \bar{\psi}(i\gamma^\mu D_\mu - m)\psi - \frac{1}{4}F_{\mu\nu}F^{\mu\nu}. \quad (2.13)$$

The scale dependence of the coupling ‘‘constant’’ α is much smaller than in QCD and its value increases with energy, so that a perturbation expansion is possible at all energies and can be truncated at low orders, giving very precise predictions.

As was observed experimentally [16], the weak interaction only couples to left-handed, i.e. with the spin opposite to the momentum, particles or right-handed antiparticles. Right-handed particles and left-handed antiparticles do not interact weakly. The spinors of the left-handed particles are isospin doublets, while the right-handed particles are represented by singlets. Since the eigenvalues of the isospin operators are not equal to the charge of

the particles, a further quantum number has to be introduced, the so-called hypercharge Y , fulfilling the relation

$$Q = I_3 + \frac{Y}{2} \quad (2.14)$$

The Lagrangian is required to be invariant under local gauge transformations in $SU(2)_L \times U(1)_Y$ for left-handed particles and in $U(1)_Y$ for right-handed ones:

$$U_L(\alpha(x), \beta(x)) = e^{i\alpha_j(x)\tau_j} \cdot e^{i\beta(x)Y} \quad (2.15)$$

$$U_R(\beta(x)) = e^{i\beta(x)Y}, \quad (2.16)$$

τ_j are the generators of the $SU(2)_L$ group and are assumed to be the Pauli matrices, while Y is a real number. The covariant derivatives are then

$$D_{L\mu} = \partial_\mu - i\frac{g'}{2}Y_L B_\mu - i\frac{g}{2}\tau_j W_{j\mu} \quad (2.17)$$

$$D_{R\mu} = \partial_\mu - i\frac{g'}{2}Y_R B_\mu, \quad (2.18)$$

with the couplings g and g' for $SU(2)_L$ and $U(1)_Y$ respectively and the gauge fields W_1^μ , W_2^μ , W_3^μ , B^μ . The tensors for the kinetic term have the same form as in Eq. 2.13 for B^μ and as in Eq. 2.6 with f_{abc} replaced by ϵ_{ijk} for W_i^μ .

Until now the gauge fields are massless in the theory, while W^\pm and Z^0 have been observed experimentally as massive bosons. An explicit mass term of the form $m A_\mu A^\mu$ violates the gauge symmetry, but it is possible to introduce mass terms for the gauge bosons via the Higgs mechanism [17, 18]. Adding a complex scalar isospin doublet with a potential that has a minimum for a value of the field different from zero, the symmetry is still valid, since the position of the minima is symmetric in $SU(2)_L$. However the choice of a particular ground state violates the symmetry. This mechanism is called Spontaneous Symmetry Breaking (SSB) and generates mass terms for linear combinations of the gauge bosons:

$$(W^\pm)^\mu = \frac{1}{\sqrt{2}}(W_1^\mu \mp iW_2^\mu) \quad , \quad m_W = \frac{1}{2}vg \quad (2.19)$$

$$(Z^0)^\mu = \frac{-g'B^\mu + gW_3^\mu}{\sqrt{g^2 + g'^2}} \quad , \quad m_Z = \frac{1}{2}v\sqrt{g^2 + g'^2} \quad (2.20)$$

$$A^\mu = \frac{gB^\mu + g'W_3^\mu}{\sqrt{g^2 + g'^2}} \quad , \quad m_A = 0 \quad (2.21)$$

where v is the vacuum expectation value of the scalar field. The combinations listed above correspond to the observed particles W^\pm , Z^0 and γ . Usually $(Z^0)^\mu$ and A^μ are written as a rotation of the B^μ and W_3^μ fields by the Weinberg angle θ_W with

$$\cos \theta_W = \frac{g}{\sqrt{g^2 + g'^2}} \quad (2.22)$$

$$\sin \theta_W = \frac{g'}{\sqrt{g^2 + g'^2}} \quad (2.23)$$

$$m_W = m_Z \cdot \cos \theta_W \quad (2.24)$$

In the new terms a scalar field appears, the Higgs boson, that is the only particle of the SM not yet observed.

Quarks can interact both strongly and weakly, but the eigenstates of the strong interaction do not correspond to the eigenstates of the weak interaction. The 3×3 matrix of the rotation producing the correct linear combinations for the weak interaction is the Cabibbo-Kobayashi-Maskawa (CKM) matrix [19]. The nine complex terms $V_{qq'}$ can be expressed as a function of four independent real parameters: three angles and a phase, that is responsible for the direct CP violation.

Charged kaon decays

Kaons are produced by the strong interaction of non strange hadrons, for example in a proton-proton collision, together with baryons or another kaon with opposite strangeness. But, since kaons are the lightest strange particles, they can only decay via the weak interaction in processes with $|\Delta S| \geq 1$.

In the neutral kaon system the first evidence for “indirect” CP violation was observed in 1964 [20] in the mixing of the K^0 and \bar{K}^0 states. The mixing of two neutral mesons occurs through common intermediate states and is therefore a second order weak process, with $\Delta S = 2$. The mass eigenstates are a linear combination of K^0 and \bar{K}^0 and, since they do not correspond exactly to the CP eigenstates, indirect CP violation can be observed. Its size is measured by the asymmetry parameter ϵ and is of the order of 10^{-3} .

For charged kaons no mixing can take place and CP can only be directly violated. Direct CP violation was not observed in this system yet, but only in the neutral kaons, and is expected to be of the order of 10^{-6} within the SM [21]. In other models the direct CP violation in the charged kaon system is predicted to be as high as 10^{-4} [22]. For this analysis such a difference between K^+ and K^- is negligible and it will therefore be assumed that CP is conserved.

Charged kaons decay preferably into two leptons ($\mu\nu$) or two hadrons ($\pi^+\pi^0$) with branching ratios of 63% and 21%, respectively. The remaining 16% is shared between semileptonic and hadronic three-body decays, with small contributions from decays into more than three particles and radiative ones. The interesting channels for the analysis presented in this thesis are listed in Table 2.3.

2.2. Chiral Perturbation Theory (χ PT)

Chiral perturbation theory is the quantum field effective theory, that describes hadronic interactions within the SM below the energy scale at which the chiral symmetry is broken ($E \ll \Lambda_\chi \sim 1 \text{ GeV}$).

Chirality is defined by the projection operators $\Gamma_{R,L} = \frac{1}{2}(1 \pm \gamma_5)$, that act on the Dirac spinors and extract from them respectively the right (R) and left-handed (L) component. As a function of the chiral states, the QCD Lagrangian has the form

$$\bar{q}(i\gamma^\mu D_\mu - m)q = \bar{q}_L i\gamma^\mu D_\mu q_L + \bar{q}_R i\gamma^\mu D_\mu q_R - \bar{q}_L m q_R - \bar{q}_R m q_L \quad (2.25)$$

and, in the limit of massless quarks, it is invariant for global transformations of the chiral group $SU(3)_L \otimes SU(3)_R$.

Since at low energies the QCD can not be treated perturbatively, an effective theory has to be used. The basic principle of effective theories is that, within a certain energy range, only

Decay	short name	BR	
$K^\pm \rightarrow \pi^\pm \pi^0$	$K_{2\pi}$	$(21.1 \pm 0.1)\%$	background
$K^\pm \rightarrow \pi^0 e^\pm \bar{\nu}_e$	K_{e3}	$(4.87 \pm 0.06)\%$	calibration
$K^\pm \rightarrow \pi^+ \pi^- \pi^\pm$	$K_{3\pi}$	$(5.58 \pm 0.03)\%$	background
$K^\pm \rightarrow \pi^0 \pi^0 \pi^\pm$	$K_{\pi\pi^0\pi^0}$	$(1.73 \pm 0.04)\%$	background
$K^\pm \rightarrow \pi^+ \pi^- \pi^\pm \gamma$	$K_{3\pi\gamma}$	$(1.0 \pm 0.3) \times 10^{-4}$	background
$K^\pm \rightarrow \pi^+ \pi^- e^\pm \bar{\nu}_e$	K_{e4}	$(4.08 \pm 0.09) \times 10^{-5}$	signal
$K^\pm \rightarrow \pi^\pm \pi^\pm e^\mp \bar{\nu}_e$	$K_{e4}^{\Delta S = -\Delta Q}$	$< 1.2 \times 10^{-8}$	test of $\Delta S = \Delta Q$

Table 2.3.: The interesting decays for the K_{e4} analysis and their experimentally measured branching ratios [13].

some degrees of freedom are relevant and have to be described as fields, while the remaining ones enter only in the coefficients of suitable local operators. In particular χ PT considers as fundamental particles the light pseudo-scalar mesons, that are the spectrum of the theory, while their internal structure in terms of quarks is neglected.

Studying kaon decays, the appropriate energy scale is that of the kaon mass, which is small enough to neglect terms involving heavy quarks, whose degrees of freedom are frozen. Therefore only the light mesons composed of the u , d and s quarks are considered.

In the following χ PT will be briefly presented in a formal way, but restricted to the interesting aspects for the K_{e4} decay. Complete descriptions of the theory can be found for example in [23, 24, 25].

2.2.1. The chiral symmetry

Neglecting the quark masses and the terms depending on heavy quarks, Eq. 2.7 can be written as

$$\mathcal{L}_{QCD}^{(0)} = \sum_{q=u,d,s} \bar{q} \gamma^\mu \left(i \partial_\mu + g_s t^a G_\mu^a \right) q - \frac{1}{4} G_{\mu\nu}^a G^{a\mu\nu}. \quad (2.26)$$

Apart from the invariance under local $SU(3)_c$ transformations, the Lagrangian is also invariant under global transformations of the group $SU(3)_L \times SU(3)_R \times U(1)_V \times U(1)_A$. The $U(1)_V$ symmetry has the baryon number as a generator and is exactly conserved, while the $U(1)_A$ symmetry is not conserved in the quantisation ($U(1)_A$ anomaly), so that only $G = SU(3)_L \times SU(3)_R$ is considered as the chiral group.

To each generator of G corresponds a conserved Noether current

$$J_{L,R}^{a\mu} = \bar{q}_{L,R} \gamma^\mu t^a q_{L,R} \quad (2.27)$$

with the charges

$$Q_{L,R}^a = \int d^3 x J_{L,R}^{a0}(x), \quad (2.28)$$

that follow the usual commutation relations

$$[Q_X^a, Q_Y^b] = i\delta_{XY}f_{abc}Q_X^c, \quad (2.29)$$

with X and Y equal to R or L .

The chiral symmetry, that should be valid with good approximation for the light quarks, is however not present in the hadron spectrum, since there are no degenerate multiplets with opposite parity. Instead, the octet of pseudo-scalar mesons is composed by much lighter particles than all the other hadrons. This experimental fact indicates that the chiral symmetry is spontaneously broken and that a perturbative treatment of the masses of the pseudo-scalar mesons is allowed without moving back to the typical hadron energy scale.

2.2.2. Spontaneous Chiral Symmetry Breaking (SCSB)

Considering the hadrons as ground states in the theory, of the original invariance under the G group only the symmetry $SU(3)_V \equiv SU(3)_{L+R}$ is conserved, so that, according to the Goldstone theorem [26], an octet of massless pseudo-scalar bosons has to appear. Formally [27], a symmetry is spontaneously broken if an operator O exists, for which

$$\langle 0 | [Q, O] | 0 \rangle \neq 0, \quad (2.30)$$

where Q is the Noether charge and the left term of the equation is called the order parameter of the SCSB. This condition can be satisfied only if $Q|0\rangle \neq 0$ and, since Q commutes with the Hamiltonian, the state $Q|0\rangle$ has the same energy as the vacuum. In a relativistic invariant theory this can only happen if the spectrum of the physical states contains a massless particle, the Goldstone boson ($|G\rangle$), fulfilling the relation

$$\langle 0 | J^0 | G \rangle \langle G | O | 0 \rangle \neq 0. \quad (2.31)$$

Therefore the quantum numbers of the Goldstone boson depend on the ones of J^0 and O .

If there is a set of generators that leave the vacuum state unchanged, they form a sub-algebra, since, if Q_i and Q_k annihilate vacuum, the same is valid for their commutator. As a result two groups can be considered: the symmetry group G of the Hamiltonian and the group H (sub-group of G), that is the symmetry group of the vacuum state. If n_G is the number of generators of G and $n_H < n_G$ the number of generators of H , the remaining $n_G - n_H$ generators, that belong to the ratio G/H of the two groups, do not annihilate vacuum and give origin to linearly independent minimum energy states. If they would not be linearly independent, one of their combinations would annihilate vacuum and would then belong to H .

In the chiral group the symmetry with respect to the eight axial generators $Q_A^a = Q_R^a - Q_L^a$ is broken, so that there are eight pseudo-scalar Goldstone bosons, that can be identified with the lightest meson octet. Their masses are generated by the mass matrix that explicitly breaks the global symmetry of the QCD Lagrangian.

2.2.3. The quark condensate

The operators corresponding to the broken symmetry must be pseudo-scalar: the easiest form is $O^a = \bar{q}\gamma_5\lambda^a q$, where $\lambda_a = 2 \cdot t_a$ are the Gell-Mann matrices, whose order parameter is

$$\langle 0 | [Q_A^a, \bar{q}\gamma_5\lambda^b q] | 0 \rangle = -\frac{1}{2} \langle 0 | \bar{q} \{ \lambda^a, \lambda^b \} q | 0 \rangle = -\frac{2}{3} \delta_{ab} \langle 0 | \bar{q}q | 0 \rangle. \quad (2.32)$$

The quark mean value of the vacuum (the so-called *quark condensate*)

$$\langle 0 | \bar{u}u | 0 \rangle = \langle 0 | \bar{d}d | 0 \rangle = \langle 0 | \bar{s}s | 0 \rangle \neq 0 \quad (2.33)$$

has the same value for the three light quarks in the limit of no mass because of the $SU(3)_V$ symmetry and is the natural order parameter of the SCSB. The transition matrix elements of the Noether currents between the vacuum and the Goldstone bosons, because of the Lorentz invariance, must be of the form

$$\langle 0 | J_i^\mu | \phi^a(p) \rangle = i f_i^a p^\mu, \quad (2.34)$$

where the states $|\phi^a(p)\rangle$ are orthogonal to each other and the decay constants f_i^a are real, diagonal and equal to zero for the currents of the H group.

2.2.4. The lowest order chiral Lagrangian

The low energy regime should allow for the expansion of the transition amplitudes in powers of the momentum. However the exchange of massless particles produces singularities that do not admit such an expansion. For example, each propagator contains a pole:

$$\langle 0 | T \{ \phi^a(x) \phi^b(y) \} | 0 \rangle = -i \delta^{ab} \Delta_0(x-y) \quad \Delta_0(z) = \int \frac{d^4 p}{(2\pi)^4} \frac{e^{-ipz}}{-p^2 - i\epsilon}. \quad (2.35)$$

The analysis of the low energy structure of the χ PT is based on the following hypotheses [28]:

- the Goldstone bosons generated by the spontaneous symmetry breaking are the only massless particles in the spectrum of the physical states;
- at low energy the Green functions are dominated by the poles due to the exchange of such particles;
- the vertices allow for the Taylor expansion in powers of the momentum.

The vertices correspond to the residuals of the poles from the exchange of a massless particle and the third hypothesis requires that these residuals can be expanded in a Taylor series. Combined with the first one, this condition means that the amplitudes allow for the Taylor expansion, since the poles are the only singularities. An immediate consequence of the hypotheses is that, at low energy, the symmetry forbids strong interactions between the Goldstone bosons [29]: the vertices may only be constructed from Lorentz invariants and are therefore at least quadratic functions of the momentum. In this way the interactions at low energy between the Goldstone bosons are weak, differently from the ones between quarks and gluons, and this justifies the perturbative expansion within the effective theory.

The dynamical variables are contained in the $SU(3)$ matrix

$$U(x) = e^{i \frac{\phi}{F_0}}, \quad (2.36)$$

with

$$\phi(x) = \lambda_a \phi^a(x) = \begin{pmatrix} \pi^0 + \frac{1}{\sqrt{3}} \eta_8 & \sqrt{2} \pi^+ & \sqrt{2} K^+ \\ \sqrt{2} \pi^- & -\pi^0 + \frac{1}{\sqrt{3}} \eta_8 & \sqrt{2} K^0 \\ \sqrt{2} K^- & \sqrt{2} \bar{K}^0 & -\frac{2}{\sqrt{3}} \eta_8 \end{pmatrix}. \quad (2.37)$$

$F_0 \simeq 93$ MeV is a free parameter related to the matrix element of the pion decay at tree level:

$$\mathcal{M} = -G_F V_{ud} F_0 \bar{u}_{\nu_\mu} \not{p} (1 - \gamma_5) v_{\mu+}, \quad (2.38)$$

where $G_F \simeq 1.17 \times 10^{-5}$ GeV $^{-2}$ is the Fermi constant for the weak decay and $V_{ud} \simeq 0.22$ the CKM matrix element between the u and the d quark. F_0 represents the decay constant of the mesons at tree level, in the assumption of massless mesons.

The lowest order non trivial Lagrangian, invariant under the global chiral symmetry, reads

$$\mathcal{L}_{eff} = \frac{F_0^2}{4} \text{Tr} \left(\partial_\mu U \partial^\mu U^\dagger \right) \quad (2.39)$$

and can be expanded in powers of ϕ as

$$\mathcal{L}_{eff} = \frac{1}{2} \partial_\mu \phi^a \partial^\mu \phi_a + \mathcal{L}_{int}, \quad (2.40)$$

where no mass term appears for the eight pseudo-scalar mesons and \mathcal{L}_{int} represents the interaction Lagrangian generated by higher order terms.

To introduce the mass term, that explicitly violates the chiral symmetry, the constant matrix

$$M = \begin{pmatrix} m_u & 0 & 0 \\ 0 & m_d & 0 \\ 0 & 0 & m_s \end{pmatrix} \quad (2.41)$$

is assumed to transform as the U matrix. The lowest order of the expansion in powers of M is

$$\mathcal{L}_M = \frac{F_0^2 B_0}{2} \text{Tr}(M U^\dagger + U M^\dagger). \quad (2.42)$$

The new parameter B_0 is related to the chiral quark condensate:

$$\langle \bar{u}u \rangle = \langle 0 | \bar{u}u | 0 \rangle_0 = -F_0^2 B_0, \quad (2.43)$$

where the subscript 0 indicates the limit of massless quarks. Now the mesons also get a mass, for example the pion mass is at the lowest order

$$M_\pi^2 = 2B_0 m, \quad (2.44)$$

with $m = m_u = m_d$. In χ PT B_0 is assumed to be big enough, so that the linear term in the quark masses dominates the expansion. However, B_0 can only be determined experimentally and there are no theoretical arguments supporting the assumption of a big value. Therefore the determination of B_0 is an important test of the basic principles of χ PT. In the following Sections the relation between B_0 and the K_{e4} form factors, that are measured in this analysis, will be shown in detail.

In order to compare the theoretical predictions with the experimental data, a better precision than the tree level is required. In higher orders also the interactions with external fields are included. Considering a local chiral symmetry instead of a global one, the derivative has to be replaced by a covariant derivative, acting on the U matrix as

$$D_\mu U = \partial_\mu U - i r_\mu U + i U l_\mu, \quad (2.45)$$

where r_μ and l_μ are respectively left and right-handed external fields. The field strength tensors of the external fields can also be built, but they do not contribute to the Lagrangian because they are traceless. The scalar (s) and pseudo-scalar (p) external fields are added in the combination

$$\chi = 2B_0(s + ip). \quad (2.46)$$

The mass matrix can be included as a scalar external field. The lowest order locally invariant Lagrangian then reads

$$\mathcal{L}_2 = \frac{F_0^2}{4} \text{Tr} \left[D_\mu U (D^\mu U)^\dagger \right] + \frac{F_0^2}{4} \text{Tr} \left(\chi U^\dagger + U \chi^\dagger \right). \quad (2.47)$$

Further terms \mathcal{L}_n can be added, with n even, containing d derivatives of the meson field (corresponding to momentum powers) and m powers of the mass matrix with $d + 2m = n$. For example for the next-to-leading order ($O(p^4)$) three terms have to be considered:

- one-loop graphs generated by \mathcal{L}_2
- an explicit local action of order p^4
- the contribution to account for the chiral anomaly.

2.3. The $\pi\pi$ scattering

Expanding the Lagrangian of Eq. 2.47 up to the order ϕ^4 and considering the matrix U in $SU(2)$ instead of $SU(3)$, the matrix element of the process

$$\pi^i(p_1)\pi^k(p_2) \rightarrow \pi^l(p_3)\pi^m(p_4) \quad (2.48)$$

can be calculated at tree level, giving the same result as in the notation [29]

$$\begin{aligned} \langle \pi^m(p_4)\pi^l(p_3)\text{out} | \pi^i(p_1)\pi^k(p_2)\text{in} \rangle &= \langle \pi^m(p_4)\pi^l(p_3)\text{in} | \pi^i(p_1)\pi^k(p_2)\text{in} \rangle \\ &+ i(2\pi)^4 \delta^{(4)}(P_f - P_i) T^{ik;lm}(s, t, u), \end{aligned} \quad (2.49)$$

where $P_f = p_4 + p_3$ is the total momentum of the final state, $P_i = p_1 + p_2$ the total momentum of the initial state, s , t and u are the Mandelstam variables

$$\begin{aligned} s &= (p_1 + p_2)^2 \\ t &= (p_1 - p_3)^2 \\ u &= (p_1 - p_4)^2 \end{aligned} \quad (2.50)$$

and $T^{ik;lm}(s, t, u)$ is a Lorentz invariant function. Due to isospin symmetry, $T^{ik;lm}(s, t, u)$ can be expressed in terms of a single amplitude $A(s, t, u) = A(s, u, t)$

$$T^{ik;lm}(s, t, u) = \delta^{ik} \delta^{lm} A(s, t, u) + \delta^{il} \delta^{km} A(u, s, t) + \delta^{im} \delta^{kl} A(u, t, s), \quad (2.51)$$

with, at tree level,

$$A(s, t, u) = \frac{s - M_\pi^2}{F_0^2}, \quad (2.52)$$

which is related to the size of the quark condensate by Eq. 2.43.

The combinations with definite isospin in the s -channel

$$\begin{aligned} T^0(s, t) &= 3A(s, t, u) + A(t, u, s) + A(u, s, t) \\ T^1(s, t) &= A(t, u, s) - A(u, s, t) \end{aligned} \quad (2.53)$$

$$\begin{aligned} T^2(s, t) &= A(t, u, s) + A(u, s, t) \\ & \quad (2.54) \end{aligned}$$

can be expanded into partial waves [30]

$$T^I(s, t) = 32\pi \sum_{l=0}^{\infty} (2l+1) P_l(\cos \theta) t_l^I(s). \quad (2.55)$$

Considering only the elastic region $4M_\pi^2 < s < 16M_\pi^2$ and imposing unitarity, the partial wave amplitudes $t_l^I(s)$ can be expressed as functions of real phase shifts $\delta_l^I(s)$:

$$t_l^I(s) = \sqrt{\frac{s}{s - 4M_\pi^2}} \cdot \frac{e^{2i\delta_l^I(s)} - 1}{2i}. \quad (2.56)$$

Near the threshold the partial wave amplitudes can be expanded into polynomials in q :

$$\text{Re } t_l^I(s) = q^{2l} \left(a_l^I + q^2 b_l^I + O(q^4) \right), \quad (2.57)$$

with $q^2 = s - 4M_\pi^2$. The parameters a_l^I of this expansion are the $\pi\pi$ scattering lengths. The relevant ones for the K_{e4} analysis are a_0^0 and a_0^2 , i.e. the S -wave terms with isospin 0 and 2, respectively.

2.3.1. Predictions for the scattering lengths a_0^0 and a_0^2

At Leading Order (LO) the analytical expressions for the a_0^0 and a_0^2 read [29]

$$a_0^0 = \frac{7M_\pi^2}{32\pi F_\pi^2}, \quad a_0^2 = -\frac{M_\pi^2}{16\pi F_\pi^2}, \quad (2.58)$$

with M_π^2 given by Eq. 2.44 and $F_\pi = F_0$. When considering higher orders, new terms are added to the expressions for the scattering lengths, but also M_π^2 and F_π have to be evaluated to the same order. Since M_π^2 depends on B_0 , the size of the quark condensate can be determined from the measurement of a_0^0 and a_0^2 .

In the framework of χPT the values of a_0^0 and a_0^2 have been predicted up to the Next-to-Next-to-Leading Order (NNLO), corresponding to $O(p^6)$ with the following numerical results:

$$\begin{aligned} a_0^0 &= 0.156 \quad , \quad a_0^2 = -0.045 \text{ (LO)} \quad [29] \\ a_0^0 &= 0.200 \quad , \quad a_0^2 = -0.043 \text{ (NLO)} \quad [31, 32] \\ a_0^0 &= 0.217 \quad , \quad a_0^2 = -0.041 \text{ (NNLO)} \quad [33] \end{aligned} \quad (2.59)$$

An alternative approach, the Generalised Chiral Perturbation Theory ($G\chi PT$), was proposed in [34] in order to avoid the assumption of a strong quark condensation. The counting

rule for the light quark mass terms, $m = O(p^2)$, is replaced by $m = O(p)$ and $B_0 = O(p)$. In this way the total Lagrangian is identical if all orders up to infinity are considered, but in the expansion the mass terms appear at lower order. Furthermore odd terms do not vanish and the predictions of the scattering lengths are given as functions of two free parameters α and β related to the size of the quark condensate and to the ratio m_s/m between the mass of the strange quark and the mass of u and d . At tree level the expressions for the scattering lengths are

$$a_0^0 = \frac{M_\pi^2}{96\pi F_\pi^2} (5\alpha + 16\beta), \quad a_0^2 = \frac{M_\pi^2}{48\pi F_\pi^2} (\alpha - 4\beta). \quad (2.60)$$

The χPT results are reproduced for $\alpha = \beta = 1$.

Since the publication by the BNL E865 collaboration [35] of the new experimental values for a_0^0 and a_0^2 , determined from the K_{e4} form factors, which were confirmed and improved by NA48/2 in the analysis of the cusp effect in $K^\pm \rightarrow \pi^\pm \pi^0 \pi^0$ [36], the scenario of a very small, or even vanishing, $SU(2) \bar{q}q$ condensate can be excluded and the $G\chi PT$ description is equivalent to the χPT one. At the same time, the theoretical predictions reached a precision of about 2% by the combined use of χPT and dispersion relations [37].

The dispersion relations for the partial wave amplitudes (called *Roy equations*) [38] read

$$t_l^I(s) = k_l^I(s) + \sum_{I'=0}^2 \sum_{l'=0}^{\infty} \int_{4M_\pi^2}^{\infty} ds' K_{ll'}^{II'}(s, s') \text{Im} t_{l'}^{I'}(s'), \quad (2.61)$$

with

$$k_l^I(s) = a_0^I \delta_l^0 + \frac{s - 4M_\pi^2}{4M_\pi^2} \cdot (2a_0^0 - 5a_0^2) \cdot \left(\frac{1}{3} \delta_0^I \delta_l^0 + \frac{1}{18} \delta_1^I \delta_l^1 - \frac{1}{6} \delta_2^I \delta_l^0 \right). \quad (2.62)$$

The kernels $K_{ll'}^{II'}(s, s')$ are explicitly known functions. These equations are valid on the interval $-4M_\pi^2 < s < 60M_\pi^2$. The integration is splitted into a low energy interval up to an energy $E_0 \simeq 0.8$ GeV (called *matching point*) and the remaining high energy interval. A numerical solution for the low energy can be computed using as input the two S -wave scattering lengths, the elasticity parameters below the matching point and the imaginary parts above it [39].

The elasticity parameters are assumed to be equal to 1 up to the matching point, since the only open inelastic channel is $2\pi \rightarrow 4\pi$, that is strongly suppressed at low energies. The $\pi\pi$ phase shifts in the intermediate region, i.e. between 0.8 and 2 GeV, are mainly determined from the reaction $\pi N \rightarrow \pi\pi N$. The most precise measurement was performed by the CERN-Munich collaboration on $\pi^- p \rightarrow \pi^- \pi^+ n$ [40]. The remaining contributions, that are summarised into the so-called driving term, are evaluated using experimental information on the resonances in partial waves with $l \geq 2$ in the intermediate energy region and Regge representations for the high energy $\pi\pi$ scattering amplitude.

Not only the contribution to the Roy equation above the matching point is used as input, but also the values of the phase shifts at that point. The solution of the equations is then a boundary value problem: at threshold the phases vanish and at the matching point they are given by the input. The dependency of the interpolation on the value at the boundary is therefore stronger than on the imaginary parts above it. The experimental values for δ_0^0 and δ_1^1 at the matching point are obtained from the high energy, high statistics $\pi N \rightarrow \pi\pi N$ experiments.

The numerical solutions are determined by a function for $\delta_l^I(s)$, where the parametrisation in [41] is used, allowing for an additional free parameter in the polynomial part:

$$\tan \delta_l^I = \sqrt{1 - \frac{4M_\pi^2}{s}} \cdot q^{2l} \cdot \left\{ A_l^I + B_l^I q^2 + C_l^I q^4 + D_l^I q^6 \right\} \left(\frac{4M_\pi^2 - s_l^I}{s - s_l^I} \right), \quad (2.63)$$

with $q = \sqrt{\frac{s-4M_\pi^2}{4M_\pi^2}}$ and where the parameters A , B , C and D have been determined explicitly for the combinations $l = 0, I = 0, 2$ and $l = 1, I = 1$ as a function of a_0^0 and a_0^2 . The numerical values can be found in Appendix D of [39].

The chiral representation and the one based on the dispersion relations have the same structure and can be matched at a point where the χPT can make accurate predictions [42]. The following results are obtained for the scattering lengths:

$$\begin{aligned} a_0^0 &= 0.220 \quad , \quad a_0^2 = -0.045 \quad (NLO) \\ a_0^0 &= 0.220 \quad , \quad a_0^2 = -0.044 \quad (NNLO). \end{aligned} \quad (2.64)$$

At NNLO the uncertainties are estimated to be 0.005 and 0.001 for a_0^0 and a_0^2 , respectively.

For a fixed value of a_0^0 and of the other input parameters, the Roy equations admit a solution without cusp only for a single value of a_0^2 , so that a_0^2 is not a free parameter anymore, but can be expressed as a function of a_0^0 , given the remaining input parameters. This function is called universal curve [43] and becomes a band (the *universal band*) when the experimental uncertainties on the input at intermediate and high energies are considered. From the calculations in [39] the universal curve was determined to be

$$a_0^2 = -0.0849 + 0.232 \cdot a_0^0 - 0.0865 \cdot (a_0^0)^2, \quad (2.65)$$

while the upper and lower boundaries of the universal band are

$$\begin{aligned} a_0^2 &= -0.0774 + 0.240 \cdot a_0^0 - 0.0881 \cdot (a_0^0)^2 \\ a_0^2 &= -0.0922 + 0.225 \cdot a_0^0 - 0.0847 \cdot (a_0^0)^2. \end{aligned} \quad (2.66)$$

Imposing the constraints from the chiral symmetry, the allowed band for a_0^2 as a function of a_0^0 restricts to [42]

$$a_0^2 = -0.0444 + 0.236 \cdot (a_0^0 - 0.22) - 0.61 \cdot (a_0^0 - 0.22)^2 - 9.9 \cdot (a_0^0 - 0.22)^3 \pm 0.0008, \quad (2.67)$$

which has a much smaller uncertainty than the universal band in Eq. 2.66. The universal band and the region allowed by the chiral symmetry are shown in Figure 2.2.

2.4. The K_{e4} decay

The $\pi\pi$ S -wave scattering near threshold can be studied very cleanly in the K_{l4} decays, where l indicates a muon or an electron, because the two pions are the only hadrons in the final state. In the following the theoretical predictions for the $K^+ \rightarrow \pi^+\pi^-e^+\nu_e$ decay, will be presented, but the corresponding matrix elements and form factors for any other K_{l4} decay can be deduced via isospin relations and using the proper values of the masses.

The tree level Feynman diagram within the SM for the decay $K^+ \rightarrow \pi^+\pi^-e^+\nu_e$ is shown in Figure 2.3. In the framework of χPT the mesons are considered instead of the single quarks.

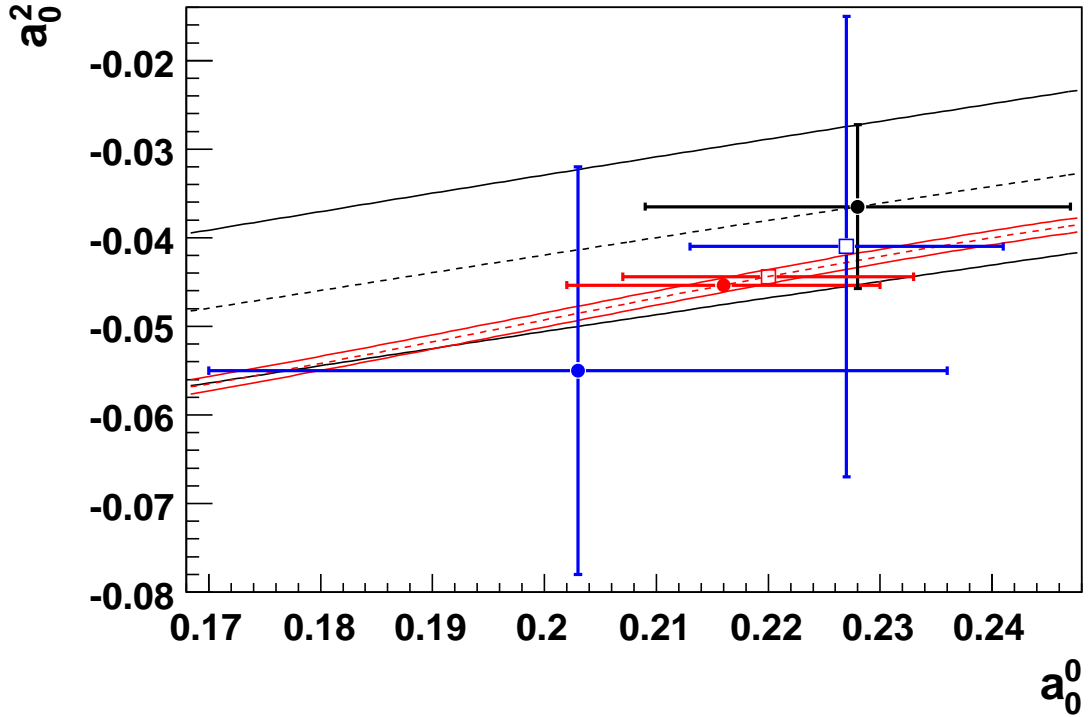


Figure 2.2.: The universal band (between the black solid lines) with the universal curve at its centre (black dashed line) [39] and the narrower band determined imposing the constraints from the chiral symmetry (red curves) [42]. The filled circles are the measurements performed by the E865 experiment in K_{e4} decays [35]: without constraints between a_0^0 and a_0^2 (blue), with the constraint of the universal curve (black) and with the chiral symmetry constraint (red). The empty squares represent the measurements of NA48/2 in $K^\pm \rightarrow \pi^0 \pi^0 \pi^\pm$ decays [36]: without constraints (blue) and with the chiral symmetry constraint (red). For all the experimental points the error bars include statistical, systematic and external uncertainties.

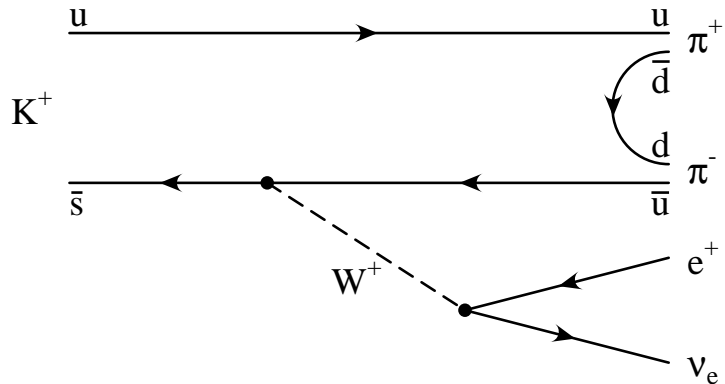


Figure 2.3.: The tree level standard model Feynman diagram for the K_{e4} decay.

2.4.1. The Cabibbo-Maksymowicz variables

The full kinematics of the decay can be described by five variables, first introduced by Cabibbo and Maksymowicz [44], that are shown in Figure 2.4. Considering the three reference frames Σ_K (the K^+ rest frame), $\Sigma_{\pi\pi}$ (the $\pi^+\pi^-$ centre of mass system) and $\Sigma_{e\nu}$ (the $e^+\nu$ centre of mass system), the variables are defined as follows:

s_π the invariant mass squared of the dipion system,

s_e the invariant mass squared of the dilepton system,

θ_π the angle between the π^+ in $\Sigma_{\pi\pi}$ and the dipion line of flight in Σ_K ,

θ_e the angle between the e^+ in $\Sigma_{e\nu}$ and the dilepton line of flight in Σ_K ,

ϕ the angle between the plane formed by the pions and the one formed by the leptons in Σ_K .

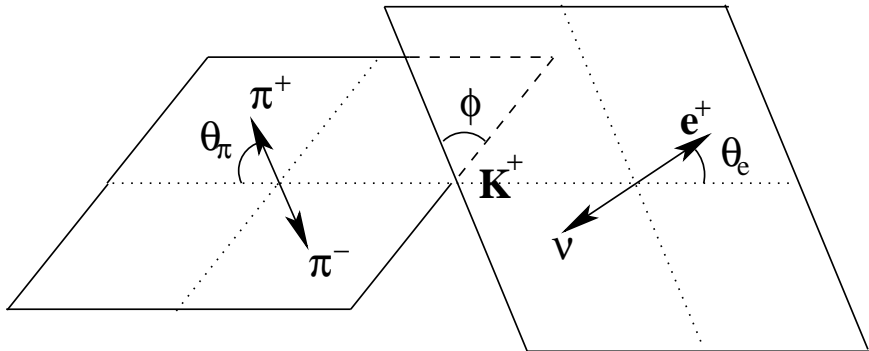


Figure 2.4.: The kinematic variables of the K_{e4} decay.

The following combinations of four momenta and Lorentz invariants are also useful to describe the matrix element and the form factors:

$$\begin{aligned}
 P &= p_{\pi^+} + p_{\pi^-} \quad , \quad Q = p_{\pi^+} - p_{\pi^-} \\
 L &= p_{e^+} + p_\nu \quad , \quad N = p_{e^+} - p_\nu \\
 PL &= \frac{1}{2} \left(M_K^2 - s_\pi - s_e \right) \quad , \quad X = \sqrt{(PL)^2 - s_\pi s_e} \\
 z_e &= \frac{M_e^2}{s_e} \quad , \quad \sigma_\pi = \sqrt{1 - 4 \frac{M_\pi^2}{s_\pi}}.
 \end{aligned} \tag{2.68}$$

2.4.2. Matrix element and decay rate

The matrix element can be written as a precisely known QED factor for the leptonic part and a general $V - A$ (vector minus axial-vector, due to the coupling of the weak interaction only to left-handed particles) current for the hadronic part [45]:

$$T = \frac{G_F}{\sqrt{2}} V_{us}^* \bar{u}(p_\nu) \gamma_\mu (1 - \gamma_5) v(p_e) (V^\mu - A^\mu), \tag{2.69}$$

with

$$\begin{aligned} V_\mu &= -\frac{H}{M_K^3} \epsilon_{\mu\nu\rho\sigma} L^\nu P^\rho Q^\sigma \\ A_\mu &= -\frac{i}{M_K} [P_\mu F + Q_\mu G + L_\mu R]. \end{aligned} \quad (2.70)$$

F, G, R and H (the *form factors*) are real analytical functions of the variables s_π, s_e and θ_π .

The partial decay rate as a function of the five kinematic variables defined above reads [44]

$$d\Gamma_5 = G_F^2 |V_{us}|^2 \frac{(1 - z_e)\sigma_\pi X}{2^{13}\pi^6 M_K^5} J_5(s_\pi, s_e, \theta_\pi, \theta_e, \phi) ds_\pi ds_e d(\cos \theta_\pi) d(\cos \theta_\pi) d\phi, \quad (2.71)$$

where the expression for J_5 as a function of the form factors, the Lorentz invariants and the four momenta is given in Eq. 2.68 of [45].

2.4.3. The Form Factors (FF)

For a measurement of the form factors a more suitable parametrisation was proposed in [46], where the dependence on the kinematic variables is displayed explicitly:

$$\begin{aligned} J_5 &= 2(1 - z_e) \left[I_1 + I_2 \cos 2\theta_e + I_3 \sin^2 \theta_e \cos 2\phi + I_4 \sin 2\theta_e \cos \phi + I_5 \sin \theta_e \cos \phi \right. \\ &\quad \left. + I_6 \cos \theta_e + I_7 \sin \theta_e \sin \phi + I_8 \sin 2\theta_e \sin \phi + I_9 \sin^2 \theta_e \sin 2\phi \right], \end{aligned} \quad (2.72)$$

with

$$\begin{aligned} I_1 &= \frac{1}{4} \left\{ (1 + z_e) |F_1|^2 + \frac{1}{2} (3 + z_e) (|F_2|^2 + |F_3|^2) \sin^2 \theta_\pi + 2z_e |F_4|^2 \right\} \\ I_2 &= -\frac{1}{4} (1 - z_e) \left\{ |F_1|^2 - \frac{1}{2} (|F_2|^2 + |F_3|^2) \sin^2 \theta_\pi \right\} \\ I_3 &= -\frac{1}{4} (1 - z_e) \left\{ |F_2|^2 - |F_3|^2 \right\} \sin^2 \theta_\pi \\ I_4 &= \frac{1}{2} (1 - z_e) \operatorname{Re}(F_1^* F_2) \sin \theta_\pi \\ I_5 &= -\{\operatorname{Re}(F_1^* F_3) + z_e \operatorname{Re}(F_4^* F_2)\} \sin \theta_\pi \\ I_6 &= -\{\operatorname{Re}(F_2^* F_3) \sin^2 \theta_\pi - z_e \operatorname{Re}(F_1^* F_4)\} \\ I_7 &= -\{\operatorname{Im}(F_1^* F_2) + z_e \operatorname{Im}(F_4^* F_3)\} \sin \theta_\pi \\ I_8 &= \frac{1}{2} (1 - z_e) \operatorname{Im}(F_1^* F_3) \sin \theta_\pi \\ I_9 &= -\frac{1}{2} (1 - z_e) \operatorname{Im}(F_2^* F_3) \sin^2 \theta_\pi \end{aligned} \quad (2.73)$$

and

$$\begin{aligned} F_1 &= X F + \sigma_\pi (P \cdot L) \cos \theta_\pi \cdot G \\ F_2 &= \sigma_\pi (s_\pi s_e)^{1/2} G \\ F_3 &= \sigma_\pi X (s_\pi s_e)^{1/2} \frac{H}{m_K^2} \\ F_4 &= -(PL) F - s_e R - \sigma_\pi X \cos \theta_\pi G. \end{aligned} \quad (2.74)$$

The form factor R only appears in the combination $s_e \cdot R$ in F_4 , which enters the decay rate always preceded by z_e , i.e. R is multiplied by M_e^2 ($\simeq 0.25 \times 10^{-6}$ GeV $^2/c^4$) in the decay rate. The electron channel has therefore no sensitivity to R , that can only be measured in the $K_{\mu 4}$ decay.

Parametrisation

In order to perform a fit of the form factors on experimental data, F , G , R and H are expanded into partial waves:

$$\begin{aligned} F &= \sum_{l=0}^{\infty} P_l(\cos \theta_\pi) f_l - \frac{\sigma_\pi P L}{X} \cos \theta_\pi G \\ G &= \sum_{l=1}^{\infty} P'_l(\cos \theta_\pi) g_l \\ R &= \sum_{l=0}^{\infty} P_l(\cos \theta_\pi) r_l + \frac{\sigma_\pi s_\pi}{X} \cos \theta_\pi G \\ H &= \sum_{l=1}^{\infty} P'_l(\cos \theta_\pi) h_l, \end{aligned} \quad (2.75)$$

where P_l are the Legendre polynomials and $P'_l(\cos \theta_\pi) = \frac{d}{d(\cos \theta_\pi)} P_l$. The partial wave amplitudes f_l , g_l , r_l and h_l depend in general on s_π and s_e , while the phases coincide with the phase shifts δ_l^I with $I = 0$ for even values of l and $I = 1$ for odd values of l .

In [46] no assumption was made on the dependence of f_l , g_l , r_l and h_l on s_π and s_e , so that in principle independent values of the partial wave amplitudes and of the phase shifts have to be determined in each (s_π, s_e) bin. Later a simpler parametrisation was proposed [47], that allows for a reduction of the number of parameters to 11 plus the number of bins in s_π for the measurement of the phase shift difference. Considering different models and approximations, it was observed that the dependence of F and G on s_e is linear and the slope is independent of s_π , while the s_π dependence of the coefficient of $\cos \theta_\pi$ is well described by $\sigma_\pi X$. R is neglected and for H a linear dependence on s_π should be a sufficient parametrisation:

$$\begin{aligned} F &= (f_s + f'_s s_\pi + f''_s s_\pi^2 + f_e s_e) e^{i\delta_0^0(s_\pi)} + \tilde{f}_p \sigma_\pi X \cos \theta_\pi e^{i\delta_1^1(s_\pi)} \\ G &= (g_p + g'_p s_\pi + g_e s_e) e^{i\delta_1^1(s_\pi)} + g_d \sigma_\pi X \cos \theta_\pi e^{i\delta_2^0(s_\pi)} \\ H &= (h_p + h'_p s_\pi) e^{i\delta_1^1(s_\pi)}, \end{aligned} \quad (2.76)$$

where \tilde{f}_p is a combination of f_p and g_p .

This parametrisation allows to use the statistics of the experiment more effectively than the one in [46], but it has to be tested if it is actually sufficient to describe the data.

Theoretical prediction

At leading order the form factors in the chiral representation are [48]

$$F = G = \frac{M_K}{\sqrt{2} F_\pi} = 3.74$$

$$\begin{aligned} R &= \frac{M_K}{2\sqrt{2}F_\pi} \left(\frac{Z}{s_e - M_K^2} + Q \right) \\ H &= 0, \end{aligned} \tag{2.77}$$

where $Z = s_\pi - 2\sigma_\pi X \cos \theta_\pi$ is the pole part of R , related to the $KK \rightarrow \pi\pi$ amplitude, and $Q = 1$ its regular part.

At NLO four additional terms have to be considered [49, 50]: the tree graphs at order p^4 , the unitarity corrections generated by the one loop graphs, some logarithms independent of the kinematics and the chiral anomaly [51, 52, 53]. In general the FF at NLO can be written as

$$I(s_\pi, u, t) = I^{LO} \left\{ 1 + \frac{1}{F_\pi^2} (U_I + P_I + C_I) \right\}, \tag{2.78}$$

with $I = F, G, Z, Q$. The U_I terms include the unitarity corrections, P_I are the polynomials obtained from the tree graphs and C_I the logarithmic terms independent of the kinematics. The complete expressions for the different contributions can be found in [54]. The terms P_I have in general the form

$$P_I(s_\pi, t, u) = \sum_{j=1}^9 p_{j,I}(s_\pi, t, u) L_j^r, \tag{2.79}$$

where the coefficients $p_{j,I}$ are different for the various FFs and some of them vanish. The quantities L_j^r are the renormalised coupling constants, that parametrise the effective Lagrangian at order p^4 [55]. They are scale dependent, but the loop contribution compensate the dependence, so that the observable quantities are independent of the scale. The coupling constants are free parameters of the theory and have to be determined experimentally. The K_{e4} decay is particularly sensitive to L_1 , L_2 and L_3 .

The anomaly is the first non vanishing contribution to H in the chiral expansion:

$$H = -\frac{\sqrt{2}M_K^3}{8\pi^2 F_\pi^3} = -2.66. \tag{2.80}$$

The contribution of higher order terms in the S -wave amplitude of the form factor F has been estimated by use of a dispersive representation [56], determining the subtraction constants from χPT [54]. This estimate also takes into account the non negligible contribution from the final state interaction in the $I = 0$ S -wave amplitude.

2.4.4. The $K^- \rightarrow \pi^+ \pi^- e^- \bar{\nu}_e$ decay

Since NA48/2 is the first experiment that can measure K_{e4} decays both from K^+ and K^- , it is important to correctly apply the theoretical predictions for the positive kaons to the negative ones.

The matrix element for the $K^- \rightarrow \pi^+ \pi^- e^- \bar{\nu}_e$ decay was explicitly computed in [57]: without any assumption on CP and CPT invariance, the following transformations have to be performed on the kinematic variables

$$\begin{aligned} s_\pi &\rightarrow s_\pi & s_e &\rightarrow s_e \\ \theta_\pi &\rightarrow \theta_\pi & \theta_e &\rightarrow \pi - \theta_e \\ \phi &\rightarrow \pi + \phi \end{aligned} \tag{2.81}$$

and the form factors can in general have different values for the K^+ and the K^- decay. Furthermore the amplitudes for different values of the third component of the angular momentum of the two pions do not have to be equal.

CPT invariance implies

$$\Gamma(K^+ \rightarrow \pi^+ \pi^- e^+ \nu_e) + \Gamma(K^+ \rightarrow \pi^0 \pi^0 e^+ \nu_e) = \Gamma(K^- \rightarrow \pi^+ \pi^- e^- \bar{\nu}_e) + \Gamma(K^- \rightarrow \pi^0 \pi^0 e^- \bar{\nu}_e), \quad (2.82)$$

while invariance under time reversal cancels the dependence on the third component of the angular momentum.

Finally, in the assumption of CP invariance, the angle transformations become

$$\begin{aligned} \theta_\pi &\rightarrow \theta_\pi & \theta_e &\rightarrow \theta_e \\ \phi &\rightarrow -\phi \end{aligned} \quad (2.83)$$

and the form factors are identical. This is equivalent to the use of the transformations in Eq. 2.81 and a change of sign in the H form factor. In this way the validity of the assumption can be tested.

2.4.5. The $K_{e4}^{\Delta S=-\Delta Q}$ decay

The decay $K^\pm \rightarrow \pi^\pm \pi^\pm e^\mp \bar{\nu}_e$ violates the empirical rule $\Delta S = \Delta Q$, where S is the strangeness and Q the total charge of the hadronic particles and is therefore expected to happen with a much smaller probability than the K_{e4} decay. Considering the tree level standard model Feynman diagram, shown in Figure 2.5, it can be seen that actually two weak vertices are necessary and therefore the ratio of the branching ratios $BR(K_{e4}^{\Delta S=-\Delta Q})/BR(K_{e4})$ is expected to be of the order of $G_F^2 \cdot M^2 \leq 10^{-10}$, where M is a mass scale, that can be at most equal to the kaon mass.

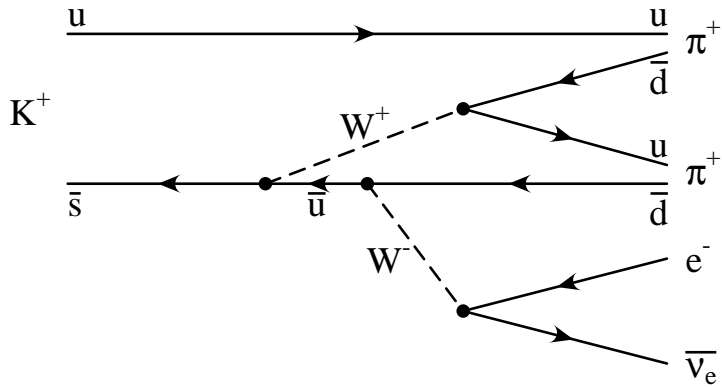


Figure 2.5.: The tree level standard model Feynman diagram for the $K_{e4}^{\Delta S=-\Delta Q}$ decay.

2.5. Previous experimental results

2.5.1. $\pi\pi$ scattering lengths

The scattering length a_0^0 was first measured by the Geneva-Saclay experiment in 1976 [58]. About 30,000 K_{e4} events were collected and a_0^0 was determined from a fit of the phase

2. Theoretical predictions and previous results

difference $\delta_0^0 - \delta_1^1$ in five bins of $M_{\pi\pi}$, using the parametrisation proposed in [59]:

$$a_0^0 = 0.28 \pm 0.06. \quad (2.84)$$

A more precise measurement was published in 2003 by the BNL E865 collaboration, based on 388,000 K_{e4} events [35]. The fit of the scattering lengths a_0^0 and a_0^2 was performed with the parametrisation of Eq. 2.63 and three results were obtained, according to the constraint applied between a_0^0 and a_0^2 (see Figure 2.2). Without any constraint, the two variables are strongly correlated and the measurement is not very precise (blue filled circle in Figure 2.2):

$$\begin{aligned} a_0^0 &= 0.203 \pm 0.033 \text{ (stat)} \pm 0.004 \text{ (syst)}, \\ a_0^2 &= -0.055 \pm 0.023 \text{ (stat)} \pm 0.003 \text{ (syst)}. \end{aligned} \quad (2.85)$$

Imposing the universal curve as constraint and assigning to a_0^0 a theoretical uncertainty given by the shift when using as constraint the lower or the upper bound of the universal band, the following values were obtained (black filled circle in Figure 2.2):

$$\begin{aligned} a_0^0 &= 0.228 \pm 0.012 \text{ (stat)} \pm 0.004 \text{ (syst)} {}^{+0.012}_{-0.016} \text{ (theor)}, \\ a_0^2 &= -0.0365 \pm 0.0023 \text{ (stat)} \pm 0.0008 \text{ (syst)} {}^{+0.0031}_{-0.0026} \text{ (theor)}^1. \end{aligned} \quad (2.86)$$

Applying the tight constraint given by the χPT , the theoretical uncertainty becomes negligible (red filled circle in Figure 2.2):

$$\begin{aligned} a_0^0 &= 0.216 \pm 0.013 \text{ (stat)} \pm 0.004 \text{ (syst)} \pm 0.002 \text{ (theor)}, \\ a_0^2 &= -0.0454 \pm 0.0031 \text{ (stat)} \pm 0.0010 \text{ (syst)} \pm 0.0008 \text{ (theor)}. \end{aligned} \quad (2.87)$$

The latest measurement of the scattering lengths was performed by the NA48/2 collaboration, based on $2.287 \times 10^7 K^\pm \rightarrow \pi^0 \pi^0 \pi^\pm$ decays [36]. In the M_{00}^2 distribution, the squared invariant mass of the two neutral pions, a cusp-like structure was observed at the threshold of the $\pi^+ \pi^-$ production. Fitting the distribution in the range $0.074 < M_{00}^2 < 0.097$ (GeV/c²)² with the rescattering model described in [60], the following results were obtained without any constraint between the two parameters (blue empty square in Figure 2.2):

$$\begin{aligned} a_0^0 - a_0^2 &= 0.268 \pm 0.010 \text{ (stat)} \pm 0.004 \text{ (syst)} \pm 0.013 \text{ (theor)}, \\ a_0^2 &= -0.041 \pm 0.022 \text{ (stat)} \pm 0.014 \text{ (syst)}, \end{aligned} \quad (2.88)$$

and with the χPT constraint between a_0^0 and a_0^2 (red empty square in Figure 2.2):

$$\begin{aligned} a_0^0 &= 0.220 \pm 0.006 \text{ (stat)} \pm 0.004 \text{ (syst)} \pm 0.011 \text{ (theor)}, \\ a_0^2 &= -0.0444 \pm 0.0014 \text{ (stat)} \pm 0.0009 \text{ (syst)} \pm 0.0008 \text{ (theor)}. \end{aligned} \quad (2.89)$$

The Geneva-Saclay measurement was in disagreement with the tree-level theoretical prediction available at that time, but the more recent results agree perfectly with the NNLO χPT predictions.

¹The statistical and systematic uncertainties, that can be obtained from the propagation of the uncertainties on a_0^0 , were clearly mis-typed in [35]. The correct values are reported.

2.5.2. K_{e4} form factors

The measurement performed by the Geneva-Saclay collaboration [58] was based on the Pais-Treiman parametrisation [46] and yielded:

$$\begin{aligned}\lambda &= 0.08 \pm 0.02, \\ f_p/f_s &= 0.009 \pm 0.032, \\ g/f_s &= 0.855 \pm 0.041, \\ h/f_s &= -0.48 \pm 0.12,\end{aligned}\tag{2.90}$$

where λ corresponds to f'_s/f_s , g to g_p and h to h_p in the parametrisation used in this analysis. \tilde{f}_p corresponds to $f_p \cdot \frac{4M_\pi^2}{\sigma_\pi X}$

The E865 collaboration performed both a fit in multiple bins of s_π , obtaining a result compatible with the Geneva-Saclay experiment, and to the whole data set at once to improve the statistical precision [35]. The fit to the whole data sample was based on the parametrisation of Eq. 2.76 where s_π was substituted by $q^2 = \frac{s_\pi}{4M_\pi^2} - 1$ and s_e by $\frac{s_e}{4M_\pi^2}$ in order to have dimensionless parameters. The following values were obtained:

$$\begin{aligned}f_s &= 5.75 \pm 0.02 \text{ (stat)} \pm 0.08 \text{ (syst)}, \\ f'_s &= 1.06 \pm 0.10 \text{ (stat)} \pm 0.40 \text{ (syst)}, \\ f''_s &= -0.59 \pm 0.12 \text{ (stat)} \pm 0.40 \text{ (syst)}, \\ g_p &= 4.66 \pm 0.05 \text{ (stat)} \pm 0.07 \text{ (syst)}, \\ g'_p &= 0.67 \pm 0.10 \text{ (stat)} \pm 0.04 \text{ (syst)}, \\ h_p &= -2.95 \pm 0.19 \text{ (stat)} \pm 0.20 \text{ (syst)}.\end{aligned}\tag{2.91}$$

The fit was performed under the assumption that the decay rate does not depend on s_e and that the P -wave contribution to F is negligible, i.e. fixing to zero the parameters f_e , g_e and \tilde{f}_p . In order to test this approximation, they were added once at a time as free parameters of the fit and found to be consistent with zero:

$$\begin{aligned}\tilde{f}_p &= -0.34 \pm 0.10 \text{ (stat)} \pm 0.27 \text{ (syst)}, \\ f_e &= -0.32 \pm 0.10 \text{ (stat)} \pm 0.24 \text{ (syst)}, \\ g_e &= 0.04 \pm 0.34 \text{ (stat)} \pm 0.88 \text{ (syst)}.\end{aligned}\tag{2.92}$$

2.5.3. Limits on $\Delta S = -\Delta Q$

The most precise measurement of the relative amount of decays with $\Delta S = -\Delta Q$ with respect to the ones with $\Delta S = \Delta Q$ was performed by the CPLEAR experiment:

$$\begin{aligned}\text{Re}(x) &= -0.0018 \pm 0.0041 \text{ (stat)} \pm 0.0045 \text{ (syst)} [61] \\ \text{Im}(x) &= 0.0012 \pm 0.0019 \text{ (stat)} \pm 0.0009 \text{ (syst)} [62],\end{aligned}\tag{2.93}$$

with $x = A(\overline{K^0} \rightarrow \pi^- \ell^+ \nu) / A(K^0 \rightarrow \pi^- \ell^+ \nu)$.

In the charged kaon system only upper limits on the branching ratios of the $\Delta S = -\Delta Q$ $K_{\ell 4}$ decays were determined:

$$\begin{aligned}BR(K^+ \rightarrow \pi^+ \pi^+ e^- \bar{\nu}_e) &< 3 \times 10^{-4} \cdot BR(K^+ \rightarrow \pi^+ \pi^- e^+ \nu_e) \text{ at 90\% CL [63]} \\ BR(K^+ \rightarrow \pi^+ \pi^+ \mu^- \bar{\nu}_\mu) &< 3 \times 10^{-6} \text{ at 95\% CL [64].}\end{aligned}\tag{2.94}$$

2. Theoretical predictions and previous results

The $K_{e4}^{\Delta S = -\Delta Q}$ measurement, performed on a sample of about 11,000 K_{e4} decays by the Geneva-Saclay collaboration, is about one order of magnitude worse than the corresponding limit on $|x|^2$, but could be significantly improved with the higher statistics collected by the NA48/2 experiment.

3. Experimental apparatus

The analysis presented in this thesis was performed using data collected in 2003 by the NA48/2 experiment at the SPS accelerator at CERN.

The NA48 experiment is the 48th experiment of the North Area and was originally designed to measure the direct CP violation in the neutral kaon system via the double ratio of the K_S and K_L decays into two charged or neutral pions. For this purpose data were taken from 1997 to 2001 and the final result, with a precision of 2×10^{-4} on the parameter $\text{Re}(\epsilon'/\epsilon)$, was published in 2002 [65].

A first extension [66] (NA48/1) was obtained for the year 2002 to study rare K_S decays, which led to the first observation of the decays $K_S \rightarrow \pi^0 e^+ e^-$ and $K_S \rightarrow \pi^0 \mu^+ \mu^-$ [67, 68], and to perform measurements of hyperon decays and lifetimes.

NA48/2 is the second extension of NA48 and has the aim of a precision measurement of charged kaon decay parameters [69]: the asymmetry of the slopes in the Dalitz plots between K^+ and K^- , which gives the size of the direct CP violation in charged kaons, can be measured with a precision of a few times 10^{-4} in the decays $K^\pm \rightarrow \pi^+ \pi^- \pi^\pm$ and $K^\pm \rightarrow \pi^0 \pi^0 \pi^\pm$; the $\pi\pi$ scattering length a_0^0 can be extracted from charged K_{e4} decays with an uncertainty of 0.01 (this analysis); many predictions of the Chiral Perturbation Theory (χPT) can be tested, for example in the radiative decays; in the K_{e3} decays the CKM matrix element V_{us} can be extracted from the branching ratio and form factor measurements and the sensitivity to deviations from the V-A theory is higher than in previous experiments.

The collaboration running this experiment consists of 11 institutions from 7 countries (Cambridge, CERN, Dubna, Ferrara, Firenze, Mainz, Perugia, Pisa, Saclay, Torino, Vienna). The complete data sample was collected in 2003 and 2004, but only part of it will be used in the present analysis.

3.1. The Super Proton Synchrotron (SPS) accelerator at CERN

Protons for the accelerator complex at CERN are produced in a Duoplasmatron source, injected into a linear accelerator (Linac2) and accelerated to an energy of 50 MeV. An 80 m long beam transport carries the Linac2 beam to the first ring accelerator of the chain: the PS Booster (PSB). In this four-deck synchrotron the protons reach an energy of 1.4 GeV and the bunches from each ring can be recombined in various ways at the injection into the Proton Synchrotron (PS). The PS was the first synchrotron built at CERN and started being operative in 1959. It can accelerate protons up to an energy of about 25 GeV and is still used as injector to the higher energy machines, as, for example, the Super Proton Synchrotron (SPS). A schematic representation of the CERN accelerator complex is shown in Figure 3.1. A detailed description of the CERN synchrotrons can be found in [70].

The SPS is operative since 1976 and is installed in an underground tunnel tangent to the CERN site, with a radius of 2.2 km. It was foreseen for fixed target experiments in the West

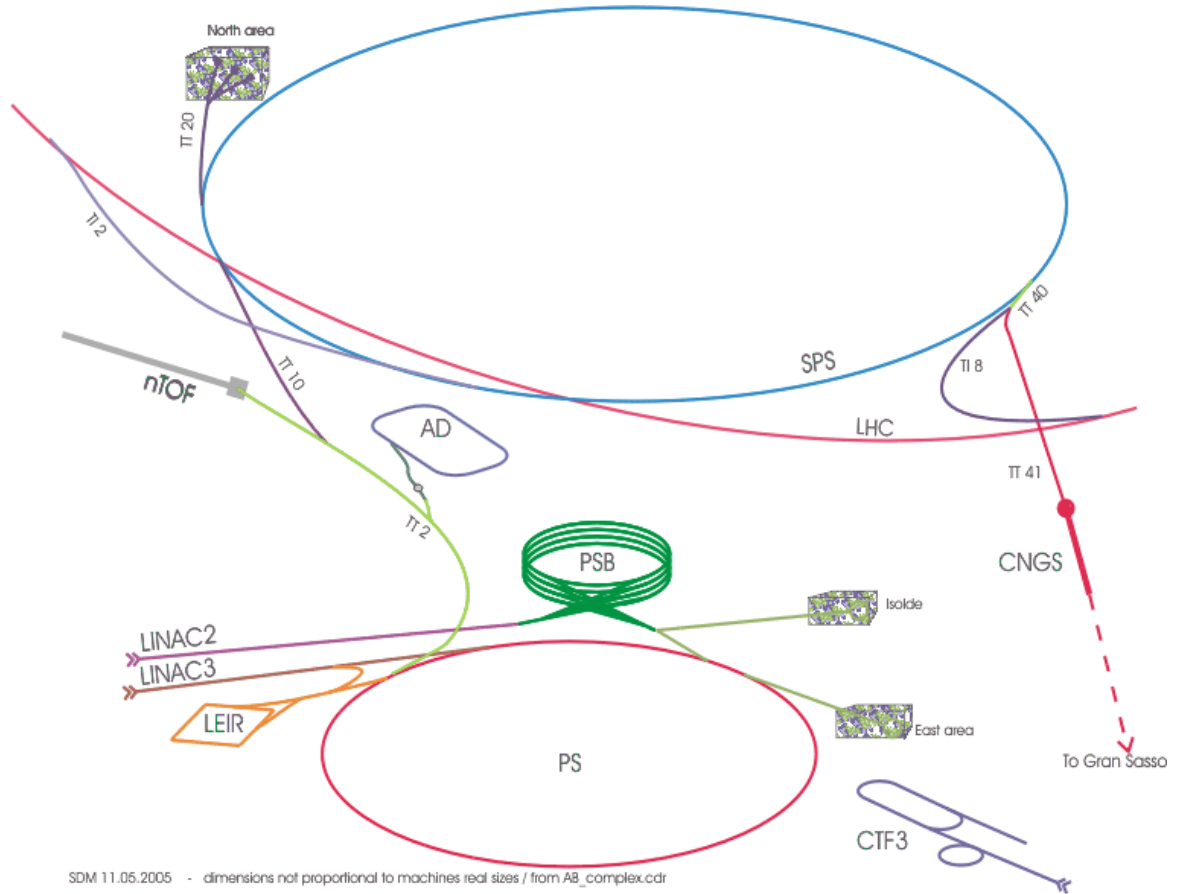


Figure 3.1.: Schematic representation of the CERN accelerator complex [71].

and in the North Experimental Areas and is still actively used today. The SPS was also used as a proton-antiproton collider for the UA-1 and UA-2 experiments that observed for the first time the W and Z bosons. It served as an injector for the Large Electron Positron collider (LEP) and it will be the last injector of the Large Hadron Collider (LHC). In addition it will provide a neutrino beam to Gran Sasso and protons to the North Area. The maximum proton energy that can be reached at the SPS is 450 GeV.

3.2. The NA48/2 beam line

Since the NA48 and NA48/1 experiments had analysed neutral kaon decays, a new beam line [72] connecting the NA48/2 target to the detector in the North Experimental Area had to be designed and built to simultaneously produce and transport positively and negatively charged kaons with a central momentum of 60 GeV/c . A schematic vertical section of the beam line can be seen in Figure 3.2.

Different charged particles (mainly pions and kaons) are produced in a 2 mm diameter, 400 mm long beryllium target by a 400 GeV/c primary proton beam, impinging at zero

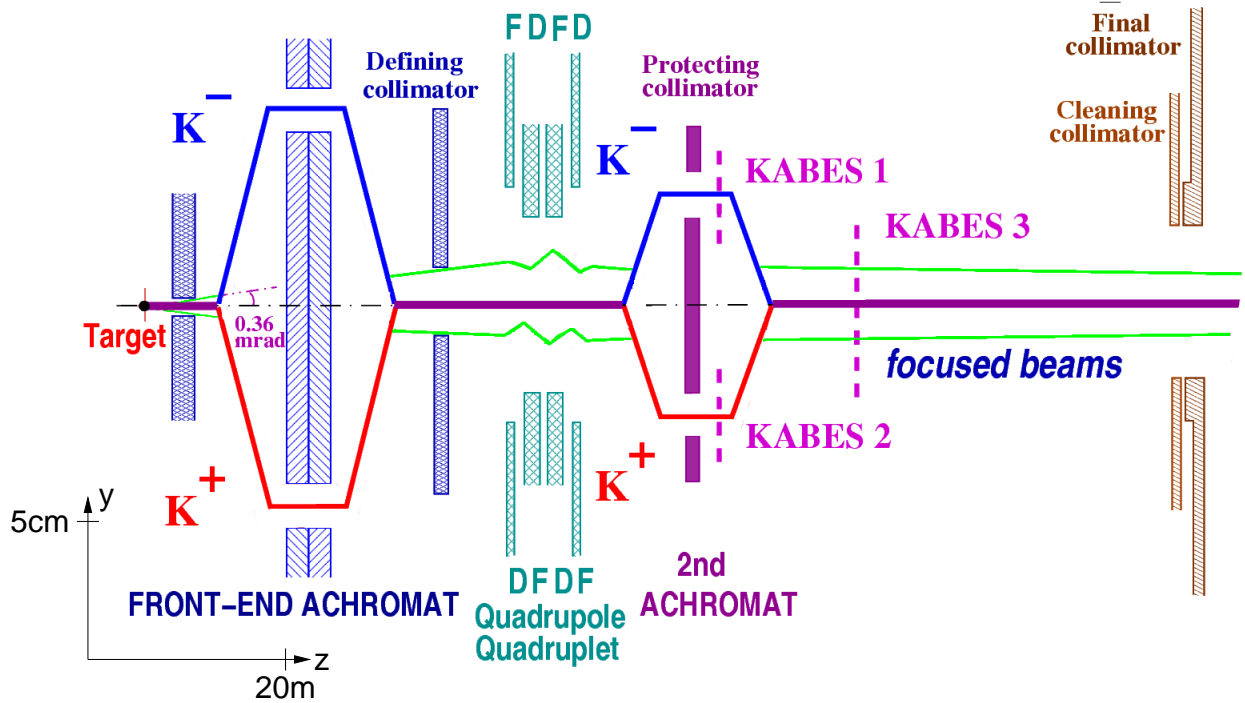


Figure 3.2.: Schematic vertical section of the NA48/2 simultaneous K^+ and K^- beam line. The blue and red lines show the centre of the K^+ and K^- beams respectively. The green lines indicate the width of the beam outside the dipole magnets [73].

degrees angle, at a nominal intensity of 7×10^{11} particles per pulse (burst), with a duty cycle of 16.8 s and 4.8 s flat-top. The two beams of opposite charge are deflected vertically by a front-end achromat, consisting of four dipole magnets, in order to select the momentum band for the two charges, which has a width (root mean square) of $\pm 3.8\%$. The first two dipole magnets with opposite-sign field separate positively from negatively charged particles. The central momentum and the momentum interval of each beam are then defined by the passage through a pair of collimators (TAX), which also serve as dumps to absorb the remaining primary protons and the neutral kaons. The last two deflection magnets return the two beams onto a common axis. During the data taking the paths of the positively and negatively charged beams were inverted regularly, in order to investigate possible systematic effects.

The opening angle of ± 0.36 mrad in both planes is defined by a common water cooled, copper collimator placed 24 m downstream of the target. After the collimator a system of four alternating-gradient quadrupoles focuses particles of each sign at the beginning of the detector to spots centred at the beam axis of about 5 mm width. Aim of the focusing is to create spots that are as small and as similar as possible, so that acceptance differences due to the different momentum distribution inside the spot are minimised. A second achromat separates again the two beams vertically, allowing the momentum and charge measurement of each kaon by the KAon BEam Spectrometer (see Section 3.3.1), and recombines them afterwards. A protecting collimator with openings for the two charged beams serves to stop

3. Experimental apparatus

all neutral and many charged particles produced on the defining collimator.

In order to reduce the flux of muons originating from pion and kaon decays, a cleaning collimator, consisting of magnetised-iron sweeping elements around the beam line, has been installed before the final collimator. At the end of the final collimator the total beam flux was estimated to be 3.8×10^7 positive and 2.6×10^7 negative particles per pulse, of which $2.2 \times 10^6 K^+$ and $1.3 \times 10^6 K^-$, thus allowing to reconstruct a few $10^4 K^\pm$ decays per burst. The muon background level was found to be compatible with the expected pion and kaon decays downstream of the final collimator.

3.2.1. The vacuum tank

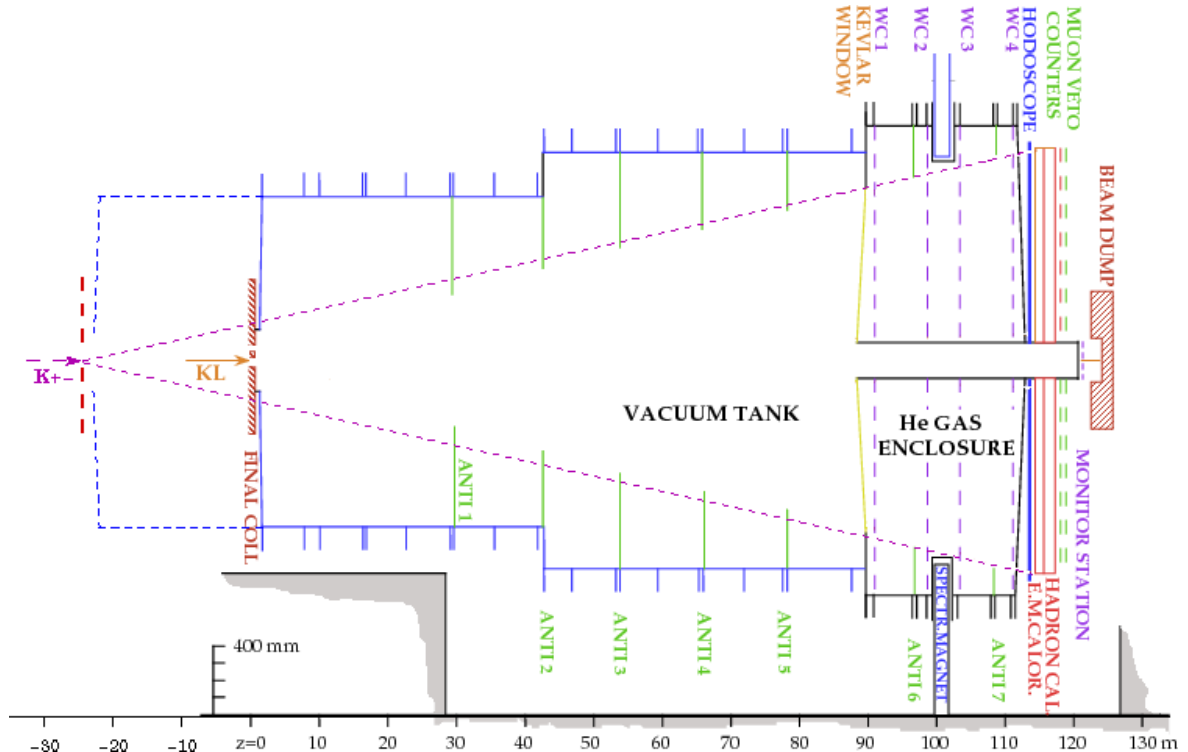


Figure 3.3.: The decay region in the vacuum tank. The solid lines refer to the shape and dimension of the tank until 2002 [74]. For the NA48/2 experiment the tank was extended by 24 m in order to increase the acceptance. The new position is shown by the dashed lines.

The decay region is contained in a cylindrical evacuated steel tank with a pressure of less than 10^{-4} mbar in order to have a negligible probability that the kaons interact with matter instead of decaying in flight and to reduce the multiple scattering of the decay products.

Until 2002 the vacuum tank had a volume of 330 m^3 , with a diameter of 1.92 m in the first 39 m and of 2.4 m afterwards, so that the geometrical acceptance of the decay products is not limited by the width of the tank. To achieve an increase in the acceptance of about 30% in

NA48/2, the vacuum tank was extended upstream by 24 m (see Figure 3.3) to a total length of 114 m, starting from the final collimator and ending at a kevlar window, which separates the decay region from the helium tank where the spectrometer (see Section 3.3.2) is situated.

In order to avoid interactions of the undecayed beam particles, a 1.1 mm thick aluminium beam pipe with a diameter of 152 mm starts at the kevlar window and goes through the whole detector. The vacuum inside it and the small amount of material in the pipe itself ensure a low scattering probability.

3.3. The NA48/2 detector

The NA48 detector was originally built to study the direct CP violation in the neutral kaon system and was therefore optimised for the detection of two pion decays. New sub-detectors, as well as modifications and upgrades of existing systems were necessary to obtain a better reconstruction of charged kaon decays, mainly into three charged, or one charged and two neutral, pions.

The original detector (see Figure 3.4) consisted of: a beam spectrometer (see Section 3.3.2) with four drift chambers, two before and two after a dipole magnet for the momentum measurement of charged particles; a pair of scintillator planes (see Section 3.3.3) for the precise time measurement of charged particles; a homogeneous electromagnetic calorimeter filled with liquid krypton (see Section 3.3.4) to measure the energy and position of photons and to identify electrons, separating them from pions; a hodoscope made of bunches of scintillating fibres (see Section 3.3.5) to determine precisely the time of the photons; a hadronic sampling calorimeter (see Section 3.3.6) consisting of alternated iron and scintillator planes for the energy measurement of hadrons; a muon anti-counter (see Section 3.3.7) to distinguish muons from pions; a system of seven scintillator rings (see Section 3.3.8) to veto photons escaping the decay volume and the detector.

The main changes applied in 2003 were: the installation of Hall probes for the monitoring of the magnetic field inside the spectrometer magnet; the addition of two new sub-detectors: the KAon BEam Spectrometer (see Section 3.3.1) for the momentum measurement of each kaon and a beam position monitor (see Section 3.3.9) to check the time stability of the beam geometry; the full instrumentation of the third drift chamber in order to increase the reconstruction efficiency and the reorganisation of the read-out electronics into a left-right symmetric configuration.

A coordinate system, which will be used in the rest of this thesis, is defined with the z axis along the beam ($z = 0$ is 18 m downstream of the collimator, where the K_S target was positioned till 2002), the x axis pointing to the right and the y axis upwards. $x = 0$ and $y = 0$ are at the centre of the beam axis.

The common timing signal to all the sub-detectors is given by a 40 MHz clock [76], whose signal is transported through a special high-quality cable together with the information of the start and end of burst. By sending the signal through the same chain back to the clock, the propagation speed can be monitored with an accuracy of 60 ps.

3.3.1. The KAon BEam Spectrometer (KABES)

The KABES detector [77] consists of six Time Projection Chambers (TPCs), using a MICRO MEsh GAseous Structure (MICROMEGAS) [78]. As shown in Figure 3.5, in each chamber

3. Experimental apparatus

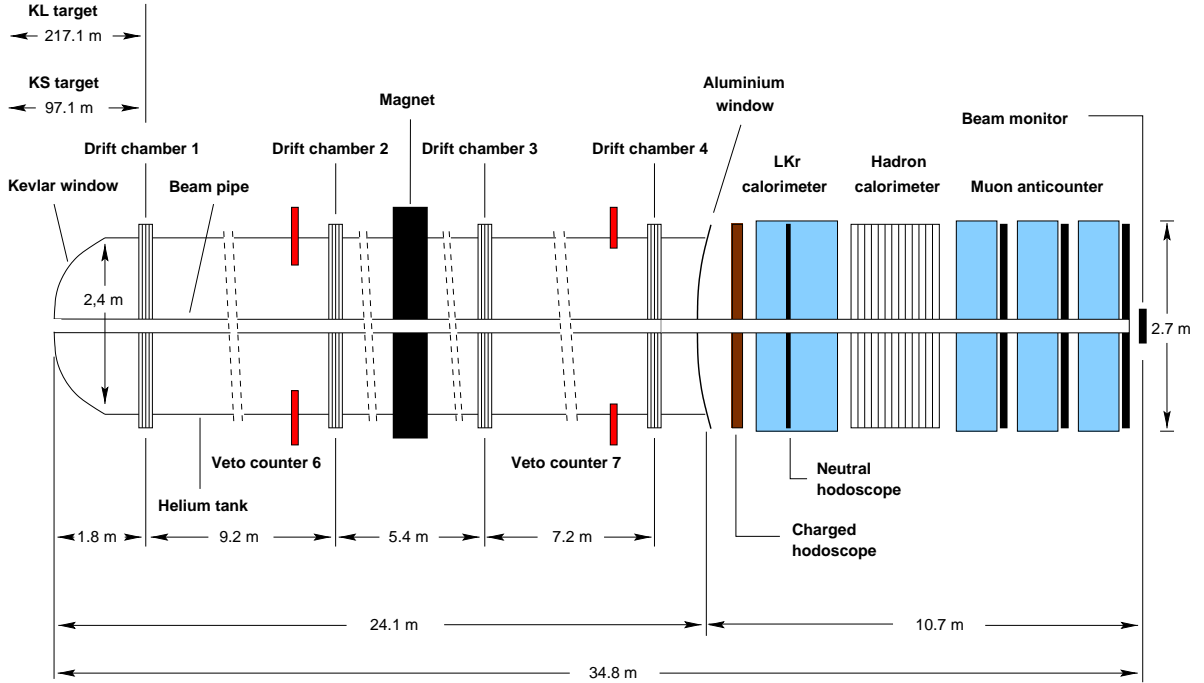


Figure 3.4.: Cross section of the NA48 detector [75].

an electric field is produced between grounded anode strips and a cathode. When a charged particle goes through the detector, the gas contained in the chamber (a mixture of 79% Ne , 11% C_2H_6 and 10% CF_4) is ionised and the electrons that are produced travel opposite to the applied electric field and deposit their charge on a certain strip. Each chamber contains 48 strips, 4 cm long, positioned parallel to the beam, with a 0.835 mm pitch. The y coordinate is given by the signal of the strips, while the x coordinate can be extracted, knowing the drift velocity, from the time difference of the signals in the two chambers with opposite drift field.

Micro-strip gas chambers are used for the detection of high fluxes of particles and provide a good spatial resolution. Their gain, limited to about 10^4 because of the positive ion accumulation on the insulator, can be improved by adding a thin micro-mesh close to the microstrip plane. The small gap, in this case of 50 μm , is kept by precise insulating spacers. This two-stage parallel plate avalanche chamber is called MICROMEGAS. The particular configuration of a micro-mesh separating the conversion space of 6 cm from the amplification gap of only 50 μm , allows a very high electric field in the amplification region and a much lower one in the drift region. The ratio between the two electric fields of about 60 ensures the fast collection of the ion cloud on the micro-mesh while only a fraction of it, inversely proportional to the field ratio escapes to the conversion region.

In the specific case of KABES, the meshes had a size of $4 \times 4 \text{ cm}^2$ and were produced from a 50 μm thick copper-plated Kapton foil in which the 5 μm thick copper layer was etched to produce 25 μm diameter holes every 60 μm . The Kapton was used as spacer to keep the thickness of the gap between the strips and the copper layer uniform.

To improve the field uniformity, cages with equipotential lines engraved on thin Mylar

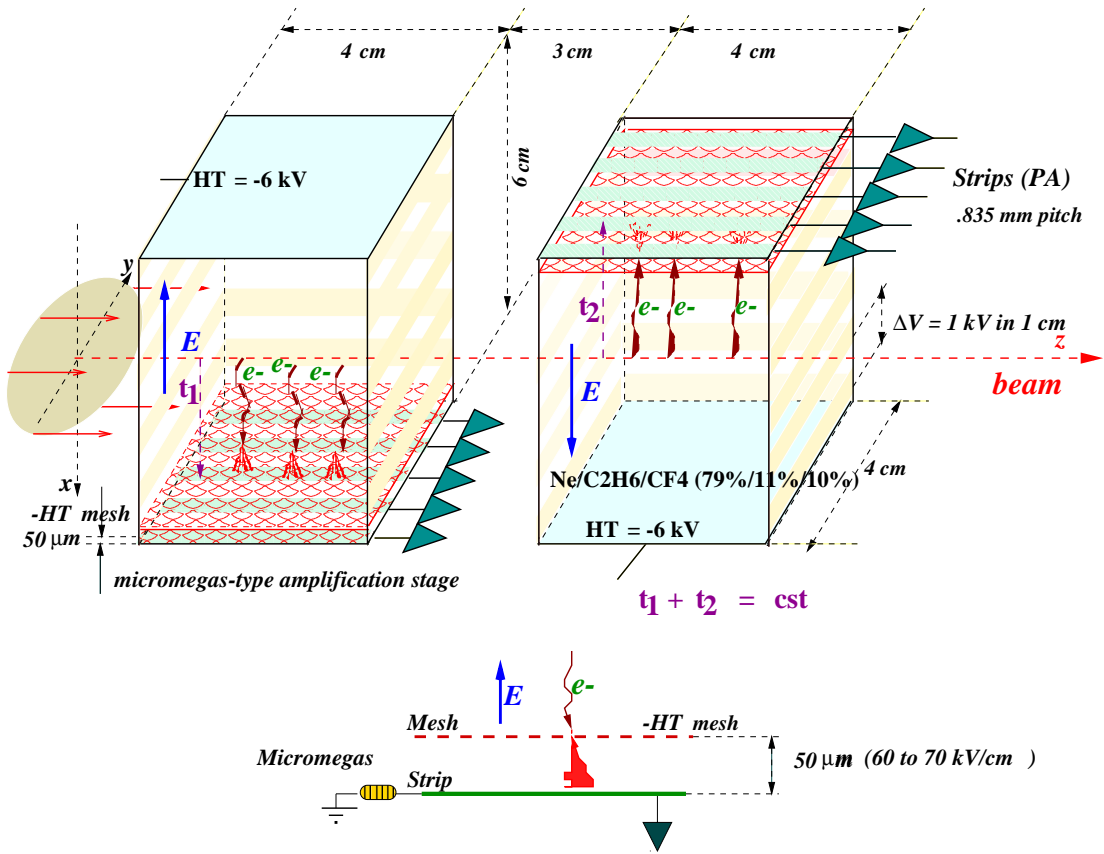


Figure 3.5.: Working principle of a KABES double station [79].

windows were used instead of capacitor plates. Such cages provide a constant gradient of 0.83 kV/cm, which corresponds to a uniform drift velocity of 8 cm/ μ s.

The whole spectrometer consists of three double stations, each measuring the x and y position and the time of the particles. The first two stations, KABES-1 (up) and KABES-2 (down) are located at the centre of the second achromat, where the beams are split and run parallel to each other (see Figure 3.2), so that the presence of a signal in one station identifies the charge of the particle. The last station, KABES-3, is installed 8 m further downstream and is common for the two beams. The momentum of the beam particles can be extracted from the slope in the y coordinate of the track obtained between one of the first stations and the third one, but this measurement relies on the knowledge of the beam focusing.

The front-end electronics connecting each strip to the read-out system consists of a pre-amplifier, an amplifier, a shaper and a discriminator and delivers for each channel the times of the leading and of the trailing edge. The difference of these two times is the so-called Time over Threshold (ToT), which provides a fast and reliable estimate of the amplitude of the signals in each strip. The sum of the strip coordinates, weighted with the signal amplitude gives the position of the measured particle.

The read-out has to cope with a total of 288 channels (48 strips \times 6 chambers) and an

3. Experimental apparatus

expected hit rate up to 40 Mhits/s with a maximum of 8 Mhits/s per strip, corresponding to a total data rate of 960 MB/s per chamber. The High Performance Time to Digital Converter (HPTDC) chip [80] was chosen for its programmable resolution better than 1 ns and its very short dead-time. For each chamber a Read-Out Card (ROC) with 6 HPTDCs can extract and buffer the data requested by a fast Level 1 trigger (L1, see Section 4.1) and, in case of a positive decision of the Level 2 trigger (L2, see Section 4.2), read them out and send them via a 200 m long S-link optical cable to a standard desktop PC. At the end of each burst, the KABES data can be transmitted via Ethernet to the event-building PCs (see Section 4.3.1) and combined with the information of the other sub-detectors for the same event.

By choosing the voltages in order to minimise the signal overlap on a strip and to maximise the detection efficiency a mean cluster size of 1.5 strips per track and a ToT of about 35 ns were obtained, while the momentum resolution was about 1% after alignment and calibration and the time resolution better than 0.6 ns. The mistagging probability, i.e. the probability of associating the wrong KABES track to an event, mainly due to signal overlap, is about 4% without using information from other sub-detectors as constraint.

Since in K_{e4} decays the neutrino cannot be detected, the usage of KABES in the reconstruction would improve the background rejection and the resolution of the kinematic variables used for the fit of the form factors. However the simulation of this detector is not yet describing the data precisely enough to be introduced in a form factor measurement. Fortunately the momentum bite of the beam is small enough to allow a good reconstruction also assuming that every kaon has exactly a momentum of 60 GeV/c and flies along the beam axis.

3.3.2. The magnetic spectrometer

The magnetic spectrometer (see Figure 3.6) consists of four Drift CHambers (DCH1-4) [81], two upstream and two downstream of a dipole magnet with an aperture of 2.45×2.4 m 2 and a vertical magnetic field of up to 0.37 T at its centre. Outside of the centre the magnetic field falls down very rapidly and reaches 0.02 T at the closest drift chamber.

A charged particle travelling through a chamber ionises the gas contained in it and the electrons that are freed in such a process drift, accelerated by an electric field, with a known velocity, towards a sense wire. The position of the particle can be measured with a better resolution than the distance between the sense wires by exploiting the information given by the drift time.

The drift chambers were designed to reach a detection efficiency as close as possible to 100% and a spatial resolution for the hits of about 100 μ m, with a fine granularity of the wires corresponding to drift distances of a few millimetres, necessary to stand the high particle flux (more than 1 MHz). Furthermore, a minimal amount of material should be used in order to avoid energy loss for electromagnetic interacting particles. In addition the position of each chamber has to be known to better than 10^{-4} to keep the uncertainty on the momentum scale to the same level.

To meet these requirements the geometry shown in Figure 3.7 was chosen. 256 gold-plated tungsten sense wires with a diameter of 22 μ m and a spacing of 10 mm from each other form a plane. On each side of it, at a distance of 3 mm, gold-plated titanium-copper wires with a diameter of 120 μ m and the same spacing as the sense wires generate the electric field. Each so-called view contains two planes of sense wires in order to resolve left-right ambiguities. The views are separated from each other by 22 μ m thick mylar foils coated with graphite,

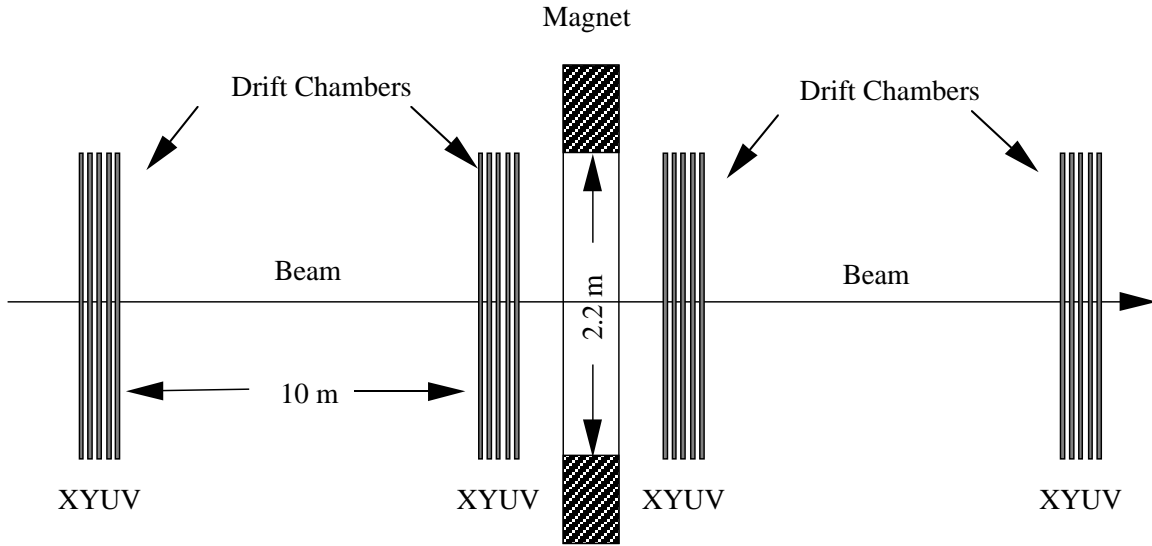


Figure 3.6.: Schematic view of the magnetic spectrometer with four drift chambers and a dipole magnet [82].

which also serve to shape the electric field.

A drift chamber contains four views with different orientations orthogonal to the beam axis: X along the x axis, Y along the y axis, U at -45° with respect to the x axis and V at $+45^\circ$ with respect to the x axis. The chambers have an octagonal shape and a transverse width of 2.9 m, with a 160 mm diameter central hole for the beam pipe. Each chamber measures the position of the particles and the time of the signal. The redundancy in the position measurement given by the four views is used to compensate the inefficiencies of the single views.

The whole spectrometer has a length of about 24 m and is contained in a tank filled with helium at atmospheric pressure, so that the multiple scattering can be reduced, but 50 μm thick mylar foils coated with graphite are enough to separate the chamber from the outside volume. The helium tank is delimited upstream by a 900 μm thick spherical window with a radius of 1.3 m consisting of three layers of epoxy coated kevlar (0.003 radiation lengths (X_0)) and downstream by a 4 mm (0.045 X_0) thick aluminium window.

From the hit positions in the two chambers before the magnet, the trajectory of the particles without deflection is computed and the position of the decay vertex can be extracted. The two chambers after the magnet give information on the deflection angle due to the magnetic field, which allows to measure the momentum. Actually one chamber after the magnet would be sufficient for this purpose, but also in this case the redundancy improves the detection and reconstruction efficiency.

The signals of the sense wires are amplified and discriminated by the front-end electronics that sends the standardised signals to the TDCs for the drift time measurement, given by the difference between the passage of the charged particle, corresponding to the L1 trigger time and the arrival of the ionisation cloud at the sense wire. The present read-out system was

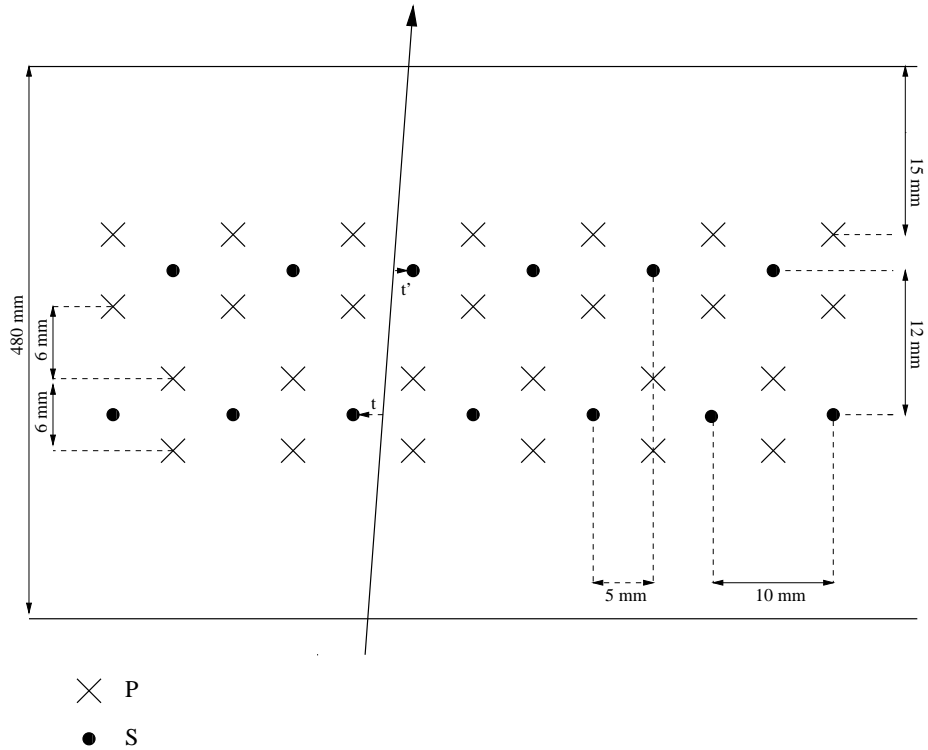


Figure 3.7.: Geometry of one DCH view. The crosses (P) represent the potential wires and the filled circles (S) the sense wires [81].

installed in 2002 and was explicitly developed to cope with the higher rates of the NA48/1 and NA48/2 experiments with respect to NA48. Each plane of wires is read out by a pair of TDC and Readout Buffer (TDC&RB) cards, each equipped with 16 TDC chips, mounted on four mezzanine cards, characterised by an intrinsic time resolution of 120 ps and multi-hit capabilities, so that a rate of 500 kHz per channel can be sustained by the read-out system. The TDC&RB cards record the arrival time of signals from the DCH and store them in 40 MHz pipelined ring memories. On request of the L1 trigger data are extracted from the memory and sent to a processor farm (MassBox, see Section 4.2.2) for the charged L2 trigger. If the Trigger Supervisor (TS, see Section 4.2.3) decides that the event has to be kept, the corresponding data are extracted a second time from the memory and sent to the PC-Farm (see Section 4.3.1) for the event building. A complete description of the new DCH read-out can be found in [83].

During the data taking in 2003 the drift chambers were filled with a mixture of 49.7% argon, 49.7% ethane and 0.6% water and were operated at -2250 V on the potential wires and -1405 V on the mylar foils, while the sense wires were grounded. Under these conditions the maximum drift path of 5 mm corresponds to a drift time of about 100 ns, with a gain in the gas of 6×10^4 . For a single plane the mean efficiency was about 98% and the resolution in x and y 150 μ m. With a momentum kick of about 120 MeV/c given by the dipole magnet,

this spatial resolution leads to a momentum resolution [36]

$$\frac{\sigma(p)}{p} = 1.02\% \oplus 0.044\% \times p[\text{GeV}/c], \quad (3.1)$$

where the first term is due to the Coulomb scattering and the second one to the effect of the spatial resolution.

The reconstruction of the K_{e4} decays depends completely on the momentum measurement of the three charged particles, since the neutrino cannot be detected. Therefore the magnetic spectrometer has to be efficient and precise. Furthermore, a good resolution in the momentum measurements helps to reject background from events without missing transverse momentum and to identify electrons by comparing the energy deposited in the electromagnetic calorimeter with the momentum measured by the spectrometer. For the form factor measurement it is also important that the inefficiencies can be precisely located and implemented into the simulation, to avoid an unexpected dependency of the acceptance on the hit position.

3.3.3. The Charged HODoscope (CHOD)

The hodoscope for charged particles [84] is a system of scintillator counters mainly used to provide time information to the L1 trigger. To fulfil this task a high granularity, a good detection efficiency and a time resolution better than 300 ps are needed.

The chosen material was the NE110 plastic scintillator, which is fast and has a high light output. 64 vertical and 64 horizontal counters are arranged into two parallel octagonal planes (see Figure 3.8), divided into four quadrants, spaced by 75 cm and designed to contain a circle of 121 cm radius. The distance between the planes and to the electromagnetic calorimeter (80 cm) were chosen to reduce the effect of the back-scattering from the calorimeter to the hodoscope. The counters are 2 cm thick, so that the total material in the beam is about 0.1 X_0 , 6.5 or 9.9 cm wide, according to their distance from the beam axis, and between 60 and 121 cm long. At the centre of the detector is a hole of 12.8 cm radius for the beam pipe. The dead space between the counters was reduced by polishing of the surfaces, while for each counter the side at the centre of the detector was coated with black paint in order to avoid light transmission.

The scintillation light produced at the passage of a charged particle is collected at the external side of a counter from a plexiglass fish-tail shaped light guide connected to a photomultiplier. Each counter and light guide was wrapped into a 25 μm thick aluminised mylar sheet and each plane was wrapped into a black cover to avoid fake signals from external light.

The read-out system consists of an analogue and a digital part, both hosted in a Pipeline Memory Board (PMB). The photomultiplier pulses are sent both directly and through a discriminator to the analogue board, where the analogue signal is shaped, digitised, sampled every 25 ns and read out by a 10 bit Fast Analogue to Digital Converter (FADC) card to measure the pulse height, while the discriminated signal goes to a Fast Time to Digital Converter for the precise time measurement. The digital board, based on the PMChip [86], was designed to be dead-time free, since it can store data inside a digital pipeline waiting for the trigger decision and extract the data requested by the trigger without stopping the data recording. The discriminated signal is also sent to the fast logic electronics, that produces topological and multiplicity triggers used by the L1.

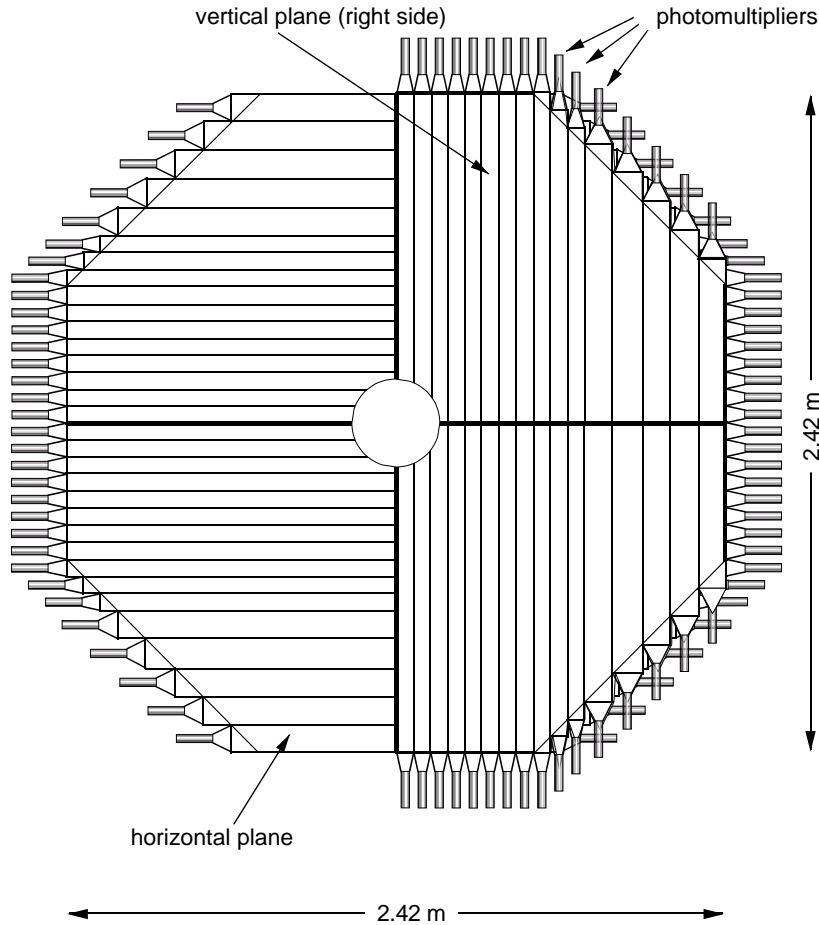


Figure 3.8.: Schematic view of the two planes of the charged hodoscope [85].

In 2003 the trigger inefficiencies due to the hodoscope were below 10^{-4} and the time resolution after the offline reconstruction was about 250 ps.

In the analysis of the K_{e4} decays the hodoscope information is not directly used, but it is necessary for the triggering of charged decays and it also gives the reference time for the drift time measurement and for the track time of the chambers.

3.3.4. The Liquid Krypton electromagnetic calorimeter (LKr)

In order to reconstruct the decays of neutral kaons into two neutral pions, the NA48 experiment needed an electromagnetic calorimeter with good energy, position and time resolution, precise charge calibration, long-term stability and a fast read-out.

To meet these requirements, a quasi homogeneous liquid krypton calorimeter with a tower structure geometry was built [87]. A photon or an electron entering the active volume produces an electromagnetic shower via repeated pair production and bremsstrahlung processes until the energy of the single particles is below the critical energy. The *critical energy* is defined as the energy at which the radiation loss equals the collision loss. The low energy

Property	Symbol	Unit	Value
Atomic number	Z		36
Mass number	A		84
Density at 120 K	ρ	g/cm ³	2.41
Radiation length	X_0	cm	4.7
Molière radius	R_M	cm	4.7
Mean energy for electron-ion pair creation	W	eV	20.5
Nuclear interaction length	λ_I	cm	60
Boiling temperature at 1 bar	T_b	K	119.8
Fusion temperature	T_m	K	116
Drift velocity of electrons at 1 (5) KV/cm	v_d^e	mm/μs	2.7 (3.7)
Critical energy	E_c	MeV	21.51
Radioactivity		Bq/cm ³	500
Dielectric constant	ϵ		1.72

Table 3.1.: Properties of liquid krypton [88].

charged particles in the shower can then ionise the krypton atoms producing a certain numbers of electron-ion pairs, which is proportional to the deposited energy. The calorimeter works as an ionisation chamber: all the electrons produced and accelerated towards the anode are collected before they can recombine, but the electrons do not get enough energy to produce secondary ionisation.

The homogeneity ensures a good energy resolution, the granularity improves the spatial resolution and allows to separate showers close to each other, the precise construction and calibration give a small constant term of the energy resolution and the tower structure with a fast read-out reduces the occupancy, so that it is possible to cope with high rates.

Liquid krypton was chosen [88] to ensure long-term stability and a low recombination probability, since, after purification, the mean lifetime of the electrons in the medium is about 100 μ s, while the drift time of the electrons to the next anode is about 3 μ s. Radioactivity is negligible with respect to electronic noise and has therefore no effect on the resolution, but, due to the low boiling temperature of krypton at 120 K, the whole detector has to be kept inside a cryostat where only temperature variations of ± 0.3 K are allowed, since the drift velocity of the electrons depends strongly on the temperature ($\Delta v_d/v_d \sim -0.87\% \times \Delta T/T$). The material of the cryostat corresponds to $0.65 X_0$ and is therefore the biggest contribution to energy loss before the calorimeter. The properties of liquid krypton are listed in Table 3.1.

The LKr is octagonal, containing a circle of 128 cm radius, 127 cm thick, corresponding to about 27 X_0 , and has a hole at the centre of 9 cm radius for the beam pipe. The total active volume of about 7 m³ liquid krypton is divided into 13248 cells (towers) by 18 mm wide, 40 μ m thick copper-beryllium ribbons at a distance of 1 cm from each other (see Figure 3.9). The ribbons are used as electrodes to collect the ionisation signal. A cell consists of a central anode and two cathodes, one at each side, so that each cathode is in common between two cells. The high voltage applied to the electrodes during the data taking and the test beams was 3 kV. The separation between two cell layers is 2 mm.

The electrodes are zig-zag shaped (see Figure 3.10) with an angle of 48 mrad between

3. Experimental apparatus

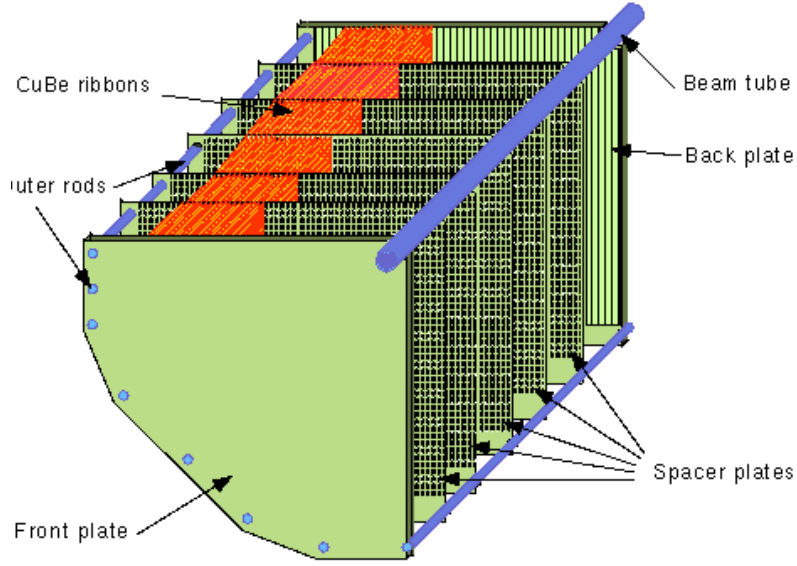


Figure 3.9.: Section of a quadrant of the LKr calorimeter [89].

two segments, in order to avoid that the centre of the electromagnetic shower produced by a particle can remain along the electrode for the whole calorimeter. In this case the measurement would be strongly affected by non-uniformities, since the detector response depends in general on the shower position with respect to the electrode.

The cells do not have a constant section through the whole calorimeter, but a projective geometry, pointing towards the centre of the decay region (about 114 m upstream of the calorimeter), so that the section increases linearly in the beam direction with a total variation of 1.1%. For a ionisation chamber, the projective geometry does not spoil the energy measurement, while it avoids the dependency of the measured position from the depth of the shower, which is different between electrons and photons.

The geometry of the ribbons is obtained by inserting five 5 mm thick spacers every 21 cm, where the electrodes can be fixed in order to avoid any electrostatic instability due to long free metallic pieces and to guarantee the correct positioning of the whole structure, which results in a better position resolution of the calorimeter.

The read-out system is based on the technique of the initial induced current measurement, that consists in the integration of the obtained signal, which lasts as long as the drift time of the electrons inside the calorimeter, only over a short time interval. The initial current is proportional to the number of deposited electrons and therefore to the energy of the shower, while the total induced charge fluctuates as a function of the spatial distribution of the ionisation. This method has furthermore the advantage of a fast response, but the shaping time has to be optimised to keep a good signal to noise ratio and the uniformity over the whole calorimeter is only possible with a very precise construction, allowing a tolerance on the drift gap of less than 100 μm .

The anode signal is sent through a blocking high voltage capacitor of 3 nF to the front-end electronics, consisting of a preamplifier and a calibration system, mounted directly on the back of the calorimeter, inside the cryostat. The low temperature has the advantage of

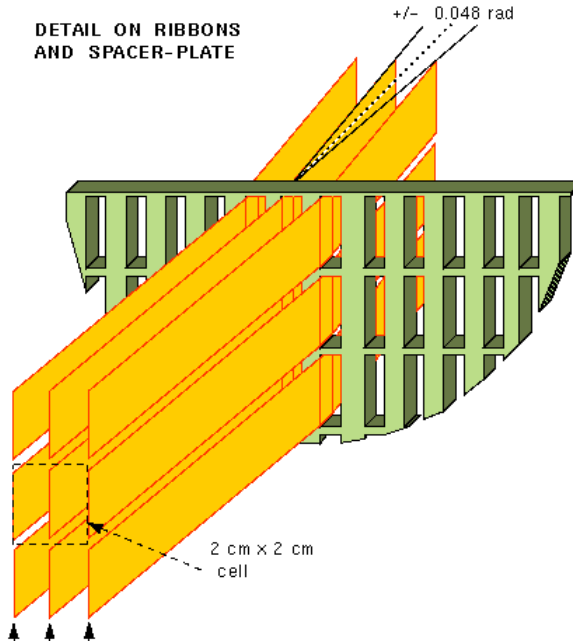


Figure 3.10.: Detailed view of a cell with the zig-zag shaped ribbons and the spacer-plates [89].

reducing the noise in the transistors and to improve the time stability.

The calibration system is used to check the stability and the uniformity of the response over the entire active volume, performing an inter-calibration of the channels in order to compensate possible changes in the electronic gains and allowing to identify channels that are not working properly. Each pre-amplifier is connected to a pulser that can inject eight different known charge signals into it. In this way the stability of the response was kept within 0.1% during the whole data taking period.

The signals are then transported through low-noise transceivers outside the cryostat to the digitiser electronics called Calorimeter Pipeline Digitiser (CPD) located about 10 m away from the calorimeter and consisting of a shaper, ADC, interface circuits and memory [90]. The transceiver signal is filtered by the shaper to an almost Gaussian peak with a Full Width at Half Maximum (FWHM) of 72 ns and a 3% undershoot which lasts as long as the drift time of the electrons in the calorimeter cell. In the ADCs the waveform is digitised at a rate of 40 MHz and stored temporarily in a memory.

Since at the time of the design only low-cost 10-bit ADCs able to sustain a sampling rate of 40 MHz were available, a dynamic range expansion with an energy dependent switching was implemented, maintaining the resolution of the ADC. The whole energy range from 3.5 MeV to 50 GeV is divided into four subranges, each corresponding to a different gain. The gain switching logic consists of three discriminators.

Each CPD module covers an 8×8 square matrix of calorimeter cells and contains 32 daughter cards with shaper, ADC and pipeline, a decoding card, a memory address controller and a trigger sum card, that receives a separate copy of the signal and builds 2×8 analogue

3. Experimental apparatus

sums in both x and y projections. The whole read-out consists of 216 CPD modules.

The memory of each module is divided into a circular and a linear buffer. The digitised samples are first stored in the circular buffer and upon arrival of a L2 trigger a time window of ten samples around the trigger timestamp is selected and copied into the linear buffer, from which the data are transferred via one optical link per CPD module to the Data Concentrator (DC) [91] where the zero suppression is performed.

At a trigger rate of 10 kHz with 10 samples per channel, the CPDs produce about 4 GByte/s of data, but most of the channels contain only pedestals, since no energy has been deposited there. To reduce the amount of data without losing energy resolution, a special algorithm is used to mark the cells with an energy peak and in a second phase the channels up to a given radius from the centre. All other channels are set to zero, such reducing the amount of data by a factor 20-30. The samples of the cells surviving the zero suppression are sent to the event building PCs.

Since the LKr, due to the bottleneck of the data transfer to and from the DC, was the only sub-detector not able to stand a trigger rate of about 60,000 events per burst, the read-out speed was increased by introducing in 2002 a Super-Event (SE) read-out sequence [92]. This allowed for a significant increase of the sensitivity of the NA48/1 and NA48/2 experiments. The basic idea of the Super-Event read-out is to collect two consecutive triggers in the linear buffer of the CPDs and send them together to the DC, so that they are treated as a single event in the rest of the chain. The sustained trigger rate was almost doubled in this way.

The performances of the calorimeter have been tested during specific tests with an electron beam [87] and checked during the normal data taking. Clusters are defined as the sum of the signals contained in a box of cells around a peak in time and space. The cluster energy is then the sum of the energies in each cell and its position is the centre of gravity of the cluster, computed as the weighted sum of the coordinates of each cell with the energy deposited in it.

The position resolution measured with a 3×3 box can be parametrised as [87]

$$\sigma_x = \left(\frac{4.2}{\sqrt{E[\text{GeV}]}} \oplus 0.6 \right) \text{mm} \quad (3.2)$$

$$\sigma_y = \left(\frac{4.3}{\sqrt{E[\text{GeV}]}} \oplus 0.6 \right) \text{mm}, \quad (3.3)$$

where the first term is given by the statistical fluctuation of the particles in the shower and the second one is due to the size of the cells. For a typical energy of 20 GeV, the spatial resolution is 1.1 mm in each coordinate.

The energy resolution for an 11×11 box is [36]

$$\frac{\sigma(E)}{E} = \frac{0.032}{\sqrt{E[\text{GeV}]}} \oplus \frac{0.09}{E[\text{GeV}]} \oplus 0.0042, \quad (3.4)$$

with the usual parametrisation containing a statistical term, whose main contribution is the lateral leakage of the shower outside the box, a noise term due to the electronics and a constant term accounting for non-linearity and inter-calibration effects. A 20 GeV particle has for example an energy resolution of about 200 MeV.

These features, together with a time resolution of a few hundred picoseconds, are extremely important for the selection of the K_{e4} events and the separation between signal and

background. The electron identification and the pion rejection are completely based on informations from the LKr, like the shower energy compared to the momentum of the particle measured in the spectrometer, the shower width or the association in space and time between track and cluster.

3.3.5. The Neutral HODoscope (NHOD)

In order to have an independent and more precise time measurement of the electromagnetic clusters in the calorimeter, 256 bundles of scintillating fibres, each contained in a 7 mm diameter, 2 m long epoxy-fibre-glass tube, are fixed to the second spacer plate of the LKr electrodes (see Figure 3.11), so that they form a layer perpendicular to the beam axis at a depth of $9.5 X_0$, corresponding to the maximum of the electromagnetic shower produced on average by a 25 GeV energy photon [93]. The bundles are immersed in the liquid krypton volume, together with the 32 photomultipliers (8 per quadrant) used to read out the signals. The read-out chain is based on the PMB system as the charged hodoscope (see Section 3.3.3).

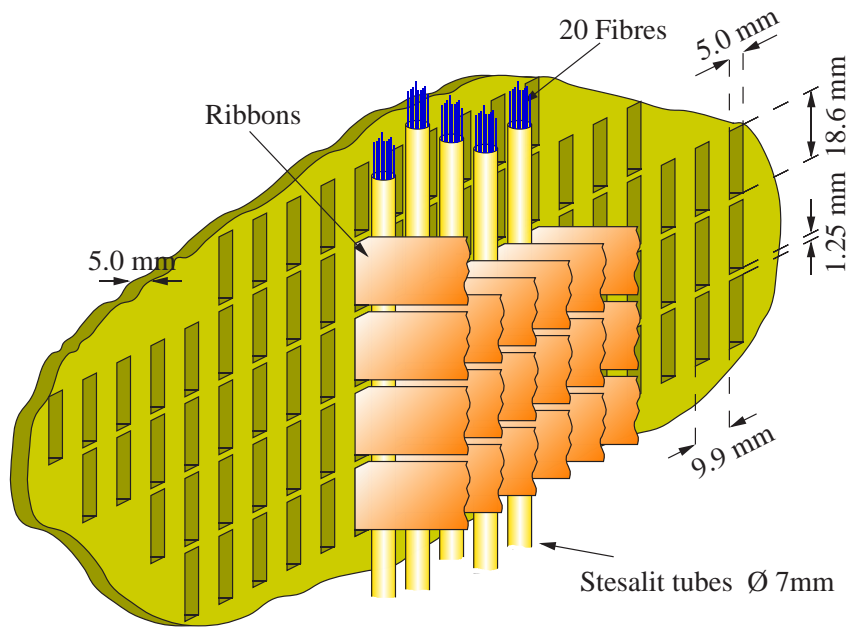


Figure 3.11.: Schematic view of the scintillating fibre bundles composing the neutral hodoscope [94].

The NHOD can achieve a time resolution better than 300 ps and the resolution of the LKr can be improved by combining the two measurements. The signals of the neutral hodoscope are also used for a minimum bias trigger with which the efficiency of the more complex neutral triggers or of the fast charged trigger can be measured. The efficiency reached for clusters with at least 25 GeV energy is 95%, for energies above 35 GeV the inefficiency is about 1%.

3.3.6. The HAdron Calorimeter (HAC)

Downstream of the LKr a conventional iron-scintillator sandwich HAdron Calorimeter (HAC) [95] is used to measure the energy of hadrons produced in the decays, like charged pions, protons and neutrons. The HAC consists of two modules (a front and a back one) with 88 channels each and has a total depth of 1.2 m, that corresponds to 6.7 nuclear interaction lengths (λ_0). Each module contains 24 iron plates 25 mm thick with an area of 2.7×2.7 m² alternated with scintillator planes consisting of 44 strips, 4.5 cm thick, about 12 cm wide and 112 cm long (see Figure 3.12). In iron the incoming particle produces a shower, while in the scintillator planes the charged particles of the shower that were not absorbed in iron convert into a number of photons proportional to the deposited energy. The scintillator strips are alternately aligned in the horizontal and vertical direction and the light produced in the strips with the same alignment and position is transported via a single plexiglass light-guide to a photomultiplier.

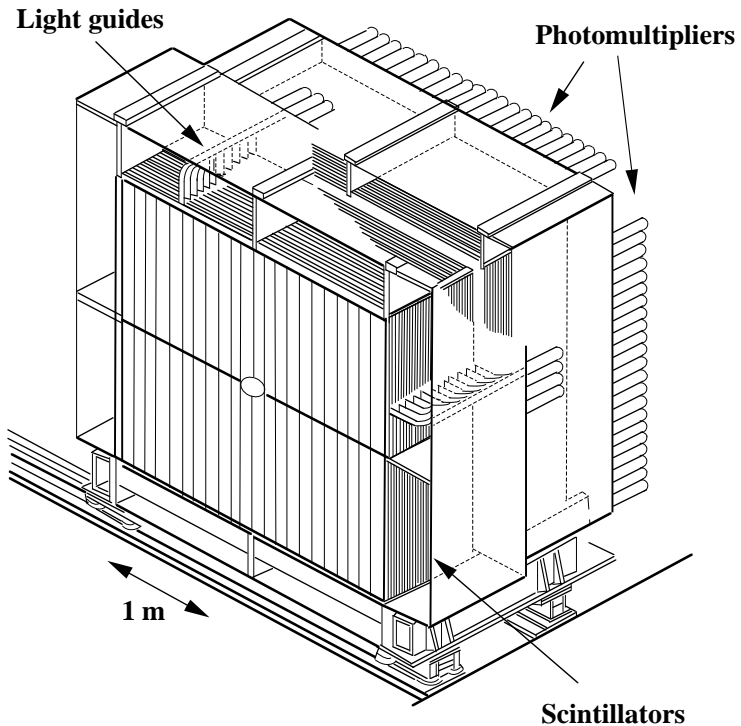


Figure 3.12.: Schematic representation of the hadron calorimeter [82].

The read-out system is based on the same CPD modules used for the LKr (see Section 3.3.4), one for each group of 44 channels. In order to be able to use the CPDs without modifications, the photomultiplier signals have to be shaped to a form similar to the LKr ones.

The energy resolution was measured during a test beam in 1995 to be

$$\frac{\sigma(E)}{E} = \frac{69\%}{\sqrt{E[\text{GeV}]}} \quad \text{for hadronic showers and} \quad (3.5)$$

$$\frac{\sigma(E)}{E} = \frac{23\%}{\sqrt{E[\text{GeV}]}} \quad \text{for electromagnetic showers} \quad (3.6)$$

Since the leakage of the electromagnetic and hadronic showers starting in the LKr is, at least partially, deposited in the HAC, the sum of the energies measured in the two calorimeters gives the total energy of the event, which can be used for trigger decisions.

In this analysis, the information of the HAC could in principle help to separate electrons from pions, but, due to the poor space resolution and to the width of the hadronic shower produced by the pions it is impossible to assign unambiguously a cluster in the HAC to the corresponding cluster in the LKr. For this reason only in the selection of non-hadronic decays the HAC total energy can be used to veto hadronic background, but no positive identification of hadrons can be performed.

3.3.7. The MUon Veto (MUV)

Both pions and muons produce a charged track in the magnetic spectrometer and deposit only a small amount of their energy in the electromagnetic calorimeter. In order to distinguish them, a MUon Veto detector (MUV) [96], consisting of three planes of NE110 plastic scintillators, each preceded by a 0.8 m thick iron wall, was installed downstream of the HAC. Only muons, since they do not interact strongly, survive the passage through the big amount of matter and produce a signal in the scintillators. The probability of a signal from a pion (punch through) is of the order of a few times 10^{-3} .

Planes 1 and 2, the only ones used for the particle identification and the trigger, have an area of $2.7 \times 2.7 \text{ m}^2$ and consist of 2.7 m long, 0.25 m wide, 1 cm thick scintillator strips oriented respectively horizontally and vertically. The central strip is divided to leave a $22 \times 22 \text{ cm}^2$ hole for the beam pipe. The strips are read-out at both ends by photomultipliers, connected to them via semi-adiabatic light guides. Plane 3, used purely for monitoring purposes, contains six strips, each 2.7 m long, 0.45 m wide and 0.6 cm thick.

The signals from the photomultipliers are discriminated and sent to logic units that form coincidences between the hits in the first two planes, defining muon hits in the 120 regions with an area of $25 \times 25 \text{ cm}^2$ at the intersection of a horizontal and a vertical strip.

The information provided by the MUV is mainly used in the L1 trigger to reject for example the $K \rightarrow \pi\mu\nu$ background and in the analysis for the π/μ separation (this is also the case in the K_{e4} selection). For these purposes a high hit efficiency is necessary, which was measured to be more than 99% for muons with at least 10 GeV energy.

3.3.8. The photon anti-counters (AKL)

In the NA48 experiment the decays $K_L^0 \rightarrow 3\pi^0$ had to be rejected to reconstruct the less probable decays $K_L^0 \rightarrow 2\pi^0$. In order to properly identify events in which 4 photons were inside the detector acceptance and 2 outside it, seven rings of iron and scintillator were installed around the detector (as shown in Figure 3.3) to cover the angular region starting at about 10 mrad from the beam axis. The system of seven photon anti-counters is called, due to its original function, Anti- K_L (AKL) [97].

Each ring contains two pockets (see Figure 3.13) consisting of a 35 mm thick iron layer, in which the photons convert into an electron-positron pair, followed by scintillator counters, connected each to photomultipliers at both ends. The read-out system is based on the PMB

3. Experimental apparatus

modules also used for the hodoscopes (see Section 3.3.3). The efficiency was measured during test runs to be 97% with a time resolution of 2 ns.

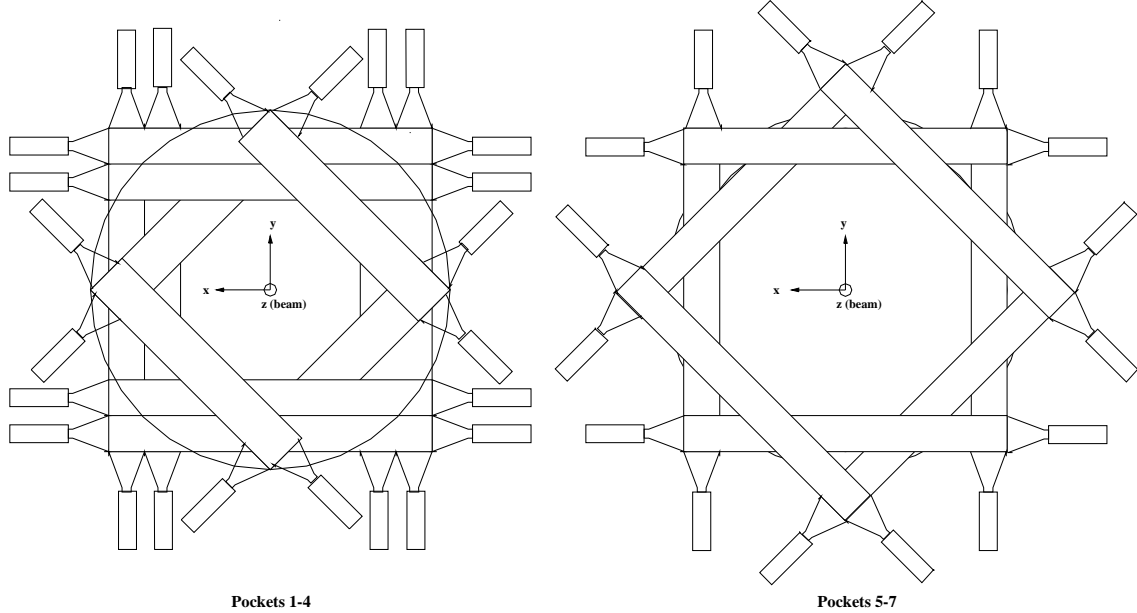


Figure 3.13.: Schematic view of an anti-counter pocket for the rings 1-4 (left) and 5-7 (right) [85].

In NA48/1 and NA48/2 the AKL was used as veto signal in the trigger, to reduce the rate, and in the selection of rare decays, to reject events with photons outside the detector acceptance. In this analysis the AKL is not explicitly used in the selection to reject background events with high transversal momentum, because the requirement of having no hit in the AKL is already present at trigger level (see Section 4.1).

3.3.9. The beam position monitor

Since small changes in the beam position can strongly affect the measurement of the asymmetry in the decay modes $K^\pm \rightarrow 3\pi$, for NA48/2 a new beam monitor [72] was built, tested and installed, in order to measure not only the beam intensity, but also the position of its centre.

The monitor is installed at the end of the experimental hall, downstream of the MUV and covers a total area of about 50×50 mm 2 to fully contain the beams that have a width of about 6 mm. It consists of two 8×8 matrices of scintillators, each 9 mm thick, separated by aluminium foils to minimise the optical cross-talk. The centre of each matrix is aligned with one of the two beams, whose centres are about 100 mm apart. The light produced in each matrix of scintillators by the passage of a beam particle is collected by a 8×8 pixel multi-anode photomultiplier, connected to the scintillators via a filter mask used to inter-calibrate the channels by changing their transparency. With this method a uniformity better than 10% was reached.

The signals of the photomultipliers were read-out digitally ten times per burst and the number of hits in each pixel was recorded in fast scalers. The resolution obtained was better than 0.1 mm, so that the displacement of the beams, due to the movement of the primary protons on the target during the burst, could be precisely measured.

The movement of the beam centre at the end of the hall of about 2 mm within one burst is not expected to affect the measurement of the K_{e4} form factors significantly. Therefore the information of the beam monitor is not used in this analysis.

3. Experimental apparatus

4. Trigger and data acquisition

The aim of the trigger system is to select fast and efficiently the wanted events and to reduce the data rate by rejecting as many as possible of the uninteresting ones. Without any selection the data rate to be recorded (of the order of 1 MHz) would be too high for all the sub-detectors. The NA48/2 trigger system reduces this rate in three stages. The first stage, called Level 1 (L1), is described in Section 4.1. It combines information from AKL, CHOD, NHOD, DCHs, MUV, LKr and HAC to give a fast response, so that potentially interesting signals in the sub-detectors are kept in memory for a longer time. The Level 2 (L2, see Section 4.2) consists of a neutral and a charged part whose output is combined by a Trigger Supervisor (TS), that decides to record or reject the event. A scheme of the first two stages of the NA48/2 trigger system is shown in Figure 4.1.

The data of the triggered events are collected from all the sub-detectors, combined and written to disk by a farm of event building PCs (PC-Farm, see Section 4.3.1). The data in raw format are then sent by the Central Data Recording (CDR, see Section 4.3.2) to the Level 3 trigger (L3, see Section 4.4), a software filter that combines the information of all the sub-detectors to flag and select the different decays. The events selected by the L3 are recorded to disk in a compact format, more suitable for the analysis (see Section 5.1).

4.1. The Level 1 trigger (L1)

The first trigger level has to reduce the rate of events by about one order of magnitude down to about 100 kHz. This is obtained by a fast identification of potentially interesting decays. The L1 consists of a pre-trigger (L1C) and a trigger supervisor (L1TS). The pre-trigger is composed of programmable Computer Automated Measurement And Control (CAMAC) modules, that can synchronise and combine with simple logical operations the signals from the sub-detectors and produce a result within a few microseconds.

The following signals were available as input to the L1C in 2003:

Q_{OR} : At least one signal in the horizontal or in the vertical plane of the CHOD.

Q₁ : At least one sub-coincidence between the horizontal and the vertical plane of the CHOD.

A *sub-coincidence* is defined as the association in space and time of signals in a group of horizontal and vertical scintillator counters. Each quadrant of the CHOD is divided into a group of 7 counters near the beam pipe and another group of the remaining 9 counters. In this way 16 regions (4 per quadrant) are defined, in which a sub-coincidence can be found.

Q₂ : At least two sub-coincidences between the horizontal and the vertical plane of the CHOD.

AKL : At least one signal in at least one of the pockets 2–7 of the AKL.

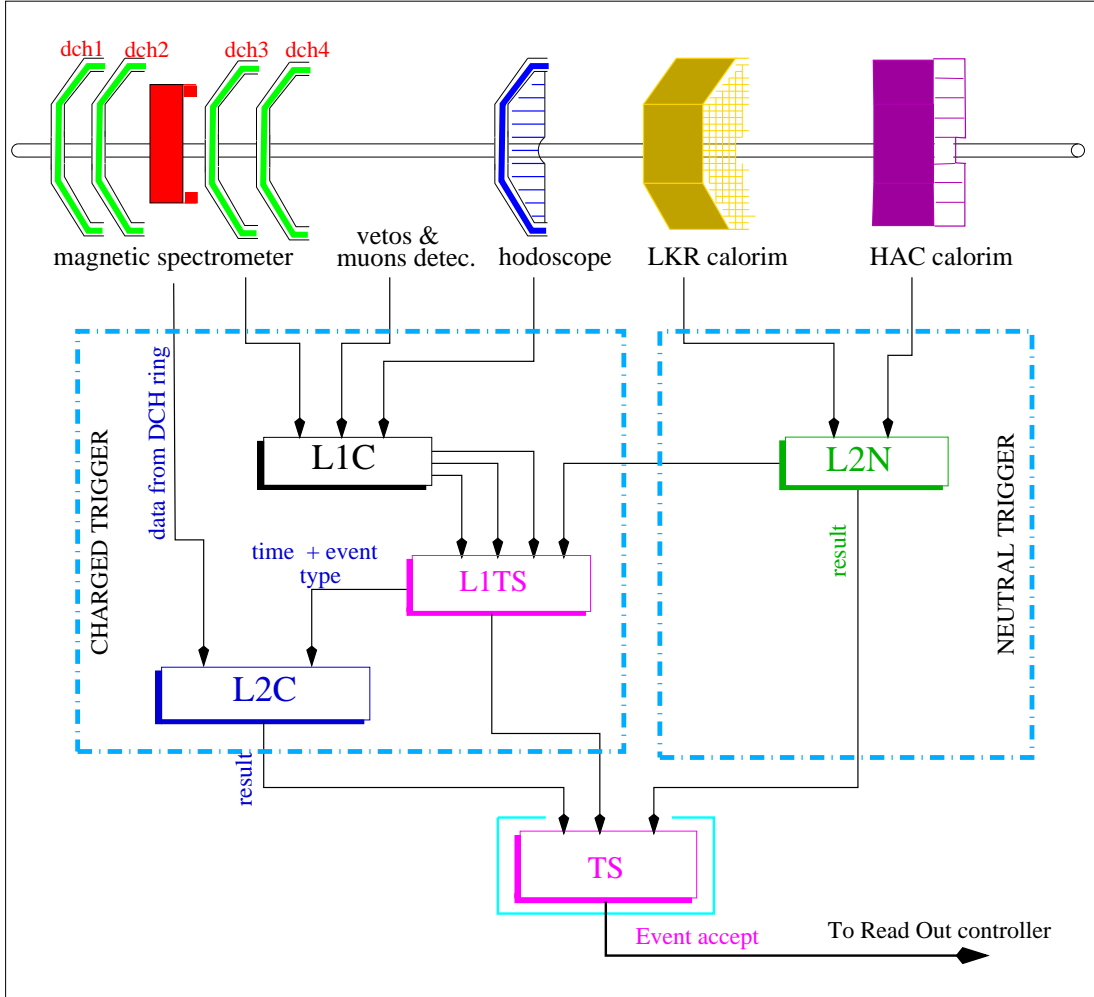


Figure 4.1.: Simplified scheme of the Level 1 and Level 2 trigger stages at NA48/2 [94].

1 μ : At least one coincidence in time between the signals in the horizontal and in the vertical planes (planes 1 and 2) of the MUV.

T_N^0 : At least one left-right or top-bottom coincidence of signals in the NHOD, i.e. at least two different quadrants of the NHOD must have at the same time at least one signal each.

Of the different combinations built by the L1C, the relevant ones for the analysis presented here are $Q_2 \cdot \overline{AKL}$ (“.” indicates the logical operation *and*, a line over a signal the logical operation *not*), Q_1 down-scaled by a factor 100 ($Q_1/100$) and T_N^0 . The first two are used as input to the MassBoX (MBX, see Section 4.2.2) and as control trigger to measure the efficiency of the L2 trigger, while the T_N^0 is sent directly to the TS and serves as independent trigger to estimate the efficiency of the L1C.

The signals produced as output of the L1C are sent, if necessary after being down-scaled,

to the L1TS, where they can be further combined with the information from the calorimeters (see Section 4.2.1).

The L1TS is a fully pipelined system working at a frequency of 40 MHz. It can combine up to 28 signals into a 3-bit trigger code, that is sent to the MBX and to the TS. The input signals are synchronised and shaped to fit one cycle of the clock (timeslice). Each timeslice is uniquely identified by the number of clock cycles from the beginning of the burst (timestamp). One of the input signals, used for all the three trigger conditions, is sent to a Fine Time (FT) module, where its precise time within the clock cycle is coded into two bits that are used by the MBX at a later stage.

In order to increase the efficiency of the coincidences and reduce the effect of jitter, some of the input signals can be widened to three timeslices before being combined with the others. The widening is made by replicating the signal, inside the pipeline, in the preceding and in the following timeslice. The decisional part of the L1TS consists of a three level Look-Up Table (LUT).

The combinations corresponding to the three output bits of the L1TS in 2003 are show in Table 4.1. The signal sent to the FT was $Q_1 + Q_2$, which is present in all the three bits.

bit	description
0	$(\text{npeaksloose} + Q_1/10 \cdot \text{LKRmbias} + Q_1 \cdot \overline{Q_2} \cdot 1\mu \cdot \overline{AKL}/100 \cdot \text{KMU3-PRE}) \cdot (Q_1 + Q_2)$
1	$(Q_1 \cdot \overline{Q_2} \cdot \overline{1\mu} \cdot \overline{AKL}/100 + Q_1 \cdot \overline{Q_2} \cdot 1\mu \cdot \overline{AKL}/100 \cdot \text{KMU2-PRE} + Q_1/100) \cdot (Q_1 + Q_2)$
2	$(Q_2 \cdot \overline{AKL} + Q_1/100 + \text{random}) \cdot (Q_1 + Q_2)$

Table 4.1.: The L1TS trigger codes used during the data taking in 2003 as input to the MBX. “.” indicates the logical operation *and*, “+” the logical operation *or*, the line above the signal the logical operation *not* and “/” the down-scaling. The hierarchy of the operations is *not*, down-scaling, *and*, *or*. The meaning of the single signals can be found in Sections 4.1 and 4.2.1. “random” is a control trigger used to study accidental background.

To trigger events with three tracks, the MBX used events with bit 0 or bit 2 set to one (see MBX algorithm in Figure 4.3).

4.2. The Level 2 trigger (L2)

The L2 consists of two independent systems for “neutral” (L2N) and “charged” (L2C) decays and of a Trigger Supervisor (TS), that combines the information of the two parts and produces a trigger-word as output. The rate is reduced again after this stage by one order of magnitude to about 10 kHz. The NeUtral Trigger (NUT) can only use information from the LKr and the HAC, while the MassBoX (MBX) performs a fast reconstruction of the tracks in the magnetic spectrometer.

The output of the two systems can be combined, but no information on single clusters and tracks is available simultaneously. Due to this limitation, it is not possible, for example, to

distinguish between electrons and pions, according to the fraction of energy deposited in the LKr, at trigger level. Therefore the K_{e4} events were triggered together with all the decays into three charged particles by the MBX.

4.2.1. The NeUtral Trigger (NUT)

The NUT [98] is implemented in a 40 MHz dead-time free pipeline with a total latency of 128 clock cycles, corresponding to $3.2 \mu\text{s}$. As shown in Figure 4.2, the NUT receives the information on the energy in each super-cell (2×8 or 8×2 LKr cells in the x and y view respectively) from the analogue sum module of the CPDs (see Section 3.3.4). The trigger consists of three sub-systems: the Filter Module (FM), the Peak Sum System (PSS) and the Look-Up Table (LUT).

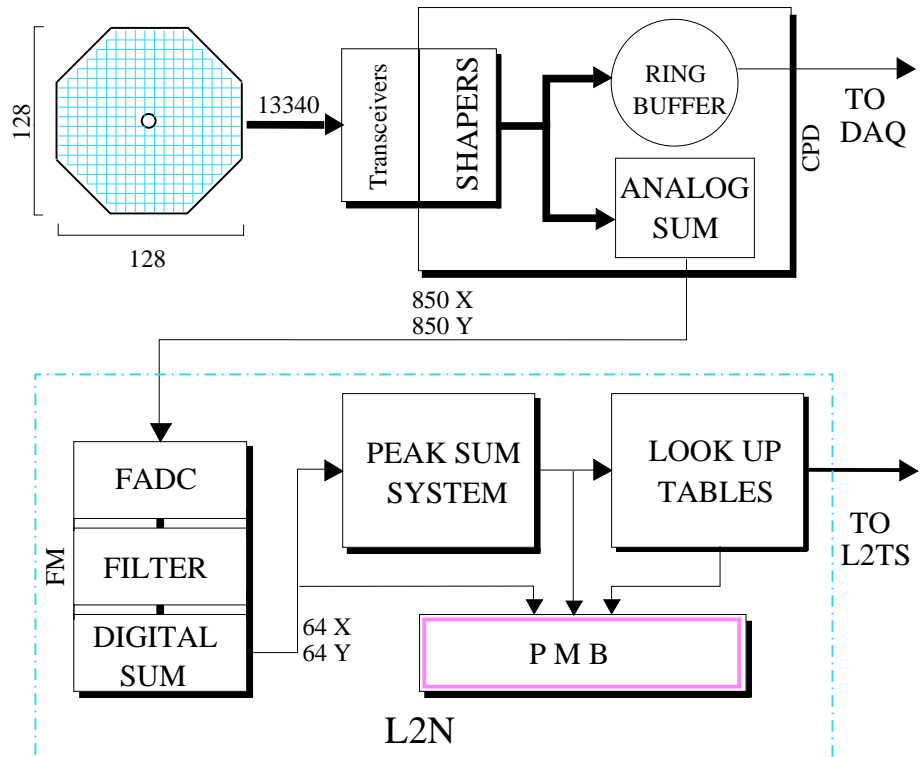


Figure 4.2.: Schematic representation of the neutral trigger and its connection to the LKr read-out system [94].

The Filter Module digitises the signals of the super-cells and filters them, to suppress the ones below a certain threshold. Then the signals of up to 16 super-cells in a row or in a column are summed to build 64 horizontal and 64 vertical projections. The output of the FM is sent both to a SPY system read out by PMBs, that allows to constantly monitor the NUT, and to the Peak Sum System.

The Peak Sum System [99] computes, separately in the horizontal and vertical views, the total energy (m_0) and its first (m_1) and second (m_2) spatial moments and counts the number

of peaks in each projection (n_{px} and n_{py}). A *peak* is defined as a local maximum in time and space with an energy above a certain threshold.

The Look-Up Table [100] system combines the values computed for the two views to obtain the physical quantities necessary for the trigger decision. The total deposited energy in the LKr,

$$E_{LKr} = \frac{m_{0x} + m_{0y}}{2}, \quad (4.1)$$

is computed from three timeslices around the maximum in time with a parabolic interpolation. At this stage also the total energy deposited in the HAC (E_{HAC}) and the sum of the energy in the two calorimeters ($E_{TOT} = E_{LKr} + E_{HAC}$) are computed. This information can be obtained fast enough, to be available already for the L1 trigger decision. Therefore it is sent to the L1TS, in order to be combined with the output of the L1C.

$$COG = \frac{\sqrt{m_{1x}^2 + m_{1y}^2}}{E_{LKr}} \quad (4.2)$$

is the centre of gravity of the event, assuming all the energy is deposited in the LKr.

$$z_{vtx} = z_{LKr} - \frac{\sqrt{E_{LKr}(m_{2x} + m_{2y}) - (m_{1x}^2 + m_{1y}^2)}}{M_K} \quad (4.3)$$

is the z coordinate of the decay vertex position in the small angle approximation. z_{LKr} is the z position of the calorimeter and M_K the nominal kaon mass.

The following bits were available as output of the NUT in 2003:

COG: $COG \leq 30$ cm

LKRmbias: $E_{LKr} \geq 10$ GeV

npeaksloose: $n_{px} > 2 + n_{py} > 2$

Etot: $E_{TOT} \geq 30$ GeV

KMU3-PRE: $E_{LKr} \geq 15$ GeV

KMU2-PRE: $E_{LKr} \leq 10 \text{ GeV} \cdot E_{HAC} \leq 10 \text{ GeV}$

KE2-PRE: $E_{LKr} \geq 15 \text{ GeV} \cdot E_{HAC} \leq 10 \text{ GeV} \cdot m_2 = m_1^2$

NPRE: $z_{vtx} \leq 9500 \text{ cm} \cdot E_{LKr} \geq 15 \text{ GeV} \cdot COG \leq 30 \text{ cm}$

vertex: $z_{vtx} \leq 9500 \text{ cm}$

with the usual convention for the logical operations. The bits containing only the number of peaks and the total deposited energy (“LKRmbias”, “npeaksloose”, “Etot”, “KMU3-PRE” and “KMU2-PRE”) are sent both to the L1TS and to the TS.

4.2.2. The MassBoX (MBX)

If at least one of the output bits of the L1TS is set, then the three L1 trigger bits, the timestamp and the fine time are sent to the DCH read-out. The information on the time of the hits in DCH 1, 2 and 4 for the event with the requested timestamp is read out, the coordinates of the hits are obtained from a look-up table and sent, together with the data from the L1TS, to the MBX via an Event Dispatcher (ED).

The MBX [101] is an asynchronous queued system, consisting of 8 Event Workers (EWs), that receives the 12 coordinate packets (3 DCHs \times 4 views) and builds out of them space points (coordinates of a point in a chamber), tracks, decay vertices and invariant masses. Events fulfilling different requirements are flagged accordingly and the result, consisting of the tagging bits and the timestamp, is sent to the TS. The part of the algorithm used in 2003 to trigger three tracks events is shown in Figure 4.3.

The MBX must process each event within a maximum latency of $100\ \mu\text{s}$, otherwise the event is flagged “not in time” and discarded. The actual latency depends on the complexity of the event and on the waiting time to enter the queue. In order to reduce the queueing time, an X_{off} mechanism prevents the L1TS to send further requests when the system is already too busy. This is done by setting the L1ON signal temporarily to zero. The X_{off} mechanism reduces the inefficiency by increasing the dead-time, which is preferable, since statistical biases due to dead-time can be better controlled.

4.2.3. The Trigger Supervisor (TS)

The TS [102] is a fully pipelined 40 MHz digital system, which correlates trigger information coming from the local sources (L2C, NUT and L1TS) to produce the final trigger-word. As shown in Figure 4.4, it consists of four stages.

The input stage contains four identical sub-detector cards, one for each trigger source (L1TS, L2C, NUT and miscellaneous signals). Each card can receive up to 24 bits of data, that do not need any further time adjustment, since the signals were already aligned in time among themselves at the source. The trigger information belonging to one event is uniquely identified by a 30-bit timestamp indicating the number of clock cycles from the beginning of the burst. The data are continuously stored into dual-ported Random Access Memories (RAMs). Simultaneously other data can be read out sequentially via the second port after a fixed delay of $100\ \mu\text{s}$ (which corresponds to the maximum latency of the L2C).

In order to avoid inefficiency produced by time jitter between the different trigger systems, whenever a coincidence between different conditions is required, the signal used as time reference is left unchanged, while all the others are widened to the preceding and to the following timeslice. Furthermore, for monitoring purposes, all the trigger data read by the TS are also sent to an external acquisition system, called Pattern Units (PUs).

In the second stage of the TS the trigger-word is formed by a flexible routing and combining network implemented in Field-Programmable Gate Arrays (FPGAs) and RAMs. This system allows for an easy change of the trigger configuration via software. In three steps the 96 input bits are combined and reduced to the final 16-bit trigger-word. Each bit of the trigger-word can be individually down-scaled by a factor up to 65535, so that small unbiased samples of events with looser requirements can be kept to test the efficiency of the main (non-down-scaled) triggers. The 16 bits of the trigger-word are used to generate a validation bit, called

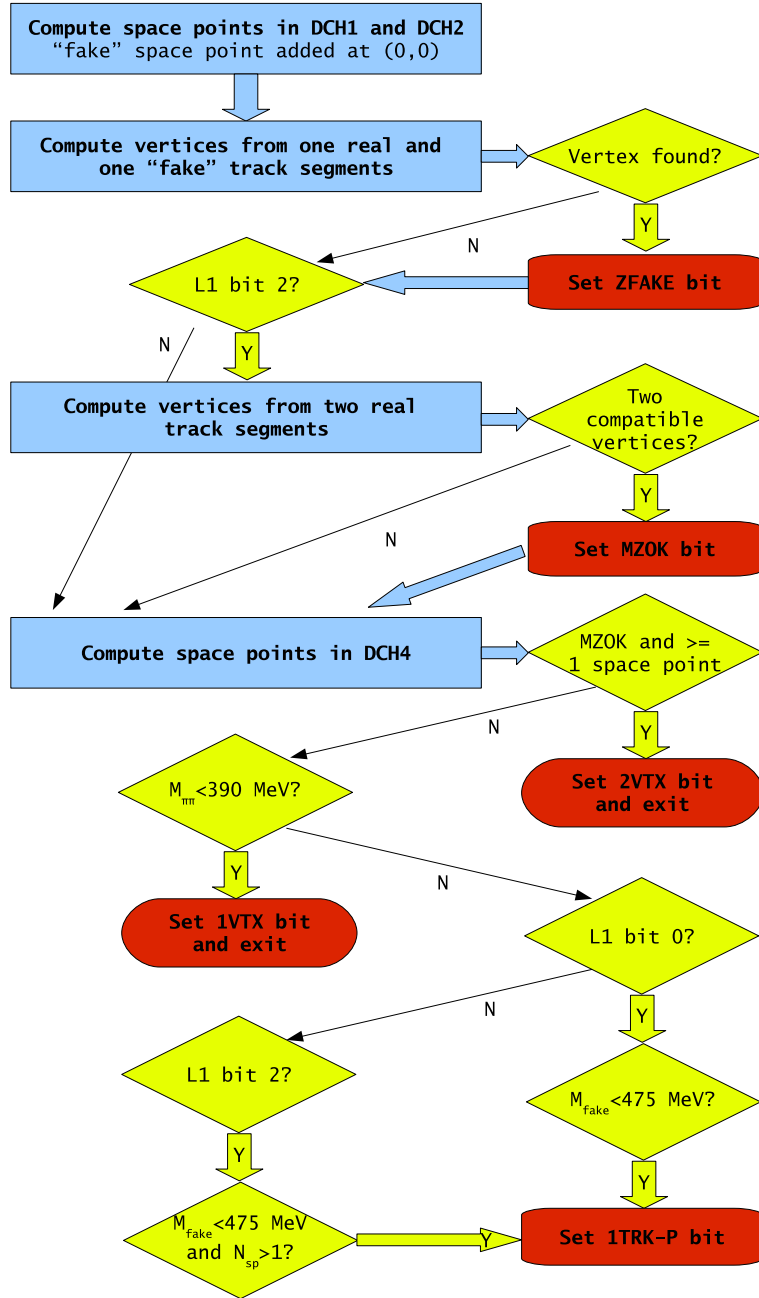


Figure 4.3.: The part of the MBX algorithm used during the data taking in 2003 for the three tracks events. $M_{\pi\pi}$ is the invariant mass computed from two tracks of each real vertex, assuming the pion mass for each track. M_{fake} is computed for each “fake” vertex and is defined as $M_{fake}^2 = M_K^2 + M_\pi^2 - (P_K - P_\pi)^2$, where P_K is assumed to be 60 GeV/c along the z axis and P_π is the momentum of the real track. $N_{sp} > 1$ requires at least two DCHs with at least two real space points each.

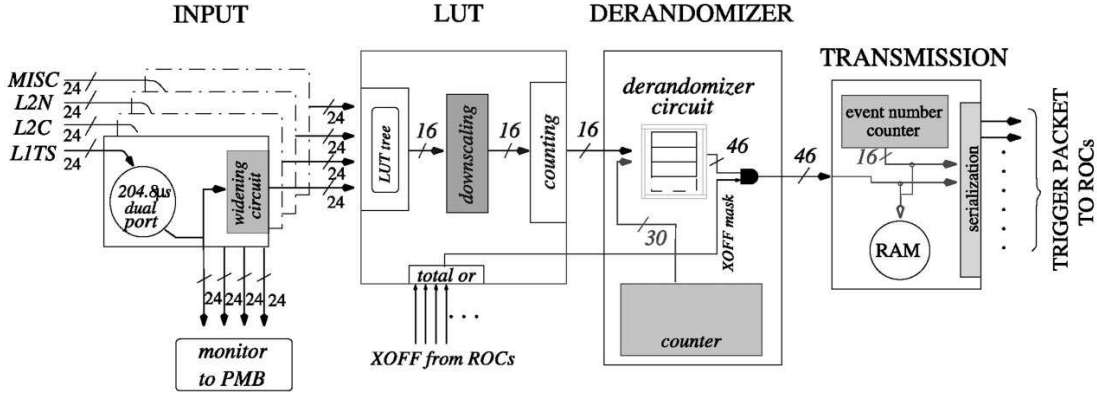


Figure 4.4.: Block diagram of the Trigger Supervisor [102].

strobe, according to which the event is kept or rejected. Since any combination of the 16 bits can be used to generate the strobe, it is possible to temporarily disable individual triggers.

The third stage of the TS consists of the Trigger Queue Buffer (TQB), where the trigger word and a 30-bit timestamp are written whenever the strobe signal is present. The purpose of the TQB is to buffer fast sequences of triggers, allowing for a fixed minimum time between the broadcast of two consecutive triggers. This circuit is called “derandomizer”.

Before extracting the trigger-word of an event from the queue, the TQB checks that no X_{off} condition is present. The X_{off} condition can be issued by the Read-Out Controller (ROC) of any sub-detector in order to stop the transmission of triggers whenever the amount of data in its output buffer exceeds a predefined upper limit.

At the transmission stage a 64-bit packet of data, consisting of the event number (a sequential, burst-based number), the trigger-word and the timestamp is sent simultaneously to the ROCs of 10 sub-detectors over fast dedicated serial links.

For the present analysis the bits of the trigger-word listed in Table 4.2 are used as main or control triggers.

bit	name	description	D
0	MB-2VTX	2VTX bit from MBX	1
1	MB-1VTX	1VTX bit from MBX	1
3	C-PRE	$Q_2 \cdot \overline{AKL} + Q_1/100$	100
4	MB-1TRK-P	1TRK-P bit from MBX	1
9	N-MBIAS	T_N^0	200

Table 4.2.: The bits of the trigger-word used for the K_{e4} analysis as main (0, 1 and 4) or control (3 and 9) triggers. D indicates the down-scaling factor applied by the TS.

4.3. The Data AcQuisition (DAQ)

The DAQ of the NA48/2 experiment consists of two parts: the PC-Farm situated at the experimental area, that combines the information from each sub-detector into complete events and writes them to disk, and the Central Data Recording (CDR) system that sends the data to the L3 and manages the offline processing of the burst files. The data are sent from one system to the other via 7 km long optical Gbit connections. A schematic view of the two subsystems is shown in Figure 4.5.

In order to easily distinguish data taken under different beam, detector or trigger conditions, a progressive run number is assigned to each data taking period, typically a few hours long and containing about one thousand bursts. Every time something was changed in the set-up or after eight hours of stable data taking a new run was started.

4.3.1. The PC-Farm

The PC-Farm for the online processing of the events [103] consists of 24 PCs, that can be divided into three groups: the sub-detector PCs, the Event Building (EB) PCs and the control PC. All PCs are connected via 100 Mbit Ethernet cards to a switch that is in turn connected with the CERN computing centre via Gbit Ethernet.

Each time the TS sends a trigger to the sub-detectors, their read-out systems extract the corresponding data and transfer them to the sub-detector PC. Each sub-detector has one PC, apart from the LKr that, due to its high data rate, needs eight PCs. The data of all the events in a burst are kept in memory till the end of the burst. As soon as all the sub-detector PCs have collected all the events of one burst, the data are sent through the network to the Event Building PCs. In order to increase the transfer rate for the data of the LKr, its sub-detector PCs are connected to the switch with two Ethernet cards each, that can be used in parallel.

The bursts are split into subsamples, called burstlets. Each burstlet is sent to one of the used EB PCs. In 2003, 9 dual Pentium-III PCs were available for this purpose. An EB PC “builds” each event by collecting from the sub-detector PCs the corresponding data and writes the burstlet in raw format to its local disk after sorting the events according to their number. This process runs during the inter-spill, i.e. between two beam extractions. The burstlets are normally copied within a few minutes to the disk servers situated in the CERN computing centre, but in case of network problems the local disks can be used as buffer with a total capacity of 540 GB, corresponding to about four hours of normal data taking. The number of EB PCs actually used to build the events can be adjusted according to the data rate and was normally set to 8 in 2003. This mechanism has the advantage of allowing for a normal data taking also in case of failure in one of the EB PCs.

Since the introduction of the Super-Event in the LKr read-out, one more process has to run at the event building stage, namely the Ghost Cluster (GC) suppression. In the Data Concentrator the Super-Event is seen as a single event and only cells that are empty in both events are zero suppressed. When the Super-Event is split into two single events in the EB PC, there are groups of cells that are read out even though they are empty, because they are the image of clusters existing in the partner event. These empty cells form the Ghost Clusters. The GC suppression algorithm [92] loops over all read out cells, looking for a seed cell with an energy above a certain threshold. If a seed cell is found, an outward expansion with a predefined box radius is performed around it and all cells within the box radius are

marked to be read out. The cells that are not marked by the expansion are instead discarded from the raw data.

The control PC is responsible for the supervision and the monitoring of the DAQ. The control program running on it starts all the necessary processes in the sub-detector and EB PCs and checks that they are working properly. Furthermore the accessibility of each PC over the network is monitored regularly. In case a PC is not reachable anymore, it is automatically rebooted without requiring any human intervention.

4.3.2. The Central Data Recording (CDR)

The CDR system is a software consisting of a few daemon programs responsible for the combination of the burstlet files into a list for each burst, the update of the burst database, the submission of the jobs running the L3 trigger program to the queue, the collection of the results of these jobs and the copy of the data to tape.

During the data taking of 2003, for the first time, the CERN infrastructure was adopted to run the L3 program and for the copy of the files to tape. The jobs were sent to “lxbatch”, a farm of about 1500 dual-processor machines running the Load Sharing Facility (LSF) queueing system, while for the data storage the “Cern Advanced STORage manager” (CASTOR) [104] was used.

For each burst written in raw format by the PC-Farm an entry has to be added to the database with information on the path of the file, its size and the time at which the data was taken. The bursts are then processed by the L3 trigger program, which produces different output streams of data (see Section 4.4). Every time a L3 job succeeds, the CDR adds an entry to the database for each new data file produced and copies the files to CASTOR.

In total about 80 TB of data were written to tape in 2003, with a loss due to the CDR of less than 1%.

4.4. The Level 3 trigger (L3)

The L3 is a software trigger [105], that fulfils two tasks: it flags events that are suitable for physics analysis or for monitoring purposes and it converts the raw data into the COnPACT format (see Section 5.1). To keep the program as flexible as possible, most of the parameters defining its behaviour are contained in a configuration file, a text file that can be edited at any time during the data taking.

As a first step, the program checks which actions have to be performed on each event. An *action* is defined in the configuration file as a list of operations to be executed on events, whose trigger-word contains a certain combination of bits. Possible operations are down-scaling (for each action a different factor can be chosen), sending the event to one or more selection filter and/or writing it directly to a stream. Each action attaches to the event new flags if operations have to be executed, for which no flag was set yet.

A *filter* is a selection function that is called if the corresponding flag is set. In the configuration file at most 16 filters can be defined. For each filter a different down-scaling factor can be set, a certain fraction of the events that have been sent to it can be kept independently of the response of the filter (the so-called “auto-pass” events used to measure the filter efficiency) and a list of streams can be defined to which the selected events have to be written.

Before passing the event to the filters, the decoding and reconstruction routines (see Section 5.1.1) are called, so that all the physical quantities are available for the selection. This is the main difference with respect to the hardware trigger stages: a proper particle identification can be performed only at the L3, where it is possible for example to associate a track in the spectrometer to a cluster in the LKr or to a hit in the MUV and define criteria to distinguish electrons, pions and muons. Most of the parameters used for the selection in the filters are also defined as constant values in the configuration file, so that they can be easily modified.

Each filter corresponds to one bit in the L3 trigger-word and is set to zero or one according to the response of the selection function. Since there are in general more than 16 interesting physics channels, two words are necessary for their identification. The filters corresponding to the L3 trigger-word bits are called “main” filters and form the first word, while the “sub-filters” are flagged by the second word, which has 32 bits. These bits are set inside the selection functions and their definition cannot be easily changed through the configuration file. Another 16-bit word is used for the auto-pass events with the same order and definition of the bits as for the main filters.

The L3 can write as output a maximum of 8 streams. For each *stream* a down-scaling factor and a format can be defined in the configuration file. The flags indicating to which stream each event has to be written are attached to the event by the program according to the actions and the selection response. If no stream flags are set, the event is rejected.

In 2003 the L3 was run in the so-called “flagging mode”, i.e. no events were rejected, everything was written out in the COnPACT format for the offline analysis. Furthermore a “flat” configuration was used, in which events triggered by any L2 trigger bit were sent to all the filters. Of the main filters three were used for calibration and monitoring purposes, while the remaining 13 selected a total of 28 physics channels.

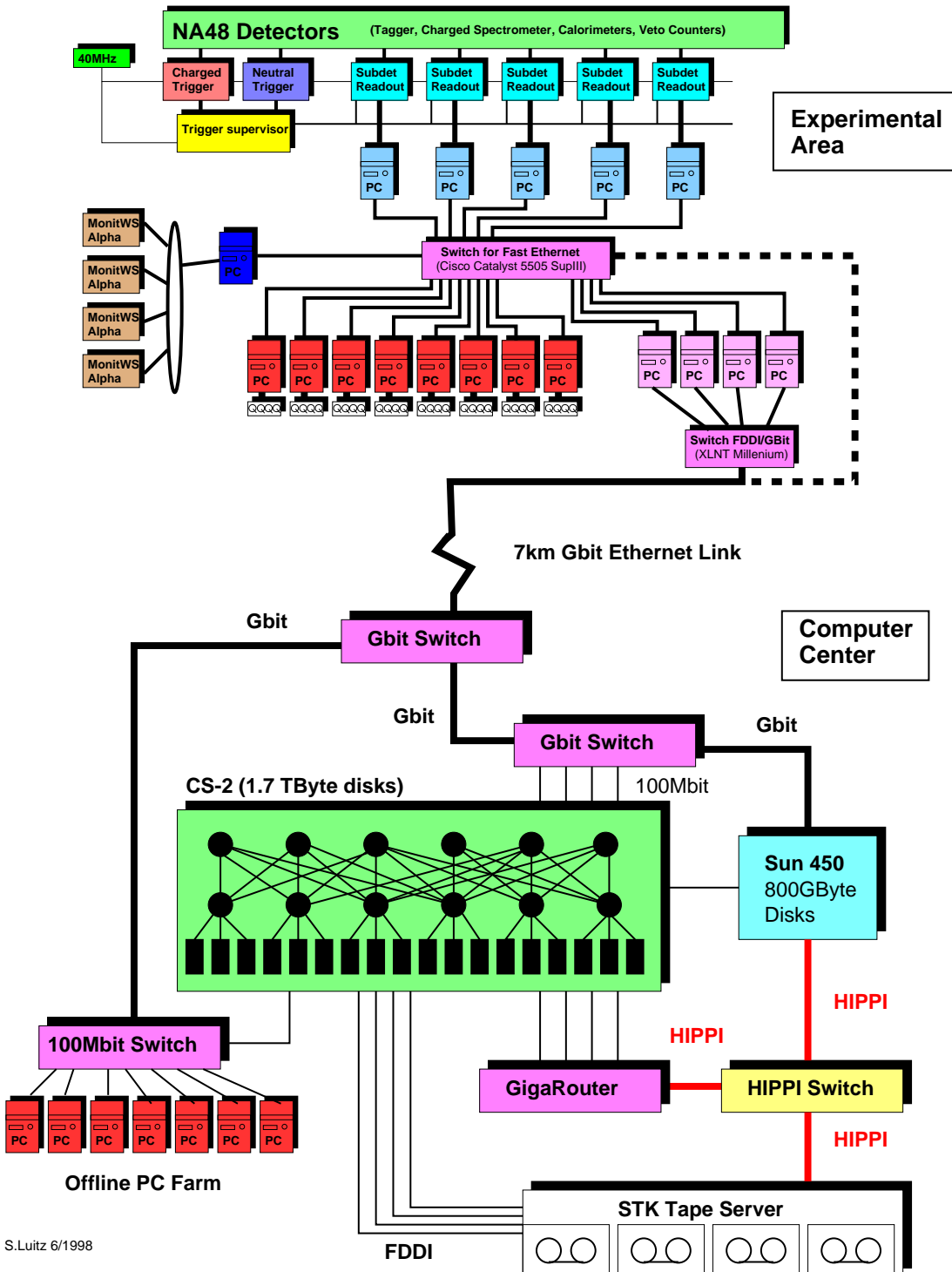


Figure 4.5.: Schematic view of the data acquisition system consisting of the PC-Farm (on the top) and the CDR (on the bottom) [89].

5. Reconstruction

The raw data written to disk by the PC-Farm (see Section 4.3.1) are just a long list of numbers: the pointers to the different parts of the event and the values read by the electronics of each sub-detector. In order to build physical objects out of them, the L3 program (see Section 4.4) calls for each sub-detector a decoding and a reconstruction routine. This procedure is described in Section 5.1.

To analyse the data, that are now written in COmPACT format, a reader program is used, that can also apply corrections or filter the sample. The basic features of this program are presented in Section 5.2.

5.1. The physical objects

In this Section the way from the raw data to the format read by a program called “C Optimised Program for Accessing Countless Terabytes” (COmPACT) [106] is described (see Section 5.1.1). Particular attention is given to the objects used to select and reconstruct the K_{e4} decays: the tracks in the magnetic spectrometer (see Section 5.1.2), the clusters in the LKr calorimeter (see Section 5.1.3) and the hits in the MUV (see Section 5.1.4).

5.1.1. Decoding, reconstruction and COmPACT output

The first step to obtain physical quantities from the raw data is to assign each value to the variable it represents. This is done in the *decoding* routines, that read the event in raw format as input and fill one of the so called “pre-processed” ZEBRA [107] bank as output. Such banks contain typically the information on the single signals, for example the pulse height and the time of each hit.

Starting from the pre-processed banks, the *reconstruction* routines combine the signals into more complex objects, like the tracks in the DCHs and the clusters in the LKr. This information is saved in the “reconstructed” ZEBRA banks.

In order to save disk space, the data are written in COmPACT format, where they are organised in C structures, instead of ZEBRA banks. Furthermore only quantities that cannot be derived from other ones are written and some information present in the banks for debugging purposes is removed.

5.1.2. Track reconstruction

The pre-processed bank of the DCH signals contains for each hit the plane number, the wire number and the drift time.

The alignment of the DCH planes was checked during special runs with a muon beam and no magnetic field in the spectrometer. Forcing the muon tracks to form straight lines in the spectrometer, two arrays of corrections were determined: a shift and a rotation for each

plane. The alignment correction is applied in the calculation of the hit position starting from the plane number and the wire number. Furthermore a precise alignment is performed for each single wire with a similar set of constants.

The hits in each view are first combined into *clusters*, defined as (mostly two, in some rare cases three) contiguous hits in the two planes of a view. Then all the possible combinations of a cluster in DCH1 and a cluster in the corresponding view in DCH2 are built. These associations are called *segments*. Some loose geometrical cuts are applied to the segments, in order to discard the ones that cannot be part of a physical track originating from the kaon beam. A *front track* is built from the association of at least two segments in different views. Further geometrical requirements are applied and only the physical front tracks are kept. If the front track consists of only two segments, a cluster in a third view is required in each chamber.

To build complete tracks, *space points* are formed in DCH4 combining compatible clusters in three or four views. The front tracks and the space points are then associated with the only constraint of an almost straight line in the y coordinate, since the deflection due to the dipole magnet of the spectrometer is only in the x direction. The uncertainty in the prediction of the impact point of the track in DCH4 due to multiple scattering is taken into account in the association.

The information on the drift time of the hits is introduced only now: the track time is calculated and a compatibility variable is defined between 0 and 1. In these calculation a correction is applied to take into account the signal propagation along the wire. A track can be rejected if the compatibility is less than 0.75, if the hit drift times are too far from each other, or if the coordinates of the hits in a cluster are not compatible anymore after correcting the position for the drift time.

The track time is improved looking at the difference of the coordinates in the two planes of a view and a *quality* variable is defined as the number of hits belonging to doublets and triplets divided by the total number of hits belonging to the track.

The physical parameters of the track (position, slope in x and y and momentum) are computed using a Kalman filter [108] for each space point. The Kalman filter is the optimal recursive estimator of the state vector of a linear dynamic system. The evolution of the state vector is described by a linear transformation plus a random smearing and the measured values are linear functions of the state vector with an uncertainty. In the specific case of the track parameter calculation the evolution of the state vector is the transport equation from a space point to the next one. The uncertainty on the track parameters and the whole covariance matrix are written into the reconstructed track bank together with the fitted values.

Once the tracks are built, the clusters in DCH3 compatible within the uncertainty with the position extrapolation are attached to the track and its physical parameters are recalculated. In case two space points in DCH4 belonging to two different tracks have at least two clusters in common, only the track with the best χ^2 is kept, while the other one is rejected as *ghost track*.

A detailed description of the reconstruction routines can be found in [109].

At this stage the vertex reconstruction can already be performed, but, in order to save disk space, all the track parameters and their uncertainties are saved into the COnPACT structures, so that it is possible to reconstruct the vertices at runtime (see Section 5.2.2).

5.1.3. LKr cluster reconstruction

Starting from the pre-processed LKr bank, that contains the pulse information for each cell which has been read out, the reconstruction routine attempts to find clusters in the whole time window. This procedure allows to build both the signal clusters and the *accidental* ones for background studies. Accidental clusters are mostly due to particles produced in a decay before or after the triggered one.

First of all a list of the cluster seed candidates is created. In a loop over all the cells in the bank it is checked if they were working properly (if not they are marked as *dead cells*), then the average value of the first three samples in time is subtracted if it is more than 20 MeV away from zero. In the first three samples no energy is expected from clusters in time with the event and this method is used to correct the energy of showers sitting on the undershoot of a previous pulse. In the same loop the cells that have enough energy are marked as cluster seed candidates.

If a seed candidate is a local maximum and its energy is above a threshold defined by the average energy of the eight surrounding cells, a cluster is defined around the seed. In this search only the time slice of the seed, the preceding and the following ones are considered. The cluster position is estimated as the barycentre of the energy deposition in 3×3 cells. If a dead cell is among these nine, a 5×5 box is used to measure the cluster position.

To compute the energy of a cluster, all the cells in a 19×19 box around the seed are considered. If a cell belongs only to one cluster, its energy is added to the cluster energy after reconstructing the pulse with the digital filter method. If a cell belongs to more than one cluster at the same time, its energy is shared among them, according to weights determined from Monte Carlo simulation. The weight is a function of the cluster energy in the 3×3 box, of the distance between the cluster and the cell and of the expected energy profile. In the case of a cell contributing to clusters at different times, the digital filter is used to superimpose the pulses and perform a time sharing. The energy that would have been deposited in a dead cell is estimated from the energy profile.

The width of the cluster is computed as the RMS in the x and y directions of the energy distribution in a 5×5 box.

The following corrections are applied to the first estimates of the energy, position, time and width of the clusters:

Position: The first estimate gives the position at the front of the calorimeter in the assumption that the neutral particle producing the shower comes from the point where the LKr cells are projecting.

The x coordinate is corrected for the motion of the centre of gravity of the shower with the energy and for the zig-zag shape of the electrodes. The function used for the correction has 12 parameters that are derived from electron data.

In the y coordinate no particular shape of the electrodes has to be taken into account. Therefore the position has only to be corrected for the non linearities in the response of the LKr with respect to the distance between the centre of the shower and the electrode. The correction is independent of the energy, but depends on the impact point in x within the cell.

Shower width: The estimators are corrected for the dependence on the impact point in the cell, with different parameters for the two directions.

Energy: The energy depends on the impact point within the cell in the y direction due to electric field variations between electrodes and in the x directions due to the reduced charge collection efficiency near the anode.

The energy of clusters with a radial position between 14 and 20 cm is corrected for the loss in the beam hole. The correction is derived from Monte Carlo and parametrised as a third degree polynomial in the radial position. A similar correction is also applied to clusters near the outer edges of the LKr.

The absolute energy scale is also adjusted to a level better than 10^{-3} .

Time: The time of the pulses is corrected for the difference in the time offset of the single cells.

The reconstruction program and its performances are described in more detail in [110, 111].

5.1.4. MUV hits

For the MUV hits no reconstruction is applied at this stage: the hit information is copied to the COmPACT structure and the association with the tracks is performed when reading the event.

5.2. The COmPACT reader program

The files in COmPACT format are read by the analysis program that can apply further corrections to the stored variables (see Section 5.2.1). It also computes quantities that are not stored, since they can be derived from other ones, like the vertices (see Section 5.2.2) or the muon tracks (see Section 5.2.3). To reduce the size of the data sample to be analysed, the COmPACT reader program can write a filtered output file according to a selection written by the user and further compress the events into the so called “SuperCOmPACT” format (see Section 5.2.4).

5.2.1. Corrections

At COmPACT level further corrections can be applied when reading the events, so that they do not need to be reprocessed from the raw data every time a parameter value is updated. To improve the flexibility of the system, most of the information used by the correction routines is saved in a database, that can be updated independently of the program. In the following the relevant corrections for the K_{e4} selection are described.

Bad bursts

The data quality of the whole sample was checked and bursts or runs where one or more detectors were not working properly were added to the database. In the same way also bursts containing less than 3000 selected decays into three charged pions (a normal burst contains about 20000) were flagged as bad bursts for physics analyses. The database contains lists of bad bursts and bad runs for each detector and for physics, so that the bursts can be rejected if the detectors that are necessary for the selection are not reliable. Skipping entire bursts or runs has the advantage of saving the time necessary to unpack the event structures.

Track momentum

Computing the invariant mass of the kaon from decays into three charged pions, two effects can be observed: a difference between the masses of K^+ and K^- events and a shift of both values with respect to the nominal kaon mass. Both effects are very sensitive to small changes in the detector and beam setup, so that they must be corrected on a burst by burst basis.

The first difference is due to the misalignment of DCH4 with respect to DCH1 and DCH2. An empirical momentum correction can be applied [112]:

$$p_{corr} = p \cdot (1 + \alpha \cdot q \cdot p), \quad (5.1)$$

where p_{corr} is the corrected momentum of the track, p its measured momentum, q its charge and α is obtained for each burst as

$$\alpha = -\text{sign}(B) \cdot \frac{\langle m_{K^+} \rangle - \langle m_{K^-} \rangle}{1.7476}. \quad (5.2)$$

B is the magnetic field in the spectrometer magnet, $\langle m_{K^+} \rangle$ and $\langle m_{K^-} \rangle$ the mean values over one burst of the measured K^+ and K^- masses, respectively. The values of α for the 2003 run are at most a few times 10^{-4} .

The residual shift with respect to the nominal kaon mass can be corrected with a second parameter [112]:

$$p_{corr} = p \cdot (1 + \beta \cdot p), \quad (5.3)$$

with

$$\beta = \frac{m_K^{nom} - \langle m_K \rangle}{0.2 \cdot m_K^{nom}}. \quad (5.4)$$

m_K^{nom} is the nominal kaon mass, while $\langle m_K \rangle$ is the measured one after applying the α correction. β is of the order of 10^{-3} .

The values of α and β for each burst are saved in the database and can be used to apply the correction at runtime.

Cluster position and energy

The cluster position can be corrected for displacements (shift and rotation) with respect to the DCH position using a clean electron sample from $K \rightarrow \pi e \nu$ decays.

The cluster energy can be corrected for the following effects:

- The energy dependence on the radial distance from the beam axis for clusters with a radial distance below 22 cm.
- The energy loss due to the threshold in the Data Concentrator.
- The non linearity in the calorimeter response for clusters with an energy below 15 GeV.
- The energy sharing between clusters. This is only a fine tuning of the correction already applied in the reconstruction.
- The mis-match between the energy deposited in the LKr and the momentum measured in the spectrometer for electrons. This can be compensated by an overall energy scale correction of the order of 10^{-3} and a fine tuning as a function of energy.

- The energy baseline. The pedestals were already subtracted cell by cell in the reconstruction, but some fine tuning can be performed adjusting the cluster energy. The correction is of the order of a few MeV.

For the pedestal correction one value every ten bursts is saved in the database, while the other ones only need a few parameters that are hard-coded in the program.

5.2.2. Vertex reconstruction

Starting from the coordinates and the slopes in DCH1 of two, three or four tracks, the vertex reconstruction routine computes the best vertex coordinates and the slopes of the tracks and of the mother particle at the vertex [113].

In the initialisation phase the vertex coordinates are estimated from the calculation of the closest distance of approach between two tracks. If more than two tracks form the vertex, the pair with the biggest slope difference is used. For this computation the tracks are extrapolated as straight lines with the slopes measured in DCH1 from the chamber to the vertex. The slopes at the vertex are initialised to the measured values at DCH1.

The algorithm used for the parameter optimisation is based on a Kalman filter, as the one for the track parameter computation (see Section 5.1.2). This calculation is equivalent to a χ^2 method when all measurement uncertainties are taken into account, as well as the smearing due to the multiple scattering in the Kevlar window and in the helium before DCH1. The transport equation from the state vector in DCH1 to the one at the vertex includes the deflection due to the magnetic field inside the vacuum tank (called “blue field” because of the colour of the tank).

5.2.3. Muon reconstruction

A muon is reconstructed every time at least two hits in the MUV can be associated in space and time to a track in the magnetic spectrometer.

Each track is extrapolated from DCH4 to the MUV, the corresponding channels in which a hit is expected are flagged and the reconstruction routine looks for hits in them. If at least two hits within 10 ns of the track time are found in two different planes, the muon structure is filled.

5.2.4. SuperCOmPACT production and filtering

In order to reduce the data size by about a factor five, the events are converted into the SuperCOmPACT format, which is the standard format used for analyses. The reduction is obtained by removing all the variables that are necessary to test the data quality, but not to perform physics analysis and by saving all the variables as integers after scaling the real numbers with appropriate factors. In the conversion to integers some accuracy is lost, but for most of the variables this loss is negligible.

Since the SuperCOmPACT data are first produced when the correction parameters are known, the corrections that have to be used for all the analyses are already applied. Of the corrections listed in Section 5.2.1, the ones for the cluster position and energy were applied at this stage.

While converting the COmPACT files into SuperCOmPACT, a filter can be applied. The filter consists of a user selection routine that can use all the information available in the structures, since all the reconstructions and corrections performed at runtime are called before it. It is also possible to filter the events without format conversion.

5. Reconstruction

6. Monte Carlo simulation

In order to compare any theoretical prediction with the data, it is necessary to perform a simulation of all the physical processes taking place from the beam production to the signal read-out in the detector. Since many complex effects have to be taken into account, it is not possible to describe analytically the expected distributions. Instead, the Monte Carlo (MC) method is used: single events are generated, according to weights given by the expected probability distributions, like the differential decay rates or the efficiencies and resolutions of the sub-detectors.

The MC events have the same format as the data, but the “true values”, i.e. the four-vectors of the generated particles, their type and their production and decay positions, are known as well (see Section 6.4). This allows to apply the same event selection to data and MC, to measure the detector acceptance (i.e. the ratio between the number of selected events and the number of generated events) and the detector resolution for any variable and to predict the distributions of signal and background events after the selection, to be compared with the data.

The simulation program available for the NA48/2 experiment is called Charged kaons Monte Carlo (CMC) and is based on the GEometry ANd Tracking (GEANT) package of the CERN libraries [114]. It is a precise, but quite CPU-consuming simulation, that is necessary for precision measurements based on the comparison between data and MC.

6.1. Kaon beam

The kaon beam is simulated using a package called “Trace Unlimited Rays Through Lumped Elements” (TURTLE) [115]. The parameters are tuned on a run by run basis, separately for K^+ and K^- , in order to reproduce the momentum distribution of the beam.

Due to the method used to measure the K_{e4} form factors, a precise simulation of the beam momentum is necessary, since the neutrino momentum is measured as the difference between the kaon and the visible particles and the computation of the kinematic variable requires a boost of the four-momenta of the decay particles into the kaon rest frame. Therefore the MC sample is generated with a population of events per run reproducing the one of the data.

The simulated momentum can be chosen by the user, but, due to the narrow momentum spread of the beam, the range between 50 and 70 GeV/c (as in the MC samples used in this analysis) already contains the whole spectrum (see Figure 6.1).

6.2. Kaon decay

The z range in which the decays can take place is also a parameter set by the user and should include a few meters more than the accepted region in the event selection. In the MC samples

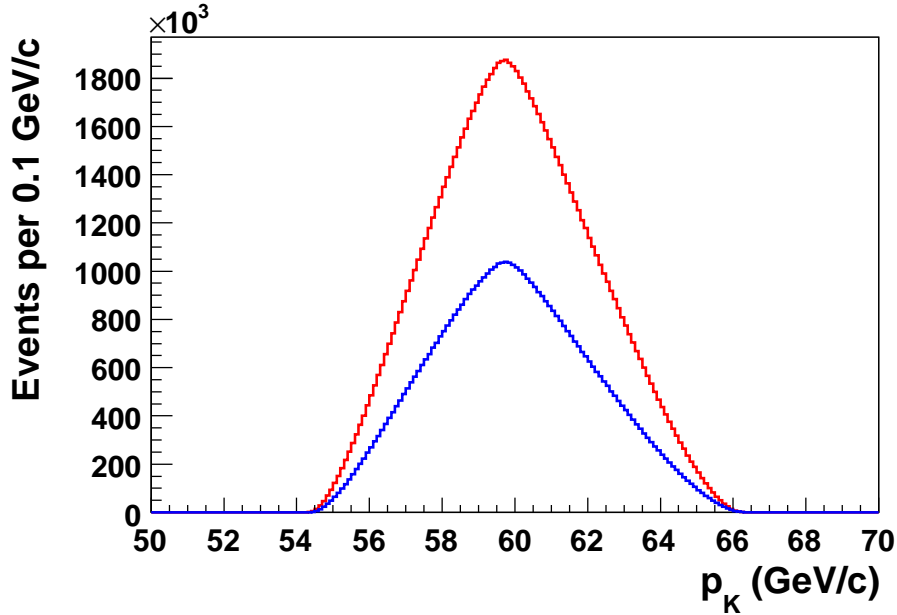


Figure 6.1.: The kaon spectrum in CMC for K^+ (red) and K^- (blue) for the complete sample of generated $K^\pm \rightarrow \pi^\pm \pi_D^0$. The relative fraction of K^+ and K^- as well as the number of events per run have been computed from selected events in the data.

analysed here, decays with a z coordinate between -22 m and 80 m were simulated, while, for reference, the end of the final collimator is at $z = -18$ m and DCH1 at $z = 97$ m.

The probability for a kaon with energy E_K to decay at a certain position z_d is

$$P(z_d) = \frac{1}{\gamma c \tau} \cdot e^{-\frac{z_d}{\gamma c \tau}}, \quad (6.1)$$

where $\gamma = E_K/M_K$, with $M_K = 0.493677 \text{ GeV}/c^2$ [13], is the boost factor of the kaon, c the speed of light and τ the mean lifetime of the kaon.

CMC can generate only one decay channel at a time, i.e. one kaon decay mode and, in case a π^0 is produced, one specific decay mode for it. Due to the very short lifetime of the π^0 ($\tau \simeq 10^{-16}$ s), its decay vertex would be only a few micrometers away from the kaon decay vertex. Since this distance is orders of magnitude smaller than the resolution of the vertex reconstruction, it is assumed that the two decay vertices coincide. Producing one decay mode at a time, the weighting of the number of events according to the branching fractions has to be taken into account when comparing data with MC or combining events from different channels.

The four-momenta of the decay products are first generated in the kaon rest frame according to the phase space distribution using the routine genbod of the CERN libraries [116], then weighted with the proper matrix element and finally boosted to the laboratory frame.

6.2.1. The K_{e4} generator

For the matrix element Eqs. 2.71–2.74 are used, with the parametrisation

$$\begin{aligned} F &= (f_s + f'_s q^2 + f''_s q^4 + f_e \frac{s_e}{4M_\pi^2}) e^{i\delta_0^0(s_\pi)} + \tilde{f}_p \sigma_\pi X \cos \theta_\pi e^{i\delta_1^1(s_\pi)} \\ G &= (g_p + g'_p q^2 + g_e \frac{s_e}{4M_\pi^2}) e^{i\delta_1^1(s_\pi)} \\ H &= (h_p + h'_p q^2) e^{i\delta_1^1(s_\pi)}, \end{aligned} \quad (6.2)$$

which is equivalent, apart from the advantage of having dimensionless parameters, to Eq. 2.76, with $q = \sqrt{\frac{s_\pi - 4M_\pi^2}{4M_\pi^2}}$. The value of M_π , the mass of the charged pion, was set to 0.13947018 GeV/c² [13]. The D -wave term is omitted, since it is expected to be negligible.

The phase shifts are obtained from Eq. 2.63 with the coefficient values given in [39] and the constraint of Eq. 2.67 between a_0^0 and a_0^2 . R is assumed to be zero and the values of the parameters f , g , h and a_0^0 are taken from previous experimental results [35]. The complete matrix element implemented in CMC can be found in Appendix A.

6.2.2. Other generators

Samples of simulated events were produced also for the main background channels: $K_{3\pi}$, including also $K^\pm \rightarrow \pi^+ \pi^- \pi^\pm \gamma$, $K_{2\pi}$ with the π^0 undergoing a Dalitz decay (into $e^+ e^- \gamma$) and $K_{\pi\pi^0\pi^0}$ with one of the π^0 s decaying Dalitz.

For the $K_{3\pi}$ the matrix element [13]

$$M(u, v) = 1 + g \cdot u + h \cdot u^2 + k \cdot v^2 \quad (6.3)$$

was used, with

$$\begin{aligned} u &= 2M_K \cdot \frac{M_K/3 - E_{\pi_3}}{M_\pi^2} \\ v &= 2M_K \cdot \frac{E_{\pi_1} - E_{\pi_2}}{M_\pi^2}, \end{aligned} \quad (6.4)$$

where the energies are measured in the kaon rest frame, π_3 indicates the pion with opposite charge with respect to the kaon (odd pion), while π_1 and π_2 are the even pions. The chosen parameter values were $g = -0.2154$, $h = 0.012$ and $k = -0.0101$, that correspond to the measured values for K^+ decays [13]. The same parameters are used for K^+ and K^- decays.

The $K_{\pi\pi^0\pi^0}$ decay was generated with the same form of the matrix element but different parameter values (in this case π_1 and π_2 are the two neutral pions and π_3 is the charged one). The parameter values were chosen to be $g = 0.638$ [13], $h = 0.0825$ and $k = 0$.

$K_{2\pi}$ is a two-body decay and requires therefore only the random generation of the angle between the directions of the kaon and that of one decay product, uniformly distributed in space. All the other quantities are fixed and no matrix element has to be taken into account.

The Dalitz decay of the π^0 (π_D^0) is generated in two steps: $\pi^0 \rightarrow \gamma\gamma^*$ and $\gamma^* \rightarrow e^+ e^-$. The mass (m) of the virtual photon (γ^*) is generated with a flat distribution within the kinematic limits $[2M_e, M_{\pi^0}]$ and then weighted with the function [117]

$$f(m) = \frac{1}{m} \left(1 - \frac{m^2}{M_{\pi^0}^2}\right)^3 \left(1 + 2\frac{M_e^2}{m^2}\right) \sqrt{1 - 4\frac{M_e^2}{m^2}} \left(1 + 0.032\frac{m^2}{M_{\pi^0}^2}\right)^2, \quad (6.5)$$

with $M_{\pi^0} = 0.1349764 \text{ GeV}/c^2$ and $M_e = 0.000511 \text{ GeV}/c^2$ [13]. The $\gamma^* \rightarrow e^+e^-$ decay is weighted according to the distribution [117]

$$f(y, m) = 0.3 \left(1 + y^2 + 4 \frac{M_e^2}{m^2} \right), \quad y = \frac{E_{e_1} - E_{e_2}}{p_{\gamma^*}}, \quad (6.6)$$

where the energies and momenta are measured in the rest frame of the π^0 .

6.2.3. Radiative corrections

For the simulation of bremsstrahlung photons emitted by charged particles, the latest version of the PHOTOS package [118] was used. Instead of performing systematic calculations order by order in the perturbation theory, the “exponentiation method” is used, a rigorous scheme of reshuffling the dominant terms between different orders in the expansion. Furthermore, in the leading-log approximation, it is possible to write the matrix element of a decay with bremsstrahlung emission as a product of terms without QED corrections times the bremsstrahlung factor. In the same way, also the differential formula for the Lorentz invariant phase space of a decay with bremsstrahlung photons can be factorised. The bremsstrahlung factor depends only on the four-momenta of the particles taking part in the decay and not on the actual process.

The leading-log approximation takes into account both real and virtual corrections. The terms due to QED interference were added only in the latest version of PHOTOS and are very important for the semileptonic kaon decays. The interference term is described by a universal weight, valid for any decay channel, depending only on the charges and momenta of the decay products and on the energy of the emitted photon. A universal implementation is now possible because the interference is calculated from the four-momenta and not from internal angular variables, as was the case earlier.

After generating an event without any correction, PHOTOS reads in the four-momenta, masses and type of the particles and produces, with a certain probability, one or more additional photons, correcting the four-momenta of the emitting particles, so that energy and momentum conservation are assured. CMC reads back the modified event and proceeds with the boost into the lab system.

The radiative corrections were included in all the MC samples generated for the K_{e4} analysis. For the $K_{3\pi}$ and K_{e4} samples PHOTOS was used in the “exponentiated” mode, i.e. the number of generated photons follows a Poissonian distribution, and with the infrared cut-off parameter (the minimal photon energy as a fraction of the mass of the decaying particle) set to 10^{-7} . The universal interference weight was enabled with a maximum value of 2^{n-1} , where n is the number of charged particles in the final state. The decay $\gamma^* \rightarrow e^+e^-$ was corrected for the emission of at most one bremsstrahlung photon with the cut-off parameter set to 10^{-5} . The radiative corrections are expected to play no important role in the $K_{2\pi}$ and $K_{\pi\pi^0\pi^0}$ decays and have not been implemented in the simulation.

6.2.4. Coulomb correction

In order to take into account the electric attraction or repulsion between the charged particles in the final state, a weighting factor

$$P_{ij} = \frac{2\pi n}{e^{2\pi n} - 1}, \quad n = \frac{\alpha e_i e_j}{\beta_{ij}} \quad (6.7)$$

is multiplied to the probability distribution for each pair of charged pions in the final state. In Eq. 6.7, α is the QED coupling constant, e_i and e_j the charges of the two interacting particles in units of the electron charge and β_{ij} their relative velocity in units of c . P_{ij} is, in the quantum mechanical description of the Coulomb scattering of an incident beam with velocity $c \cdot \beta_{ij}$, the particle density at the target, divided by the effective area seen by the impinging particles [119].

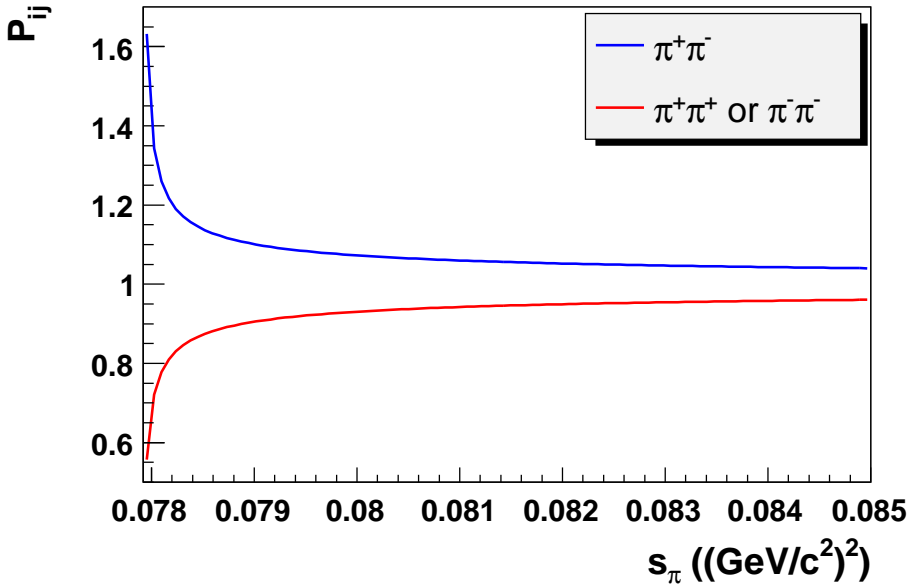


Figure 6.2.: Size of the Coulomb correction as a function of the dipion invariant mass squared for a pair of same (red) and opposite (blue) sign pions.

Since P_{ij} is close to 1 for small values of n , corresponding to high relative velocities and high invariant masses (see Figure 6.2), only pion pairs produced at threshold (with an invariant mass close to twice the pion mass) are significantly affected by this corrections, while the interaction between a pion and an electron or between two electrons can be neglected. Therefore three factors are considered in the generation of the $K_{3\pi}$ decay, one in K_{e4} and none in the Dalitz decay of the π^0 .

6.3. Tracking in the detector

Each decay product is followed through the whole detector: at each plane its position and energy loss are computed. A particle can interact with the material producing a signal and/or

secondary particles that are added to the list and will also be tracked. Many effects that can distort the measurement are taken into account, for example:

- multiple scattering in the helium between the drift chambers
- photon conversion into an electron-positron pair, mainly at the Kevlar window
- bremsstrahlung in the drift chambers
- δ -rays crossing the detector
- dead cells in the LKr
- misalignment of the chambers (see Section 5.2.1).

All the signal information available in raw format is simulated, except for the time. Since no accidentals are simulated, the time coincidence between different signals and different sub-detectors does not need to be tested: all signals are produced by the simulated event and must therefore be assumed to be in-time.

In order to estimate the efficiency of the background rejection, the two most important features are the simulation of the electromagnetic showers in the LKr and the decay in flight of charged pions. They will be described in detail in the following Sections.

6.3.1. Electromagnetic showers

The complete simulation of an electromagnetic shower in the calorimeter with GEANT is very CPU-time consuming. In order to speed up the generation of millions of events, samples of electromagnetic showers for different particles and energies have been generated and saved into “shower libraries”. CMC can read back a shower chosen randomly for the necessary particle and energy bin and use the saved pattern of energy deposit in the LKr cells. The disadvantage of this method is the limited statistical precision, so that effects of the order of 10^{-6} in the LKr energy and position measurements can not be simulated precisely, even with a large sample of events.

The cluster width, on the other hand, is not simulated precisely by GEANT itself: the mean shower widths for electrons and photons agree within a few percent between data and MC, but can not easily be corrected in the reconstruction. Therefore any selection cut involving this variable has to be adjusted to give the same efficiency in data and MC.

A much bigger discrepancy between data and MC affects the shower simulation of mesons and baryons: the cluster width, the probability of shower fluctuations (small secondary clusters up to about 40 cm away from the projection of the track to the LKr) and the fraction of energy deposited in the electromagnetic calorimeter differ in some cases by a factor of 10. The background rejection based on these variables has therefore to be studied on a clean data sample.

6.3.2. Pion decay in flight

Charged pions have a mean lifetime $\tau \simeq 2.6 \times 10^{-8}$ s [13], that, at an average energy of 20 GeV, corresponds to a mean decay length of about 1100 m. In the decay and detector

volume, together about 140 m long, the probability of a pion decay is therefore a few percent and can not be neglected in the simulation.

The decay $\pi \rightarrow \mu\nu$ has a branching ratio of 99.9877% [13] and is the only channel to be included in the simulation by default. Furthermore, only decays before the LKr produce a mis-measurement of the “pion” momentum, while the ones in or after the LKr only give a signal in the MUV, but the momentum measured in the spectrometer is correct. Simulating only decays before the LKr has the advantage to allow for the use of the shower libraries, instead of tracking the particles in the LKr and afterwards. The disadvantage is a small (a few 10^{-3}) disagreement in the hit rate in the MUV. For the same reason also the punch through of the pions in the MUV is not simulated.

In order to study the $K_{3\pi}$ background to K_{e4} decays, a private correction [120] was applied and a separate sample with the pions decaying only into $e\nu$ was generated. The number of events simulated with this special setting is proportional to the ratio 1.23×10^{-4} [13] of the branching ratios for the two decays channels of the pion.

6.4. Reconstruction and corrections

In general the same decoding, reconstruction and corrections are applied to data and MC, with a few exceptions that will be briefly described in this Section.

The information on the generated particles is written by CMC into a ZEBRA bank, that contains the type of each particle, its four-momentum in the laboratory frame, its mass, the coordinates of its production and decay vertex and a link to the bank of the mother particle. Furthermore the coordinates, slopes and energy deposit at each tracking plane are available, as well as the number of hits in each detector. Only one structure per particle is instead available in COmPACT and SuperCOmPACT format, containing the particle type, four-momentum, production and decay vertex.

In order to improve the agreement between data and MC, a correction is applied only to simulated events, reproducing the non-Gaussian tails in the energy resolution of the LKr due to hadronic showers induced by a photon. The total probability and the parametrisation of the energy loss as a function of the photon energy has been extracted from K_{e3} data [106]. On the other hand the energy sharing and energy baseline corrections described in Section 5.2.1 are not applied. The track momentum correction was not yet implemented for MC, but should in principle be applied, since the distortions have been included into the simulation.

6.4.1. The generated four-momenta in SuperCOmPACT

The four-momenta of the generated particles are saved in a SuperCOmPACT structure, but only after the boost into the laboratory frame. Therefore the true values can be used to compute the kinematic variables of the event, but they have a limited numerical precision due to the conversion to integer values (see Section 5.2.4) and to the boost of the decay products back to the rest frame of the kaon. The precision of this procedure has been studied on a sample of simulated K_{e4} decays where the true values of the kinematic variables were saved as well as the boosted four-momenta. Significant discrepancies have been found only for events with s_e below 100 (MeV/ c^2)² [121].

7. Event selection and reconstruction

7.1. Data and MC samples

The data sample collected in 2003 and 2004 was divided into so-called “Super-Samples” (SS), i.e. samples of consecutive runs containing all the four possible configurations of magnetic fields in the spectrometer and in the achromat. For the present analysis, the data of SS 1, 2 and 3 have been used, corresponding to about one month of data taking in 2003. This sample was chosen as a clean and well understood set of data and was expected to contain about as much statistics as the data used for the analysis published by the BNL collaboration [35].

The following MC samples were generated as described in Chapter 6 and analysed for background and acceptance estimates:

- 325 million $K_{3\pi}$ events, where pions were only allowed to decay into $\mu\nu$. The number of selected events corresponds to about 1/10 of the data statistics
- 4 million $K_{3\pi}$ events with pions allowed only to decay into $e\nu$, corresponding to about ten times the data statistics
- 160 million $K_{2\pi D}$ events. After the selection this sample contains about as much statistics as the data
- 26 million $K_{\pi\pi^0\pi_D^0}$, roughly the same as the data statistics
- 82 million K_{e4} events, i.e. more than 40 times the data statistics.

7.2. Selection criteria

As far as possible, the selection criteria were optimised using signal and background MC, in order to obtain a high acceptance and a low background contamination. Timing and particle identification cuts were tested on clean data samples, since the MC contains no timing information and shows significant discrepancies from the data in the electromagnetic showers.

The two control channels $K_{3\pi}$ and $K_{2\pi D}$ are used to test the agreement between data and MC in the variables that are critical for the measurement of the form factors. Therefore it is particularly important to keep the selection of the signal and control events as similar as possible. For example, the vertex selection is identical for the channels listed above, since they all have a three track vertex.

7.2.1. Pre-selection

In order to reduce the sample of events to be analysed, some simple requests are applied at the very beginning of the selection:

- the trigger word must contain bit 0 or bit 1 or bit 4 (MBX trigger)
- the bad bursts for DCH, LKr, MBX, MUV and physics are rejected
- the event must contain at least three reconstructed tracks
- at least one combination of three tracks must build a vertex, i.e. they are generated by the same decay
- for K_{e4} decays only: in the LKr at least one cluster must have been reconstructed (for the electron)
- for $K_{2\pi D}$ decays only: in the LKr at least three clusters must have been reconstructed (one electron, one positron and one photon in the Dalitz decay of the π^0).

7.2.2. Vertex selection

Before looking for a good vertex, the ghost tracks are flagged, so that they can be ignored in the rest of the selection. For this purpose, all pairs of tracks are considered and, if the distance between them at DCH1 is less than 1 cm, the track with the worst quality is flagged as ghost track. Vertices containing one or more ghost tracks are rejected.

Each of the three tracks building the vertex must have:

- quality (see Section 5.1.2 for the definition) greater than 0.8
- momentum between 2 and 50 GeV/c
- distance to all other non-ghost tracks greater than 2 cm at DCH1
- radial distance from the centre of the beam pipe greater than 12 cm at DCH1
- radial distance of the extrapolated position at the LKr from the centre of the beam pipe between 15 and 113 cm
- no hit in MUV associated to the track within 4 ns if the time measurement of the hodoscope is available, within 8 ns otherwise.

The momentum range is wide enough to contain pions and electrons produced in the decay of a kaon with a momentum of about $60 \text{ GeV}/c$. Below $2 \text{ GeV}/c$ the momentum measurement is not precise enough. The momenta are not corrected with the α and β parameters (see Section 5.2.1) neither in data, nor in MC, since the parameter values to be used for the MC were not yet available. Tracks closer than 2 cm at DCH1 are normally produced by photon conversions in the Kevlar window and must be rejected. The radial cuts at DCH1 and in the extrapolation to the LKr assure that the track is well contained in the detector and that no associated cluster was missed.

Events with a pion decaying in flight into a muon and a neutrino are a dangerous background source for K_{e4} decays, since they have a high transverse momentum. Therefore tracks must not have a hit in the MUV associated to it in space and time. Due to this cut, about 5% of the K_{e4} statistics is rejected. For consistency, the same cut is applied also to the other channels. The acceptance loss is proportional to the number of pions produced in the decay.

Further selection criteria are applied to the vertex, in order to assure that the three tracks actually come from the same kaon decay and to define the decay region in z :

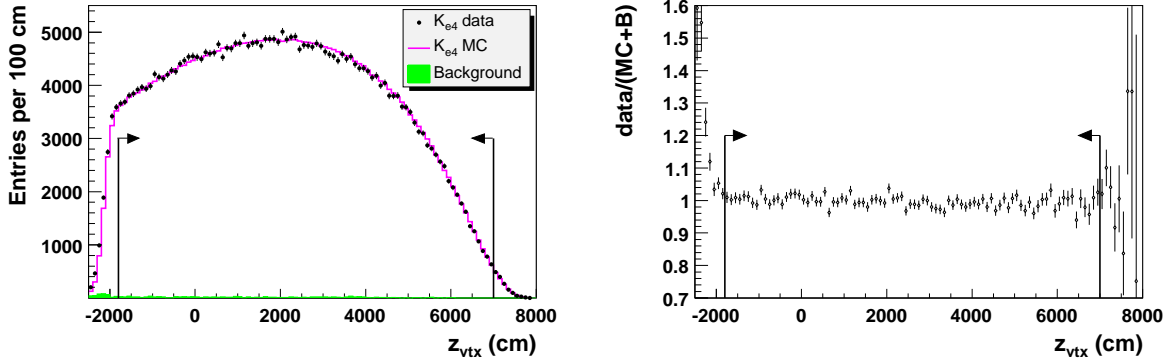


Figure 7.1.: z position of the decay vertex for data (black points), K_{e4} MC (magenta open histogram) and background estimated from the wrong sign events (green filled histogram) in linear scale (left). The MC distribution is normalised to the difference between data and background. Ratio between the data and the sum of MC and background (right). The complete K_{e4} selection, except the cut on the z coordinate of the decay vertex, is applied. The signal region is indicated by the arrows.

- the sum of the track charges must be $+1$ or -1
- the three tracks building the vertex must be within 2 ns of their average time, if the hodoscope time is available for all the tracks. Otherwise, the DCH times are compared and the accepted time window is ± 6 ns around the average time. The “vertex time” is defined as the average time of the three tracks
- any non-ghost track in the event, not belonging to the considered vertex, must be outside of the time windows around the vertex time defined above
- the z coordinate of the decay vertex must be between -18 and 70 m
- the radial position of the decay vertex must be less than 5 cm away from the beam axis
- the χ^2 of the vertex fit (see Section 5.2.2) must be less than 20
- any AKL hit must be outside of a time window of ± 3 ns around the vertex time
- out of the three considered tracks, three two-track vertices can be built. The minimum distance between any pair of them must be less than 2.5 m.

The choice of the accepted decay region is based on the necessity to have good agreement between data and MC (see Figure 7.1). The agreement is not perfect at the collimator due to the simulation itself and to the background from particles deflected at the edge of the collimator.

In order to avoid differences in the event topology between data and MC, the cut against AKL hits in time with the event, present in the trigger, has been repeated offline. This cut is useful to reduce the background from events with high transverse momentum.

For events with a big distance between the two-track vertices, the trigger efficiency drops very fast. On the other hand, the agreement between data and MC in this distribution is not good enough to allow for a correction of the MC. Therefore these events, corresponding to about 6% of the statistics, are rejected (see Section 8.3.1).

If more than one vertex in the event fulfils all the selection criteria, the one with the lowest χ^2 is kept.

7.2.3. Particle identification

For the pion and electron ID, a loose and a tight selection are defined: the tight selection is used to reduce the background level, while the loose one produces an unbiased sample useful to compute the efficiency of the tight selection, for example for comparisons between data and MC. The particle identification efficiencies are measured on clean samples of events, selected with simple criteria based on the kinematic constraints (see Sections 7.3.2 and 7.3.3). In the description of the tight selection, only the additional criteria to the loose one are listed.

The main difference between pions and electrons is the fraction of energy deposited in the LKr, that is expected to be about 1 (in units of c) for electrons and less for pions. In order to estimate this fraction, it has first of all to be checked if a cluster in the calorimeter is associated to the track. This is the case if a cluster is within 5 cm of the projected position of the track to the LKr. Then the variable E/p is defined as the ratio between the energy of the cluster associated to the track and the track momentum. The E/p distributions for pions and electrons in the data are shown in Figure 7.2.

Only the tracks building the selected vertex can be identified as pions or electrons.

Loose pion ID

Tracks with a momentum greater than $5 \text{ GeV}/c$ are assumed to be pions.

This assumption is justified in case of kinematically very clean samples, as is the case for $K_{3\pi}$ events.

Tight pion ID

A track is identified as a pion if one of the following conditions is fulfilled:

- no cluster is associated to the track
- a cluster is associated to the track, but the time difference between cluster and track is greater than 7 ns if the hodoscope time is available for the track, greater than 10 ns otherwise
- a cluster is associated to the track, its time is within the time windows defined above and E/p is less than $0.8 c$. In order to assure that the low E/p is not due to mis-measurements in the LKr, it is also required that the cluster has a distance of at least 2 cm from the closest dead cell and that its radial position is between 15 and 113 cm from the centre of the beam pipe.

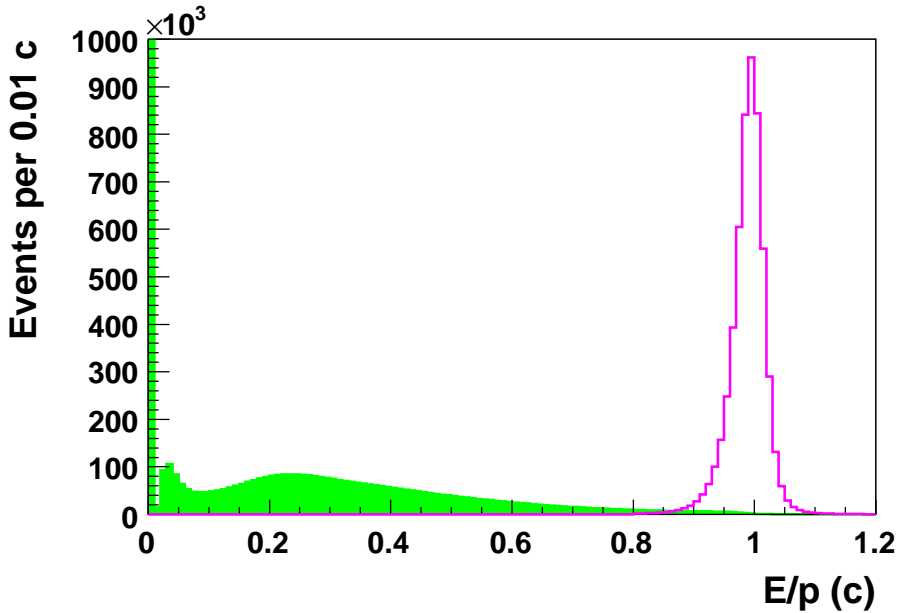


Figure 7.2.: E/p distribution for pions from $K_{3\pi}$ data with complete kinematic selection and loose pion ID (green filled histogram) and for electrons from $K_{2\pi D}$ data with complete kinematic selection, tight pion ID, loose ID for the considered electron and tight ID for the other one (magenta open histogram). The first bin contains about 1.6 million pions without any associated cluster. The two distributions were normalised to the same area.

Loose electron ID

In the case of negligible background levels from pion mis-identification, as in $K_{2\pi D}$ decays, an electron is identified whenever a track has an associated cluster with at least 80% of the expected energy. The detailed requirements are:

- a cluster associated to the track
- time of the cluster within the same time windows around the track time as for the tight pion ID
- distance of the cluster to the closest dead cell greater than 2 cm
- radial position of the cluster between 15 and 113 cm from the centre of the beam pipe
- E/p greater than $0.8 c$.

Tight electron ID

In addition to the requirements of the loose selection, in the tight one, the following selection criteria are applied:

- E/p greater than $0.9 c$ and less than $1.1 c$

- distance of the candidate cluster to the extrapolated position in the LKr of any other cluster in the event greater than 10 cm
- distance of the candidate cluster to any non-ghost track in the event (except the associated one) greater than 20 cm
- cluster energy greater than 3 GeV.

A too high E/p is mainly due to the wrong association between track and cluster or to a momentum mis-measurement, therefore also an upper cut is applied. Clusters closer than 10 cm to each other cannot be distinguished well enough. Because of shower fluctuations, a pion track can produce clusters also far away from its impact point in the LKr, therefore the distance to the pion track must be big enough to reduce the probability of overlapping. The energy resolution below 3 GeV drops fast and the measurement is subject to large non-linear effects, therefore no clusters below 3 GeV are accepted.

Linear Discriminant Analysis (LDA)

Since about 1% of the pions would survive the tight electron identification described above, a Linear Discriminant Analysis [122] is added to the selection criteria for K_{e4} events. The linear discriminant analysis is a step-wise method that allows to identify the variables with the highest discriminating power and to build an optimised linear combination out of them.

The LDA used for the electron identification in this analysis is based on three variables: E/p , the radial cluster width ($\text{RMS}_r = \sqrt{\text{RMS}_x^2 + \text{RMS}_y^2}$) and the normalised radial distance between track and cluster ($d_n = d \cdot \sqrt{p}$, where d is the distance between the cluster and the track position extrapolated to the LKr and p the track momentum). Assigning different weights to these variables, the quantity y can be defined as

$$y = 39.49729 - 82.20312 \cdot E/p + 32.76240 \cdot \text{RMS}_r + 1.597024 \cdot d_n, \quad (7.1)$$

where E/p is measured in units of c , RMS_r in units of the LKr cell width (2 cm) and d_n in $\text{cm} \cdot \sqrt{\text{GeV}/c}$. The LDA is a function $f(y)$ that can be applied to any track with an associated cluster and returns as output a number close to 1 for electrons (see Figure 7.3):

$$f(y) = 1.000964 - 0.9863838 \cdot \frac{1}{1 + e^{-y}} \quad (7.2)$$

For the selection of K_{e4} events, the LDA output for the electron candidate is required to be greater than 0.9, which causes a loss in the acceptance of about 2%.

7.2.4. Differences in the MC selection

In general, the same selection is applied to data and MC events, with the exception of

- trigger mask: a trigger simulation is available, but was not used in the analysis presented here. Instead, the trigger efficiency is determined from data and applied to the MC as a correction.
- timing cuts: accidentals are not included in the simulation
- LDA: instead of applying it as a selection criterion, the events are reweighted with its efficiency as a function of the electron momentum (see Figure 7.3).

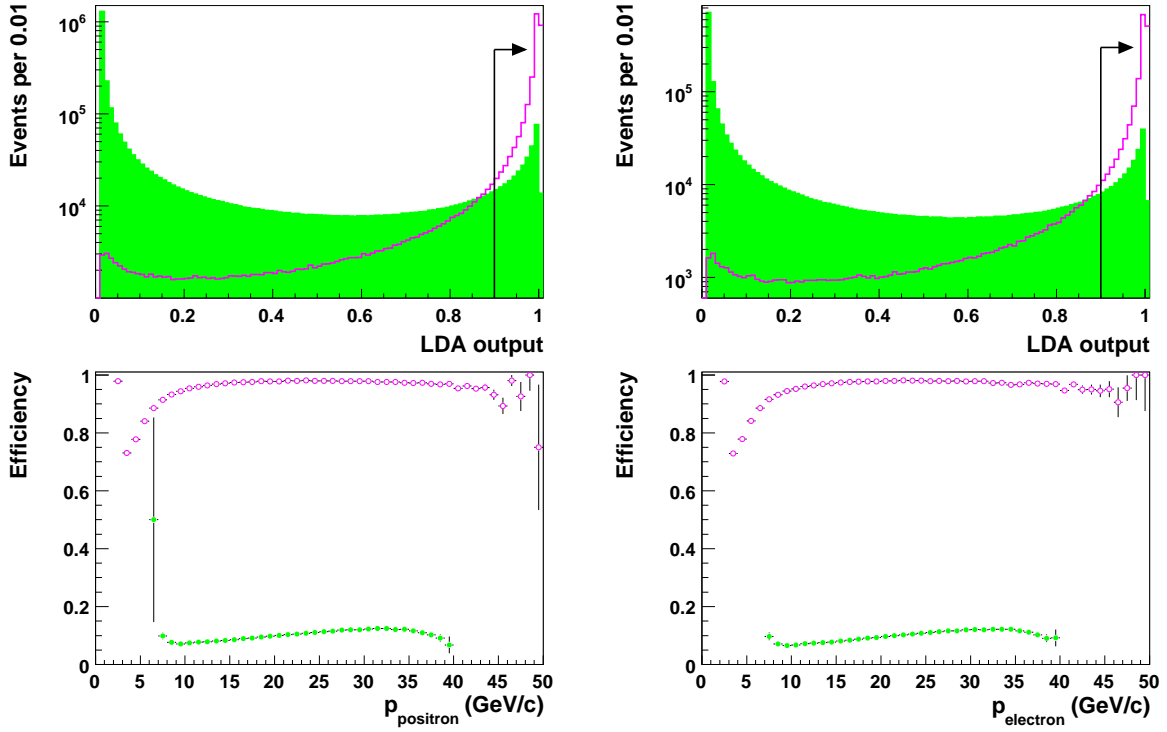


Figure 7.3.: LDA output (upper plots) in logarithmic scale for π^+ (left) and π^- (right) from $K_{3\pi}$ data with complete kinematic selection and tight electron ID (green filled histogram) and for e^+ (left) and e^- (right) from $K_{2\pi D}$ data with complete kinematic selection, tight pion ID and tight electron ID (magenta open histogram). The signal region is indicated by the arrow.

Efficiency of the selection criterion LDA output > 0.9 (lower plots) for π^+ (left) and π^- (right) from $K_{3\pi}$ data with complete kinematic selection and tight electron ID (green filled circles) and for e^+ (left) and e^- (right) from $K_{2\pi D}$ data with complete kinematic selection, tight pion ID and tight electron ID (magenta open circles).

7.3. Event reconstruction and background rejection

Further selection criteria, mainly based on kinematic constraints, are applied to each decay channel in order to obtain a clean signal. They will be presented in the following Sections. A summary of the selected events, acceptance and background contamination at each stage can be found in Tables 7.1–7.2. While $K_{3\pi}$ and $K_{2\pi D}$ events are assumed to be background free, for K_{e4} decays, the background is estimated using the so-called “wrong sign” events, as described in Section 7.4.1.

7.3.1. K_{e4} events

An event with a good vertex and total charge q can be selected as a K_{e4} , if it fulfils the following criteria:

- one track with charge q is identified as an electron with tight ID and LDA
- one track with charge q and one with charge $-q$ are identified as pions with tight ID
- no LKr clusters with an energy greater than 3 GeV and a distance to any track of the vertex greater than 20 cm are inside a time window of ± 7 ns around the vertex time, if the hodoscope time is available for all tracks, of ± 10 ns otherwise.

The cut against extra clusters in the LKr is used to reduce the background from $K_{2\pi D}$ and $K_{\pi\pi^0\pi^0_D}$ decays (see Sections 7.4.5 and 7.4.6), which consist of the same number of charged particles as K_{e4} , but contain also photons. Clusters with very low energy or close to a track are not considered as photon candidates, since they could be originated by shower fluctuations produced by the pions.

The four-momenta of the decay products are then computed, using for the pion and the electron momenta the slopes of the tracks at the vertex (output parameters of the Kalman filter, see Section 5.2.2) and imposing the nominal masses to determine the energy. The neutrino momentum is obtained as the difference between the momentum of the kaon and that of the “visible” (detected) particles (π^+ , π^- and e^\pm), where the kaon is assumed to fly along the z -axis and to have a momentum of $60 \text{ GeV}/c$. The neutrino energy is computed assuming its mass to be zero. Finally, the following requirements are applied to reduce the background contamination:

- the invariant mass of the $K^\pm - \pi^\pm$ system (“missing mass”), where the kaon is assumed to fly along the z -axis with a momentum of $60 \text{ GeV}/c$, must be greater than $0.18 \text{ GeV}/c^2$
- in the plane $m_{3\pi}$ (invariant mass of the $\pi\pi e$ system, with the energy of the electron computed assuming the pion mass) vs. p_T (transverse momentum of the three visible particles), the events within an ellipse centred at $(0, M_K)$ with semi-axes $25 \text{ MeV}/c$ and $10 \text{ MeV}/c^2$ are rejected
- the invariant mass of the $\pi\pi e\nu$ system ($m_{K_{e4}}$) must be within $20 \text{ MeV}/c^2$ of the nominal kaon mass.

The missing mass cut rejects the few remaining $K_{2\pi D}$ background events (see Section 7.4.5 and Figure 7.4) with a negligible loss in the K_{e4} acceptance, while the ellipse cut reduces the background from $K_{3\pi}$ decays with pion mis-identification (see Section 7.4.4) with a loss of about 1% of the K_{e4} statistics (see Figure 7.5). The kaon mass cut is used to reject further $K_{3\pi}$ background. The poor resolution in the invariant mass, due to the undetected neutrino, together with the necessity of applying a tight cut to reduce the background contamination (see Figure 7.6), produces a statistics loss of about 17%, mainly for events with a kaon momentum far from $60 \text{ GeV}/c$.

In the analysed data sample, 342,859 K_{e4} candidates were selected, including the background contamination that will be estimated below. The acceptance of the complete selection is estimated from MC to be about 18%, taking into account the LDA efficiency, but without corrections for those selection criteria where small discrepancies are expected between data and MC.

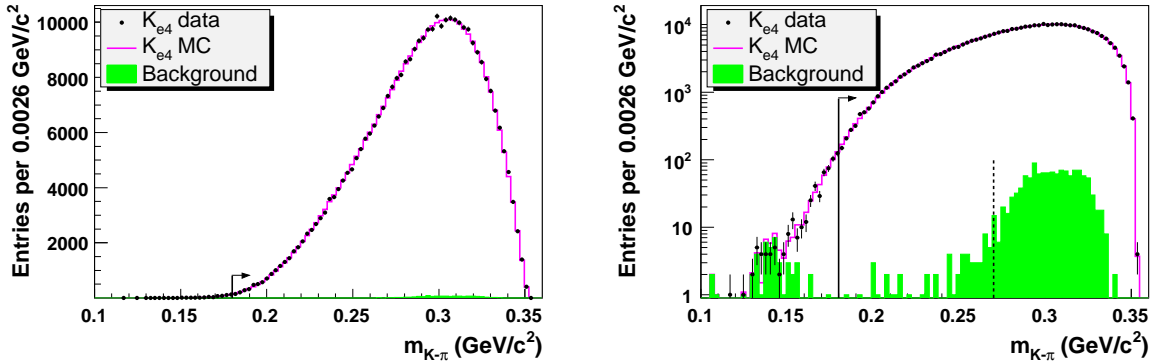


Figure 7.4.: Invariant mass of the $K^\pm - \pi^\pm$ system for data (black points), K_{e4} MC (magenta open histogram) and background estimated from the wrong sign events (green filled histogram) in linear (left) and logarithmic (right) scale. For the wrong sign events the closest value to the nominal π^0 mass was chosen. The complete K_{e4} selection, except the missing mass cut, is applied. The signal region is indicated by the solid line. Wrong sign events on the right side of the dashed line are scaled by a factor of two. The MC distribution is normalised to the difference between data and background.

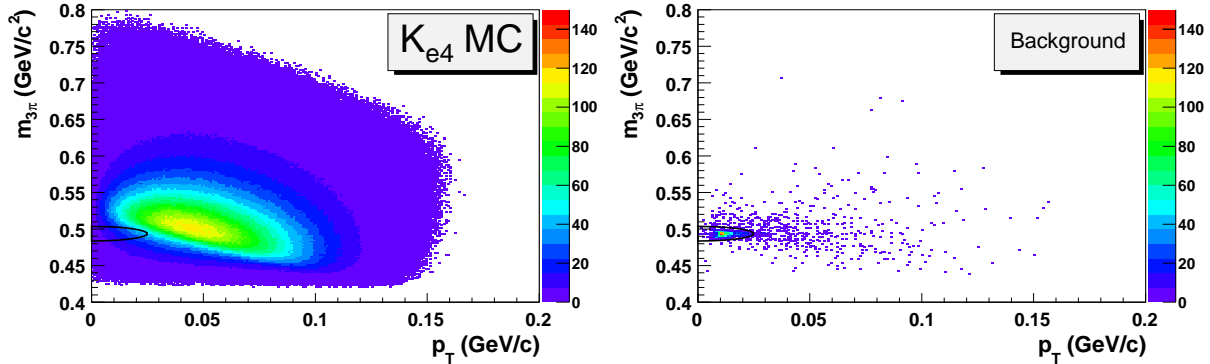


Figure 7.5.: $m_{3\pi}$ vs. p_T plane for K_{e4} MC (left) normalised to the number of signal events in the data and background estimated from the wrong sign events (right). The complete K_{e4} selection, except the cut in this plane, is applied. The signal region is outside the ellipse.

7.3.2. $K_{3\pi}$ events

Since the $K_{3\pi}$ decay channel has a negligible background, the requirement of a good vertex and the fulfilling of kinematic constraints is sufficient to obtain a clean sample:

- the three tracks building the vertex must be identified as pions with loose ID
- the transverse momentum (p_T) of the three pions must be less than 25 MeV/ c
- the total momentum (p_K) of the three pions must be between 50 and 70 GeV/ c

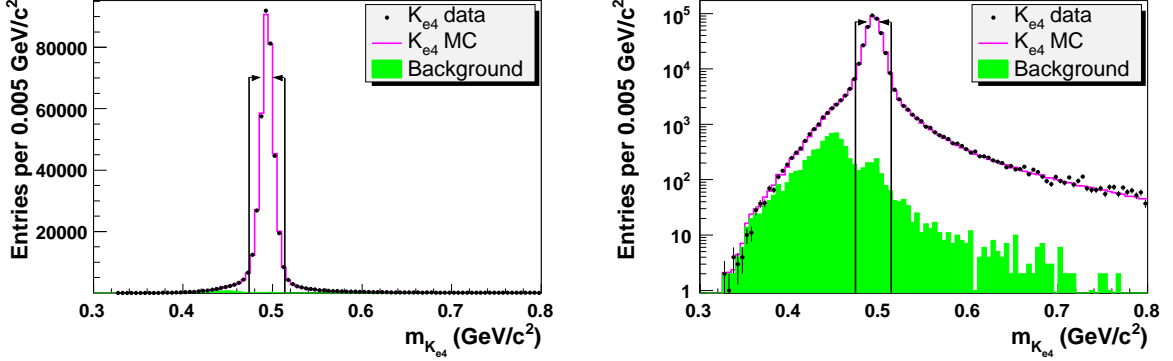


Figure 7.6.: Invariant mass of the $\pi\pi\epsilon\nu$ system for data (black points), K_{e4} MC (magenta open histogram) and background estimated from the wrong sign events (green filled histogram) in linear (left) and logarithmic (right) scale. The complete K_{e4} selection, except the $m_{K_{e4}}$ cut, is applied. The signal region is indicated by the lines. The MC distribution is normalised to the difference between data and background.

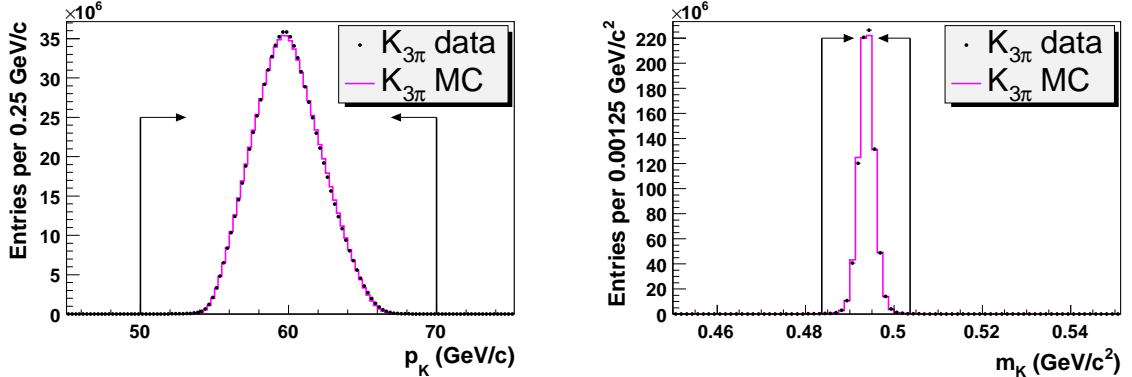


Figure 7.7.: Kaon momentum (left) and invariant mass (right) for data (black points) and $K_{3\pi}$ MC (open magenta histogram). The complete selection, apart from the cut in the shown variable, is applied. The signal region is indicated by the lines. The MC distribution is normalised to the data.

- the invariant mass ($m_{3\pi}$) of the three pion system must be within $10 \text{ MeV}/c^2$ of the nominal kaon mass.

The sample of $K_{3\pi}$ data obtained from the selection described above consists of about 827 million events and is used as a control channel to measure the trigger efficiency and as a huge sample of clean and unbiased pions, to measure the ID efficiencies. The kaon momentum and invariant mass distributions for data and MC are shown in Figure 7.7

7.3.3. $K_{2\pi D}$ events

Due to the additional constraint of the π^0 mass, the $K_{2\pi D}$ events can also be selected very cleanly, without applying strong requirements on the particle identification. The following

selection criteria are applied to the events where a vertex with charge q was selected:

- one track with charge q must be identified as a pion with tight ID
- one track with charge q and one with charge $-q$ must be identified as electron and positron with loose ID
- one LKr cluster must be selected as a photon, i.e. it must have
 - energy greater than 3 GeV
 - distance from the closest dead cell greater than 2 cm
 - distance to any other cluster in the LKr greater than 10 cm
 - distance to the position of any non-ghost track extrapolated to the LKr greater than 20 cm
 - radial distance from the beam axis between 15 and 113 cm
 - absolute value of the time difference to the vertex time less than 7 ns, if the vertex time was computed from the hodoscope times of the tracks, less than 10 ns otherwise
- invariant mass of the $ee\gamma$ system (m_{π^0}) within $10 \text{ MeV}/c^2$ of the nominal π^0 mass
- p_T of the $\pi ee\gamma$ system less than 25 MeV/c
- total momentum (p_K) of the four particles between 50 and 70 GeV/c
- invariant mass (m_K) of the reconstructed decay products within $20 \text{ MeV}/c^2$ of the nominal kaon mass.

About 7 million events were selected in the analysed data sample, applying the criteria listed above. For the efficiency measurement of the tight electron ID and of the LDA, only the electron with charge q is left unbiased and selected with the loose ID, while the sample is further cleaned by applying the tight ID to the track with charge $-q$.

7.4. Background estimate

The background contamination of the selected K_{e4} events is expected to be dominated by $K_{3\pi}$ events and to amount to less than 10^{-2} of the statistics, due to the high rejection power of the LDA and of the kinematic cuts.

Two methods allow for a precise estimate of the residual background: the selection of “wrong sign” events ($\pi^\pm\pi^\pm e^\mp \bar{\nu}_e^{(-)}$) in the data and the sum of the expected contributions of different channels from the MC simulation. The difference between the estimates of the two methods indicates the size of the systematic uncertainty on the background expectation.

7.4.1. “Wrong sign” events

Since the branching ratio of the $K_{e4}^{\Delta S=-\Delta Q}$ decay is expected to be about 10^{-10} times the one of the K_{e4} decay, no events with the signature $\pi^\pm\pi^\pm e^\mp \nu_e^\mp$ (called “wrong sign” events, because the electron has the “wrong” charge with respect to the kaon) are expected to be correctly reconstructed kaon decays. On the other hand, positive and negative pions have roughly the same probability to be mis-identified as a positron or an electron, respectively. The same argument is also valid for electrons and positron mis-identified as pions. Therefore, the number of $\pi^\pm\pi^\pm e^\mp \nu_e^\mp$ events in the data corresponds to the background contamination of the K_{e4} events times the relative mis-identification probability. As a first approximation, the wrong sign events produced by $K_{2\pi D}$ and $K_{\pi\pi^0\pi_D^0}$ decays do not need any rescaling, while the ones from $K_{3\pi}$ have to be multiplied by a factor of two. In order to distinguish between the two background classes, the missing mass is computed with each of the pions and the one closer to the nominal π^0 mass is considered. If this value is greater than $0.27 \text{ GeV}/c^2$, the wrong sign event is rescaled with a factor of two.

The selection of the wrong sign events is identical to the K_{e4} selection, apart from the application of the tight electron ID and of the LDA to the track with opposite charge with respect to the vertex. The two tracks with the same charge have to fulfil the tight pion ID.

With this method, a total background contamination (B) of $1,153 \pm 46 \text{ (stat)}$ events was estimated, corresponding to about 0.3% of the signal.

7.4.2. Accidental background

The main contribution to the accidental background is expected to come from the combination of two pions from a $K_{3\pi}$ decay and an electron from a K_{e3} decay, taking place at the same time. The following cases have to be considered:

$$\begin{array}{llll}
 a) & \left. \begin{array}{l} K^+ \rightarrow \pi^+ \pi^+ (\pi^-) \\ K^- \rightarrow (\pi^0) e^- (\bar{\nu}) \end{array} \right\} & \pi^+ \pi^+ e^- & \text{wrong sign (+)} \\
 b) & \left. \begin{array}{l} K^+ \rightarrow \pi^+ \pi^- (\pi^+) \\ K^+ \rightarrow (\pi^0) e^+ (\nu) \end{array} \right\} & \pi^+ \pi^- e^+ & K_{e4}^+ \\
 c) & \left. \begin{array}{l} K^- \rightarrow \pi^+ \pi^- (\pi^-) \\ K^+ \rightarrow (\pi^0) e^+ (\nu) \end{array} \right\} & \pi^+ \pi^- e^+ & K_{e4}^+ \\
 d) & \left. \begin{array}{l} K^- \rightarrow \pi^- \pi^- (\pi^+) \\ K^+ \rightarrow (\pi^0) e^+ (\nu) \end{array} \right\} & \pi^- \pi^- e^+ & \text{wrong sign (-)} \\
 e) & \left. \begin{array}{l} K^- \rightarrow \pi^- \pi^+ (\pi^-) \\ K^- \rightarrow (\pi^0) e^- (\bar{\nu}) \end{array} \right\} & \pi^- \pi^+ e^- & K_{e4}^- \\
 f) & \left. \begin{array}{l} K^+ \rightarrow \pi^- \pi^+ (\pi^+) \\ K^- \rightarrow (\pi^0) e^- (\bar{\nu}) \end{array} \right\} & \pi^- \pi^+ e^- & K_{e4}^-
 \end{array} \tag{7.3}$$

In the second column the pairs of original decays are indicated, the undetected particles are in parentheses. The detected particles are listed in the third column and the kind of event that can be reconstructed out of them in the fourth one.

Assuming the same geometrical acceptance for K^+ and K^- decays, the same probability for the loss of each pion (i.e. the probability to detect both even pions is half of the probability

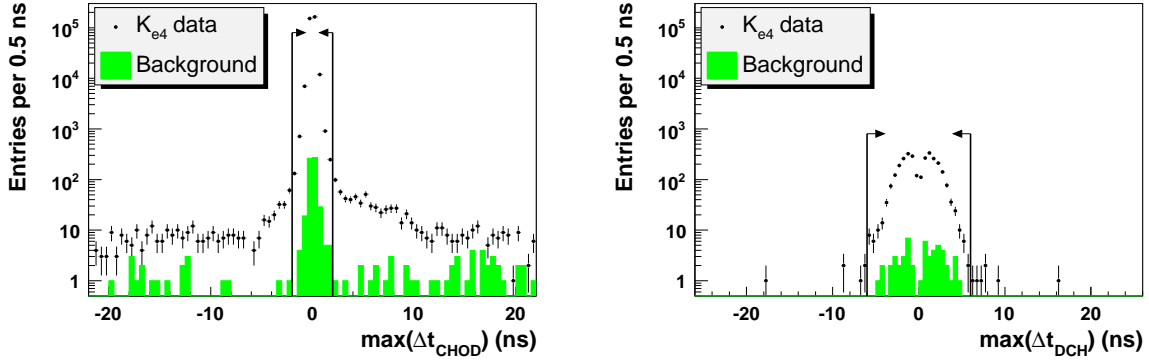


Figure 7.8.: Time difference between track and vertex for data (black points) and non-scaled wrong sign events (green filled histogram) measured with the CHOD (left) or the DCH (right). The complete K_{e4} selection is applied with a wider allowed window for the time difference between track and vertex. The signal regions are indicated by the arrows.

to detect one even and one odd pion from the same $K_{3\pi}$ decay) and the intensity of the K^+ beam to be exactly 1.8 times higher than the one of the K^- beam, the following relations can be extracted:

$$\begin{aligned}
 P_b &= 2 \cdot 1.8 \cdot P_a, \\
 P_c &= 2 \cdot P_a, \\
 P_d &= P_a \\
 P_e &= 2 \cdot 0.56 \cdot P_d = 2 \cdot 0.56 \cdot P_a \\
 P_f &= 2 \cdot P_d = 2 \cdot P_a.
 \end{aligned} \tag{7.4}$$

It follows that the probability to accidentally reconstruct a K_{e4} event is about 4.4 times higher than the one to reconstruct a wrong sign event, considering K^+ and K^- events together.

The size of the accidental background can be estimated by relaxing the cut on the time difference between track and vertex and comparing the sidebands of the time difference distribution with the signal region (see Figure 7.8). The number of events in the sidebands is supposed to consist of resolution tails, proportional to the number of events in the signal region, and of accidental background:

$$\begin{cases} N_{SB}^W = B + r \cdot N^W \\ N_{SB} = 4.4 \cdot B + r \cdot N \end{cases}, \tag{7.5}$$

where N_{SB} is the number of K_{e4} candidates in the sidebands, N the number of K_{e4} candidates in the signal region, B the expected background contribution and r the proportionality constant between resolution tails and number of events in the signal region. The superscript W indicates wrong sign events.

Reading the values of the various N s from the distributions shown in Figure 7.8 and determining r and B for each of the two time distributions separately, the expected contribution from the accidental background consists of 27^{+5}_{-4} (stat) K_{e4} events, while r is of the order of

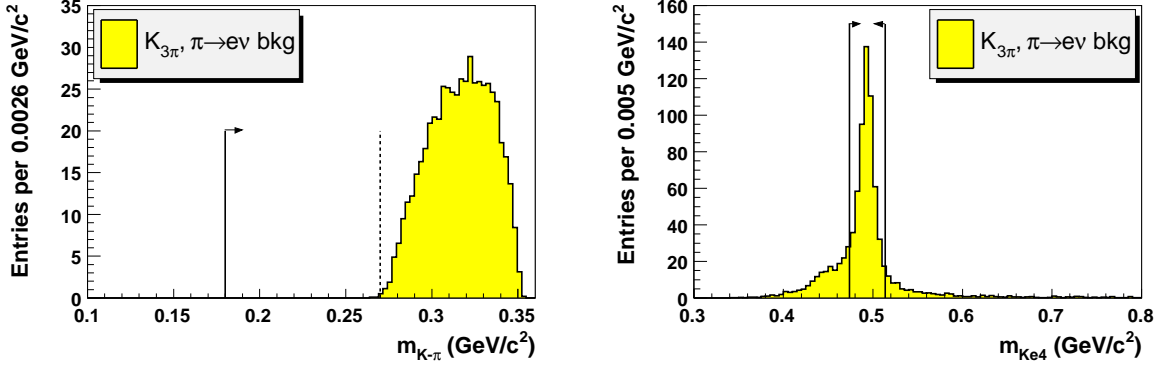


Figure 7.9.: Missing mass (left) and $m_{K_{e4}}$ (right) distributions for the expected background contamination from $K_{3\pi}$ events with a pion decaying to $e\nu$. The estimate has been performed using MC events with complete K_{e4} selection, except the cut on the displayed variable. The distribution are normalised to $K_{3\pi}$ decays, according to the $\pi \rightarrow e\nu$ branching ratio. The solid lines indicate the signal region, while the dashed line separates the regions where different scaling factors are applied to the wrong sign events.

10^{-3} . Since not all the events in the tails of the time distribution are actually background events, it is not possible to obtain an expected distribution, for example in $m_{K_{e4}}$. If the assumption on its origin is correct, the accidental background is supposed to have values of the missing mass above the 2π threshold and to be flatly distributed in $m_{K_{e4}}$.

7.4.3. $K_{3\pi}$ with $\pi \rightarrow e\nu$

The decay $K_{3\pi}$ with a pion decaying in flight into $e\nu$ can not be easily distinguished from K_{e4} , since in both cases the invariant mass corresponds to the nominal kaon mass (see Figure 7.9) and the presence of a neutrino assures a high transverse momentum. On the other hand, the branching ratio of the $\pi \rightarrow e\nu$ decay is $(1.230 \pm 0.004) \times 10^{-4}$ [13] and the probability that a pion decays in flight before the end of the magnetic spectrometer is of the order of a few percent, so that the background contamination from this channel is expected to be at most a few times 10^{-3} of the signal.

Applying the complete K_{e4} selection to MC events, including the LDA efficiency determined from the data, the expectation value of the background contamination was estimated to be 544 ± 7 (stat) ± 2 (syst) events, with a scaling factor with respect to the wrong sign events of the same MC sample compatible with two. All the selected events have values of the missing mass above 0.27 GeV/c^2 , i.e. they are in the region where the background is assumed to consist mainly of $K_{3\pi}$ events. The systematic uncertainty on the estimate is dominated by the uncertainty on the branching ratio measurement used for the scaling.

7.4.4. $K_{3\pi}$ with pion mis-identification

The background from $K_{3\pi}$ decays, where one even pion is mis-identified as an electron, is the most dangerous one, since the $K_{3\pi}$ branching ratio is more than 1000 times higher than the

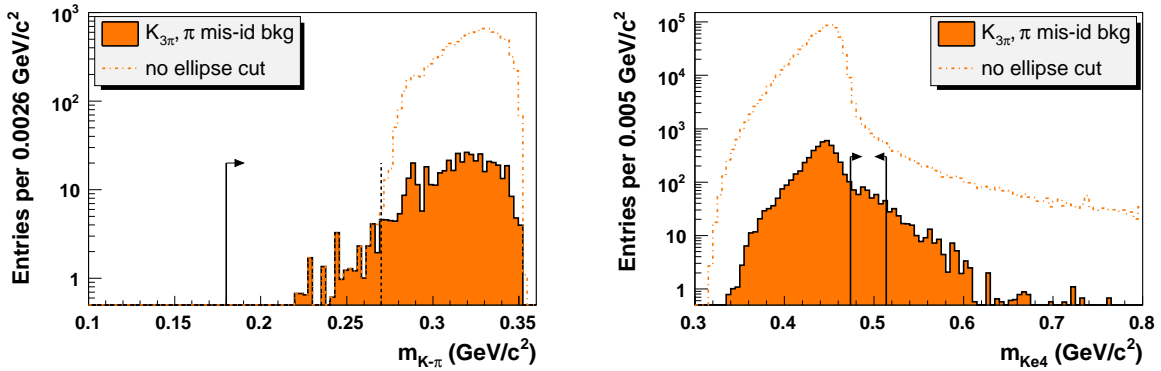


Figure 7.10.: Missing mass (left) and m_{Ke4} (right) distributions for the expected background contamination from $K_{3\pi}$ events with a pion mis-identified as electron. The estimate has been performed using MC events with complete K_{e4} selection, except the cut on the displayed variable (filled histogram) and without the elliptical cut in the $m_{3\pi}$ vs. p_T plane (open histogram). Corrections and particle identification efficiencies computed from the data have been applied. The distributions are normalised to the kaon flux. The solid lines indicate the signal region, while the dashed line separates the regions where different scaling factors are applied to the wrong sign events.

one of the K_{e4} decay and about 1% of the pions are identified as electrons by the tight electron ID. Without any further reduction the signal to background ratio would be worse than one to ten. A significant reduction of the background contamination is obtained with the LDA cut, that rejects about 89% of the $K_{3\pi}$ events (the rejection power of a cut is estimated after applying all the other selection criteria). The most important rejection criteria are otherwise the elliptical cut in the $m_{3\pi}$ vs. p_T plane (95%) and the m_{Ke4} cut (96%), as shown in Figure 7.10.

$K_{3\pi}$ MC events were selected as K_{e4} decays, requiring only the loose ID for the electron. The mis-identification probabilities for pions to be selected by the loose electron ID, tight electron ID and LDA, respectively, were measured in a high statistics sample of selected $K_{3\pi}$ data with loose pion ID, as a function of the pion momentum. For the loose electron ID, the mis-identification probability was also determined in selected $K_{3\pi}$ MC events. A correction for the loose electron ID was computed from the ratio of the probabilities for data and MC and applied to the MC events selected as K_{e4} , together with the efficiencies for tight ID and LDA from the data. Furthermore, an overall correction for the different probability in data and MC for a $K_{3\pi}$ event to be outside of the ellipse in the $m_{3\pi}$ vs. p_T plane was applied.

The background contribution from $K_{3\pi}$ decays with a mis-identified pion was estimated to be of 501 ± 19 (stat) ± 1 (syst) events. This is a factor of 2.33 ± 0.15 (stat) ± 0.01 (syst) more than the wrong sign events selected in the same MC sample. The discrepancy from the expected factor of two is due to the different rejection power of the LDA cut for π^+ and π^- (see Figure 7.3). Most of the events have a missing mass greater than $0.27 \text{ GeV}/c^2$, with the exception of a small resolution tail.

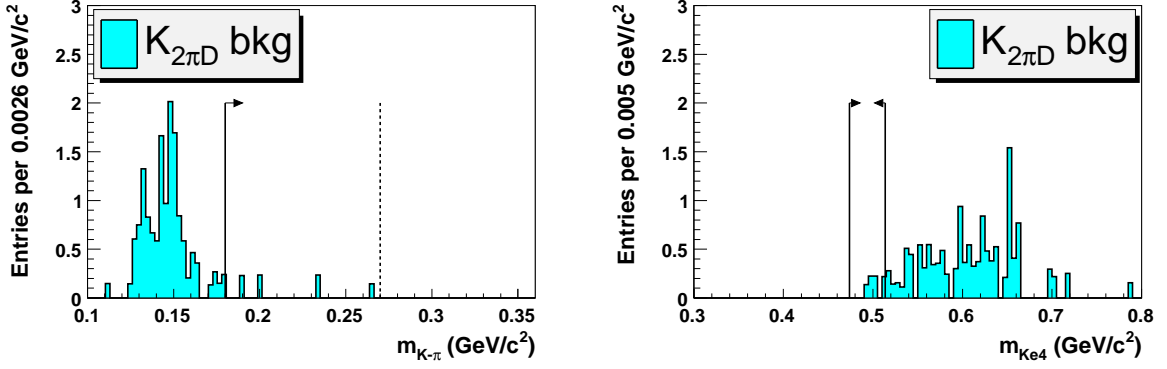


Figure 7.11.: Missing mass (left) and m_{Ke4} (right) distributions for the expected background contamination from $K_{2\pi D}$ events with an electron mis-identified as a pion. The estimate has been performed using MC events with complete K_{e4} selection, except the cut on the displayed variable. Corrections and efficiencies computed from the data have been applied. The distributions are normalised to the kaon flux. The solid lines indicate the signal region, while the dashed line separates the regions where different scaling factors are applied to the wrong sign events.

7.4.5. $K_{2\pi D}$

A $K_{2\pi D}$ event can be selected as a K_{e4} candidate, if an electron is mis-identified as a pion with the tight ID. The $K_{2\pi D}$ branching ratio is about 60 times higher than the K_{e4} branching ratio, while the mis-identification probability of an electron into a pion, selected with the tight ID, is of the order of 0.1%. Therefore the background contribution from this channel would be of a few percent, if no rejection criteria were applied. A very powerful cut against this background contribution is the missing mass criterion: for a $K_{2\pi}$ decay, $m_{K-\pi}$ is supposed to have a value close to the nominal π^0 mass, while almost no K_{e4} signal is expected in this region. The missing mass cut rejects about 94% of the $K_{2\pi D}$ background. Furthermore, the assignment of the pion mass to an electron, while in most of the cases a low energetic photon is lost, lead to a value of m_{Ke4} higher than the nominal kaon mass. Therefore the m_{Ke4} cut rejects 96% of the $K_{2\pi D}$ background contamination (see Figure 7.11). The AKL and extra cluster cuts have a rejection power of 17% and 64%, respectively.

After the complete K_{e4} selection, applying the LDA efficiency and the electron mis-identification probability computed from $K_{2\pi D}$ data as a function of the momentum and normalising to the $K_{3\pi}$ events, only 0.8 ± 0.4 (stat) events are expected to remain in the data, with a negligible systematic uncertainty. The scaling factor between wrong sign events and K_{e4} candidates is compatible with one.

7.4.6. $K_{\pi\pi^0\pi_D^0}$

The branching ratio of the decay $K_{\pi\pi^0\pi^0}$ is about a factor ten smaller than the two-pion decay, while the probability that one of the two π^0 's decays Dalitz is two times higher. Therefore, the background contamination from this channel is expected to be below the percent level, even without further reduction. On the other hand, the cut on the missing mass has no rejection

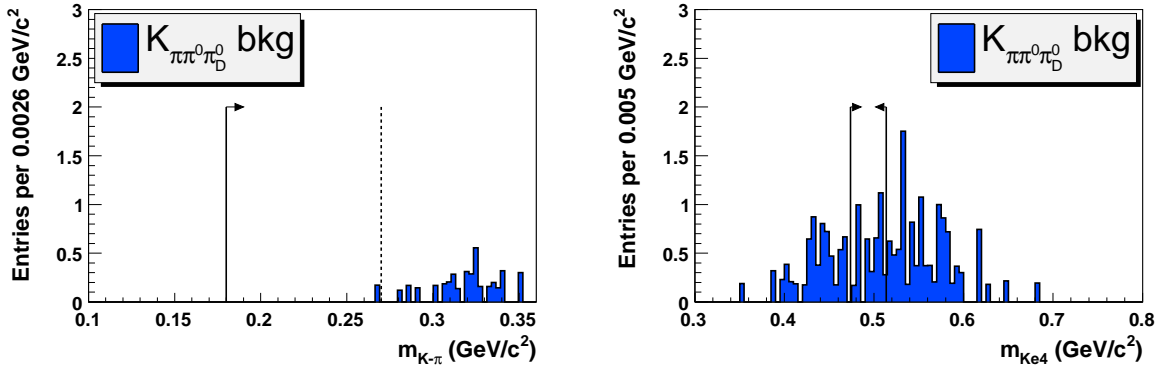


Figure 7.12.: Missing mass (left) and $m_{K_{e4}}$ (right) distributions for the expected background contamination from $K_{\pi\pi^0\pi_D^0}$ events with an electron mis-identified as a pion. The estimate has been performed using MC events with complete K_{e4} selection, except the cut on the displayed variable. Corrections and efficiencies computed from the data have been applied. The distributions are normalised to the kaon flux. The solid lines indicate the signal region, while the dashed line separates the regions where different scaling factors are applied to the wrong sign events.

power, since the expected value is at least twice the π^0 mass. The $m_{K_{e4}}$ cut rejects only 81% of the events, since it is more probable to exactly compensate the higher mass given to the electron with the energy loss of the three undetected photons (see Figure 7.12). The most powerful rejection criteria against this background contamination are the AKL and extra cluster cuts, with a rejection power of 76% and 97% respectively.

The background contamination after the K_{e4} selection is expected to consist of 4.2 ± 0.8 (stat) ± 0.2 (syst) events. The same corrections and efficiencies computed from the data and the normalisation to the $K_{3\pi}$ events have been applied, as for the $K_{2\pi D}$ background. The scaling factor between wrong sign events and K_{e4} candidates is compatible with one.

7.4.7. Total background estimate with systematic uncertainty

The total expected background from MC simulation and accidental superposition of two events is of $1,077 \pm 21$ (stat) ± 2 (syst) events, i.e. 76 ± 51 events less than the estimate from the scaled wrong sign data. The main contributions come from the $K_{3\pi}$ decays, about half of it is due to the decay $\pi \rightarrow e\nu$ and the other half to the mis-identification of a pion. Comparing the distributions of the wrong sign events and of the background contamination with the corresponding expectation from the MC simulation (see Figure 7.13), a small discrepancy can be observed, probably due to the underestimation of the $K_{3\pi}$ background with pion mis-identification. With an acceptance for the K_{e4} selection applied to $K_{3\pi}$ MC events of about 2×10^{-7} , it is not surprising that the MC simulation, even corrected for the expected different efficiencies in the particle identification, does not describe perfectly the shape of the data. For the $K_{3\pi}$ events with a pion decaying into $e\nu$, the discrepancy between data and MC could be due to the different resolution of the vertex reconstruction (the electron track should not match the vertex built by the two pions and the χ^2 of the vertex is expected to be high), but this effect is expected to be smaller than in the case of pion mis-identification.

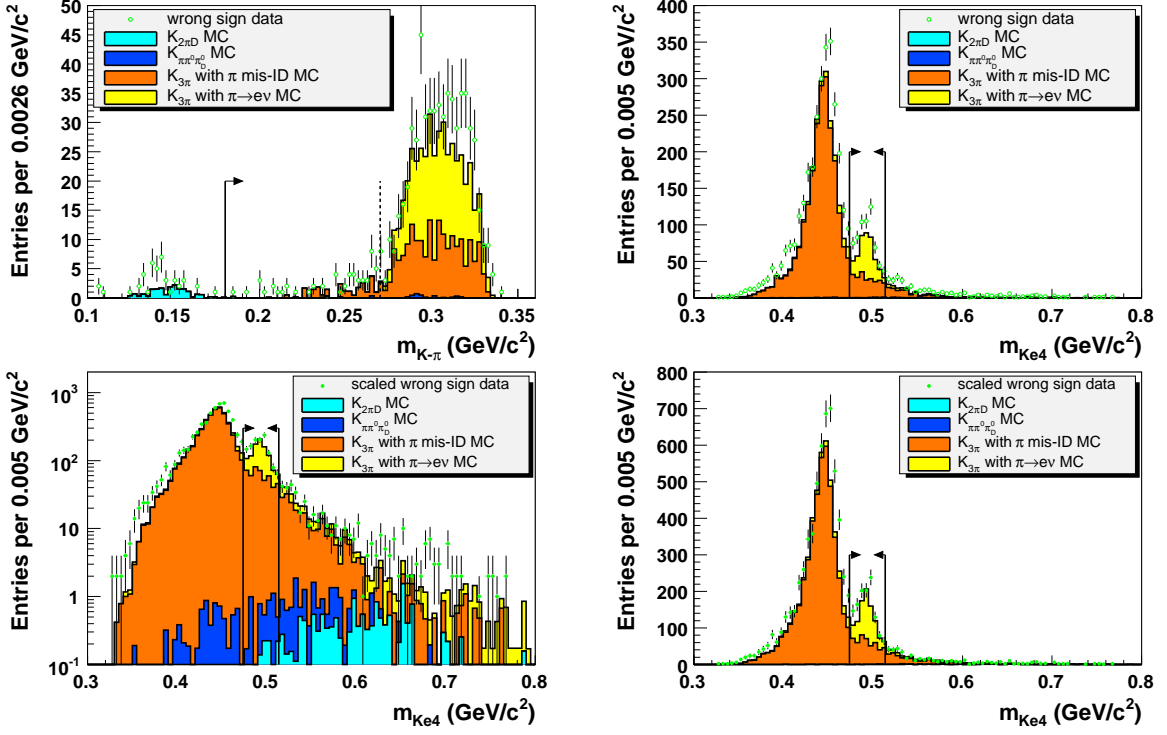


Figure 7.13.: Upper plots: missing mass (left) and $m_{K_{e4}}$ (right) for wrong sign events in data and in the 4 MC channels expected to contribute to the background. Lower plots: $m_{K_{e4}}$ in logarithmic (left) and linear (right) scale for the expected background from scaled wrong sign events and K_{e4} candidates in MC. The accidental background is not included.

For the fit of the form factors, the wrong sign events assure a better description of the background shape as a function of the kinematic variables, since they have the correct resolution. This could be biased in the MC, due to the many corrections that have to be applied. The wrong sign events were scaled with a factor of two and the MC estimate indicated that the correct scaling factor would be 2.13 ± 0.15 (stat) ± 0.01 (syst). The difference of 0.13 between the scaling factors is considered as a systematic uncertainty on the background estimate, even if they are compatible with each other within their uncertainty. Therefore the total background is estimated to be of $1,153 \pm 46$ (stat) ± 100 (syst) events, where the differences between the two estimates in the total number of events and in the scaling factors have been taken as the systematic uncertainty. All background distributions will be obtained from the scaled wrong sign events.

7.5. Summary of selected events, acceptance and background contamination

The numbers of signal events at different stages of the selection are shown in Table 7.1 for data and in Table 7.2 for MC. The indicated selection criteria are applied consecutively and

the actual cut values may be different for different channels, in particular in the particle ID, as explained in Section 7.2. p_K indicates the requirements in the transversal momentum and in the total momentum for $K_{3\pi}$ and $K_{2\pi D}$, while the ellipse cut is applied in K_{e4} . In the data, the electron ID in K_{e4} includes the LDA cut, while in the MC only the tight electron ID is applied. No efficiencies or corrections are applied to the MC, so that it is possible to compute a raw acceptance from Table 7.2, but it does not correspond to the correct value to be used for the branching ratio measurement. In Table 7.1, the number of selected wrong sign events (without scaling) is also reported. Since preselection and vertex selection are identical for the two samples, wrong sign events can be distinguished from K_{e4} candidates only after applying the particle ID.

Selection criteria	K_{e4} data	$K_{3\pi}$ data	$K_{2\pi D}$ data	wrong sign
Preselection	1,831,064,965	1,868,827,103	973,932,088	1,831,064,965
Vertex selection	837,839,517	847,838,455	472,141,464	837,839,517
Particle ID	1,646,702	840,021,593	7,474,496	616,173
Extra clusters	1,615,633	—	—	597,489
Missing mass	1,609,695	—	—	592,723
p_K or ellipse cut	424,254	830,257,285	6,942,473	4,963
Invariant mass(es)	342,859	827,349,934	6,753,756	655

Table 7.1.: Selected signal events in different data channels and wrong sign events at different stages of the selection. No number is given (“—”) if a criterion is not applied to a certain decay.

Selection criteria	K_{e4} MC	$K_{3\pi}$ MC	$K_{2\pi D}$ MC
Generated	79,268,452	280,226,389	141,211,540
Preselection	44,198,354	197,195,678	56,435,356
Vertex selection	21,311,919	89,662,445	11,651,759
Particle ID	18,264,173	89,631,938	8,937,659
Extra clusters	17,936,319	—	—
Missing mass	17,899,897	—	—
p_K or ellipse cut	17,712,930	89,498,433	8,607,193
Invariant mass(es)	14,635,604	89,318,467	8,405,964

Table 7.2.: Selected signal events in different MC channels at different stages of the selection. No number is given (“—”) if a criterion is not applied to a certain decay. As generated events, only the ones inside the decay volume are considered.

8. Fit method

After computing the necessary kinematic variables (see Section 8.1), the fit of the form factors is performed by comparing the five-dimensional distributions of data and MC in the Cabibbo-Maksymowicz variables. In order to avoid fake dependencies due to discrepancies between data and MC, corrections are applied to the MC distribution (see Sections 8.3). A binned maximum likelihood fit is then performed in two iterations (see Sections 8.4–8.6).

8.1. Computation of the Cabibbo-Maksymowicz variables

The main issue in the computation of the kinematic variables is the loss of precision (see also Section 6.4.1) due to the Lorentz boost back into the rest frame of a 60 GeV energy kaon. The resolution problem is worsened by the assumption that all kaons have a momentum of exactly 60 GeV/ c and fly along the z axis. For the computation of the $\pi\pi$ and $e\nu$ invariant masses, the momenta do not need to be boosted back, but the same resolution problem appears in the extraction of small differences out of big numbers. Since the kaons are flying almost in the z direction, instead of computing the mass squared as a difference between the energy and the total momentum (both dominated by the z component of the momentum), a Taylor expansion is used. The ratios $\frac{p_x^2}{p_z^2}$, $\frac{p_y^2}{p_z^2}$ and $\frac{M_\pi^2}{p_z^2}$ are in general very small (at most of the order of 10^{-5}), so that an expansion up to the linear terms around zero is sufficient. The invariant mass squared of the two pion system is therefore computed as [123]

$$s_\pi \simeq 2M_\pi^2 - 2p_{1x}p_{2x} - 2p_{1y}p_{2y} + \frac{p_{2z}}{p_{1z}} \left(p_{1x}^2 + p_{1y}^2 + M_\pi^2 \right) + \frac{p_{1z}}{p_{2z}} \left(p_{2x}^2 + p_{2y}^2 + M_\pi^2 \right), \quad (8.1)$$

where p_1 and p_2 are the momenta of the two pions. The z components of the momentum appear only as factors and not anymore in a subtraction. Furthermore, the ratio of the z components is of order one and all the terms are of the same order of magnitude.

The same formula is used also for the $e\nu$ invariant mass, but instead of considering it as a sum of electron and neutrino, it is computed as the difference between the kaon and the dipion system. Otherwise the problem of obtaining a small difference from big numbers would appear in the computation of the neutrino momentum.

$$\begin{aligned} s_e &\simeq M_K^2 + s_\pi + 2p_{Kx}p_{2\pi x} + 2p_{Ky}p_{2\pi y} \\ &- \frac{p_{2\pi z}}{p_{Kz}} \left(p_{Kx}^2 + p_{Ky}^2 + M_K^2 \right) - \frac{p_{Kz}}{p_{2\pi z}} \left(p_{2\pi x}^2 + p_{2\pi y}^2 + s_\pi \right), \end{aligned} \quad (8.2)$$

where p_K is the kaon momentum, set to $(0,0,60 \text{ GeV}/c)$, and $p_{2\pi}$ the momentum of the dipion system.

The angles θ_π and θ_e are reconstructed by boosting the four-vectors first into the kaon rest frame and then into the required dipion or dilepton system. θ_π is the angle between the pion with the same charge as the kaon in the dipion rest frame and the $\pi\pi$ system in the kaon

rest frame, θ_e the angle between the electron or positron in the dilepton rest frame and the $e\nu$ system in the kaon rest frame.

In order to reconstruct the angle ϕ , the vectors \vec{v} , \vec{c} and \vec{d} are introduced [45]: \vec{v} is the direction of flight of the dipion system in the kaon rest frame; \vec{c} is a unit vector along the projection of the pion with the same charge as the kaon in the dipion rest frame and is perpendicular to \vec{v} ; \vec{d} is a unit vector along the projection of the electron or positron in the dilepton rest frame and is perpendicular to \vec{v} . ϕ is then obtained from the following relations:

$$\cos \phi = \vec{c} \cdot \vec{d}, \quad \sin \phi = (\vec{c} \times \vec{v}) \cdot \vec{d}. \quad (8.3)$$

For the generated values, exactly the same method is used, starting from the momenta of the particles in the laboratory frame saved in the SuperCComPACT variables and computing the energies with the nominal masses. This is more precise than using the stored values also for the energies.

8.2. Preliminary checks

The checks presented in this Section were performed on a K_{e4} MC sample generated with the form factor parametrisation reported in Appendix A and the following values of the parameters [35]:

$$\begin{aligned} f_s &= 5.75, & f'_s &= 1.06 \\ f''_s &= -0.59, & f_e &= 0 \\ \tilde{f}_p &= 0, & g_p &= 4.66 \\ g'_p &= 0.67, & g_e &= 0 \\ h_p &= -2.95, & h'_p &= 0 \\ a_0^0 &= 0.216. \end{aligned} \quad (8.4)$$

The number of selected events in MC is about 42 times the data statistics.

8.2.1. Acceptance

The acceptance as a function of each kinematic variable (integrating over the others) is shown in Figure 8.1. It is a smooth function, slowly decreasing to zero at high values of s_π and s_e . Since the sensitivity to a_0^0 increases with s_π , it is important that the acceptance does not vanish too fast. The measurement of a_0^0 is obtained from the asymmetry in the ϕ distribution, so that any fake asymmetry due to the geometrical acceptance would bias this measurement. As can be seen in the lowest plot of Figure 8.1, the acceptance is almost flat in ϕ and symmetric around π , so that no fake asymmetry is expected to be introduced.

8.2.2. Resolution

The five-dimensional space of the Cabibbo-Maksymowicz variables is divided into equal spaced bins, whose number depends on the resolution in each variable. The difference between the reconstructed and the generated values of the kinematic variables is computed for

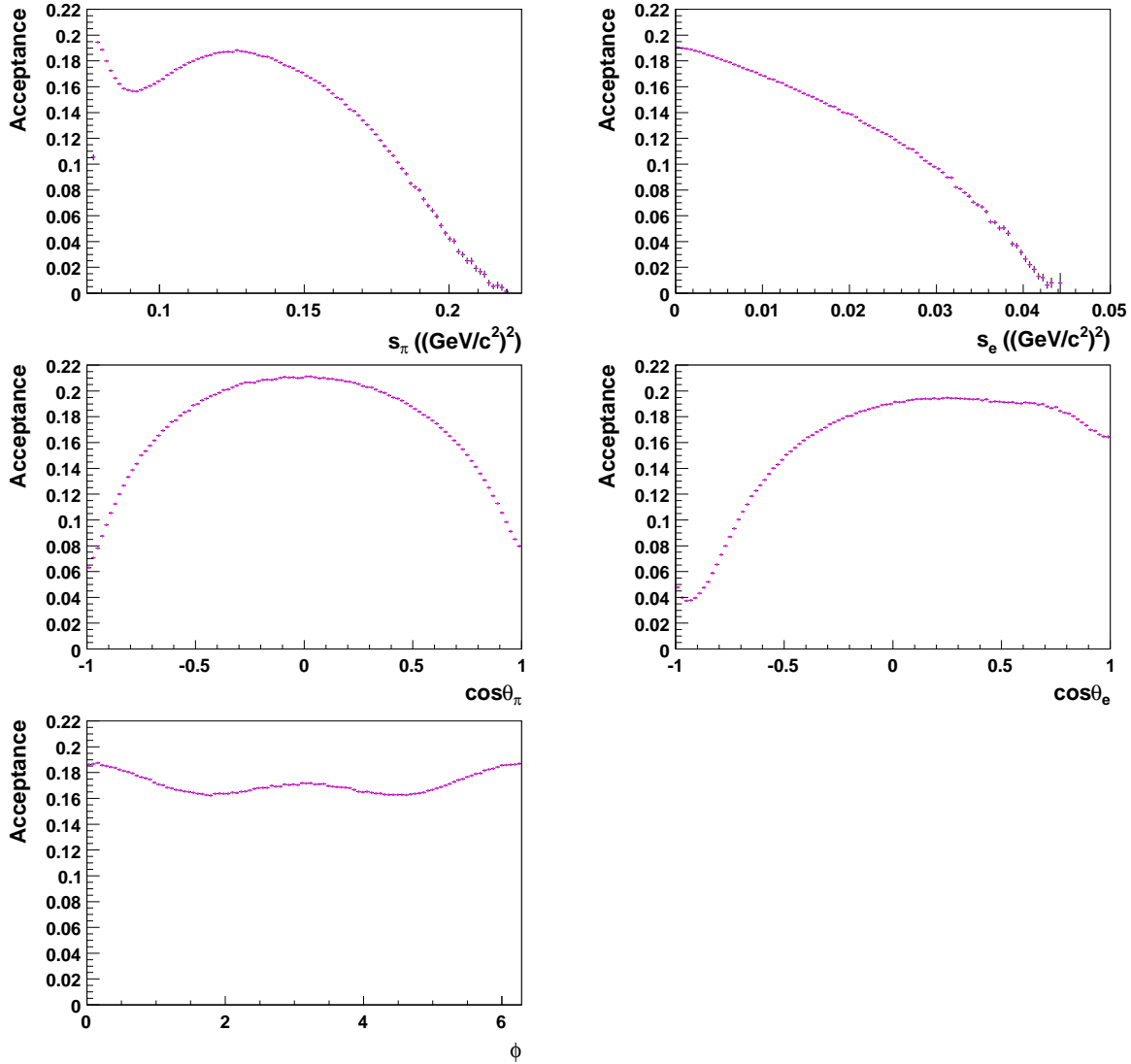


Figure 8.1.: Selection acceptance as a function of the Cabibbo-Maksymowicz variables extracted from K_{e4} MC.

each MC event and the resolution is defined as the RMS of these distributions (see Figure 8.2).

In order to reduce the effect of possible discrepancies in the resolution between data and MC, without losing sensitivity, a bin width equal to about three times the resolution was chosen, when possible. This leads in s_e , $\cos\theta_\pi$ and $\cos\theta_e$ to 8, 10 and 8 bins, respectively. In s_π this criterion would lead to more than 40 bins and in ϕ to 5. In order to have a total number of bins below 200,000, s_π was subdivided into 15 bins (having a width of about ten times the resolution). On the other hand, to precisely measure an asymmetry in ϕ , more than 5 bins are needed. It was decided to have 14 bins, as wide as the resolution in ϕ .

In conclusion, the fit was performed dividing the five-dimensional space into $15 \times 8 \times 10 \times$

8. Fit method

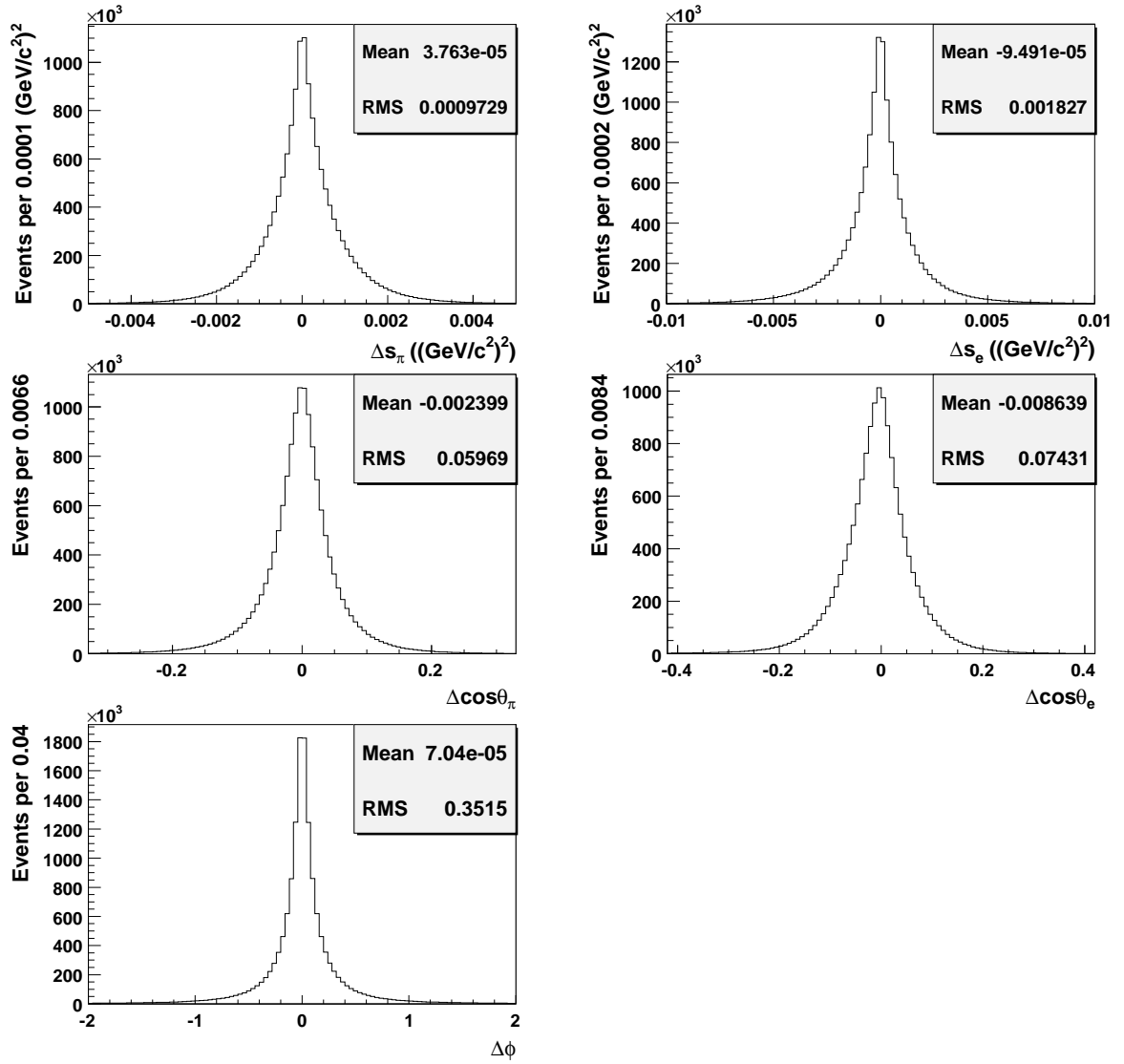


Figure 8.2.: Difference between the generated and the reconstructed values of the kinematic variables obtained from K_{e4} MC.

$8 \times 14 = 134,400$ bins, of which only about 50,000 are populated, because of the kinematic constraints and of the acceptance.

The data and MC plus background distributions in the Cabibbo-Maksymowicz variables before the fit are shown in Figure 8.3.

8.3. Corrections applied to the MC

Since the trigger simulation was not included in the MC and the efficiencies of the E/p and LDA cuts are not well reproduced, some efficiencies and corrections computed from independent data samples are applied to the MC. The choice of applying all corrections to

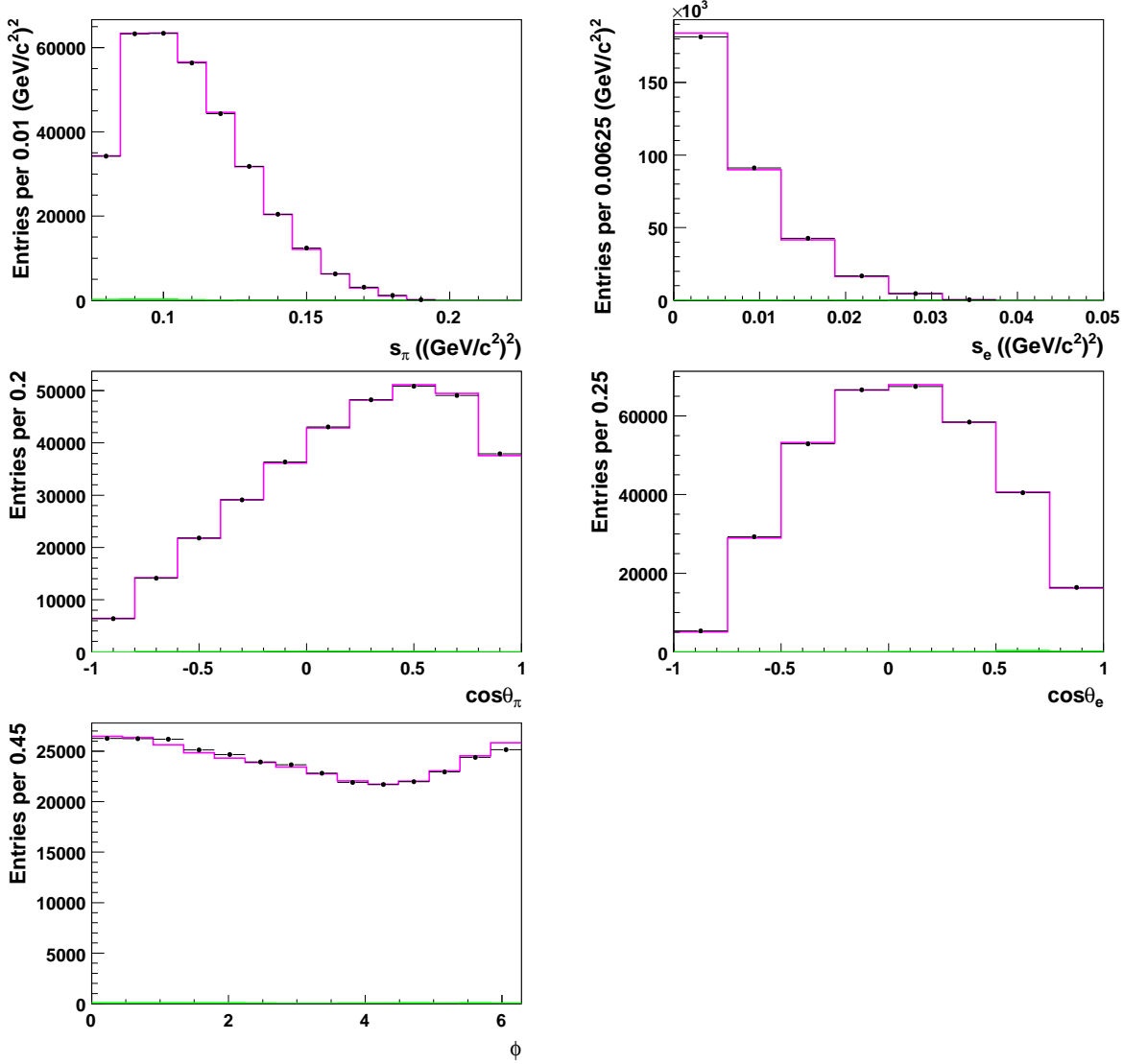


Figure 8.3.: Data (black points), MC (magenta open histogram) and background (green filled histogram) projected distributions in each of the kinematic variables before the fit. The MC was generated with the form factor parameters listed in Eq. 8.4 and is normalised to the expected number of signal events.

the MC and not to the data assures that the statistical uncertainty on the fitted parameters originates only from the data statistics, while all other uncertainties have to be evaluated separately and included into the systematic uncertainty.

8.3.1. Trigger efficiency

Since the K_{e4} data statistics collected by the control triggers is not sufficient to compute the trigger efficiency as a function of the sensitive variables, other decay channels with higher statistics have to be used. In order to reduce the overall inefficiency and therefore also the

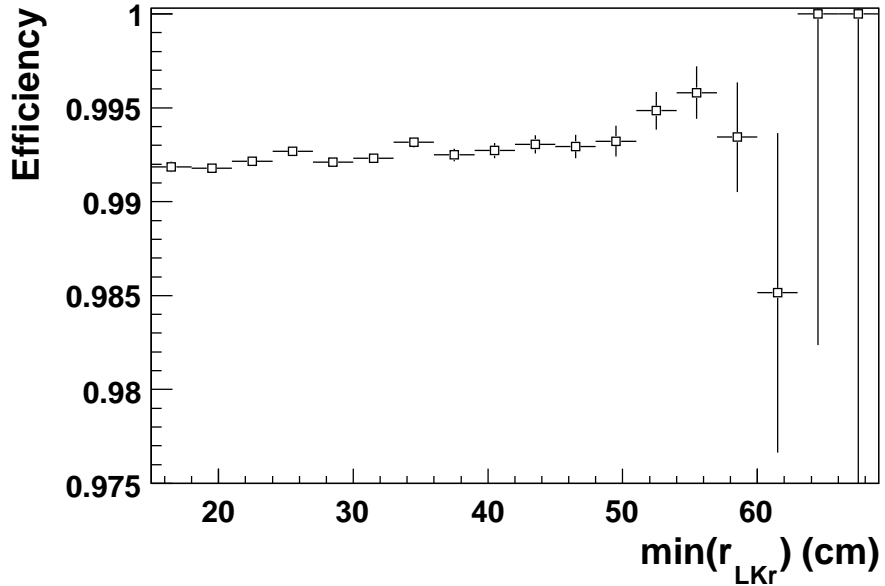


Figure 8.4.: L1 trigger efficiency as a function of the minimum distance between the radial positions of the tracks in the selected vertex extrapolated to the LKr and the centre of the beam pipe. The efficiency was determined from $K_{3\pi}$ data events triggered by N-MBIAS and selected with kinematic cuts and loose pion ID.

possible discrepancy between different channels, special selection criteria were applied, like the cut in the distance between the two-track vertices or in the radial position of the tracks at DCH1. Furthermore, for each trigger component, a quantity is considered, that is supposed to be sensitive to the efficiency of that component and not correlated to the others.

The efficiency of the L1 trigger C-PRE (see Section 4.1) was measured from $K_{3\pi}$ data events triggered by the N-MBIAS trigger and selected with kinematic cuts and loose pion ID. The N-MBIAS trigger is expected to be completely uncorrelated to the C-PRE trigger, since the first requires signals in the neutral hodoscope, that correspond to electromagnetic showers in the calorimeter, while the latter requires signals in the charged hodoscope, produced by charged particles. The total efficiency of the C-PRE trigger was found to be $(99.236 \pm 0.008)\%$, where most of the inefficiency (about 0.6%) is due to the random veto of the \overline{AKL} bit. This inefficiency is not considered to be dangerous for the measurement of the form factors, since it is only expected to produce a reduction of the total statistics, without any strong dependence on the kinematics of the event. The inefficiency of the CHOD (and therefore of the Q_1 and Q_2 bits) depends instead on the radial position of the track and is higher for tracks close to the beam pipe. The L1 trigger efficiency was measured as a function of the minimum radial distance between the positions of the track extrapolations and the centre of the beam pipe at the LKr, called $\text{min}(r_{\text{LKr}})$ (see Figure 8.4). The position at the LKr can be used instead of the one at the CHOD, since the two detectors are very close to each other in z and no deflection takes place in between.

The L2 trigger condition consists of the three massbox bits 2VTX, 1VTX and 1TRK-P (see Section 4.2.2). Due to the structure of the MBX algorithm (see Figure 4.3), all events go

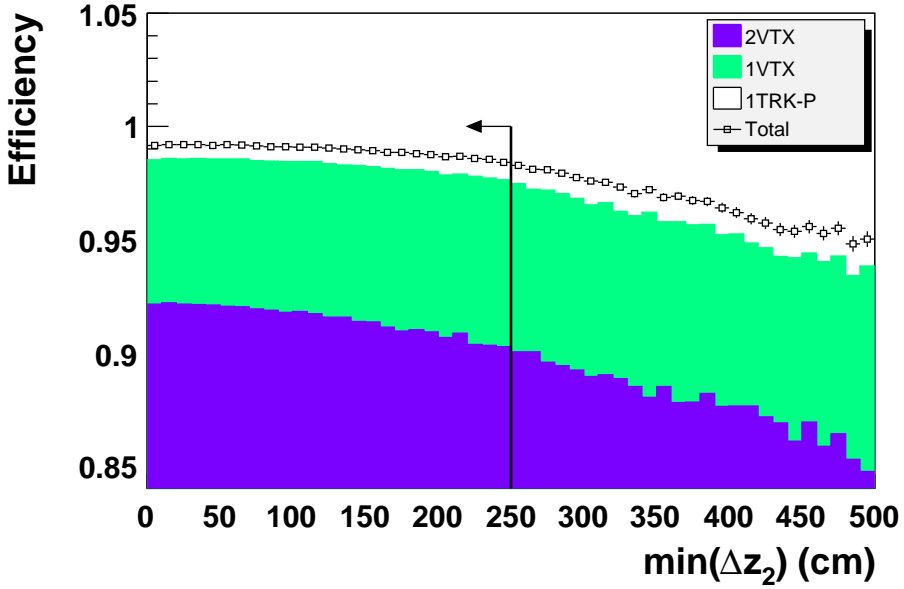


Figure 8.5.: L2 trigger efficiency as a function of the minimum distance between the z positions of the two-track vertices. The efficiency was determined from $K_{3\pi}$ data events triggered by C-PRE and selected with kinematic cuts and loose pion ID. The cut in $\min(\Delta z_2)$ was relaxed. The standard value of the cut is indicated by the arrow. The contribution of the three trigger components are shown in different colours.

through the 2VTX selection, where they are either flagged, or passed to the 1VTX selection. Again, the flagged events are not further analysed and only the ones that do not fulfil any of the previous conditions undergo the 1TRK-P selection. In this way, no events can have more than one flag and the next bit is used to compensate the inefficiencies of the previous one.

Two variables are expected to be sensitive to the trigger selection: the minimum distance between the two-track vertices that can be built out of the tracks in the selected vertex (called “ $\min(\Delta z_2)$ ”) and s_π . The first variable is particularly sensitive to the 2VTX trigger efficiency and the second one to the 1VTX bit, so that they are not correlated with each other. Because of the MBX algorithm, in both cases the total L2 efficiency (with the three bits) is considered, so that the compensation mechanism can take place and the efficiency dependence on the variable is reduced.

The trigger efficiency as a function of $\min(\Delta z_2)$ was measured from $K_{3\pi}$ data events triggered by the C-PRE trigger and selected with kinematic cuts and loose pion ID (see Figure 8.5). The total L2 trigger efficiency for the $K_{3\pi}$ events is $(99.126 \pm 0.003\text{ (stat)})\%$: almost 92% of the events is triggered by the 2VTX trigger, about 6.5% by 1VTX and less than 1% by 1TRK-P.

The dependence of the trigger efficiency on s_π can not be tested with the same data sample, since $K_{3\pi}$ events can not have values of s_π greater than $(M_K - M_\pi)^2 \simeq 0.125\text{ (GeV}/c^2)^2$, while the range covered by K_{e4} events reaches the kaon mass squared. Therefore, a sample of $K_{2\pi D}$ events was used (see Figure 8.6). The events were triggered by the C-PRE trigger

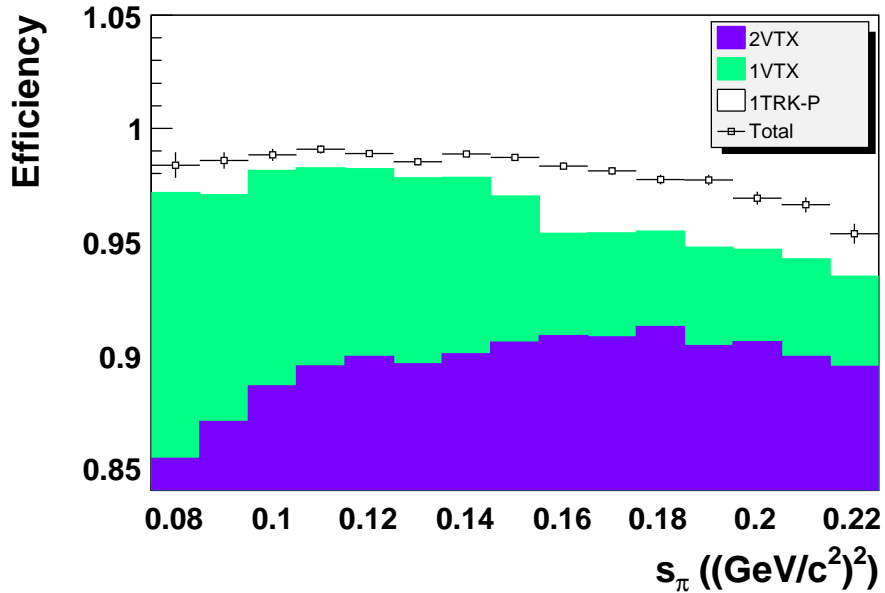


Figure 8.6.: L2 trigger efficiency as a function of s_π . The efficiency was determined from $K_{2\pi D}$ data events triggered by C-PRE and selected with kinematic cuts and loose electron ID. The contribution of the three trigger components are shown in different colours.

and selected with kinematic cuts and loose particle ID. s_π was computed assigning the pion mass both to the pion and to the lepton with the opposite charge. In this way, even values of s_π higher than the kaon mass squared could be obtained, but they have a very low efficiency and they are not interesting for the application to K_{e4} decays. Therefore the requirement s_π less than $0.225 (\text{GeV}/c^2)^2$ was applied, leading to a total L2 trigger efficiency for this $K_{2\pi D}$ sample of $(98.15 \pm 0.06 \text{ (stat)})\%$. The total efficiency and relative size of the three components are similar, but not identical, to the ones of the $K_{3\pi}$ sample: 90% of the events are flagged by 2VTX, 6% by 1VTX and 2% from 1TRK-P.

K_{e4} events have a total L2 efficiency, measured directly from selected K_{e4} data triggered by C-PRE, of $(99.3 \pm 0.1 \text{ (stat)})\%$, consisting of 91.5% 2VTX, 6.7% 1VTX and 1.1% 1TRK-P. Both total efficiency and composition are closer to the $K_{3\pi}$ events than to the $K_{2\pi D}$ decays, as expected from the topology of the events.

8.3.2. Electron identification

The LDA efficiency is determined from $K_{2\pi D}$ data events (see Figure 7.3) and applied to the K_{e4} MC. Furthermore, two corrections are applied, in order to take into account the possible discrepancies between data and MC in the efficiency of the tight electron ID and the effect of the different topology of $K_{2\pi D}$ and K_{e4} events of the LDA efficiency.

The first correction was determined from $K_{2\pi D}$ data and MC selected with kinematic cuts (see Section 7.3.3), tight pion ID and loose electron ID for the two tracks with the same charge as the kaon and tight electron ID for the remaining one. The efficiency of the tight electron ID with respect to the loose one as a function of the electron momentum was measured

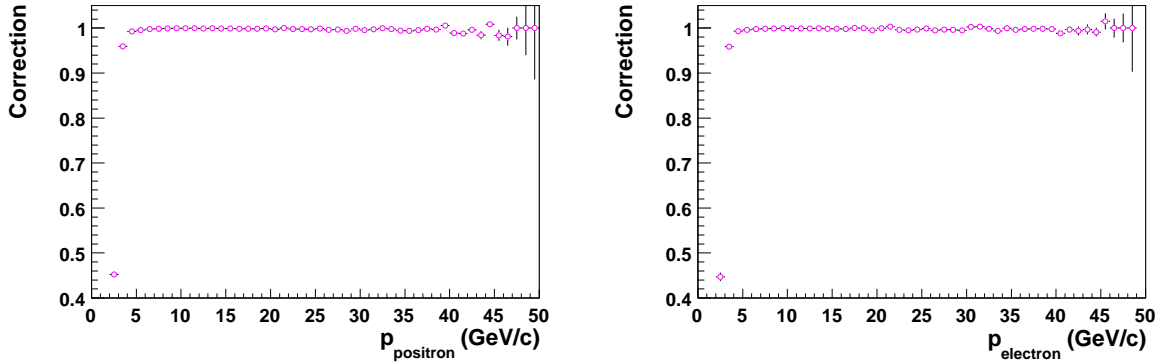


Figure 8.7.: Correction to be applied to MC events to account for the discrepancy with the data in the efficiency of the tight electron ID. The correction was determined from $K_{2\pi D}$ as the ratio of the efficiencies in data and MC for e^+ (left) and e^- (right). The events were selected with kinematical cuts, tight pion ID, loose electron ID for the considered electron and tight electron ID for the other one.

separately for electrons and positrons (see Figure 8.7). The correction is the ratio between the efficiencies in data and in MC. Since the tight electron ID consists mainly of the E/p cut (see Section 7.2.3), this correction accounts for the discrepancy in the energy deposit of the electromagnetic showers in the LKr and in the energy resolution between data and MC. As expected, the only sizeable effect appears at low electron and positron momenta, below 5 GeV/c.

The second correction was determined from K_{e4} and $K_{2\pi D}$ MC events selected with tight particle ID, but without LDA. The ratio of the LDA efficiencies as a function of the electron momentum in the two samples was used as correction (see Figure 8.8). Even if the efficiency of the LDA obtained from the MC does not agree with the one determined from the data, the ratio of the two efficiencies is expected to differ from one only because of topological effects and to reflect therefore the ratio that would be obtained in the data. This correction differs from one at most at low momenta, by about 1%.

8.3.3. Pion identification

In analogy to the electron selection, a correction is applied to also take into account the different efficiencies of the tight pion selection in data and MC. The efficiencies were determined as a function of the pion momentum, separately for π^+ and π^- , from $K_{3\pi}$ events selected with kinematic cuts and loose pion ID. The ratio of the data efficiency over the MC one was used as correction (see Figure 8.9). As for the tight electron ID, the main discrepancy between data and MC is due also in the tight pion ID to the different efficiencies of the E/p cut.

The shape of the ratio between the two efficiencies, oscillating at high momenta is due to the use of the shower libraries in the MC simulation. As can be seen in Figure B.1, the data efficiency has a smooth shape, as expected, while the oscillating values appear only in the MC efficiency.

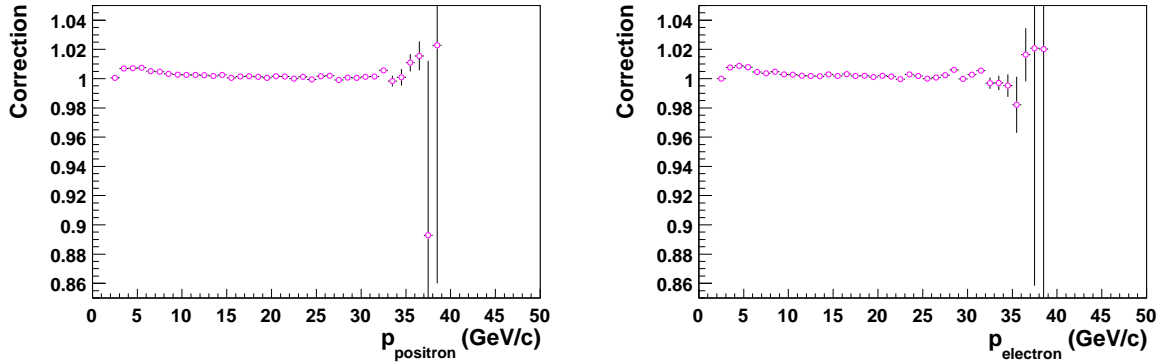


Figure 8.8.: Correction to be applied to MC events to account for the different LDA efficiency between $K_{2\pi D}$ and K_{e4} events. The correction was determined from $K_{2\pi D}$ and K_{e4} MC as the ratio of the LDA efficiencies for e^+ (left) and e^- (right). The events were selected with kinematical cuts and tight particle ID.

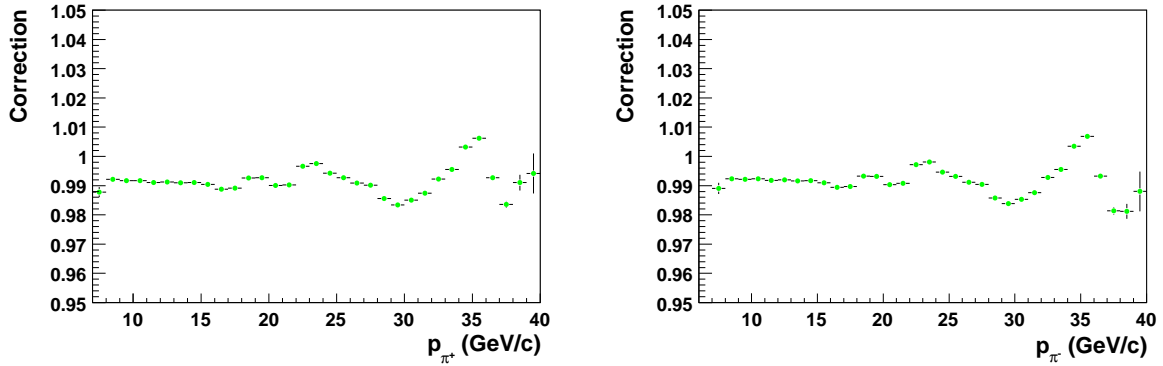


Figure 8.9.: Correction to be applied to MC to account for the discrepancy with the data in the efficiency of the tight pion ID. The correction was determined from $K_{3\pi}$ events as the ratio of the efficiencies in data and MC for π^+ (left) and π^- (right). The events were selected with kinematical cuts and loose pion ID.

8.3.4. Total weight

For each event a total weight $w_{tot} = w_{eff} \times w_{corr}$ is computed as the product of all the efficiencies and corrections mentioned above:

$$\begin{aligned} w_{eff}(\min(r_{LKr}), \min(\Delta z_2), s_\pi, p_e, q) &= \epsilon_{L1}(\min(r_{LKr})) \times \epsilon_{L2}(\min(\Delta z_2)) \\ &\times \epsilon_{L2}(s_\pi) \times \epsilon_{LDA}(p_e, q) \\ w_{corr}(p_e, p_\pi, q) &= c_{E/p}(p_e, q) \times c_{LDA}(p_e, q) \times c_{E/p}(p_\pi, q), \end{aligned} \quad (8.5)$$

where the values of the efficiencies $\epsilon_{L1}(\min(r_{LKr}))$, $\epsilon_{L2}(\min(\Delta z_2))$, $\epsilon_{L2}(s_\pi)$, $\epsilon_{LDA}(p_e, q)$ and of the corrections $c_{E/p}(p_e, q)$, $c_{LDA}(p_e, q)$, $c_{E/p}(p_\pi, q)$ are taken from Figures 8.4, 8.5, 8.6, 7.3 (lower plots), 8.7, 8.8 and 8.9, respectively.

The distributions of selected K_{e4} MC events in the variables $\min(r_{LKr})$, $\min(\Delta z_2)$, p_e and p_π are shown in Figure B.2. In two cases ($\min(r_{LKr})$ and p_π) the samples used to compute

the efficiency or the correction did not cover the whole range necessary for the K_{e4} events. For events with $\min(r_{LKr})$ above 69 cm, ϵ_{L1} was set to 1, with the same uncertainty as the last available bin. The same procedure was applied, for $c_{E/p}$, to the events with p_π greater than 40 GeV.

The L2 efficiency ϵ_{L2} appears twice in w_{eff} : while the dependence on the two variables is not correlated, so that the multiplication of the two efficiencies is justified, the total efficiency is at the end counted twice. This does not affect the measurement of the form factors as it is performed in this analysis, but would have to be corrected for if at the same time also the branching ratio (or the value of f_s) would be extracted from the fit.

The effect of the corrections applied to the MC distributions is shown in Figure 8.10.

8.4. Fit strategy

In order to compare the distributions in the kinematic variables and extract the values of the parameters, six five-dimensional histograms with 134,400 bins each are filled, separately for K^+ and K^- , with:

- K_{e4} MC events selected without LDA requirement and without any correction
- K_{e4} data events with complete selection
- background estimated from scaled wrong sign events.

Since most of the statistics is concentrated in a small region of the five-dimensional space, while many bins are almost empty, all the bins containing less than 20 MC events are marked as “empty” and ignored in the fit procedure. Since in the MC the statistics is more than 40 times higher than in the data, only bins with an expected content below 0.5 data events are neglected by this requirement. The introduction of the threshold is aimed to reduce the dependence of the fit result from statistical fluctuations of the MC distribution. The corrections described in the previous Sections and the LDA efficiency are then applied to the MC events in non-empty bins and the content of the background histogram is added to that of the MC.

The distributions of data and MC plus background are compared and the agreement between them is measured by the *extended likelihood function* in the case of binned data [124]:

$$L(\theta) = \prod_{i=1}^N \frac{[\nu_i(\theta)]^{n_i}}{n_i!} e^{-[\nu_i(\theta)]}, \quad (8.6)$$

where n_i and ν_i are the observed and expected number of events in bin i , respectively, N is the number of considered bins and θ the vector of the parameters to be optimised in the fit. The values of ν_i depend on θ , while the n_i ’s are fixed, since they are experimentally measured. The result of the fit is given by the vector of parameters that maximises the likelihood function. In order to simplify the calculation, without modifying the result, instead of $L(\theta)$, its logarithm is maximised, while the terms not depending on the parameters, i.e. containing only n_i and not ν_i , are neglected:

$$\log L(\theta) = \sum_{i=1}^N -\nu_i + n_i \log \nu_i + const. \quad (8.7)$$

8. Fit method

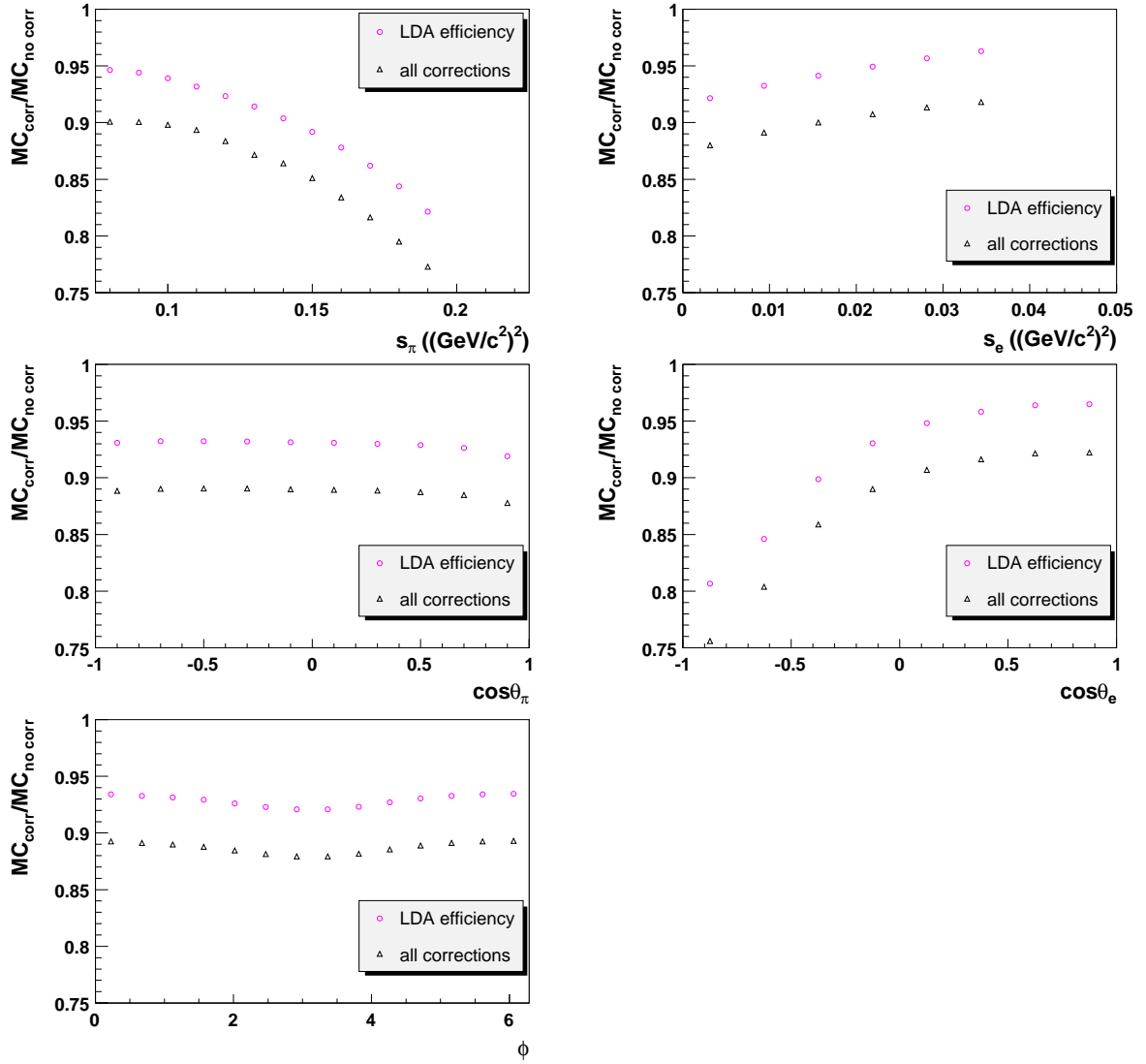


Figure 8.10.: Effect of the LDA efficiency (magenta circles) and of all the corrections (black triangles), including the LDA efficiency on the K_{e4} MC distributions in the kinematic variables, expressed as the ratios between the reweighted and the uncorrected distributions.

The extended likelihood function is based on the assumption of Poisson distributed values of n_i around ν_i , which is correct also for bins containing very few or even zero data events as is the case in the present fit. A χ^2 fit, assuming a Gaussian distribution of the bin contents, is instead suitable for histograms with a high number of entries per bin.

The maximisation of $\log L$, or actually the minimisation of $-\log L$, is done numerically using the MIGRAD routine of the MINUIT package [125], based on a variable metric method. The first derivatives G_i are computed at the starting values X_i of the parameters and the covariance matrix V_{ij} is first assumed to be the unit matrix. The first estimation of the

minimum is made by taking a “Newton step” to the values $X'_i = X_i - \sum_j V_{ij} \cdot G_j$, that correspond to the minimum of the function under the assumption that it is quadratic and that V_{ij} is the correct covariance matrix. X'_i is then taken as the vector of starting values for the parameters, the gradient at the new point is calculated, the covariance matrix is updated and a further Newton step is taken. This procedure is repeated until the convergence criteria are satisfied. The convergence is given by the Estimated Distance to Minimum, $EDM = G^T \times V \times G$, and is required to be less than 10^{-4} in order to stop the minimisation process.

The uncertainties on the fitted parameters are given by the difference between the values at the minimum and the ones for which $-\log L = -\log L_{max} + 0.5$, where L_{max} is the maximum of the likelihood function. The function $-\log L$ is assumed to be a parabola around the minimum.

Each time $-\log L$ is computed, the MC histograms are filled, assigning to each event a weight given by the ratio of the differential decay rates computed with the considered parameter values and with the values used in the MC generation. This procedure is very CPU-time consuming, because the decay rate has to be computed about 14 million times for each determination of the likelihood function and in a standard fit $-\log L$ needs to be estimated about 400 times. K^+ and K^- events are fitted simultaneously, imposing the form factor parameters to have the same value, but keeping separated histograms.

8.5. Raw result of the first iteration

The first iteration of the fit was performed using a MC sample generated with the parameter values in Eq. 8.4. Since the K_{e4} branching ratio was not measured in the analysis presented here, f_s could not be determined and was therefore included in the normalisation N , that was considered as a free parameter.

As a first try, only 6 further parameters were varied: f'_s/f_s , f''_s/f_s , g_p/f_s , g'_p/f_s , h_p/f_s and a_0^0 . The other parameters of the polynomial part were set to zero, while a_0^2 was fixed by the constraint of Eq. 2.67 as a function of a_0^0 . All the varied parameters were different from zero with a sensitivity of more than three times the statistical error (σ_{stat}). The parameters f_e/f_s , \tilde{f}_p/f_s , g_e/f_s and h'_p/f_s were then varied one at a time, in order to check the sensitivity of the measurement to each of them. The first two parameters were significantly different from zero, so that they were added to the vector of free parameters, while the last two were compatible with zero.

Since Eq. 6.2 is just a Taylor expansion of a partial wave expansion, further terms can be added, both as higher order polynomials or in the D -wave. The following polynomial terms were tried out:

$$\begin{aligned}
 & \frac{f'''_s}{f_s} q^6 e^{i\delta_0^0(s_\pi)}, \\
 & \frac{f'_e}{f_s} \frac{s_e^2}{16M_\pi^4} e^{i\delta_0^0(s_\pi)}, \\
 & \frac{f_{es}}{f_s} q^2 \frac{s_e}{4M_\pi^2} e^{i\delta_0^0(s_\pi)}, \\
 & \frac{\tilde{f}'_p}{f_s} q^2 \sigma_\pi X \cos \theta_\pi e^{i\delta_1^1(s_\pi)}, \\
 & \frac{g''_p}{f_s} e^{i\delta_1^1(s_\pi)}.
 \end{aligned} \tag{8.8}$$

Parameter	1 st iter.	σ_{stat}	2 nd iter.	σ_{stat}
f_s'''/f_s	0.057	± 0.035	0.065	± 0.035
f_{es}/f_s	-0.043	± 0.115	0.006	± 0.116
\tilde{f}_p'/f_s	-0.027	± 0.051	-0.033	± 0.052
g_p''/f_s	0.069	± 0.042	0.059	± 0.042
g_e/f_s	0.063	± 0.078	0.063	± 0.079
g_d/f_s	-0.008	± 0.020	-0.004	± 0.020
h_p'/f_s	-0.022	± 0.127	-0.017	± 0.127

Table 8.1.: Fitted values of the parameters added one by one to the standard set of parameters in the first (second column) and second (fourth column) iteration of the fit, performed with MC samples generated with the parameter values in Eqs. 8.4 and 8.11, respectively. The statistical uncertainties in the third and fifth column, take into account only the data statistics and the correlations.

Only the parameter f_e'/f_s was found to be different from zero with a sensitivity of at least $3\sigma_{stat}$, while all the others were compatible with zero. The D -wave term in the G form factor

$$\frac{g_d}{f_s} \sigma_\pi X \cos \theta_\pi e^{i\delta_2^0(s_\pi)}, \quad (8.9)$$

with [126]

$$\tan \delta_2^0 = \sqrt{\left(1 - \frac{4M_\pi^2}{s_\pi}\right)^5} \cdot \left(0.0018 + 0.0031q^2 + 0.0008q^4\right) \cdot \left(\frac{4M_\pi^2 - 83.5067M_\pi^2}{s_\pi - 83.5067M_\pi^2}\right) \quad (8.10)$$

was also varied and found to be compatible with zero within one σ_{stat} . The fitted values of all the tested parameters compatible with zero are listed in Table 8.1.

Varying all the parameters for which the fit was found to be sensitive and fixing all the others to zero, the values and the statistical uncertainties listed in Table 8.2 were obtained. The χ^2 was computed at the minimum of $-\log L$ and found to be 64977 for 63494 degrees of freedom. The number of degrees of freedom (ndf) is given by the number of bins above threshold minus the number of free parameters. The parameter values have to be corrected for the bias possibly introduced by the log-likelihood maximisation, that can be obtained by fitting a MC sample as “pseudo-data” and comparing the fit result with the true values used for the generation (see Section 9.1). In Figure 8.11 the ratios between the data and MC plus background distributions as a function of the Cabibbo-Maksymowicz variables are displayed before and after the fit.

Parameter	1 st iter.	2 nd iter.	σ_{stat}	σ_{MINOS}^+	σ_{MINOS}^-
N	0.850	0.870	± 0.006	+0.0065	-0.0064
f'_s/f_s	0.135	0.145	± 0.013	+0.0134	-0.0133
f''_s/f_s	-0.046	-0.054	± 0.013	+0.0133	-0.0133
f_e/f_s	0.252	0.259	± 0.051	+0.0514	-0.0511
f'_e/f_s	-0.615	-0.629	± 0.170	+0.1703	-0.1709
\tilde{f}_p/f_s	-0.112	-0.103	± 0.013	+0.0134	-0.0133
g_p/f_s	0.897	0.889	± 0.012	+0.0124	-0.0124
g'_p/f_s	0.110	0.117	± 0.015	+0.0153	-0.0153
h_p/f_s	-0.398	-0.397	± 0.028	+0.0284	-0.0285
a_0^0	0.244	0.246	± 0.009	+0.0088	-0.0091

Table 8.2.: Raw results of the first (second column) and second (third column) iteration of the fit, performed with MC samples generated with the parameter values in Eqs. 8.4 and 8.11, respectively. The statistical uncertainties in the fourth column, equal for both iterations, take into account only the data statistics and the correlations between the parameters. In the fifth and sixth column the uncertainties estimated by the MINOS routine in the second iteration of the fit are listed.

8.6. Raw result of the second iteration

A new MC sample, of the same size as the previous one, was generated including the new term and using parameter values close to the result of the first iteration:

$$\begin{aligned}
 f_s &= 5.75, \quad f'_s = 0.78 \\
 f''_s &= -0.26, \quad f_e = 1.45 \\
 \tilde{f}_p &= -0.64, \quad g_p = 5.16 \\
 g'_p &= 0.63, \quad g_e = 0 \\
 h_p &= -2.29, \quad h'_p = 0 \\
 a_0^0 &= 0.244, \quad f'_e = -3.54.
 \end{aligned} \tag{8.11}$$

The fit was then repeated with the same free parameters as in the first iteration, leading to the result shown in Table 8.2, with the correlation matrix in Table 8.3 and a χ^2/ndf of 65444/64006. The different number of degrees of freedom with respect to the first iteration is due to the different acceptance and therefore the different number of bins above threshold.

The correlation matrix shows the expected behaviour: the parameters belonging to the same polynomial expansion are strongly correlated, like for example f'_s/f_s with f''_s/f_s and f_e/f_s with f'_e/f_s , while between different partial waves and different polynomials, the correlations are almost negligible. h_p/f_s and a_0^0 are mostly uncorrelated from the other parameters.

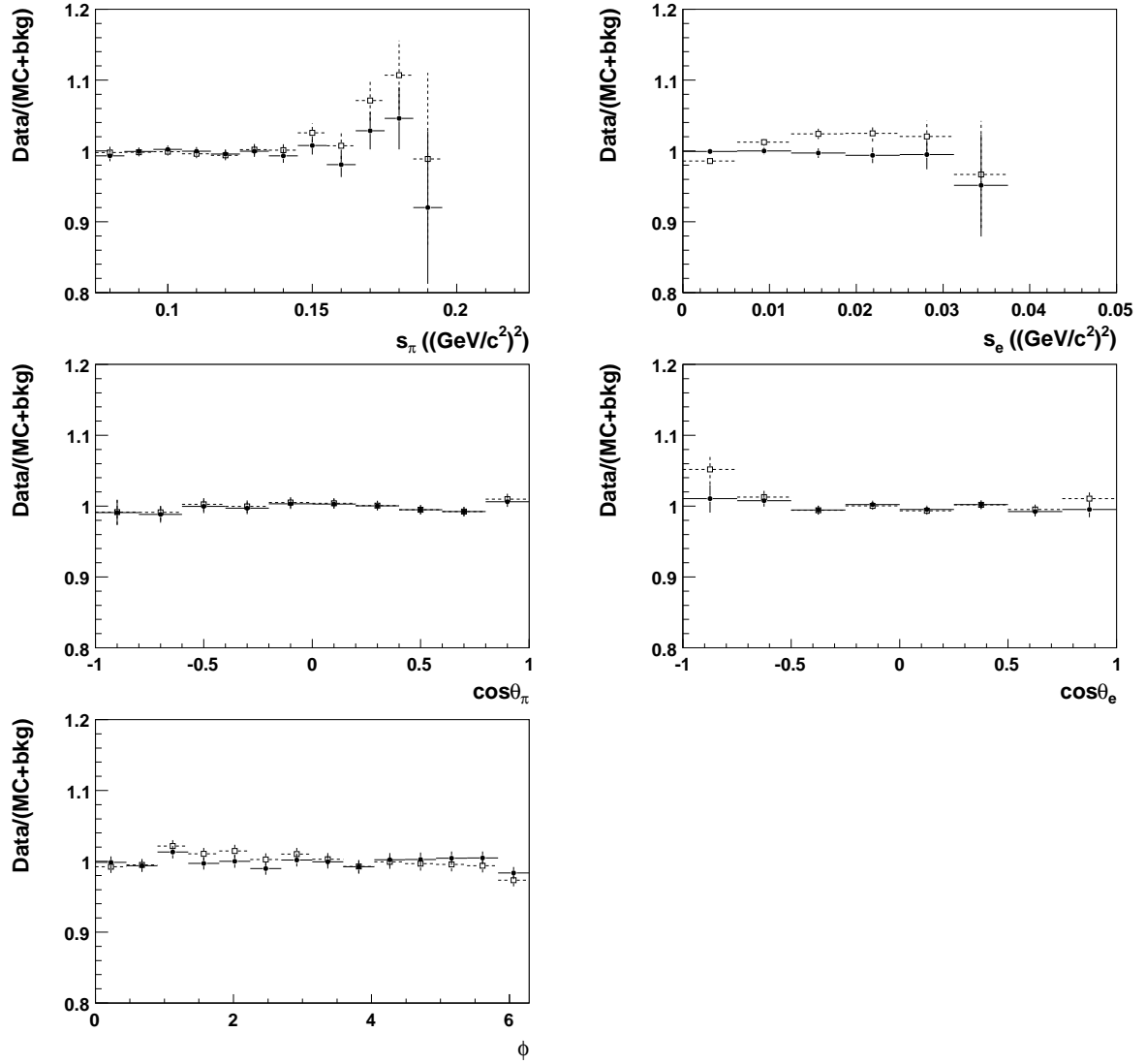


Figure 8.11.: Ratios of the data over MC plus background projected distributions in the Cabibbo-Maksymowicz variables before (empty squares and dashed lines) and after (filled circles and solid line) the first iteration of the fit of the form factors. The MC distributions before the fit is normalised to the area of data minus background, while the fitted value of N is used for the distributions after the fit.

Aim of this second iteration was to properly take into account the correlations between the selection acceptance and the form factors and to check the stability of the result using different MC samples. The two results can only be compared after correcting for the bias estimated from the MC tests, that is in general different for different samples. Since the same data statistics was used in this second iteration and the correlations between the parameters did not change significantly, the statistical uncertainties also remained the same. When comparing the two results, the 100% correlation between the statistical uncertainty has to

	N	f'_s/f_s	f''_s/f_s	f_e/f_s	f'_e/f_s	\tilde{f}_p/f_s	g_p/f_s	g'_p/f_s	h_p/f_s	a_0^0
N	1									
f'_s/f_s	-0.629	1								
f''_s/f_s	+0.422	-0.932	1							
f_e/f_s	-0.633	-0.043	+0.149	1						
f'_e/f_s	+0.481	+0.111	-0.175	-0.947	1					
\tilde{f}_p/f_s	-0.141	+0.133	-0.077	+0.069	+0.033	1				
g_p/f_s	-0.103	-0.065	+0.113	+0.136	-0.210	-0.742	1			
g'_p/f_s	-0.090	+0.233	-0.307	-0.045	+0.114	+0.392	-0.809	1		
h_p/f_s	+0.064	-0.041	+0.032	-0.035	+0.019	-0.109	+0.084	-0.047	1	
a_0^0	-0.021	+0.030	-0.053	+0.004	+0.017	+0.260	-0.202	+0.203	-0.031	1

Table 8.3.: Correlation matrix between the fit parameters obtained in the second iteration. The matrix is symmetric, identical values are written only once.

be taken into account. The non-sensitivity to the parameters fixed to zero was checked again and confirmed (see Table 8.1).

The change in the ratios of the data over MC plus background distributions is negligible with respect to the scale used in Figure 8.11. The $\Delta \log(L_{max})$ curve around its minimum as a function of a_0^0 is shown in Figure 8.12. This curve was obtained by fixing a_0^0 to the considered value and performing the fit of the remaining 9 parameters. All the one-dimensional and some two-dimensional $\Delta \log L$ curves can be found in Appendix B. To obtain each of these curves the remaining 9 parameters were fixed to the result values and no further fit was performed. In this case, the uncertainty that can be read from the distributions does not take into account the correlations with the other parameters.

The statistical uncertainties estimated from the MIGRAD routine (see column 4 of Table 8.2) assume that the function $-\log(L_{max})$ is a parabola around its minimum and predicts its shape from the covariance matrix. In order to check that this assumption is correct, the MINOS routine of the MINUIT package [125] was used. Starting from the MIGRAD prediction, the actual value of $-\log(L_{max})$ is computed and new, possibly asymmetric, values of the statistical uncertainties are estimated. The obtained values for the positive and negative uncertainties (σ_{MINOS}^+ and σ_{MINOS}^-) are listed in the last two columns of Table 8.2. The deviation from the expected parabolic shape of the $-\log(L_{max})$ curve is of 4% for a_0^0 , that enters the differential decay rate through a non-linear function, and at most 0.5% for the parameters of the polynomial function. Since σ_{stat} and σ_{MINOS} agree up to the quoted digits, the uncertainties are considered to be symmetric.

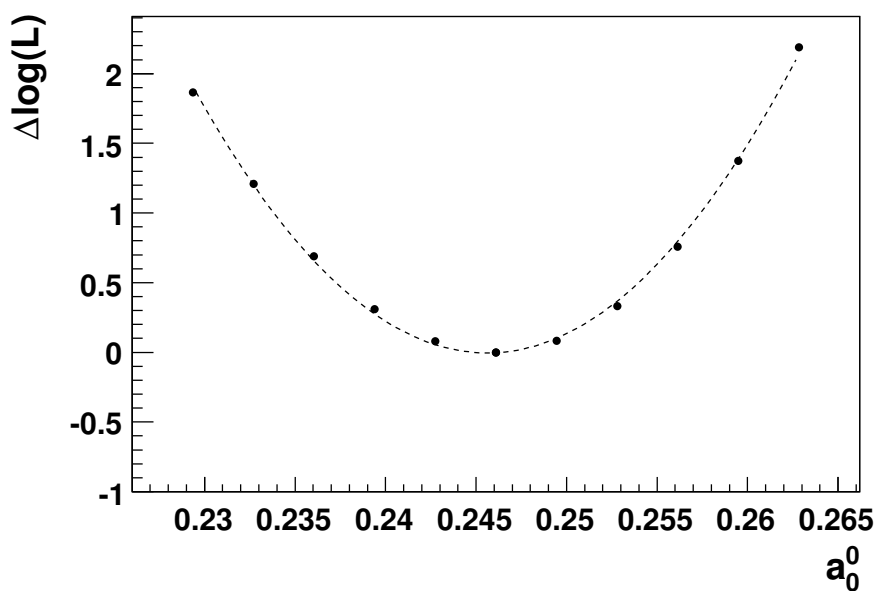


Figure 8.12.: $\Delta \log(L_{max})$ distribution as a function of a_0^0 around the minimum. The points are fitted with a parabola (dashed line). The statistical uncertainty, taking into account the correlations with the other parameters, corresponds to a variation of $-\log(L_{max})$ by 0.5.

9. Corrections and systematic uncertainties

The uncertainty on the fit parameters in Table 8.2 takes into account only the data statistics, while all the other sources of uncertainty due to the experimental method are included in the systematic uncertainty (σ_{syst}). Aim of the systematic studies is to estimate the stability of the measurement under small changes in the experimental conditions. On this purpose, all the effects were considered, to which the measurement is expected to be sensitive. In particular, the fit method itself and the agreement between data and MC simulation could be important sources of systematic uncertainty. The total uncertainty represents then the expected spread of the results when repeating the measurement many times under similar conditions.

The theoretical uncertainty due to the constraint between a_0^0 and a_0^2 is quoted separately (see Section 9.5).

9.1. MC tests

A maximum likelihood fit has, in general, a bias [127], i.e. the fit result does not correspond perfectly to the true values of the parameters. In order to estimate the size of this bias, the fit is repeated many times under the same conditions, using, instead of the data sample, independent MC samples (pseudo-data), each containing as much statistics as the data, all generated with the same values (similar to the ones obtained from the data fit) of the form factor parameters. The bias is given for each parameter by the difference between the weighted average of the fit results and the value used for the generation. The uncertainty on the determination of the bias corresponds to the uncertainty on the mean values (RMS/ \sqrt{N}) and decreases with the number N of performed fits.

In order to estimate the bias on the first iteration of the fit, 42 independent MC samples, generated with the parameter values given in Eq. 8.11 were used, while for the determination of the bias on the second iteration, the same amount of MC was generated with the following parameters:

$$\begin{aligned} f_s &= 5.75 & f'_s &= 0.84 \\ f''_s &= -0.31 & f_e &= 1.49 \\ \tilde{f}_p &= -0.59 & g_p &= 5.11 \\ g'_p &= 0.67 & g_e &= 0 \\ h_p &= -2.28 & h'_p &= 0 \\ a_0^0 &= 0.246 & f'_e &= -3.62, \end{aligned} \tag{9.1}$$

that correspond to the raw result of the second iteration. As an example, the 42 obtained values for a_0^0 in the MC test of the second iteration are shown in Figure 9.1.

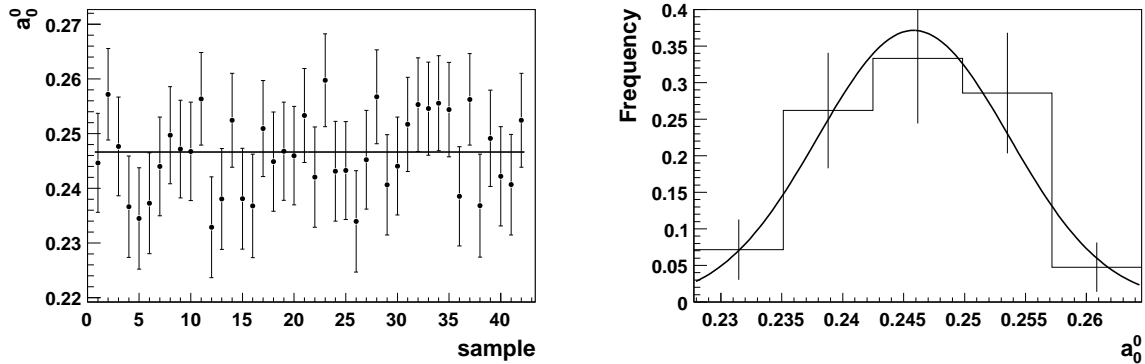


Figure 9.1.: Results obtained for a_0^0 in the MC tests of the second iteration. The 42 obtained results with their statistical uncertainty (left) are fitted with a constant, that corresponds to the weighted average. The frequency of occurrence (right) is compatible with the expected Gaussian distribution.

9.1.1. Corrected result

The bias was subtracted from the raw fit result and the uncertainty on the bias is considered as a systematic uncertainty. The bias for both iterations as well as the corrected results are reported in Table 9.1. Furthermore, it was observed that the RMS of the result distribution for each parameter, indicating, in the limit of an infinite number of performed fits, the expected statistical uncertainty, is compatible with the uncertainty given by MIGRAD.

9.2. Systematics of the fit method

Three effects have been considered as possible sources of systematics due to the fit method: the dependence of the result on the parameter values used for the MC generation, on the value of the threshold and on the number of bins in each variable. The fluctuation of the result due to the statistical uncertainty on the MC was also taken into account. The single contributions and the total systematic uncertainty for each parameter due to the fit method (computed as the sum in quadrature of the single contributions) are listed in Table 9.2.

9.2.1. Convergence

While the MC sample used for the first iteration was generated with parameters that turned out to be significantly different from the result of the data fit, in the second iteration the result changed only slightly and therefore no further iteration was performed. An estimate of the expected convergence of further iterations is given by the difference of the two results, after the bias subtraction, i.e. the difference between the values in the fifth and in the third column of Table 9.1.

9.2.2. Threshold

In a maximum likelihood fit, all bins containing at least one MC event are normally considered. Due to the limited MC statistics, however, a higher threshold was used, in order to reduce

Parameter	Bias 1 st iter.	Corr. 1 st iter.	Bias 2 nd iter.	Corr. 2 st iter.
f'_s/f_s	-0.005 ± 0.002	0.140 ± 0.013	$+0.013 \pm 0.002$	0.133 ± 0.013
f''_s/f_s	$+0.003 \pm 0.002$	-0.049 ± 0.013	-0.013 ± 0.002	-0.041 ± 0.013
f_e/f_s	$+0.046 \pm 0.008$	0.207 ± 0.051	$+0.038 \pm 0.008$	0.221 ± 0.051
f'_e/f_s	-0.206 ± 0.026	-0.409 ± 0.170	-0.171 ± 0.026	-0.459 ± 0.170
\tilde{f}_p/f_s	$+0.005 \pm 0.002$	-0.116 ± 0.013	$+0.009 \pm 0.002$	-0.112 ± 0.013
g_p/f_s	$+0.003 \pm 0.002$	0.894 ± 0.012	-0.003 ± 0.002	0.892 ± 0.012
g'_p/f_s	-0.009 ± 0.002	0.118 ± 0.015	$+0.003 \pm 0.002$	0.114 ± 0.015
h_p/f_s	-0.004 ± 0.004	-0.393 ± 0.028	-0.017 ± 0.004	-0.380 ± 0.028
a_0^0	0 ± 0.001	0.244 ± 0.009	$+0.001 \pm 0.001$	0.246 ± 0.009

Table 9.1.: Bias of the first (second column) and second (fourth column) iteration of the fit, determined from MC samples generated with the parameter values in Eqs. 8.11 and 9.1, respectively. The uncertainties on the bias are given by RMS/\sqrt{N} , with $N = 42$. In the third and fifth column, the corrected results, after the bias subtraction, are reported.

the effect of statistical fluctuations, which is expected to play an important role in the tails of the s_π and s_e distributions. The choice of the threshold is arbitrary and the stability of the result for different values has to be tested. On the other hand, even taking into account all non-empty bins, an effect similar to the variation of the threshold would be produced by using a higher or a lower MC statistics, so that the uncertainty would remain unchanged.

The threshold chosen for the standard result is 20 MC events before reweighting, in order to assure that the uncertainty on the bin content has a Gaussian behaviour. This value was changed to 0, 10, 30 and 40 for the fit of the data. For each threshold value, MC tests were performed and the result was corrected for the obtained bias. As an estimate of the systematic uncertainty due to the threshold, the maximum difference to the standard value for each parameter was used. In case of a difference within the uncorrelated statistical uncertainty (difference in quadrature of the statistical uncertainties), no systematic uncertainty was assigned.

9.2.3. Number of bins

If the resolution of the kinematic variables is not well reproduced by the MC, the result is expected to depend on the choice of the binning. This effect is due to the migration of the events from the bin in which they would be contained according to the values of the variables at generation level and the bin in which they are actually contained according to the reconstructed values of the variables. The migration probability depends also on the chosen bin size with respect to the resolution. The number of bins was varied separately

Parameter	Convergence	Threshold	Bins	MC stat.	Total	σ_{stat}
f'_s/f_s	± 0.007	—	± 0.002	± 0.002	± 0.008	± 0.013
f''_s/f_s	± 0.008	—	± 0.002	± 0.002	± 0.008	± 0.013
f_e/f_s	± 0.014	± 0.024	± 0.018	± 0.009	± 0.034	± 0.051
f'_e/f_s	± 0.050	—	± 0.054	± 0.033	± 0.081	± 0.170
\tilde{f}_p/f_s	± 0.004	± 0.009	± 0.004	± 0.003	± 0.011	± 0.013
g_p/f_s	± 0.002	± 0.008	± 0.008	± 0.003	± 0.012	± 0.012
g'_p/f_s	± 0.004	—	± 0.006	± 0.004	± 0.008	± 0.015
h_p/f_s	± 0.013	± 0.019	± 0.019	± 0.005	± 0.030	± 0.028
a_0^0	± 0.002	± 0.006	± 0.001	± 0.002	± 0.007	± 0.009

Table 9.2.: Contribution of the fit method to the systematic uncertainty. The convergence of the iterations (second column), the effect of threshold (third column) and binning (fourth column) variations, the MC statistics (fifth column) and the statistical uncertainty on the bias determination (Table 9.1) are included in the total uncertainty.

in each dimension, by $+2$, $+1$, -1 and -2 . Since in the MC a variation of the binning is expected to produce a negligible effect, no MC tests were performed and the RMS of the 20 fits was used as an estimate of the systematic uncertainty.

9.2.4. MC statistics

If no threshold would be used, the systematic uncertainty due to the limited MC statistics would be expected to be equal to the statistical uncertainty of the data fit divided by \sqrt{N} , where $N \simeq 42$ is the ratio between the number of MC events over the number of data events used for the fit. In order to properly take into account the effect of statistical fluctuations in the MC when using a threshold, the fit was repeated 100 times, varying randomly and independently the content of each bin in the two five-dimensional MC histograms, according to gaussian distributions with the mean values corresponding to the standard bin contents and the widths given by the statistical uncertainties on the bin contents. The RMS's of the result distributions for each parameters were taken as an estimate of the systematic uncertainty. In general the obtained uncertainties are slightly higher than the expected ones when performing the fit without any threshold.

9.3. Systematics from the uncertainty on efficiencies and corrections

9.3.1. Statistical uncertainty

The efficiencies and corrections applied to the K_{e4} MC (see Section 8.3) were obtained from data and MC samples containing a higher statistics than the samples used for the fit. Therefore the effect of their statistical uncertainties on the fit result is expected to be small. In order to properly take into account possible shape variations due to uncorrelated variations in each bin, the systematic uncertainty was estimated with the same method used for the MC statistics. The uncertainty on the efficiencies was computed assuming a binomial distribution, for values below one and as a confidence interval if the efficiency was equal one. For the corrections, the binomial uncertainty on each efficiency was propagated to the ratio, assuming them to be uncorrelated. The value of the efficiency or of the correction was then varied randomly in each bin according to a Gaussian distribution around the standard value, with a width given by the statistical uncertainties. For the efficiencies only values less or equal one were accepted.

In order to reduce the necessary CPU-time, the variation of the three trigger efficiencies was performed simultaneously. The LDA efficiency was varied together with the corrections for the electron ID, while a separate set of fits was performed for the pion ID correction. The resulting uncertainties are listed in Table 9.3. The main contribution to the effect of the trigger efficiency variation is due to the s_π dependence of the L2 efficiency, which can only be measured from $K_{2\pi D}$ events, i.e. with a sample about 140 times smaller than the $K_{3\pi}$ sample used to measure the dependence of the L2 efficiency on $\min(\Delta z_2)$ and about 18 times smaller than the one used to determine the L1 efficiency. For the electron ID the effect was found to be negligible (less than 0.001) for all parameters and is therefore not included in Table 9.3

9.3.2. Systematic uncertainty

In order to estimate the systematic uncertainty on the trigger efficiencies, the assumption that the same shape can be obtained even measuring them with different decay channels was tested. The dependence on $\min(r_{LKr})$ of the L1 trigger efficiency was measured using $K_{2\pi D}$ data events triggered by N-MBIAS, the ratio with the efficiency determined from $K_{3\pi}$ events was computed and fitted with a second degree polynomial (see Figure 9.2). The obtained function was implemented as a distortion of the MC distribution, additional to the standard corrections, into the fit procedure. The difference between the modified result and the standard one was used as an estimate of the systematic uncertainty, which was found to be below 0.001 for all parameters. The systematic uncertainty on the $\min(\Delta z_2)$ dependence of the L2 trigger efficiency was estimated in the same way, but starting from events triggered by C-PRE (see Figure 9.3). The obtained values are listed in the third column of Table 9.3. The s_π dependence of the L2 trigger efficiency could only be tested with K_{e4} events triggered by C-PRE, but, since their statistics is very limited, the ratio of the two efficiencies was found to be compatible with a constant value (see Figure 9.4) and therefore not considered as a contribution to the systematic uncertainty.

Parameter	Trigger (stat)	Trigger (syst)	Pion ID	Total	σ_{stat}
f'_s/f_s	± 0.010	± 0.007	± 0.001	± 0.012	± 0.013
f''_s/f_s	± 0.008	± 0.007	± 0.002	± 0.011	± 0.013
f_e/f_s	± 0.002	± 0.007	± 0.002	± 0.008	± 0.051
f'_e/f_s	± 0.009	± 0.001	± 0.005	± 0.010	± 0.170
\tilde{f}_p/f_s	—	± 0.001	± 0.001	± 0.001	± 0.013
g_p/f_s	± 0.002	± 0.001	—	± 0.002	± 0.012
g'_p/f_s	± 0.002	± 0.001	± 0.001	± 0.002	± 0.015
h_p/f_s	± 0.001	± 0.019	—	± 0.019	± 0.028
a_0^0	—	—	± 0.001	± 0.001	± 0.009

Table 9.3.: Effect of the statistical and systematic uncertainty on the trigger efficiency (second and third column) and of the statistical uncertainty on the pion ID correction (fourth column). The total contribution to the systematic uncertainty is computed as the sum in quadrature of the single components (fifth column).

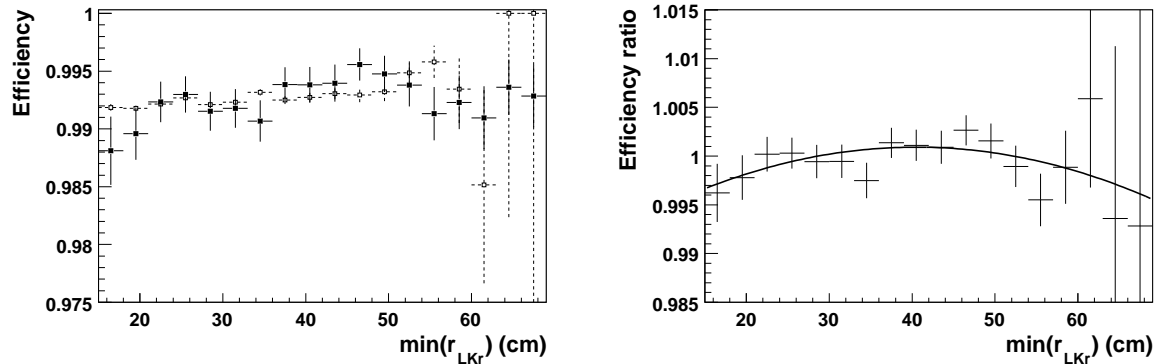


Figure 9.2.: L1 trigger efficiency as a function of $\min(r_{LKr})$, measured with selected $K_{2\pi D}$ data events, triggered by N-MBIAS (left, filled squares), compared with the standard efficiency from $K_{3\pi}$ events (left, open squares). The ratio of the two efficiencies (right), fitted with a second degree polynomial, is used to estimate the systematic uncertainty.

9.4. Systematics of the MC simulation and event selection

Since the fit of the form factors is based on the comparison between data and MC, it is important to check that acceptance and resolution are well simulated and how far the discrepancies fake a variation of the form factors.

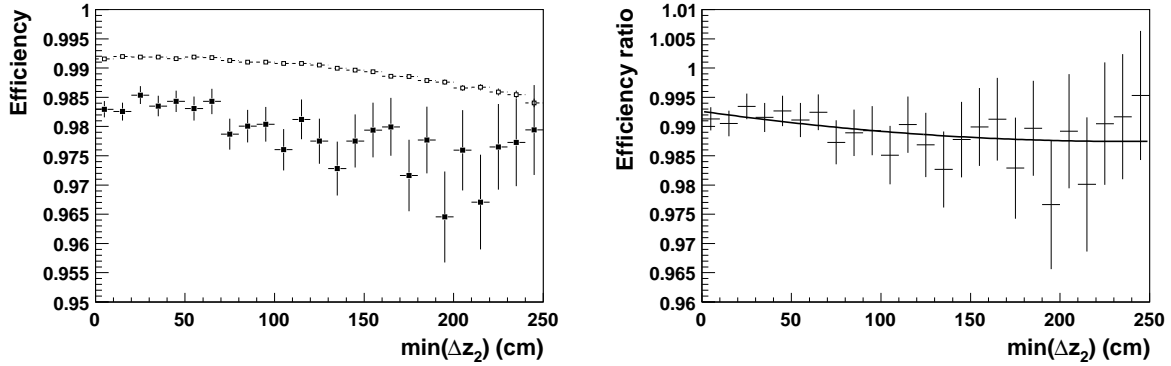


Figure 9.3.: L2 trigger efficiency as a function of $\min(\Delta z_2)$, measured with selected $K_{2\pi D}$ data events, triggered by C-PRE (left, filled squares), compared with the standard efficiency from $K_{3\pi}$ events (left, open squares). The ratio of the two efficiencies (right), fitted with a second degree polynomial, is used to estimate the systematic uncertainty.

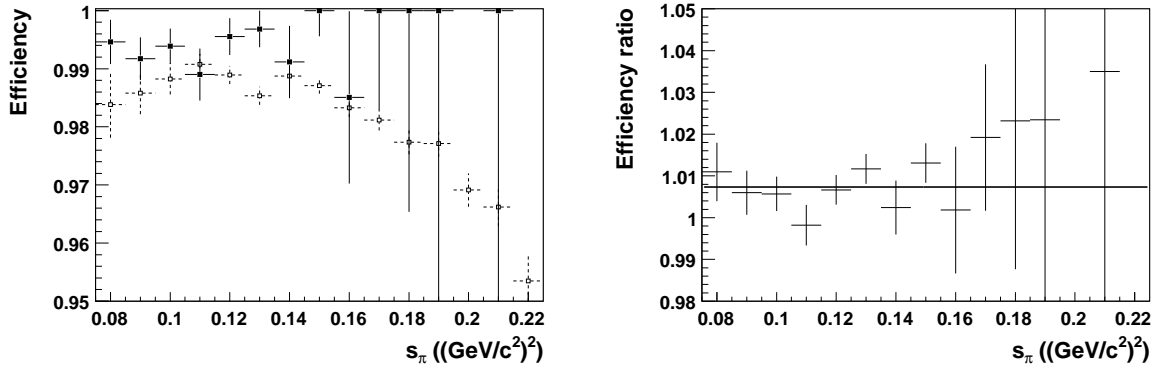


Figure 9.4.: L2 trigger efficiency as a function of s_π , measured with selected K_{e4} data events, triggered by C-PRE (left, filled squares), compared with the standard efficiency from $K_{2\pi D}$ events (left, open squares). The ratio of the two efficiencies (right) is compatible with a constant value.

9.4.1. Acceptance

In order to test how well the MC describes the acceptance, the selection criteria, for which a discrepancy between data and MC is expected and no correction is applied, were varied around the standard cut value.

The lower (up-stream) and upper (down-stream) cuts defining the z_{vtx} region, that were chosen to be at -18 m and 70 m, respectively (see Figure 7.1) were varied separately by -4 m, -2 m, +2 m and +4 m. Varying the lower cut shows the effect of the scattering at the collimator, that, due to the high geometrical acceptance of K_{e4} events at low z_{vtx} , could be significant. The upper cut rejects a much smaller fraction of events and its variation is therefore expected to have a negligible effect on the fit result.

The selection criterion, that is expected to be most sensitive to the simulation of the

detector geometry and detection efficiency, is the requirement of a radial distance between the track position at DCH1 and the centre of the beam pipe above 12 cm. Since no tracks are detected below 10 cm and no effect is expected above 14 cm, the cut value was varied by -2 cm, -1 cm, $+1$ cm and $+2$ cm.

A further known problem in the MC is the simulation of showers and shower fluctuations of pions. Apart from the E/p cut, for which a correction is applied, an effect could be seen in the cut on the distance between the track position extrapolated to the LKr and the cluster. This requirement is used in the tight electron ID (see Section 7.2.3) and in the extra cluster rejection (see Section 7.3), in both cases with a standard cut value of 20 cm. For each of the two selection criteria, the cut value was varied by -10 cm, -5 cm, $+5$ cm and $+10$ cm. A discrepancy between data and MC for the pion shower is expected to have different effects on the fit result for the two considered selection criteria: the requirement of a minimum distance between the electron cluster and the pion tracks acts on the angular distributions, while the accidental rejection of good K_{e4} events due to the mis-identification of pion shower fluctuation as photons is only expected to depend on the pion momentum.

As an estimate of the systematic uncertainty from each cut variation, the biggest discrepancy from the standard value, greater than the uncorrelated statistical uncertainty, was taken. The obtained values are listed in Table 9.4. In case of no discrepancy (difference within the uncorrelated statistical uncertainty) or of a difference less than 0.001, the contribution to the systematic uncertainty is considered to be negligible. Each single contribution is assumed to be not correlated with the other ones, since they are due to different effects. Therefore the total systematic uncertainty assigned for the MC acceptance is given by the sum in quadrature of the considered contributions.

9.4.2. Momentum resolution, kaon spectrum and background expectation

Any discrepancy between data and MC in the momentum resolution or in the kaon spectrum, as well as a not perfect description of the background expectation, would appear in the $m_{K_{e4}}$ reconstruction. Due to the choice of a tight standard cut in this variable, in order to reduce the background contamination, and to the many possible sources of systematic uncertainty, the variation of the accepted range in $m_{K_{e4}}$ is a very powerful test of the agreement between data and MC in the event reconstruction. The standard accepted mass window of $40 \text{ MeV}/c^2$, centred at the nominal kaon mass was varied to a width of 20, 30, 50 and $60 \text{ MeV}/c^2$ and the systematic uncertainty was estimated as the biggest discrepancy from the standard result for each parameter (see Table 9.5).

As a cross-check, a comparison was performed between data and MC for the electron and pion spectra. Electrons with the same charge as the kaon selected with loose ID were taken from $K_{2\pi D}$ events selected with kinematic cuts and tight ID for the other electron. The pion spectra for data and MC were obtained from $K_{3\pi}$ decays selected with kinematic cuts and loose pion ID for all the tracks in the vertex. The ratios between data and MC spectra were applied as a distortion to the K_{e4} MC spectra, separately for the electron and the pions. The differences between the standard result and the ones obtained with the modified MC spectra are shown in the third and fourth column of Table 9.5. As expected, they are small compared to the $m_{K_{e4}}$ cut variation, that should already include the effect of any discrepancy between data and MC in the momentum spectra of the decay products. Therefore only the result of the $m_{K_{e4}}$ cut variation is used as an estimate of the systematic uncertainty.

Parameter	z_{vtx} low	z_{vtx} up	r_{DCH1}	$d_{e\pi}$	$d_{\gamma tr}$	Total	σ_{stat}
f'_s/f_s	—	± 0.002	± 0.003	± 0.002	—	± 0.004	± 0.013
f''_s/f_s	± 0.002	± 0.002	± 0.003	± 0.001	—	± 0.004	± 0.013
f_e/f_s	—	± 0.003	± 0.005	± 0.014	± 0.014	± 0.020	± 0.051
f'_e/f_s	—	± 0.017	—	—	± 0.032	± 0.036	± 0.170
\tilde{f}_p/f_s	± 0.006	± 0.002	± 0.004	—	± 0.002	± 0.008	± 0.013
g_p/f_s	± 0.004	± 0.002	± 0.004	± 0.003	± 0.001	± 0.007	± 0.012
g'_p/f_s	± 0.004	± 0.003	± 0.002	± 0.004	± 0.002	± 0.007	± 0.015
h_p/f_s	—	± 0.002	± 0.008	± 0.004	± 0.003	± 0.010	± 0.028
a_0^0	± 0.002	± 0.001	± 0.002	± 0.002	—	± 0.004	± 0.009

Table 9.4.: Systematic uncertainty on the acceptance, estimated as the sum in quadrature of the contributions determined from the variation of the lower and upper z_{vtx} limits (second and third column), of the minimum radial distance between the track position at DCH1 and the centre of the beam pipe (r_{DCH1} , fourth column) and of the distance between any track and the electron ($d_{e\pi}$) and gamma ($d_{\gamma tr}$) cluster candidates, respectively (fifth and sixth column).

The background contamination, estimated from scaled wrong sign events (see Section 7.4.1), was varied by $\sigma_{tot} = \sigma_{stat} \oplus \sigma_{syst}$, corresponding to a relative uncertainty of about 10%. Due to the low background contamination with respect to the high number of bins, only a total scaling factor could be applied and the shape in the five-dimensional histogram could not be modified as would have been the case in a bin-by-bin variation. The difference to the standard result was for most of the parameters less than 0.001 (see Table 9.5). Also in this case the uncertainty due to the background estimate is considered to be included in the estimate from the $m_{K_{e4}}$ cut variation.

9.4.3. $K_{2\pi D}$ reconstructed as K_{e4}

To test the agreement between data and MC in the kinematic variables, K_{e4} events can not be used directly, since their form factors have to be measured. Instead, $K_{2\pi D}$ events selected with kinematic cuts, including the complete photon selection and pion reconstruction, as well as tight particle ID for both electrons and the pions were used to compute the Cabibbo-Maksymowicz variables in the same way as for K_{e4} events (see Section 8.1). The information on the photon energy and momentum was not taken from any signal in the detector, but computed as the missing momentum to the kaon and under the assumption of zero mass. The invariant mass of the kaon was computed and a window of $40 \text{ MeV}/c^2$ around the nominal kaon mass was accepted. Furthermore, s_π resulted to be the invariant mass squared of a pion and an electron and covered therefore a wider range than in K_{e4} (see Figure 9.5). Due to

Parameter	$m_{K_{e4}}$	(e spectrum)	(π spectrum)	(Background)	σ_{stat}
f'_s/f_s	± 0.005	± 0.002	—	—	± 0.013
f''_s/f_s	± 0.005	± 0.002	± 0.001	—	± 0.013
f_e/f_s	± 0.034	± 0.001	± 0.001	± 0.001	± 0.051
f'_e/f_s	± 0.126	± 0.001	± 0.001	± 0.002	± 0.170
\tilde{f}_p/f_s	± 0.005	± 0.001	—	—	± 0.013
g_p/f_s	± 0.006	—	—	—	± 0.012
g'_p/f_s	± 0.006	± 0.001	± 0.001	—	± 0.015
h_p/f_s	± 0.003	± 0.001	± 0.001	± 0.001	± 0.028
a_0^0	± 0.006	—	—	—	± 0.009

Table 9.5.: Estimate of the systematic uncertainty on the event reconstruction from the variation of the $m_{K_{e4}}$ cut (second column). As cross-checks, the effect of the electron (third column) and pion (fourth column) spectra and of the background estimate (fifth column) were tested, but they are assumed to be already included in the $m_{K_{e4}}$ cut variation and were therefore not added to it.

the kinematic of the decay, completely different from K_{e4} , to the geometrical acceptance of the detector and to the kinematic cuts already applied, the distributions are not as smooth as for K_{e4} .

When building the ratio between data and MC, after correcting the latter for the trigger and particle ID efficiencies, any discrepancy must be due to a difference in the resolution of the variables themselves or in the simulation of the kaon spectrum, since the matrix element of the π_D^0 decay is well known (see Section 6.2.2). Considering the ratios shown in Figure 9.6, it is evident that the biggest discrepancy is due to the resolution. Modifying the MC resolution independently in each single variable by an overall factor, without changing its dependence on the value of the variable itself, a slight improvement could be obtained. The best agreement (minimum χ^2 when fitting with a constant) was obtained for a relative correction to the resolution of -0.1% for s_π , -0.4% for s_e , -0.2% for $\cos\theta_\pi$, -1.0% for $\cos\theta_e$ and $+1.1\%$ for ϕ . These variations of the resolution were also applied, one by one, to the MC in the fit of the K_{e4} form factors, in order to check its sensitivity. As expected, the discrepancy from the standard result was smaller than the one due to the variation of the binning, that already takes into account the effect of the resolution, including its dependence on the value of the variable, in K_{e4} .

The corrected data over MC ratios of the $K_{2\pi D}$ distributions were fitted with a constant and only $\cos\theta_\pi$ was found to be compatible with it. For the other variables the fit was repeated with a second degree polynomial (see Figure 9.6). The four obtained curves were used as distortions of the K_{e4} MC in the fit of the form factors and the discrepancy from the standard result in each parameter is considered as a systematic uncertainty (see Table 9.6,

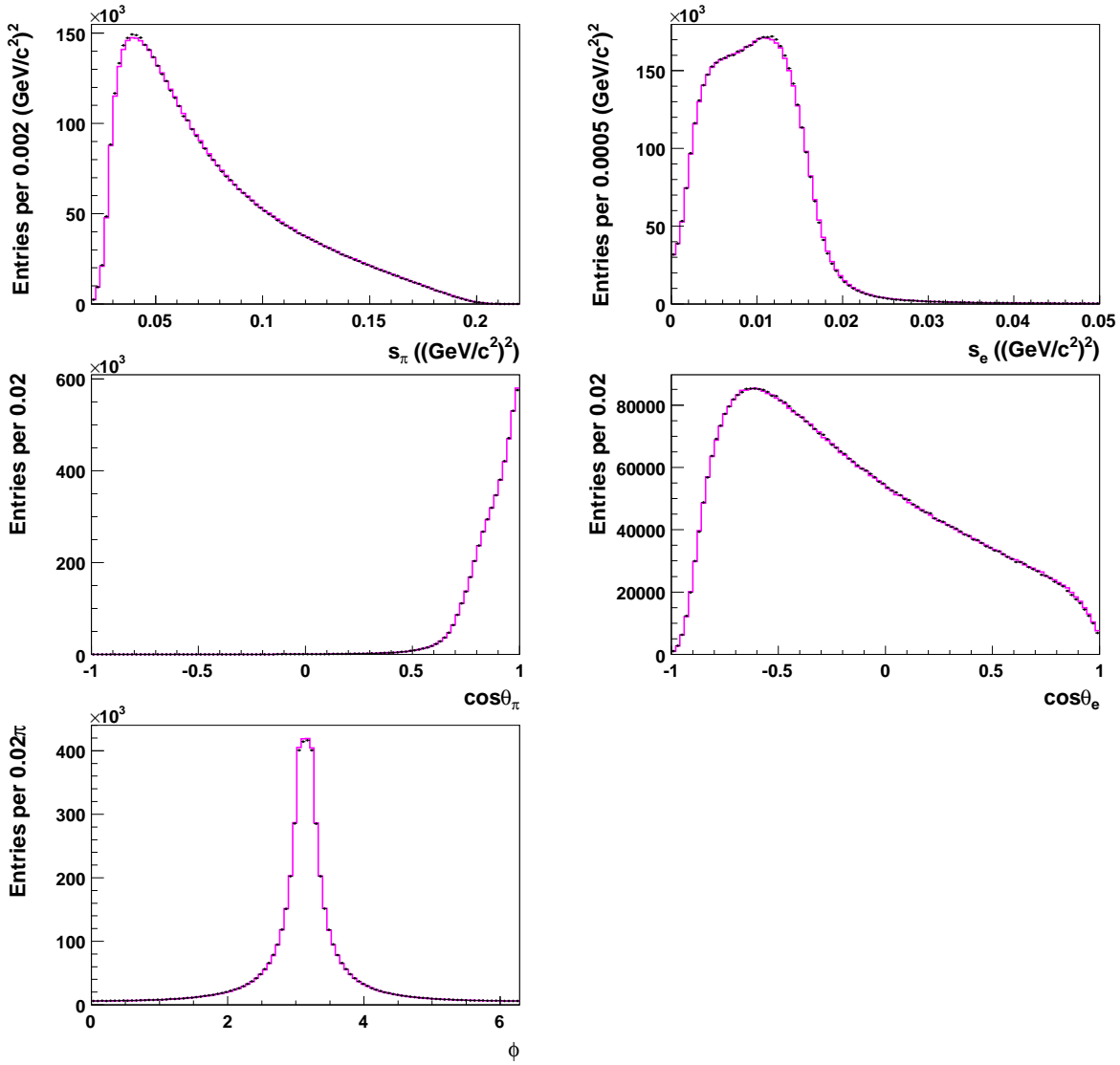


Figure 9.5.: Distributions of $K_{2\pi D}$ data (black points) and MC (magenta open histograms) events in the Cabibbo-Maksymowicz variables. The events are selected with kinematic cuts and tight particle ID for electrons and pion. The MC is normalised to the area of the data distribution. The background contribution is assumed to be negligible.

discrepancies smaller than 0.001 are neglected). Since most of the acceptance and resolution effects should already have been taken into account in the cut variations and because of the different selection of the $K_{2\pi D}$ events, that could also induce a discrepancy not present in K_{e4} , adding this uncertainty as an independent one is quite conservative. On the other hand, some uncertainties were found to be bigger than estimated in the previous studies and it is not easy to prove which effects are specific of the $K_{2\pi D}$ selection and which are already included in the other tests. Furthermore, this is the only possibility to check the agreement

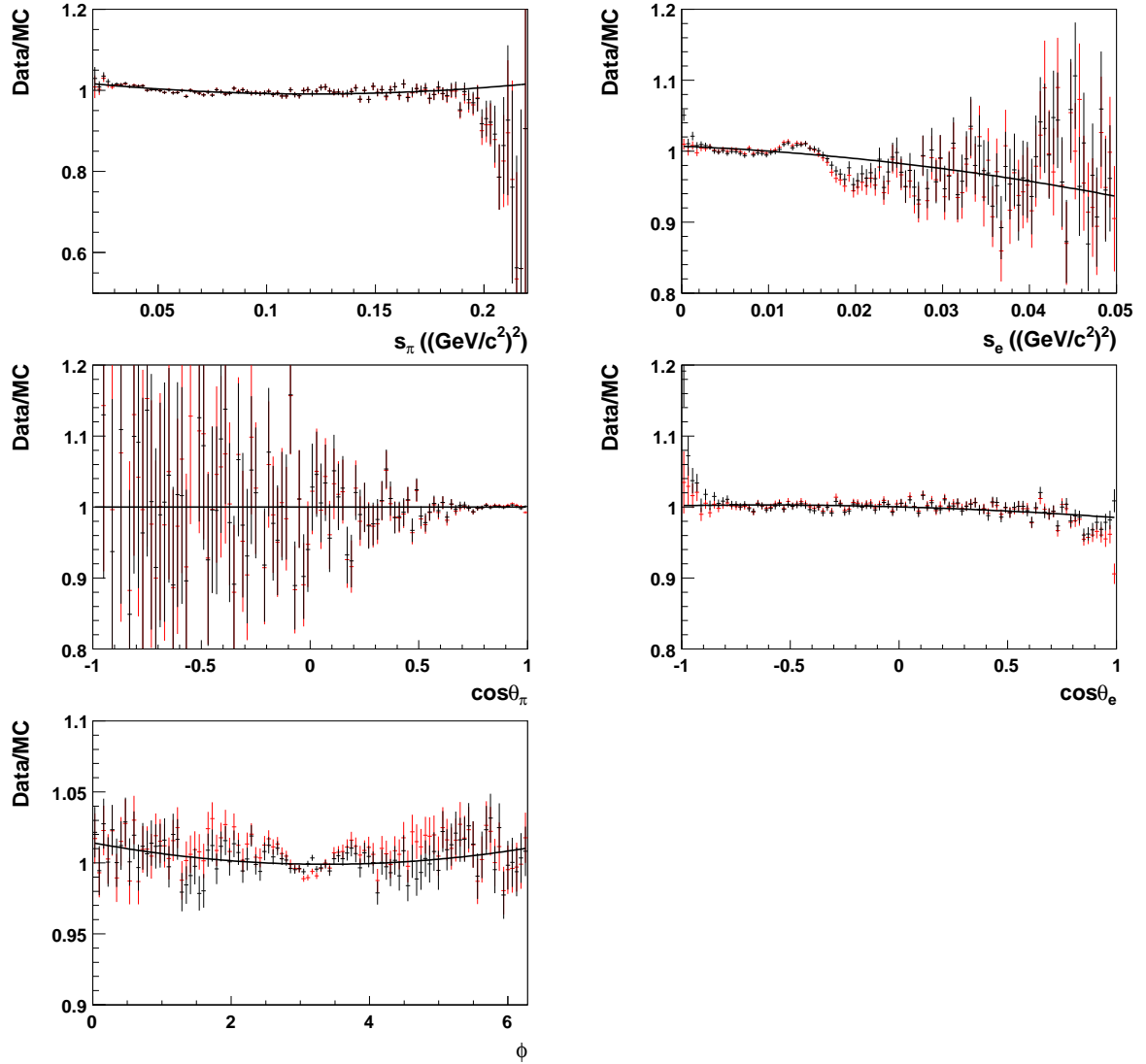


Figure 9.6.: Data/MC ratios of the distributions shown in Figure 9.5 with (black crosses) and without (red crosses) the resolution correction. The black crosses are fitted with a constant in $\cos\theta_\pi$ and with a second degree polynomial in the other variables.

between data and MC directly in the Cabibbo-Maksymowicz variables.

9.4.4. Fit of subsamples

The stability of the fit was tested with respect to the kaon charge (K^\pm), the direction of the magnetic field in the dipole magnet of the spectrometer (B^\pm) and in the achromat (A^\pm) and the three super-samples (SS1, SS2, SS3, see Section 7.1). For each of the four tests, the data and MC samples were subdivided into two or three subsamples and fitted separately.

Since the MC was generated according to the population per run of the data and in each simulated run the directions of B and A were taken into account as well as the kaon spectrum,

Parameter	s_π	s_e	$\cos \theta_e$	ϕ	Total	σ_{stat}
f'_s/f_s	± 0.010	± 0.001	± 0.001	—	± 0.010	± 0.013
f''_s/f_s	± 0.009	—	± 0.001	—	± 0.009	± 0.013
f_e/f_s	± 0.001	± 0.015	± 0.002	—	± 0.015	± 0.051
f'_e/f_s	± 0.003	± 0.089	± 0.002	± 0.002	± 0.089	± 0.170
\tilde{f}_p/f_s	—	± 0.009	± 0.004	± 0.002	± 0.010	± 0.013
g_p/f_s	± 0.002	± 0.011	± 0.003	± 0.001	± 0.012	± 0.012
g'_p/f_s	—	± 0.007	± 0.001	± 0.001	± 0.007	± 0.015
h_p/f_s	± 0.001	—	± 0.016	± 0.005	± 0.017	± 0.028
a_0^0	—	± 0.001	—	± 0.003	± 0.003	± 0.009

Table 9.6.: Estimate of the systematic uncertainty on the agreement between data and MC from the ratio of the $K_{2\pi D}$ distributions in the kinematic variables. No discrepancy was found for $\cos \theta_\pi$. The contribution of each variable is assumed to be independent from the others and the total uncertainty is computed as the sum in quadrature of the single contributions.

no disagreement is expected between the subsamples with different B and A or between the different super-samples, if the tuning of the simulation is correct. For K^+ and K^- , the only difference between the form factors is due to CP violation (see Section 2.4.4), which is expected to be a much smaller effect than it could be resolved with the present statistics. Therefore also for this test no discrepancy is expected between the two subsamples. The obtained fit results for each parameter are shown in Figures 9.7 and 9.8.

While the mean values of each parameter between K^+ and K^- correspond to the standard result, this is in general not the case for the other tests. This is due to the fact that, using a smaller MC sample and the same absolute threshold value, the number of bins actually considered in the fit is reduced. The expected effect is the same as for a variation of the threshold and it was found to be compatible with it. Since for K^+ and K^- separate histograms are used, this test is not affected.

In order to determine the level of agreement between the subsamples in each test, the χ^2 with respect to the weighted average of each parameter was computed, taking into account the correlations [128]:

$$\chi^2 = \sum_{m=1}^{N_{meas}} \sum_{i,j=1}^{N_{par}} (x_i^m - \bar{x}_i) V_{ij}^{-1}(m) (x_j^m - \bar{x}_j), \quad (9.2)$$

where N_{meas} is the number of performed fits in the test (2 or 3), N_{par} the total number of free parameters (10), x_i^m the obtained result for parameter i in the m^{th} fit, \bar{x}_i the weighted average for the i^{th} parameter over the fits and $V(m)$ the error matrix obtained in fit m . The

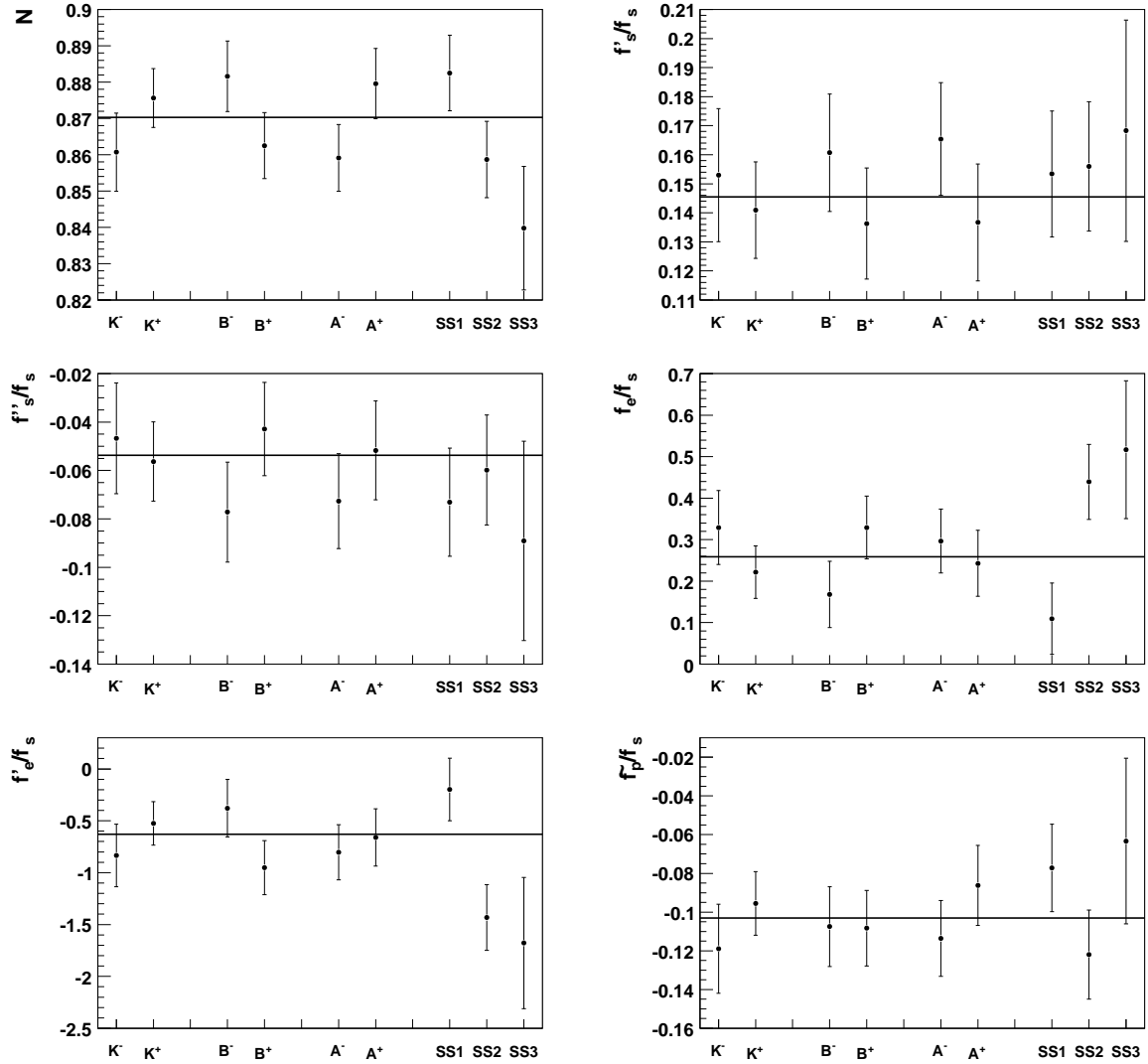


Figure 9.7.: Fit result of the subsamples indicated on the x -axis for the parameters of the F form factor. The solid lines represent the values of the standard result.

obtained values of χ^2/ndf are: 10.2/10 for K^\pm , 22.5/10 for B^\pm , 8.8/10 for A^\pm and 37.9/20 for the super-samples. If the bad agreement between B^+ and B^- is of systematic nature, a different behaviour of the data/MC ratio in the kinematic variables is expected to be seen. A double ratio of the data/MC ratios (B^+/B^-) for K_{e4} and $K_{2\pi D}$ events was built and the obtained distributions in the five kinematic variables were found to be compatible with a constant value. A similar check was performed between the super-samples, building for each one the double ratio with respect to the remaining two and again all distribution were found to be compatible with a constant. Therefore, with the present statistics it can not be concluded that the observed disagreements are of systematic nature and no uncertainty will be added to the result.

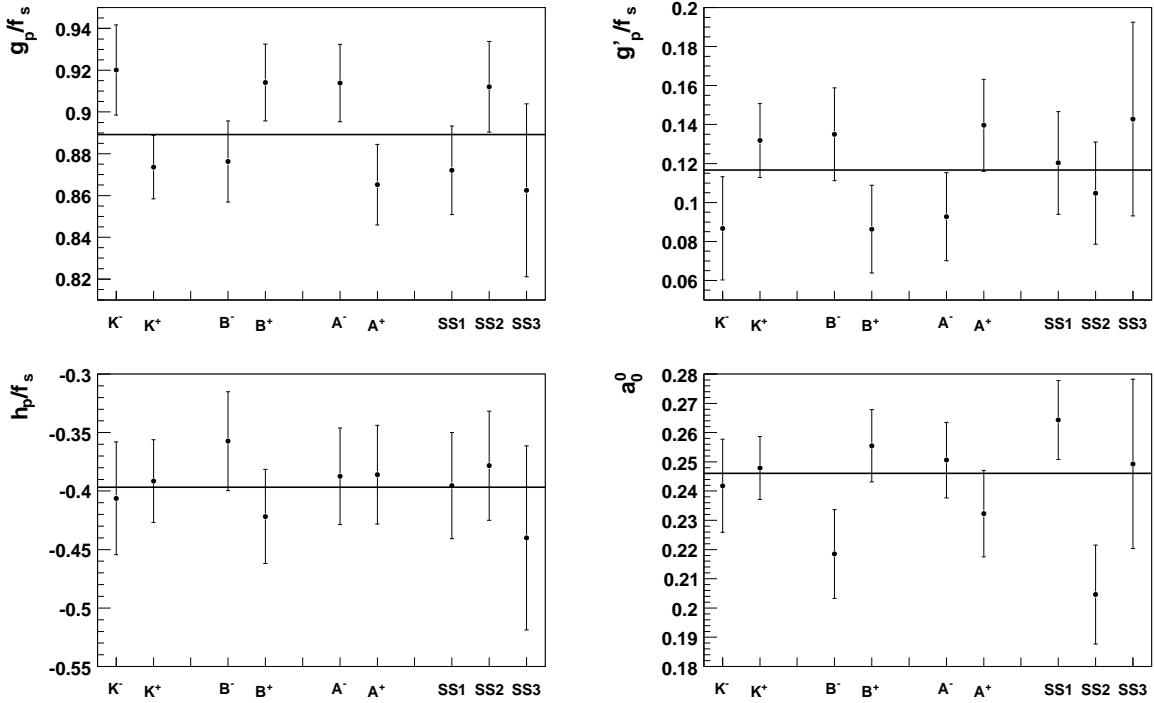


Figure 9.8.: Fit result of the subsamples indicated on the x -axis for the parameters of the G and H form factors and for a_0^0 . The solid lines represent the values of the standard result.

9.4.5. Alternative electron identification and computation of the kinematic variables

Instead of the LDA (see Section 7.2.3), a neural network (NN) was used to identify electrons and reject pions. The neural network is a function that can be called for each electron candidate consisting of a track with an associated cluster in the LKr. It uses 10 quantities as input (E/p , distance between cluster and track extrapolated to the LKr, shower width, momentum, shower width in x and y , slopes of the track after the magnet and the x and y components of the distance between track and cluster), has three hidden layers and produces as output a number between 0 (for pions) and 1 (for electrons) [129]. The NN has, with respect to the LDA, a better rejection power, but it uses more variables and it is not clear if the assumption that the efficiency only depends on the momentum of the electron is still valid and how far it biases the distributions of the kinematic variables. Since the background level can already be kept under control using the LDA, this was chosen as the standard selection criterion, while the NN is only used as a systematic check with a cut value of 0.8.

Following the same procedure as for the LDA, but without distinguishing between the charges of the tracks, the NN efficiency was measured as a function of the electron momentum from $K_{2\pi D}$ data events selected with kinematic cuts and tight particle ID for the pion and both electrons and a correction was obtained as the ratio between the efficiencies of K_{e4} and $K_{2\pi D}$ MC events (see Section 8.3). The obtained efficiency and correction are shown in

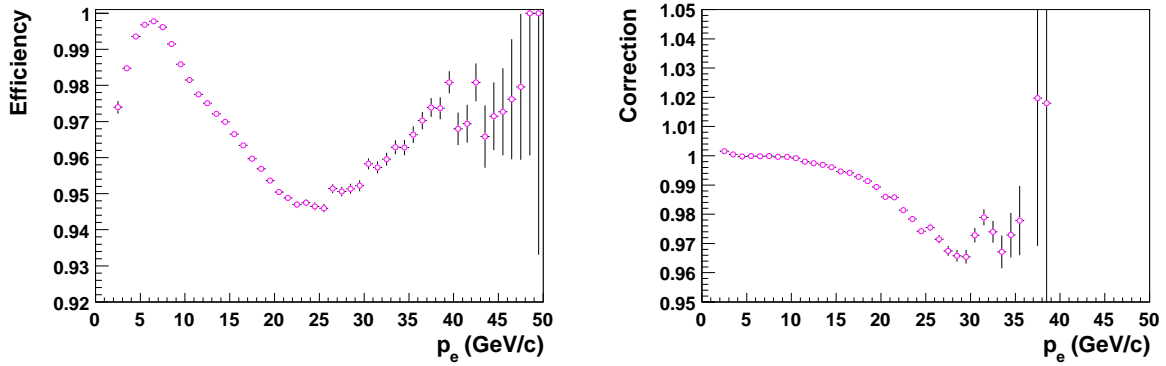


Figure 9.9.: Efficiency (left) of the neural network as a function of the electron momentum, obtained from $K_{2\pi D}$ data events selected with kinematic cuts and tight particle ID for the pion and both electrons and correction (right) to the efficiency given by the ratio of the efficiencies for K_{e4} and $K_{2\pi D}$ MC events.

Figure 9.9.

Applying the NN instead of the LDA to the data, 356,309 K_{e4} candidates were selected, with an estimated background contamination of 962 events (0.27%). The difference between the fit result of this sample and the standard one is considered as an estimate of the systematic uncertainty on the electron ID and is reported in Table 9.7.

As an alternative way of computing the kinematic variables, after applying the complete standard selection, including the cut on $m_{K_{e4}}$, instead of fixing the kaon momentum to 60 GeV/c along the z axis, the kaon mass and the kaon direction along the z axis were fixed and the kaon momentum was obtained as the one solution of the resulting quadratic equation closest to 60 GeV/c . Events with a discriminant of the quadratic equation below $-20 \text{ (GeV}/c)^2$ were rejected ($\sim 5\%$ loss of statistics), while negative discriminants between $-20 \text{ (GeV}/c)^2$ and 0 were set to 0 in order to be able to solve the equation. The main difference in the obtained values of the kinematic variables is expected to be seen in s_e , but some difference could appear also in the angles, since they require a boost into the kaon rest frame and the kaon has in general a different momentum than in the standard reconstruction. The discrepancy to the standard fit result (i.e. any difference greater than the uncorrelated statistic uncertainty) gives an estimate of the systematic uncertainty on the computation of the kinematic variables and is shown in Table 9.7.

9.4.6. Radiative and Coulomb corrections

In order to estimate the uncertainty on the radiative corrections, a fraction of the difference between the result obtained with a MC sample without radiative corrections and the standard one is taken. The ratio between the uncertainty on the PHOTOS implementation of the radiative corrections and their total effect can be measured in $K_L \rightarrow \pi^\pm e^\mp \nu$ decays comparing PHOTOS to the KLOR package [130], which was explicitly tuned for this decay. The ratio was found to be 1/9 [131]. Since no other implementation of the radiative corrections exists for K_{e4} decays, 42 samples of MC generated with the parameter values given in Eq. 9.1 and without radiative corrections were fitted as pseudo-data with the standard MC and 1/9 of the

Parameter	NN	Other reconstruction	Total	σ_{stat}
f'_s/f_s	± 0.010	± 0.004	± 0.011	± 0.013
f''_s/f_s	—	—	—	± 0.013
f_e/f_s	± 0.019	± 0.087	± 0.089	± 0.051
f'_e/f_s	± 0.040	± 0.258	± 0.261	± 0.170
\tilde{f}_p/f_s	—	± 0.014	± 0.014	± 0.013
g_p/f_s	—	± 0.014	± 0.014	± 0.012
g'_p/f_s	± 0.008	± 0.015	± 0.017	± 0.015
h_p/f_s	± 0.020	± 0.011	± 0.023	± 0.028
a_0^0	± 0.006	± 0.001	± 0.006	± 0.009

Table 9.7.: Contribution to the systematic uncertainty from the electron ID (second column) and the computation of the kinematic variables (third column). As an alternative electron identification, a neural network (NN) was applied instead of the standard LDA. The kinematic variables were computed assuming a kaon with the nominal mass flying along the z axis, whose momentum (“other reconstruction”) was determined as the solution of the resulting quadratic equation closest to 60 GeV/ c .

difference to the result obtained in the MC tests (using MC with the same parameter values and with radiative corrections as pseudo-data) was taken as an estimate of the systematic uncertainty (see Table 9.8). Contributions to the systematic uncertainties below 0.001 are, as usual, neglected.

Since for the Coulomb correction no other approximations are made, than the assumption that the interaction between pion and electron can be neglected, each event of the standard MC sample was reweighted with the product of the two terms describing the repulsive $\pi^\pm e^\pm$ and the attractive $\pi^\mp e^\pm$ interaction (see Eq. 6.7). The difference of the fit with the reweighted MC with respect to the standard one gives an estimate of the systematic uncertainty and the contributions greater or equal 0.001 are shown in Table 9.8.

9.5. Theoretical uncertainty and different constraints on a_0^0

The general formulation of the matrix element (see Section 2.4.2) is not affected by any theoretical uncertainty and its expansion into partial waves and into polynomials in s_π and s_e is truncated according to the statistical sensitivity of the experiment and not according to any theoretical model. The constraint between a_0^2 and a_0^0 (see Eq. 2.67), instead, has an uncertainty that has to be taken into account in the fit result.

Parameter	Radiative	Coulomb	Total	σ_{stat}
f'_s/f_s	± 0.015	—	± 0.015	± 0.013
f''_s/f_s	± 0.010	± 0.001	± 0.010	± 0.013
f_e/f_s	± 0.014	± 0.002	± 0.014	± 0.051
f'_e/f_s	± 0.014	± 0.005	± 0.015	± 0.170
\tilde{f}_p/f_s	± 0.005	± 0.002	± 0.005	± 0.013
g_p/f_s	± 0.006	—	± 0.006	± 0.012
g'_p/f_s	± 0.001	± 0.003	± 0.003	± 0.015
h_p/f_s	± 0.007	± 0.018	± 0.019	± 0.028
a_0^0	—	± 0.001	± 0.001	± 0.009

Table 9.8.: Contributions to the systematic uncertainty from the uncertainty on the radiative correction implementation (second column), estimated as 1/9 of the difference between the fit performed with a MC without radiative corrections and the standard one, and from the neglected Coulomb interaction between pions and electron.

9.5.1. Uncertainty on the constraint between a_0^2 and a_0^0

The uncertainty on a_0^0 due to the width of the allowed band in Eq. 2.67 is obtained by repeating the fit with the constraint varied by its uncertainty. As expected, only the obtained value of a_0^0 changed and the theoretical uncertainty was estimated to be ± 0.002 , i.e. the difference to the standard result (see Figure 9.10).

9.5.2. Universal band and free a_0^2

As a cross check, the fit was repeated using as a constraint the universal curve given in Eq. 2.65. The theoretical uncertainty on a_0^0 is then much bigger and the obtained result

$$a_0^0 = 0.258 \pm 0.009 \text{ (stat)} \pm 0.018 \text{ (theor)}, \quad (9.3)$$

is compatible with the standard one, as expected, since the tighter constraint is included in the universal band.

Furthermore, the fit was performed leaving both a_0^0 and a_0^2 as free parameters. As could be already seen in the results obtained with different constraints, the correlation between the two scattering length is very strong (0.958) and the sensitivity to both of them poor:

$$a_0^0 = 0.281 \pm 0.025 \text{ (stat)}, \quad a_0^2 = -0.015 \pm 0.016 \text{ (stat)}. \quad (9.4)$$

The standard result is 1.5σ away from the one obtained without applying any constraint. As uncorrelated uncertainty, the difference in quadrature between the statistical uncertainties on the two results is considered, while the theoretical uncertainty on the standard result can

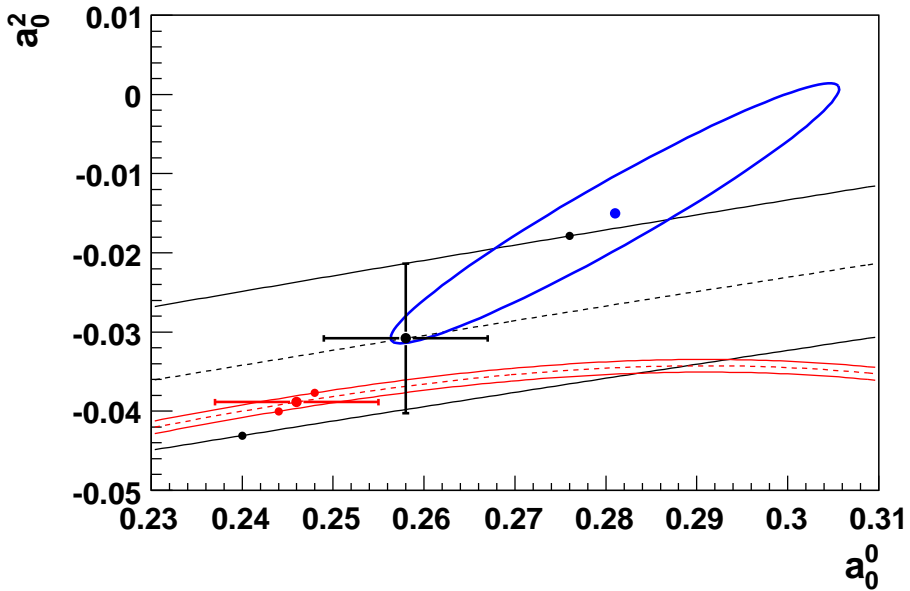


Figure 9.10.: Fit results for a_0^0 with the constraint of Eq. 2.67 (red point with error bar), with the constraint of the universal curve in Eq. 2.65 (black point with error bar) and without any constraint (blue ellipse). The error bars include for a_0^0 only the statistical uncertainty and for a_0^2 they are fixed to the width of the allowed band. The blue ellipse is the $1\sigma_{stat}$ contour, taking into account the correlation between the two scattering lengths. The points without error bars indicate the results obtained using as constraint the borders of the allowed bands. The difference in a_0^0 between the values obtained at the borders and the one at the centre is considered as the theoretical uncertainty on a_0^0 .

be neglected. Actually, the solutions to the Roy equations used for the fit are only valid inside the universal band and a fit result outside it should not be considered at all. However, the obtained result was so close to the border of the band, that it can be at least taken as an indication of a tendency toward higher values of a_0^2 than the ones allowed by the tighter constraint, but, with the present statistics, still compatible with it.

9.5.3. $\delta_0^0 - \delta_1^1$ as a function of s_π

Since a_0^0 is not strongly correlated to the other parameters and it depends on the shape of the $\delta = \delta_0^0 - \delta_1^1$ distribution as a function of s_π , the fit can also be performed in two steps, considering the value of δ in each bin of s_π as a free parameter. In this way the agreement between the experimental δ distribution and any theoretical model can be tested without having to repeat the complete fit procedure.

The obtained δ distribution from the fit of the data performed in two steps is shown in Figure 9.11. The bias on the obtained values was determined from MC tests and subtracted from the raw result. After the correction, the distribution was fitted with the same formula implemented in the standard fit and the same value for a_0^0 was obtained, with a χ^2 of 9.7/11.

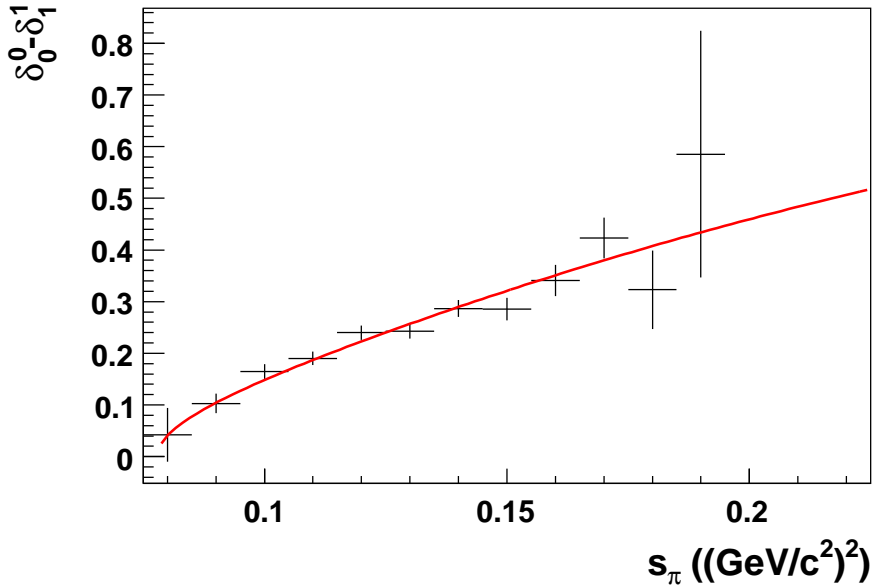


Figure 9.11.: $\delta = \delta_0^0 - \delta_1^1$ distribution as a function of s_π , obtained by fitting the δ value for each bin as a free parameter. The determination of a_0^0 was performed as a second step, fitting the distribution with the red line.

9.6. Summary of the systematic and theoretical uncertainties

All the contributions to the systematic uncertainty can now be summarised and added in quadrature in order to obtain the total uncertainty. In Table 9.9 all the contributions from Tables 9.2–9.8 are listed, together with the total systematic uncertainty and the statistical one. The largest contribution for each parameter is marked in red.

The main source of systematic uncertainty is the discrepancy in the results obtained with different assumptions on the kaon momentum for the calculation of the kinematic variables (column 4 in Table 9.9). As expected, this contribution is particularly important for the parameters depending on s_e : f_e/f_s and f'_e/f_s , but it turns out to have a sizeable effect also on the parameters depending on $\cos\theta_\pi$: \tilde{f}_p/f_s , g_p/f_s and g'_p/f_s . For h_p/f_s and a_0^0 the biggest contribution comes from the fit method, while the systematic uncertainty of f'_s/f_s is dominated by the uncertainty on the radiative and Coulomb corrections and the one of f''_s/f_s by the uncertainty on the trigger efficiency and in particular its dependence on s_π .

In general, there is not only one strongly dominating contribution: the four listed in Table 9.9 as well as the variation of the $m_{K_{e4}}$ cut and the comparison between data and MC in $K_{2\pi D}$ are the most important effects and, for most of the parameters, at least two or three of them are of the same size.

The theoretical uncertainty is given by the width of the allowed band for a_0^2 as a function of a_0^0 . It affects therefore only a_0^0 and is estimated to be ± 0.002 .

Par.	Fit	Efficiency	Acceptance	$m_{K_{e4}}$	data/MC	Other rec.	Radiative corr.	Total	σ_{stat}
f'_s/f_s	± 0.008	± 0.012	± 0.004	± 0.005	± 0.010	± 0.011	± 0.015	± 0.026	± 0.013
f''_s/f_s	± 0.008	± 0.011	± 0.004	± 0.005	± 0.009	± 0.002	± 0.010	± 0.020	± 0.013
f_e/f_s	± 0.034	± 0.008	± 0.020	± 0.134	± 0.015	± 0.089	± 0.014	± 0.105	± 0.051
f'_e/f_s	± 0.081	± 0.010	± 0.036	± 0.126	± 0.089	± 0.261	± 0.015	± 0.316	± 0.170
\tilde{f}_p/f_s	± 0.011	± 0.001	± 0.008	± 0.005	± 0.010	± 0.014	± 0.005	± 0.023	± 0.013
g_p/f_s	± 0.012	± 0.002	± 0.007	± 0.006	± 0.012	± 0.014	± 0.006	± 0.025	± 0.012
g'_p/f_s	± 0.008	± 0.002	± 0.007	± 0.006	± 0.007	± 0.017	± 0.003	± 0.022	± 0.015
h_p/f_s	± 0.030	± 0.019	± 0.010	± 0.003	± 0.017	± 0.023	± 0.019	± 0.050	± 0.028
a_0^0	± 0.007	± 0.001	± 0.004	± 0.006	± 0.003	± 0.006	± 0.001	± 0.012	± 0.009

Table 9.9: Overview of the contributions to the estimated systematic uncertainty. The total systematic uncertainty is given by the sum in quadrature of the single components. The largest contribution for each parameter is marked in red.

10. Result and discussion

The final fit result with all the uncertainties is presented in Section 10.1. Since the parameter N only measures the relative normalisation of the data with respect to the MC, no systematic uncertainty was determined for it and it will not be included in the result. The obtained result will then be compared (see Section 10.2) to the published ones, listed in Section 2.5 and to the theoretical predictions (see Section 10.3). Finally, a brief outlook on the possible improvements of the sensitivity is given in Section 10.4.

10.1. Fit result

The fitted values of the form factor parameters are:

$$\begin{aligned}
f'_s/f_s &= 0.133 \pm 0.013 \text{ (stat)} \pm 0.026 \text{ (syst)}, \\
f''_s/f_s &= -0.041 \pm 0.013 \text{ (stat)} \pm 0.020 \text{ (syst)}, \\
f_e/f_s &= 0.221 \pm 0.051 \text{ (stat)} \pm 0.105 \text{ (syst)}, \\
f'_e/f_s &= -0.459 \pm 0.170 \text{ (stat)} \pm 0.316 \text{ (syst)}, \\
\tilde{f}_p/f_s &= -0.112 \pm 0.013 \text{ (stat)} \pm 0.023 \text{ (syst)}, \\
g_p/f_s &= 0.892 \pm 0.012 \text{ (stat)} \pm 0.025 \text{ (syst)}, \\
g'_p/f_s &= 0.114 \pm 0.015 \text{ (stat)} \pm 0.022 \text{ (syst)}, \\
h_p/f_s &= -0.380 \pm 0.028 \text{ (stat)} \pm 0.050 \text{ (syst)}, \\
a_0^0 &= 0.246 \pm 0.009 \text{ (stat)} \pm 0.012 \text{ (syst)} \pm 0.002 \text{ (theor)},
\end{aligned} \tag{10.1}$$

using the parametrisation given in Eq. 6.2 and the constraint between a_0^0 and a_0^2 in Eq. 2.67. The value of a_0^2 can then be computed:

$$a_0^2 = -0.0389 \pm 0.0017 \text{ (stat)} \pm 0.0022 \text{ (syst)} \pm 0.0008 \text{ (theor)}. \tag{10.2}$$

It can be noticed that for all parameters the uncertainty is dominated by the systematics. This is mainly due to the discrepancies still present between data and MC, since the fit of the form factors relies completely on the simulation.

10.2. Comparison with previous results

In [35] both the form factors and the branching ratio of the K_{e4} decay were measured, so that the absolute values of the parameters could be obtained and not only the ones relative to f_s as is the case for the analysis presented in this thesis. Dividing the parameters in Eqs. 2.91–2.92 by f_s and assuming all uncertainties to be uncorrelated, the following values are obtained:

$$f'_s/f_s = 0.184 \pm 0.017 \text{ (stat)} \pm 0.069 \text{ (syst)},$$

$$\begin{aligned}
 f_s''/f_s &= -0.103 \pm 0.021 \text{ (stat)} \pm 0.070 \text{ (syst)}, \\
 g_p/f_s &= 0.810 \pm 0.009 \text{ (stat)} \pm 0.017 \text{ (syst)}, \\
 g_p'/f_s &= 0.117 \pm 0.017 \text{ (stat)} \pm 0.007 \text{ (syst)}, \\
 h_p/f_s &= -0.513 \pm 0.033 \text{ (stat)} \pm 0.036 \text{ (syst)}, \\
 \tilde{f}_p/f_s &= -0.059 \pm 0.017 \text{ (stat)} \pm 0.047 \text{ (syst)}, \\
 f_e/f_s &= -0.056 \pm 0.018 \text{ (stat)} \pm 0.042 \text{ (syst)},
 \end{aligned} \tag{10.3}$$

where the first five parameters were fitted at the same time, while the last two were added, as a sensitivity test, one at a time and are not included in the standard result.

The parameter values with the total uncertainty measured in this analysis and by BNL E865 are listed in Table 10.1. A comparison between the two results can not be easily done, since the fits were performed with a different number of free parameters. In particular, g_p/f_s is strongly correlated with \tilde{f}_p/f_s , that is fitted as free parameter in the analysis presented here, while it is fixed to zero in the fit performed by the BNL E865 collaboration. Considering the sign of the correlation factor, the value of g_p/f_s that would be obtained fixing \tilde{f}_p/f_s to zero is expected to be smaller than the standard one and therefore closer to the one measured by the BNL experiment. Similarly for f_e/f_s , that is correlated to f_e'/f_s , the value would decrease when fixing the higher order parameter to zero. Due to the poor sensitivity and high systematic uncertainty, no discrepancy is expected, since both measurements are compatible with zero within 2 times the total uncertainty. For f_s'/f_s , f_s''/f_s , g_p'/f_s , h_p/f_s and \tilde{f}_p/f_s , instead, compatible results are expected, since the correlations with the additional parameters are small (see Table 8.3). The measured values agree for h_p/f_s within 1.8 times the total uncertainty, while for the other parameters the difference is smaller than the total uncertainty.

In this analysis the parameters f_s'/f_s and f_s''/f_s could be measured with a smaller uncertainty, both statistical and systematic. Even if the two samples of data are of the same total size, NA48/2 can accept more events with high s_π , so that the statistical uncertainty on the parameters depending on this variable is smaller. The sensitivity on f_e/f_s and, for this analysis, on f_e'/f_s is in both experiments limited by the systematic uncertainty. The larger statistical uncertainty on f_e/f_s in the result presented in this thesis is only due to the correlation with the quadratic term in s_e . Analogously, g_p/f_s has a higher statistical uncertainty due to the correlation with \tilde{f}_p/f_s , while g_p'/f_s is again a parameter depending on s_π and can therefore be measured more precisely, from the statistical point of view. h_p/f_s , which is the only parameter sensitive to the effect of CP violation, is measured with a poor sensitivity, both from the statistical and systematic point of view.

The only result that can be easily compared with the one from the Geneva-Saclay experiment is the value of h_p/f_s , that is compatible within the total systematic uncertainty. Further comparisons are not possible due to the different choices in the parametrisation.

The comparison of the results obtained for the scattering lengths a_0^0 and a_0^2 in this analysis, in the K_{e4} measurement of the BNL E865 experiment and in the $K^\pm \rightarrow \pi^\pm \pi^0 \pi^0$ cusp analysis of the NA48/2 experiment are shown in Table 10.2

The results obtained for a_0^0 in this analysis are compatible with the ones in [35] (with both constraints) and in [36] within 1.5 and 1.3 times the uncorrelated uncertainty, respectively. The weighted average of the three measurements of a_0^0 is 0.227 ± 0.006 , with a χ^2/ndf of 3/2.

The statistical uncertainty is smaller in this analysis with respect to the other K_{e4} measure-

Parameter	This result	BNL result
f'_s/f_s	0.133 ± 0.029	0.184 ± 0.071
f''_s/f_s	-0.041 ± 0.024	-0.103 ± 0.073
f_e/f_s	0.221 ± 0.117	(-0.056 ± 0.046)
f'_e/f_s	-0.459 ± 0.359	—
\tilde{f}_p/f_s	-0.112 ± 0.026	(-0.059 ± 0.050)
g_p/f_s	0.892 ± 0.028	0.810 ± 0.019
g'_p/f_s	0.114 ± 0.027	0.117 ± 0.018
h_p/f_s	-0.380 ± 0.057	-0.513 ± 0.049

Table 10.1.: Comparison between the result obtained in this analysis (second column) and the one published in [35] (third column) for the form factor measurement, without the scattering lengths. For each parameter, the total uncertainty is computed as the sum in quadrature of statistical and systematic uncertainty. The values in parentheses are for the parameters that were not included in the standard fit of the BNL measurement.

Parameter	This result	BNL result	NA48/2 cusp
a_0^0	$0.246 \pm 0.015 \pm 0.002$	$0.216 \pm 0.014 \pm 0.002$	$0.220 \pm 0.007 \pm 0.011$
a_0^2	$-0.039 \pm 0.003 \pm 0.001$	$-0.045 \pm 0.003 \pm 0.001$	$-0.044 \pm 0.002 \pm 0.001$

Table 10.2.: Comparison between the result obtained in this analysis (second column) and the ones published in [35] (third column) and in [36] (fourth column) for the scattering lengths. The first uncertainty is computed as the sum in quadrature of statistical and systematic uncertainty. The theoretical uncertainty is quoted separately and is considered to be completely correlated between the two K_{e4} analyses, while no correlation is assumed with the theoretical uncertainty on a_0^0 in the cusp analysis.

ment, even if the total size of the analysed samples is very similar, due to the larger population of the sample at high values of s_π , where the sensitivity to the scattering lengths increases. Therefore, roughly the same total uncertainty can be achieved. In spite of a statistics 80 times higher, the measurement performed in the $K^\pm \rightarrow \pi^\pm \pi^0 \pi^0$ cusp analysis is, statistically, only 1.5 times more sensitive to a_0^0 than the one presented in this thesis. Unfortunately, the theoretical uncertainty is also much bigger than for K_{e4} .

The value of a_0^0 obtained by the Geneva-Saclay collaboration was based on a different theoretical model, that does not include any dependence on a_0^2 and was therefore not listed

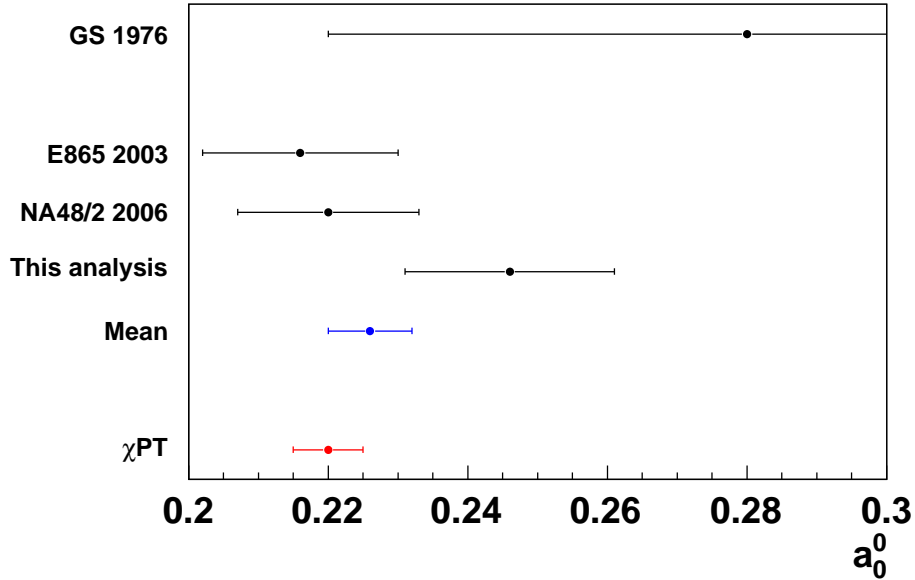


Figure 10.1.: Values of a_0^0 measured by the Geneva-Saclay experiment, by BNL E865, by NA48/2 in the cusp analysis and in the analysis presented here. The blue point shows the weighted average of the three recent measurements and the red one the prediction of χPT .

in Table 10.2. Due to the available statistics, the uncertainty is much bigger and the result is consistent with all the ones obtained in this analysis.

10.3. Comparison with the theoretical predictions

Only the measured values of the $\pi\pi$ scattering lengths can be easily compared with the theoretical prediction, while the form factors depend, within χPT , on the coupling constants L_j^r (see Section 2.4.3), so that no explicit prediction is available.

The result obtained in this analysis for a_0^0 with the constraint in Eq. 2.67 is compatible within 1.6 times the total uncertainty with the predicted value 0.220 ± 0.005 . A very small quark condensate, requiring a different power counting for the mass terms, is therefore excluded. An improvement in the statistical and systematic uncertainty would show if the tendency of this measurement towards higher values of a_0^0 , and therefore a smaller size of the quark condensate, becomes significant.

10.4. Outlook

Both the statistical and the systematic uncertainty can be reduced, by analysing all the available statistics and improving the fit method and the MC simulation. Since the uncertainty is dominated by the total systematics, but not by a single effect bigger than all the others, many tests need to be performed in order to significantly reduce the systematic uncertainty. For the fit method, for example, the effects of the threshold and of the correlations between

the parameters should be studied in more detail in order to optimise the binning and the parametrisation. In the MC most of the problems seem to arise from the simulation of the momentum resolution and of the beam spectrum, producing big variations of the result for different choices of the $m_{K_{e4}}$ cut and of the assumptions in the computation of the kinematic variables. An independent analysis of the same data is being performed in parallel within the NA48/2 collaboration, based on the assumption of a fixed kaon mass and variable kaon momentum. The comparison between the two analyses can help in the understanding of the MC simulation. Furthermore, the KABES data can be used to improve the resolution of the kinematic variables.

Once the systematic uncertainty is better under control, the use of a bigger sample of data can reduce both the statistical uncertainty and the contribution to systematic uncertainty due to the trigger efficiency. Furthermore, the comparison between data and MC with $K_{2\pi D}$ events would become more precise.

The aim declared in the proposal of NA48/2 [69], to measure a_0^0 with an uncertainty of 0.01 is not yet achieved. However, with three times more statistics, the systematic uncertainty would only need to be improved by a factor 1.5, which should be feasible.

11. Summary

The NA48/2 experiment has collected in 2003 and 2004 a large data sample of charged kaon decays. About one third of the available data were analysed and 342,859 $K^\pm \rightarrow \pi^\pm \pi^- e^\pm \nu_e$ (K_{e4}) candidates were selected. In this analysis, the background contamination in the sample could be reduced down to 0.3%, to be compared to about 1% in the Geneva Saclay experiment and about 5% in the BNL E865 experiment. The background estimate could be performed directly from the data, by selecting events with the same signature as K_{e4} , but requiring for the electron the opposite charge with respect to the kaon, the so-called “wrong sign” events. This is a clean background sample, since the kaon decay with $\Delta S = -\Delta Q$, that would be the only source of signal, can only take place through two weak decays and is therefore strongly suppressed. The background was also estimated from MC events and the two estimates agree within 10%.

The Cabibbo-Maksymowicz variables, used to describe the kinematics of the decay, were computed under the assumption of a fixed kaon momentum of 60 GeV/c along the z axis, so that the neutrino momentum could be obtained without ambiguity. The measurement of the form factors and of the $\pi\pi$ scattering length a_0^0 was performed in a single step by comparing the five-dimensional distributions of data and MC in the kinematic variables. The MC distributions were corrected in order to properly take into account the trigger and selection efficiencies of the data and the background contamination. The following parameter values were obtained from a binned maximum likelihood fit, where a_0^2 was expressed as a function of a_0^0 according to the prediction of chiral perturbation theory:

$$\begin{aligned}
f'_s/f_s &= 0.133 \pm 0.013 \text{ (stat)} \pm 0.026 \text{ (syst)}, \\
f''_s/f_s &= -0.041 \pm 0.013 \text{ (stat)} \pm 0.020 \text{ (syst)}, \\
f_e/f_s &= 0.221 \pm 0.051 \text{ (stat)} \pm 0.105 \text{ (syst)}, \\
f'_e/f_s &= -0.459 \pm 0.170 \text{ (stat)} \pm 0.316 \text{ (syst)}, \\
\tilde{f}_p/f_s &= -0.112 \pm 0.013 \text{ (stat)} \pm 0.023 \text{ (syst)}, \\
g_p/f_s &= 0.892 \pm 0.012 \text{ (stat)} \pm 0.025 \text{ (syst)}, \\
g'_p/f_s &= 0.114 \pm 0.015 \text{ (stat)} \pm 0.022 \text{ (syst)}, \\
h_p/f_s &= -0.380 \pm 0.028 \text{ (stat)} \pm 0.050 \text{ (syst)}, \\
a_0^0 &= 0.246 \pm 0.009 \text{ (stat)} \pm 0.012 \text{ (syst)} \pm 0.002 \text{ (theor)},
\end{aligned}$$

where the statistical uncertainty only includes the effect of the data statistics and the theoretical uncertainty is due to the width of the allowed band for a_0^2 .

The systematic uncertainty was estimated as the sum in quadrature of the contributions, assumed to be uncorrelated, from the fit method, the corrections to the MC and the agreement between data and MC in acceptance and resolution. The resulting uncertainty is due to a few significant contributions of the same size, and no single effect could be identified as the dominating one. The assumptions made in the computation of the kinematic variables were

found to have a big effect on most of the parameters, hinting to some imperfection in the simulation of the momentum resolution and of the kaon spectrum.

Even if the measurement is still dominated by systematics for all the parameters, f'_s/f_s , f''_s/f_s and \tilde{f}_p/f_s have a better precision than the latest published result, f_e/f_s was obtained with a higher significance and f'_e/f_s could be measured for the first time. a_0^0 has almost the same uncertainty as the most precise published measurement in K_{e4} , due to the larger acceptance at high s_π , where the statistical sensitivity increases.

No disagreement was found with respect to previous measurements and theoretical predictions, so that the hypothesis, on which χPT is based, of a large quark condensate can be confirmed. However, the value obtained in the analysis presented in this thesis is slightly higher and further away from the theoretical prediction than the ones measured with a similar precision. If the statistical and systematic uncertainties can be reduced to the level of 0.01, as was the aim declared in the proposal of NA48/2, a possible discrepancy to the theoretical prediction might be observed with a significance of 2–3 times the total uncertainty.

A reduction of the systematic uncertainty on a_0^0 by a factor 1.5 should be feasible, but is surely challenging, due to the required precision in the MC simulation and stability in the fit method. Any improvement in the MC simulation would most probably reduce the uncertainty on all the parameters, so that the systematic uncertainty can be comparable to the statistical one.

A. The K_{e4} matrix element

The following formulae were implemented in CMC and in the fit program to describe the K_{e4} matrix element (see Eqs. 2.63, 2.67, 2.71–2.74 and 6.2) [39, 42, 46, 47]:

$$\begin{aligned} J_5 &= 2(1 - z_e) \left[I_1 + I_2 \cos 2\theta_e + I_3 \sin^2 \theta_e \cos 2\phi + I_4 \sin 2\theta_e \cos \phi + I_5 \sin \theta_e \cos \phi \right. \\ &\quad \left. + I_6 \cos \theta_e + I_7 \sin \theta_e \sin \phi + I_8 \sin 2\theta_e \sin \phi + I_9 \sin^2 \theta_e \sin 2\phi \right], \end{aligned}$$

with

$$\begin{aligned} I_1 &= \frac{1}{4} \left\{ (1 + z_e) |F_1|^2 + \frac{1}{2} (3 + z_e) (|F_2|^2 + |F_3|^2) \sin^2 \theta_\pi + 2z_e |F_4|^2 \right\} \\ I_2 &= -\frac{1}{4} (1 - z_e) \left\{ |F_1|^2 - \frac{1}{2} (|F_2|^2 + |F_3|^2) \sin^2 \theta_\pi \right\} \\ I_3 &= -\frac{1}{4} (1 - z_e) \left\{ |F_2|^2 - |F_3|^2 \right\} \sin^2 \theta_\pi \\ I_4 &= \frac{1}{2} (1 - z_e) \operatorname{Re}(F_1^* F_2) \sin \theta_\pi \\ I_5 &= -\{\operatorname{Re}(F_1^* F_3) + z_e \operatorname{Re}(F_4^* F_2)\} \sin \theta_\pi \\ I_6 &= -\{\operatorname{Re}(F_2^* F_3) \sin^2 \theta_\pi - z_e \operatorname{Re}(F_1^* F_4)\} \\ I_7 &= -\{\operatorname{Im}(F_1^* F_2) + z_e \operatorname{Im}(F_4^* F_3)\} \sin \theta_\pi \\ I_8 &= \frac{1}{2} (1 - z_e) \operatorname{Im}(F_1^* F_3) \sin \theta_\pi \\ I_9 &= -\frac{1}{2} (1 - z_e) \operatorname{Im}(F_2^* F_3) \sin^2 \theta_\pi, \end{aligned}$$

where the Lorentz invariant quantities are defined in Eq. 2.68 as a function of the Cabibbo-Maksymowicz variables. The form factors are combined into four quantities

$$\begin{aligned} F_1 &= XF + \sigma_\pi (P \cdot L) \cos \theta_\pi \cdot G \\ F_2 &= \sigma_\pi (s_\pi s_e)^{1/2} G \\ F_3 &= \sigma_\pi X (s_\pi s_e)^{1/2} \frac{H}{m_K^2} \\ F_4 &= -(PL)F - s_e R - \sigma_\pi X \cos \theta_\pi G \end{aligned}$$

and expanded into partial waves

$$\begin{aligned} F &= (f_s + f'_s q^2 + f''_s q^4 + f_e \frac{s_e}{4M_\pi^2}) e^{i\delta_0^0(s_\pi)} + \tilde{f}_p \sigma_\pi X \cos \theta_\pi e^{i\delta_1^1(s_\pi)} \\ G &= (g_p + g'_p q^2 + g_e \frac{s_e}{4M_\pi^2}) e^{i\delta_1^1(s_\pi)} \\ H &= (h_p + h'_p q^2) e^{i\delta_1^1(s_\pi)}, \end{aligned}$$

A. The K_{e4} matrix element

with $q = \sqrt{\frac{s_\pi - 4M_\pi^2}{4M_\pi^2}}$.

The phase shifts are given by the numerical solutions of the Roy equation

$$\begin{aligned}\tan \delta_0^0 &= \sqrt{1 - \frac{4M_\pi^2}{s_\pi}} \cdot \left\{ A_0^0 + B_0^0 q^2 + C_0^0 q^4 + D_0^0 q^6 \right\} \left(\frac{4M_\pi^2 - s_0^0}{s_\pi - s_0^0} \right), \\ \tan \delta_1^1 &= \sqrt{1 - \frac{4M_\pi^2}{s_\pi}} \cdot q^2 \cdot \left\{ A_1^1 + B_1^1 q^2 + C_1^1 q^4 + D_1^1 q^6 \right\} \left(\frac{4M_\pi^2 - s_1^1}{s_\pi - s_1^1} \right),\end{aligned}\quad (\text{A.1})$$

with

$$\begin{aligned}A_0^0 &= a_0^0, \\ B_0^0 &= 0.2675 + 0.9231\Delta a_0^0 - 3.5341\Delta a_0^2 \\ &+ 0.2691(\Delta a_0^0)^2 + 5.3282(\Delta a_0^2)^2 - 5.8361\Delta a_0^0\Delta a_0^2 \\ &- 0.3745(\Delta a_0^0)^3 + 2.4827(\Delta a_0^0)^2\Delta a_0^2 - 17.3384\Delta a_0^0(\Delta a_0^2)^2 + 50.1966(\Delta a_0^2)^3 \\ C_0^0 &= -0.0139 + 0.0400\Delta a_0^0 - 0.4735\Delta a_0^2 \\ &+ 0.2901(\Delta a_0^0)^2 + 13.4052(\Delta a_0^2)^2 - 4.1067\Delta a_0^0\Delta a_0^2 \\ &- 0.3551(\Delta a_0^0)^3 - 1.1246(\Delta a_0^0)^2\Delta a_0^2 + 35.4340\Delta a_0^0(\Delta a_0^2)^2 - 83.4777(\Delta a_0^2)^3 \\ D_0^0 &= -0.0014 - 0.0247\Delta a_0^0 + 0.1321\Delta a_0^2 \\ &- 0.0948(\Delta a_0^0)^2 - 2.7711(\Delta a_0^2)^2 + 1.0742\Delta a_0^0\Delta a_0^2 \\ &- 0.1064(\Delta a_0^0)^3 + 2.4220(\Delta a_0^0)^2\Delta a_0^2 - 14.7496\Delta a_0^0(\Delta a_0^2)^2 + 24.9706(\Delta a_0^2)^3 \\ s_0^0 &= 36.774 \cdot M_\pi^2 \cdot \left[1 + 0.0588\Delta a_0^0 - 0.0482\Delta a_0^2 \right. \\ &\quad \left. - 2.4980(\Delta a_0^0)^2 - 42.3273(\Delta a_0^2)^2 + 20.3977\Delta a_0^0\Delta a_0^2 \right. \\ &\quad \left. - 8.2291(\Delta a_0^0)^3 + 122.155(\Delta a_0^0)^2\Delta a_0^2 - 558.778\Delta a_0^0(\Delta a_0^2)^2 + 793.892(\Delta a_0^2)^3 \right], \\ A_1^1 &= 0.0380 + 0.0813\Delta a_0^0 - 0.2940\Delta a_0^2 \\ &- 0.0636(\Delta a_0^0)^2 + 0.1179(\Delta a_0^2)^2 + 0.1190\Delta a_0^0\Delta a_0^2 \\ &+ 0.0443(\Delta a_0^0)^3 - 0.0245(\Delta a_0^0)^2\Delta a_0^2 - 0.2912\Delta a_0^0(\Delta a_0^2)^2 + 0.2354(\Delta a_0^2)^3 \\ B_1^1 &= 0.0104\Delta a_0^0 + 0.0229\Delta a_0^2 \\ &+ 0.0024(\Delta a_0^0)^2 + 0.0075(\Delta a_0^2)^2 - 0.0006\Delta a_0^0\Delta a_0^2 \\ &- 0.0082(\Delta a_0^0)^3 + 0.1468(\Delta a_0^0)^2\Delta a_0^2 - 0.7469\Delta a_0^0(\Delta a_0^2)^2 + 1.2024(\Delta a_0^2)^3 \\ C_1^1 &= -0.0001 + 0.0009\Delta a_0^0 - 0.0009\Delta a_0^2 \\ &+ 0.0006(\Delta a_0^0)^2 + 0.0081(\Delta a_0^2)^2 - 0.0047\Delta a_0^0\Delta a_0^2 \\ &+ 0.0009(\Delta a_0^0)^3 - 0.0296(\Delta a_0^0)^2\Delta a_0^2 + 0.1717\Delta a_0^0(\Delta a_0^2)^2 - 0.2984(\Delta a_0^2)^3 \\ D_1^1 &= -0.0001\Delta a_0^0 + 0.0003\Delta a_0^2 \\ &- 0.0017(\Delta a_0^2)^2 + 0.0006\Delta a_0^0\Delta a_0^2 \\ &- 0.0001(\Delta a_0^0)^3 + 0.0024(\Delta a_0^0)^2\Delta a_0^2 - 0.0143\Delta a_0^0(\Delta a_0^2)^2 + 0.0264(\Delta a_0^2)^3 \\ s_1^1 &= 30.711 \cdot M_\pi^2 \cdot \left[1 - 0.0351\Delta a_0^0 - 0.1528\Delta a_0^2 \right. \\ &\quad \left. + 0.0429(\Delta a_0^0)^2 + 0.0353(\Delta a_0^2)^2 - 0.1318\Delta a_0^0\Delta a_0^2 \right. \\ &\quad \left. - 0.0206(\Delta a_0^0)^3 - 0.2574(\Delta a_0^0)^2\Delta a_0^2 + 1.9103\Delta a_0^0(\Delta a_0^2)^2 - 3.2088(\Delta a_0^2)^3 \right]\end{aligned}\quad (\text{A.2})$$

and

$$\begin{aligned}\Delta a_0^0 &= a_0^0 - 0.220 \\ \Delta a_0^2 &= 0.236\Delta a_0^0 - 0.61(\Delta a_0^0)^2 - 9.9(\Delta a_0^0)^3 \\ a_0^2 &= \Delta a_0^2 - 0.0444\end{aligned}\tag{A.3}$$

B. Additional Figures and Tables to Chapter 8

B.1. Efficiency of tight pion ID in data and MC

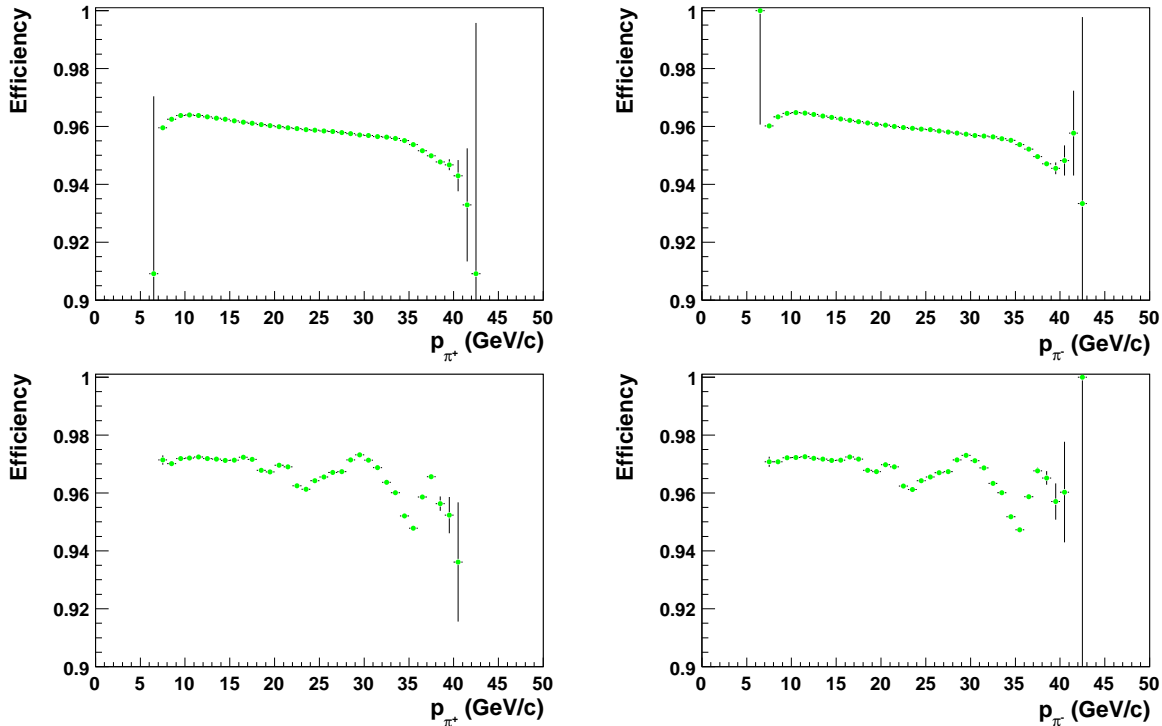


Figure B.1.: Efficiency of tight pion-ID in data (upper plots) and MC (lower plots) for π^+ (left) and π^- (right) as a function of the track momentum. In the data the efficiency is, as expected a smooth function of the momentum, while in the MC the fluctuations reflect the limited number of simulated showers in the used library.

B.2. K_{e4} MC distributions

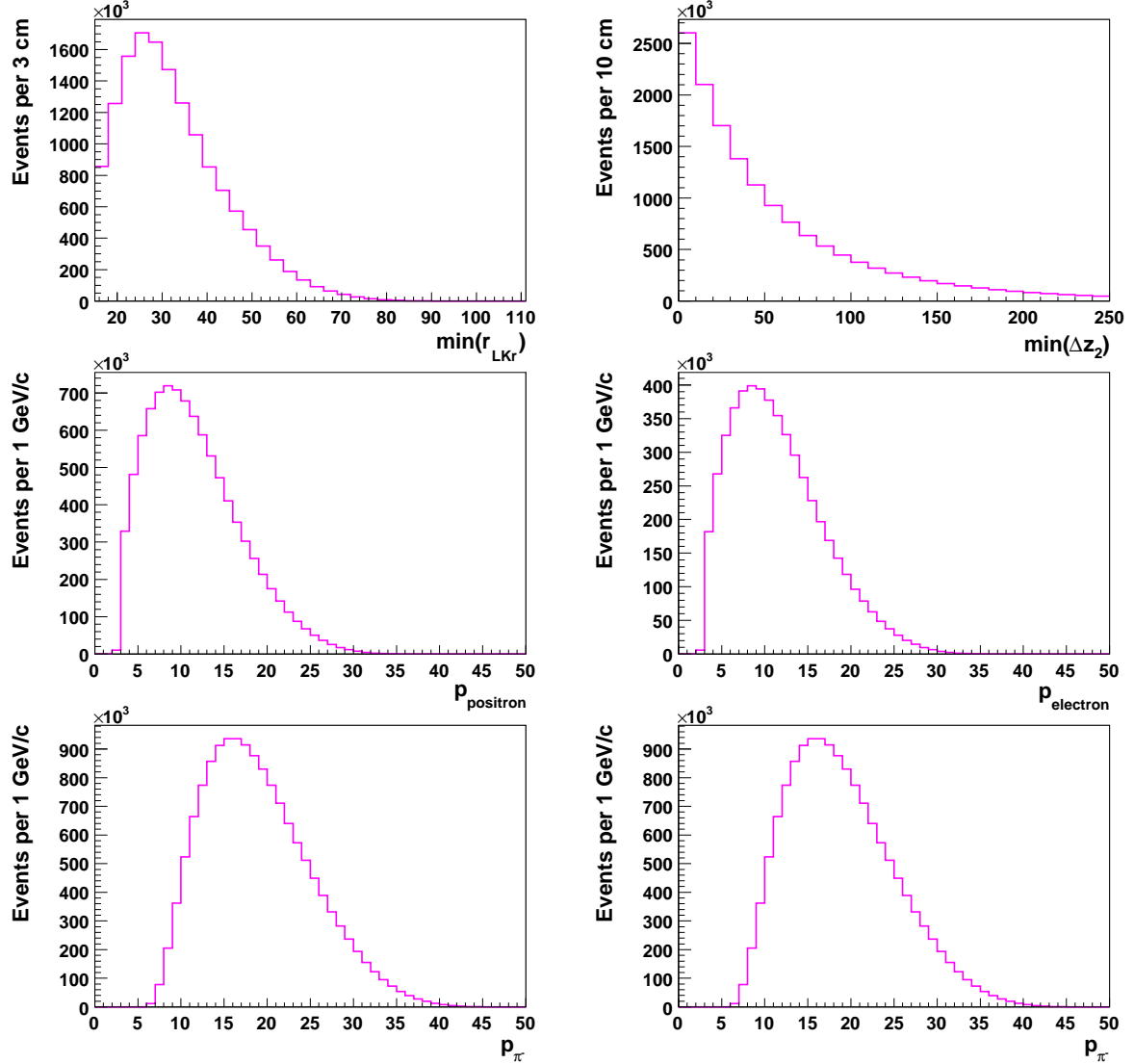


Figure B.2.: K_{e4} MC distributions after the complete event selection in the variables used to apply the efficiencies and corrections described in Section 8.3: $\min(r_{LKr})$ (upper row left), $\min(\Delta z_2)$ (upper row right), p_{e^+} (middle row left), p_{e^-} (middle row right), p_{π^+} (lower row left), p_{π^-} (lower row right).

B.3. Log-likelihood curves

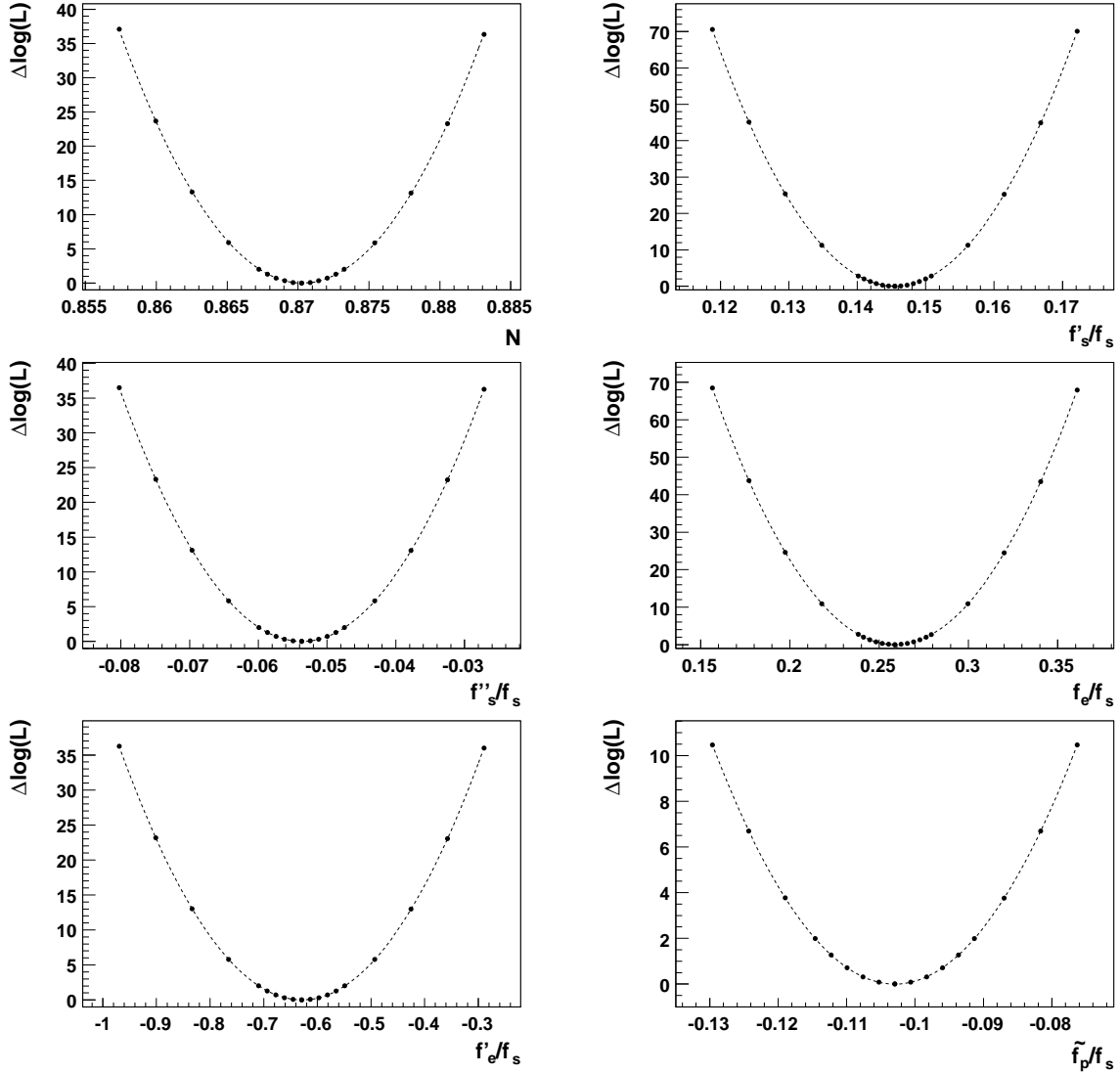


Figure B.3.: $\Delta \log L$ distribution as a function of the parameters in the F form factor around the minimum. The points were fitted with a parabola. The statistical uncertainty, without taking into account the correlations with the other parameters, corresponds to a variation of $\log L$ of 0.5. The 11 central points closer to each other cover a range of twice the uncertainty without considering the correlations, while the complete range corresponds to twice the uncertainty with correlations.

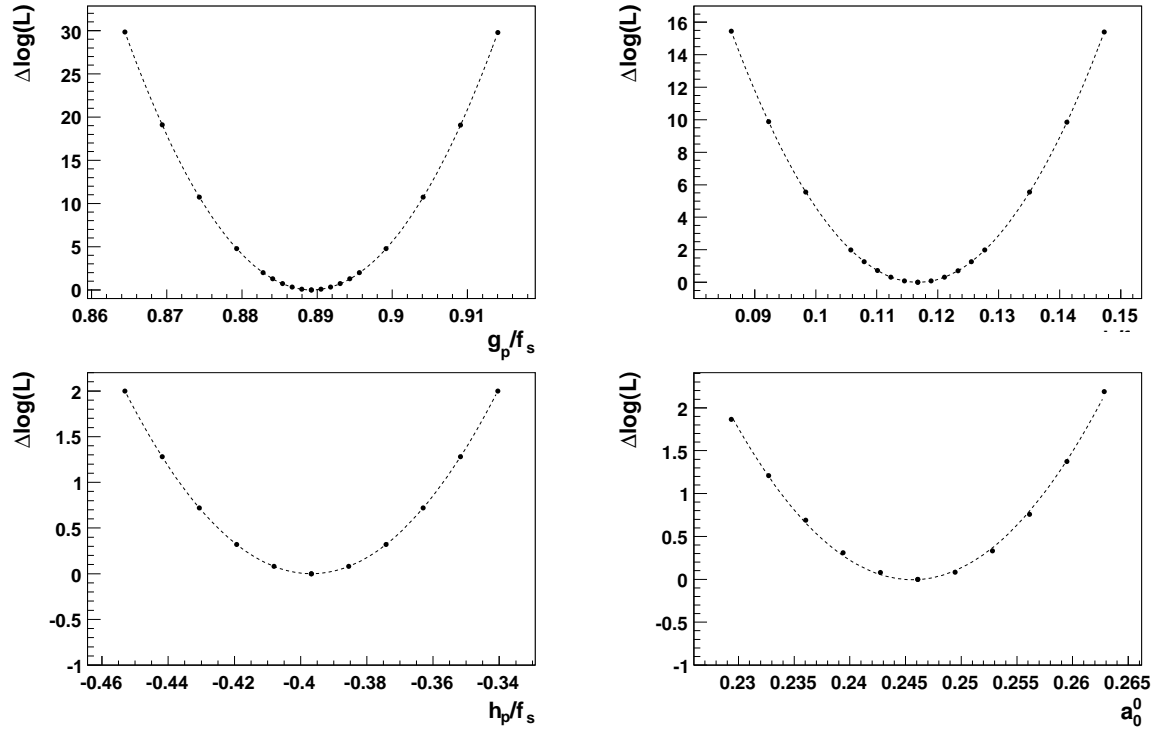


Figure B.4.: $\Delta \log L$ distribution as a function of the parameters in the G and H form factors and of a_0^0 around the minimum. The points were fitted with a parabola. The statistical uncertainty, without taking into account the correlations with the other parameters, corresponds to a variation of $\log L$ of 0.5. The 11 central points closer to each other cover a range of twice the uncertainty without considering the correlations, while the complete range corresponds to twice the uncertainty with correlations.

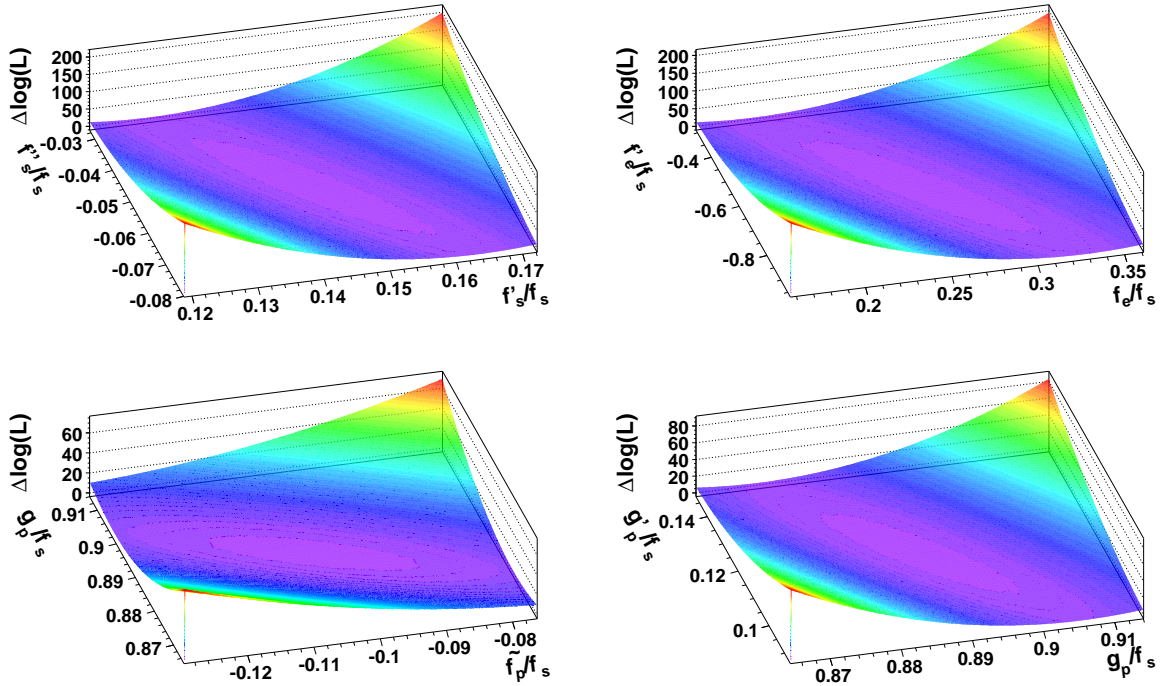


Figure B.5.: $\Delta \log L$ distribution around the minimum, as a function of four pairs of parameters strongly correlated with each other. The correlation coefficients are: -0.932 between $\frac{f'_s}{f_s}$ and $\frac{f''_s}{f_s}$, -0.947 between $\frac{f_e}{f_s}$ and $\frac{f'_e}{f_s}$, -0.742 between $\frac{f_p}{f_s}$ and $\frac{g_p}{f_s}$ and -0.809 between $\frac{g_p}{f_s}$ and $\frac{f'_p}{f_s}$, respectively. The remaining parameters are fixed to the values obtained in the global fit. The displayed ranges correspond to four times the statistical uncertainty of each parameter including all correlations. The ellipse that could be drawn at $\Delta \log L = 0.5$ would only include the correlation between the two considered parameters.

Bibliography

- [1] S. L. Glashow. Partial symmetries of weak interactions. *Nucl. Phys.*, 22:579–588, 1961.
- [2] S. Weinberg. A model of leptons. *Phys. Rev. Lett.*, 19:1264–1266, 1967.
- [3] A. Salam and J. C. Ward. Electromagnetic and weak interactions. *Phys. Lett.*, 13:168–171, 1964.
- [4] M. Gell-Mann. A schematic model of baryons and mesons. *Phys. Lett.*, 8:214–215, 1964.
- [5] G. Zweig. An SU(3) model for strong interaction symmetry and its breaking. 2. *CERN-TH-412*, 1964.
- [6] H. Fritzsch, M. Gell-Mann, and H. Leutwyler. Advantages of the color octet gluon picture. *Phys. Lett.*, B47:365–368, 1973.
- [7] D. J. Gross and F. Wilczek. Asymptotically free gauge theories. 1. *Phys. Rev.*, D8:3633–3652, 1973.
- [8] D. J. Gross and F. Wilczek. Asymptotically free gauge theories. 2. *Phys. Rev.*, D9:980–993, 1974.
- [9] H. D. Politzer. Asymptotic freedom: An approach to strong interactions. *Phys. Rept.*, 14:129–180, 1974.
- [10] D. H. Perkins. *Introduction to high energy physics*. Addison-Wesley, 1982.
- [11] F. Halzen and A. D. Martin. *Quarks and leptons: an introductory course in modern particle physics*. Wiley, 1984.
- [12] M. Maggiore. *A modern introduction to quantum field theory*. Oxford Series in Physics. Oxford University Press, 2005.
- [13] S. Eidelman et al. Review of Particle Physics. *Phys. Lett. B*, 592:1+, 2004.
- [14] W. Pauli. Exclusion principle, lorentz group and reflexion of space-time and charge. In W. Pauli, editor, *Niels Bohr and the development of physics*, pages 30–51. McGraw-Hill, 1955.
- [15] C. N. Yang and R. L. Mills. Conservation of isotopic spin and isotopic gauge invariance. *Phys. Rev.*, 96:191–195, 1954.
- [16] C. S. Wu, E. Ambler, R. W. Hayward, D. D. Hoppes, and R. P. Hudson. Experimental test of parity conservation in beta decay. *Phys. Rev.*, 105:1413–1414, 1957.

- [17] P. W. Higgs. Broken symmetries, massless particles and gauge fields. *Phys. Lett.*, 12:132–133, 1964.
- [18] P. W. Higgs. Broken symmetries and the masses of gauge bosons. *Phys. Rev. Lett.*, 13:508–509, 1964.
- [19] M. Kobayashi and T. Maskawa. CP violation in the renormalizable theory of weak interaction. *Prog. Theor. Phys.*, 49:652–657, 1973.
- [20] J. H. Christenson, J. W. Cronin, V. L. Fitch, and R. Turlay. Evidence for the 2π decay of the K_2^0 meson. *Phys. Rev. Lett.*, 13:138–140, 1964.
- [21] L. Maiani and N. Paver. CP violation in $K \rightarrow 3\pi$ decays. In L. Maiani, G. Pancheri, and N. Paver, editors, *The second DA ϕ NE physics handbook*, volume 1, pages 51–62. SIS, 1995.
- [22] A. A. Belkov, A. V. Lanev, G. Bohm, and A. Schaale. Chiral dynamics of kaon decays and the problem of CP violation. *Phys. Part. Nucl.*, 26:239–274, 1995.
- [23] A. Pich. Effective field theory. *hep-ph/9806303*, 1998.
- [24] G. Colangelo and G. Isidori. An introduction to chpt. *hep-ph/0101264*, 2000.
- [25] S. Scherer and M. R. Schindler. A chiral perturbation theory primer. *hep-ph/0505265*, 2005.
- [26] J. Goldstone. Field theories with 'superconductor' solutions. *Nuovo Cim.*, 19:154–164, 1961.
- [27] J. Goldstone, A. Salam, and S. Weinberg. Broken symmetries. *Phys. Rev.*, 127:965–970, 1962.
- [28] H. Leutwyler. On the foundations of chiral perturbation theory. *Ann. Phys.*, 235:165–203, 1994.
- [29] S. Weinberg. Pion scattering lengths. *Phys. Rev. Lett.*, 17:616–621, 1966.
- [30] J. Gasser. The $\pi\pi$ scattering amplitude in chiral perturbation theory. In L. Maiani, G. Pancheri, and N. Paver, editors, *The second DA ϕ NE physics handbook*, volume 1, pages 215–220. SIS, 1995.
- [31] J. Gasser and H. Leutwyler. Low energy theorems as precision tests of QCD. *Phys. Lett.*, B125:325–329, 1983.
- [32] J. Gasser and H. Leutwyler. Chiral perturbation theory to one loop. *Ann. Phys.*, 158:142–210, 1984.
- [33] J. Bijnens, G. Colangelo, G. Ecker, J. Gasser, and M. E. Sainio. Elastic $\pi\pi$ scattering to two loops. *Phys. Lett.*, B374:210–216, 1996.
- [34] M. Knecht, B. Moussallam, J. Stern, and N. H. Fuchs. The low energy $\pi\pi$ amplitude to one and two loops. *Nucl. Phys.*, B457:513–576, 1995.

- [35] S. Pislak et al. High statistics measurement of K_{e4} decay properties. *Phys. Rev.*, D67:072004, 2003.
- [36] J. R. Batley et al. Observation of a cusp-like structure in the $\pi^0\pi^0$ invariant mass distribution from $K^\pm \rightarrow \pi^\pm\pi^0\pi^0$ decay and determination of the $\pi\pi$ scattering lengths. *Phys. Lett.*, B633:173–182, 2006.
- [37] G. Colangelo. $\pi\pi$ scattering, pion form factors and chiral perturbation theory. *AIP Conf. Proc.*, 756:60–69, 2005.
- [38] S. M. Roy. Exact integral equation for pion pion scattering involving only physical region partial waves. *Phys. Lett.*, B36:353–356, 1971.
- [39] B. Ananthanarayan, G. Colangelo, J. Gasser, and H. Leutwyler. Roy equation analysis of $\pi\pi$ scattering. *Phys. Rept.*, 353:207–279, 2001.
- [40] G. Grayer et al. High statistics study of the reaction $\pi^-p \rightarrow \pi^-\pi^+n$: Apparatus, method of analysis, and general features of results at 17 GeV/c. *Nucl. Phys.*, B75:189–245, 1974.
- [41] A. Schenk. Absorption and dispersion of pions at finite temperature. *Nucl. Phys.*, B363:97–116, 1991.
- [42] G. Colangelo, J. Gasser, and H. Leutwyler. $\pi\pi$ scattering. *Nucl. Phys.*, B603:125–179, 2001.
- [43] D. Morgan and G. Shaw. Low-energy pion pion parameters from forward dispersion relations. *Nucl. Phys.*, B10:261–282, 1969.
- [44] N. Cabibbo and A. Maksymowicz. Angular correlations in K_{e4} decays and determination of low energy $\pi\pi$ phase shifts. *Phys. Rev.*, 137:B438–B443, 1965. Erratum: *Ibid.* 168:1926, 1968.
- [45] J. Bijnens, G. Colangelo, G. Ecker, and J. Gasser. Semileptonic kaon decays. In L. Maiani, G. Pancheri, and N. Paver, editors, *The second DA ϕ NE physics handbook*, volume 1, pages 318–388. SIS, 1995.
- [46] A. Pais and S. B. Treiman. Pion phase-shift information from K_{l4} decays. *Phys. Rev.*, 168:1958–1865, 1968.
- [47] G. Amoros and J. Bijnens. A parametrization for $K^+ \rightarrow \pi^+\pi^-e^+\nu$. *J. Phys.*, G25:1607–1622, 1999.
- [48] S. Weinberg. Current-commutator calculation of the K_{l4} form factors. *Phys. Rev. Lett.*, 17:336–340, 1966.
- [49] J. Bijnens. K_{l4} decays and the low energy expansion. *Nucl. Phys.*, B337:635–651, 1990.
- [50] C. Rigggenbach, J. Gasser, J. F. Donoghue, and B. R. Holstein. Chiral symmetry and the large N_c limit in K_{l4} decays. *Phys. Rev.*, D43:127–139, 1991.

- [51] J. Wess and B. Zumino. Consequences of anomalous Ward identities. *Phys. Lett.*, B37:95–97, 1971.
- [52] E. Witten. Global aspects of current algebra. *Nucl. Phys.*, B223:422–432, 1983.
- [53] N. K. Pak and P. Rossi. Gauged Goldstone boson effective action from direct integration of Bardeen anomaly. *Nucl. Phys.*, B250:279–294, 1985.
- [54] J. Bijnens, G. Colangelo, and J. Gasser. K_{l4} decays beyond one loop. *Nucl. Phys.*, B427:427–454, 1994.
- [55] J. Gasser and H. Leutwyler. Chiral perturbation theory: Expansions in the mass of the strange quark. *Nucl. Phys.*, B250:465–516, 1985.
- [56] J. F. Donoghue, J. Gasser, and H. Leutwyler. The decay of a light Higgs boson. *Nucl. Phys.*, B343:341–368, 1990.
- [57] T. D. Lee and C. S. Wu. Weak interactions. decays of charged K mesons. *Ann. Rev. Nucl. Part. Sci.*, 16:471–590, 1966.
- [58] L. Rosselet et al. Experimental study of 30,000 K_{e4} decays. *Phys. Rev.*, D15:574–586, 1977.
- [59] J. L. Basdevant, C. D. Foggatt, and J. L. Petersen. Construction of phenomenological $\pi\pi$ amplitudes. *Nucl. Phys.*, B72:413–453, 1974.
- [60] N. Cabibbo and G. Isidori. Pion pion scattering and the $K \rightarrow 3\pi$ decay amplitudes. *JHEP*, 03:021, 2005.
- [61] A. Angelopoulos et al. Measurement of the K_L - K_S mass difference using semileptonic decays of tagged neutral kaons. *Phys. Lett.*, B444:38–42, 1998.
- [62] A. Angelopoulos et al. T-violation and CPT-invariance measurements in the CPLEAR experiment: A detailed description of the analysis of neutral-kaon decays to $e\pi\nu$. *Eur. Phys. J.*, C22:55–79, 2001.
- [63] P. Bloch et al. New limit on the $\Delta S = \Delta Q$ rule in the K_{e4} decay. *Phys. Lett.*, B60:393–396, 1976.
- [64] R. W. Birge. Experimental study of K_{e4}^+ decay. *Phys. Rev.*, 139:B1600–B1608, 1965.
- [65] J. R. Batley et al. A precision measurement of direct CP violation in the decay of neutral kaons into two pions. *Phys. Lett.*, B544:97–112, 2002.
- [66] R. Batley et al. A high sensitivity investigation of K_S and neutral hyperon decays using a modified K_S beam. (Addendum 2). *CERN-SPSC-2000-002*.
- [67] J. R. Batley et al. Observation of the rare decay $K_S \rightarrow \pi^0 e^+ e^-$. *Phys. Lett.*, B576:43–54, 2003.
- [68] J. R. Batley et al. Observation of the rare decay $K_S \rightarrow \pi^0 \mu^+ \mu^-$. *Phys. Lett.*, B599:197–211, 2004.

- [69] R. Batley et al. Addendum 3 (to proposal P253/CERN/SPSC): For a precision measurement of charged kaon decay parameters with an extended NA48 setup. *CERN-SPSC-2000-003; SPSC-P-253-Add-3*, 2000.
- [70] G. Brianti. 50 years of synchrotrons: The CERN synchrotrons. *CERN-97-04B*, 1997.
- [71] S. De Man. <http://accel-general.web.cern.ch/accel-general/>, 2005.
- [72] V. Kekelidze and A. Gonidec. Status report on experiment NA48/2. *CERN-SPSC-2003-033; SPSC-M-707*, 2003.
- [73] M. Gersabeck. Messung des Verzweigungsverhältnisses und der Formfaktoren im Zerfall $K^\pm \rightarrow \pi^0 \pi^0 e^\pm \bar{\nu}_e$ mit dem NA48/2-Detektor. Diploma thesis, Mainz University, 2006.
- [74] N. Doble, L. Gatignon, and P. Grafstrom. <http://sl.web.cern.ch/SL/eagroup/K12beam/>, 1998.
- [75] A. Lai et al. A precise measurement of the direct CP violation parameter $\text{Re}(\epsilon'/\epsilon)$. *Eur. Phys. J.*, C22:231–254, 2001.
- [76] M. Jeitler et al. The clock and control signal distribution system for the NA48 experiment. *Nucl. Instrum. Meth.*, A400:101–106, 1997.
- [77] B. Peyaud. KABES: A novel beam spectrometer for NA48. *Nucl. Instrum. Meth.*, A535:247–252, 2004.
- [78] Y. Giomataris, P. Reboursard, J. P. Robert, and G. Charpak. MICROMEGAS: A high-granularity position-sensitive gaseous detector for high particle-flux environments. *Nucl. Instrum. Meth.*, A376:29–35, 1996.
- [79] V. Kekelidze and A. Gonidec. Status report on experiment NA48/2. *CERN-SPSC-2002-035; SPSC-M-691*, 2002.
- [80] M. Mota et al. A flexible multi-channel high resolution time to digital converter ASIC. In *Nuclear Science Symposium, Lyon, France*, 2000.
- [81] D. Bederede et al. High resolution drift chambers for the NA48 experiment at CERN. *Nucl. Instrum. Meth.*, A367:88–91, 1995.
- [82] M. Piccini. *Measurement of the Ξ^0 beta decay branching ratio in the experiment NA48/I at CERN*. PhD thesis, Perugia University, 2003.
- [83] R. Arcidiacono et al. A new drift chamber TDC readout for the high intensity program of the NA48 experiment. *Nucl. Instrum. Meth.*, A518:493–494, 2004.
- [84] NA48 Perugia and Cagliari Groups. The NA48 Charged Hodoscope. *NA48 Note 94-37*, 1994.
- [85] NA48 Mainz group. [/afs/physik.uni-mainz.de/home/na48sw/detektor/](http://afs/physik.uni-mainz.de/home/na48sw/detektor/), 2001.
- [86] A. Lai and L. Musa. PMChip: An ASIC dedicated to pipelined readout and trigger systems. *IEEE Trans. Nucl. Sci.*, 42:812–819, 1995.

- [87] G. D. Barr et al. Performance of an electromagnetic liquid krypton calorimeter based on a ribbon electrode tower structure. *Nucl. Instrum. Meth.*, A370:413–424, 1996.
- [88] V. Fanti et al. Performance of an electromagnetic liquid krypton calorimeter. *Nucl. Instrum. Meth.*, A344:507–520, 1994.
- [89] NA48 collaboration. <http://na48.web.cern.ch/NA48/Welcome/images/pictures.html>, 1998.
- [90] B. Hallgren et al. The NA48 LKr calorimeter digitizer electronics chain. *Nucl. Instrum. Meth.*, A419:680–685, 1998.
- [91] A. Gianoli et al. The NA48 LKr calorimeter readout electronics. *IEEE Trans. Nucl. Sci.*, 47:136–141, 2000.
- [92] R. Arcidiacono et al. The commissioning of the SuperEvent read-out. *NA48 Note 02-13*, 2002.
- [93] P. Lubrano et al. A proposal for a Neutral Hodoscope in NA48. *NA48 Note 94-18*, 1994.
- [94] M. Clemencic. *A measurement of the branching ratio of the Ξ^0 β -decay in the NA48 experiment at CERN*. PhD thesis, Torino University, 2004.
- [95] R. Wilhelm. Hadron calorimeter reconstruction. *NA48 Note 96-22*, 1996.
- [96] R. Moore et al. NA48 muon veto: ‘test93’ and ‘test94’ results. *NA48 Note 94-40*, 1994.
- [97] NA48 Torino group. NA48 anticounters: design, construction, installation and 93-94 test beam. *NA48 Note 96-3*, 1996.
- [98] G. Fischer et al. A 40-MHz-pipelined trigger for $K^0 \rightarrow 2\pi^0$ decays for the CERN NA48 experiment. *Nucl. Instrum. Meth.*, A419:695–700, 1998.
- [99] C. Avanzini et al. The PeakSum processing system for the NA48 experiment: A VLSI based processor. *IEEE Trans. Nucl. Sci.*, 43:1789–1794, 1996.
- [100] G. D. Barr et al. A fully software-programmable pipelined trigger-processing module. *IEEE Trans. Nucl. Sci.*, 43:1689–1694, 1996.
- [101] S. Anvar et al. The charged trigger system of NA48 at CERN. *Nucl. Instrum. Meth.*, A419:686–694, 1998.
- [102] R. Arcidiacono et al. The Trigger Supervisor of the NA48 experiment at CERN SPS. *Nucl. Instrum. Meth.*, A443:20–26, 2000.
- [103] M. Wittgen et al. The NA48 event building PC farm. *IEEE Trans. Nucl. Sci.*, 47:348–352, 2000.
- [104] J. P. Baud et al. Castor status and evolution. *ECONF*, C0303241:TUDT007, 2003.
- [105] S. Schmidt. Entwicklung einer dritten Triggerstufe für das NA48-Experiment. Diploma thesis, Mainz University, 1998.

- [106] C. Biino et al. Compact 7.2 user guide. *NA48 Documentation*, 2005.
- [107] CN/ASD Group and J. Zoll (ECP). ZEBRA Users Guide. *CERN Program Library Q100*, 1993.
- [108] R. Fröhwirth. Application of Kalman filtering to track and vertex fitting. *Wien Inst. Hochenergiephys. - HEPHY-PUB-87-503 (87,REC.JUN.)*, 1987.
- [109] J. B. Chèze. NA48 Drift Chamber Reconstruction User's Guide. *NA48 Documentation*, 1999.
- [110] G. Unal. Reconstruction program for the LKr. *NA48 Note 98-1*, 1997.
- [111] G. Unal. Neutral reconstruction. *NA48 Note 95-10*, 1995.
- [112] L. Di Lella. Alignment and corrections to the momenta. NA48 Charged Kaons Meeting, Aug 2003.
- [113] J. B. Chèze. NA48 spectrometer: Vertex Calculation. *NA48 Note 02-02*, 2002.
- [114] Application Software Group. GEANT, detector description and simulation tool. *CERN Program Library Long Writeup W5013*, 1994.
- [115] D. C. Carey. TURTLE (Trace Unlimited Rays Through Lumped Elements) : A computer program for simulating charged particle beam transport systems. *FERMILAB-NAL-064*, 1971.
- [116] F. James. N-Body Monte-Carlo Event Generator. *CERN Program Library Short Writeup W515*, 1975.
- [117] N. M. Kroll and W. Wada. Internal pair production associated with the emission of high-energy gamma rays. *Phys. Rev.*, 98:1355–1359, 1955.
- [118] P. Golonka and Z. Was. PHOTOS Monte Carlo: A precision tool for QED corrections in Z and W decays. *Eur. Phys. J.*, C45:97–107, 2006.
- [119] L. I. Schiff. *Quantum mechanics*, chapter 5, pages 138–141. McGraw-Hill, 1968.
- [120] B. Bloch-Devaux. Private communication.
- [121] B. Bloch-Devaux. Progress in K_{e4} analysis (Saclay). NA48 Analysis Meeting, Oct 2005.
- [122] B. Bloch-Devaux. Electron-identification and pion-rejection for K_{e4} analysis. NA48 Analysis Meeting, May 2005.
- [123] I. Mikulec. Evaluation of systematic uncertainties in the A_g^\pm measurement. NA48 Analysis Meeting, Oct 2004.
- [124] G. Cowan. *Statistical data analysis*, chapter 6, pages 87–89. Oxford University Press, 1998.
- [125] F. James and M. Roos. MINUIT a system for function minimization and analysis of the parameter errors and correlations. *Comput. Phys. Commun.*, 10:343–367, 1975.

Bibliography

- [126] G. Colangelo. Private communication.
- [127] G. Cowan. *Statistical data analysis*, chapter 6, pages 73–74. Oxford University Press, 1998.
- [128] G. Cowan. *Statistical data analysis*, chapter 7, page 96. Oxford University Press, 1998.
- [129] L. Litov. Neural network performance. NA48 Analysis Meeting, Jul 2005.
- [130] Troy Christian Andre. Radiative corrections in K_{l3}^0 decays. *UMI-31-49380*, 2004.
- [131] A. Winhart. Private communication.

Acknowledgements

In the summer of 2001 I was looking for a PhD position, possibly in Germany and possibly in NA48. My first choice was the University of Mainz and I was very surprised to see how easily and fast everything went. Once there, I understood that many things can be even easier, if one speaks German. For accepting me in his working group and “forcing” me from the very beginning to learn German, I would like to thank my supervisor Prof. Dr. Konrad Kleinknecht. The opportunity he offered me to travel to CERN whenever necessary, his interest for my analysis and most of all his belief in our experimental results, no matter how far they are from previous ones or from the theory, allowed me to learn a lot of physics and to develop the necessary self-confidence.

I wish to thank Dr. Rainer Wanke for his many suggestions, corrections, ideas, optimistic predictions (that were promptly “rescaled”), but most of all patience in reading through my thesis and in discussing every comment he had.

The whole group of the “mainziani” (sounds in Italian similar to Martians) that were at CERN during the data taking in 2002, 2003 and 2004 deserves a special thank. In particular, I would like to thank Matthias Behler for taking care of the L3 monitor, whose importance I always underestimated; Peter Marouelli for always speaking German to me and for understanding that sometimes I would have preferred to be somewhere else than at CERN; Uli Moosbrugger for assuring us every time that “it cannot be a fault of the PC farm”; Cristina Morales, the smallest, but the strongest one of us and Martin Wache for always finding back my disappeared home directory.

Even if they think I am German, I still have many reasons to thank the (mostly Italian) inhabitants of the control room: there was always someone to eat dinner with, someone to listen to your hardware, software or personal problems and most of the times also someone to share the 48-hours-days with. I would like to mention in particular Marco Clemencic, who saved many times the L3 from me, but also me from the L3; Giuseppe Ruggiero for making (eventually) funny jokes; Mauro Piccini for never getting angry with anybody and Teresa Fonseca, because she always managed to actually help me, even if she told me I was helping her. The dinner (and sometimes also run) coordinator Marcella Scarpa was always ready to organise us all, drive us everywhere among stuffed animals and was always there whenever a third shifter was needed. For all this, but most of all for trying to teach me how to be a good run coordinator, which I can’t learn for lack of diplomacy, I thank her.

I wish to thank the whole ETAP group and in particular its NA48 sub-group. Since it took me so long to finish my thesis, I have now to recall many names and I hope I don’t forget anybody: Matthias Behler, Andrey Belkin, Markus Bendel, Marco Gersabeck, Kirsten Eppard, Michael Eppard, Carsten Handel, Andreas Hirstius, Manuel Hita-Hochgesand, Frederik Kaster, Uwe Koch, Paulo Lopes Da Silva, Peter Marouelli, Irakli Mestvirishvili, Uli Moos-

Acknowledgements

brugger, Cristina Morales, Andi Peters, Burkhard Renk, Sven Schmidt, Ivette Schué, Khai Vinh Vi, Martin Wache, Rainer Wanke and Andi Winhart. The unlucky ones having to listen to me more often than the others: Matthias Behler, Marco Gersabeck, Cristina Morales, Martin Wache and Andi Winhart actually deserve a special award. Thanks to the admins: Uwe Koch, Peter Marouelli, Alexander Piegza, Dietrich Schroff and Martin Wache for never reducing my disk quota and for updating the system in the evening or even during holidays.

Two very special members of our group I still have to thank: Karl Heinz Geib, who can solve any technical problem and Silvia Müller who can solve any bureaucratic problem and takes care of us all. I thank them most of all for being ready to help me also when I am not able to explain them my problem because of my bad German or of my lack of understanding in the matter.

I owe a lot of my understanding of the K_{e4} form factors to the discussions with the Saclay group and in particular with Brigitte Bloch-Devaux. Even if we might have different opinions about the best analysis method, the work done together was always very agreeable and fruitful.

My parents taught me to take my own decisions, without worrying too much about what other people might think. I thank them for not regretting it, even when my decisions took me so far away from them. Two people out of the many I used to know in Ravenna, Maria Di Natale and Matteo Acciai, have all my gratitude for always finding time for me during my short and hasty visits back home. Finally, I have to thank Christian for so many reasons, but I want to mention only two: for never letting me be sad or angry more than a few minutes and for not getting upset at my making plans and not sticking to them.

Lebenslauf

Anschrift

Lucia Masetti
Essenheimer Str. 121b
55128 Mainz

Persönliche Daten

geboren: 28.04.1978 in Ravenna (Italien)
Staatsangehörigkeit: italienisch
Familienstand: verheiratet

Schulbildung

1984 – 1988 Grundschule in Ravenna
1988 – 1996 Gymnasium in Ravenna
1996 Abitur

Ausbildung

1996 – 2001 Studium der Physik an der Universität Ferrara (Italien)
2000 – 2006 Mitarbeit in der NA48-Kollaboration (CERN)
07.2000 – 03.2001 Diplomarbeit bei Prof. P. Dalpiaz und Dr. A. Ceccucci
mit dem Titel “Suche nach dem Zerfall $K_S \rightarrow \pi^0 \gamma \gamma$ ”
03.2001 Diplomprüfung im Fach Physik
2002 – 2006 Doktorandin im Fachbereich Physik der Universität Mainz
bei Prof. K. Kleinknecht